Plasma Physics Reports, Vol. 27, No. 10, 2001, pp. 819–824. Translated from Fizika Plazmy, Vol. 27, No. 10, 2001, pp. 867–872.

TOKAMAKS

History of the T-10 Tokamak: Creation and Development[1]

V. S. Strelkov

Institute of Nuclear Fusion, Russian Research Centre Kurchatov Institute, pl. Kurchatova 1, Moscow, 123182 Russia
e-mail: strelkov@nfi.kiae.ru

Received: May 24, 2001

Abstract—The heating and thermal insulation of a hot plasma with the purpose of achieving a controlled thermonuclear reaction have been investigated for almost 50 years. Experiments in the T-10 tokamak, which have been carried out for 25 years, have played an important role in such investigations. This paper presents a history of the device, the physical and technological foundations underlying the project, and the results obtained in the ohmic heating mode during the first years of the device operation. © *2001 MAIK "Nauka/Interperiodica".*

Investigations of the creation of a hot plasma and its thermal insulation by a toroidal magnetic field were initiated at the Kurchatov Institute, where the first TMP tokamak [1] was developed in 1954–1955. The TMP device was based on the concept of a magnetic thermonuclear reactor proposed by I.E. Tamm and A.D. Sakharov [2–4]. It had a porcelain toroidal discharge vessel (R = 0.8 m, r = 0.13 m). Equilibrium along the major radius was provided by the interaction between the magnetic field of the plasma current and the image currents induced in copper screens surrounding the discharge chamber. The plasma current attained 200 kA. The conditions of the discharge ignition and the stability of the plasma column were studied. The generation of runaway electrons in the toroidal discharge was observed [5].

Over the next two decades, a series of tokamaks were built at the Kurchatov Institute. These were the T-1, T-2, T-3, and T-4 devices; TM-series devices; and also T-5, T-6, and T-11 tokamaks. In the early 1970s, the results of experiments in these tokamaks and their theoretical interpretations led to a reorientation of scientific programs in fusion centers all over the world.

The T-1 tokamak had a thin-walled all-metal unbaked vessel (liner). In order to investigate the global plasma stability, a diaphragm was inserted into one of the ports. Initially, this diaphragm was intended to limit the region where the current flowed in order to observe the bending of the plasma column through the other port. The diaphragm was a forefather of modern limiters and divertor plates, which are now essential elements of any tokamak. Quantitative measurements of radiative loss showed that, in a tokamak with an unconditioned wall, a considerable part of the deposited power (80–90%) is lost due to the line radiation of impurity atoms and ions [6, 7], as in electrode discharges. To reduce the fraction of radiative loss in the plasma energy balance, a higher level of vacuum purity was required. This problem was solved in the T-2 tokamak, whose all-metal silphon liner could be baked up to 400°C and whose high-vacuum pumps provided an initial pressure at a level of $(2–3) \times 10^{-8}$ torr [8]. As a result, the fraction of radiative loss decreased to 30% and the electric conductivity and plasma temperature increased. However, a strange and initially unexplained phenomenon was observed: the current pulse did not repeat the waveform of the loop voltage, but had a two-humped shape; i.e., the electric conductivity and the electron temperature first decreased without visible reason and then increased again [9]. Later, it was understood that the two-humped current waveform was caused by the shift of the equilibrium plasma position in the equatorial plane under the action of stray magnetic fields. Issues concerning equilibrium were investigated in detail in the T-5 and T-6 experiments [10]. The accumulated data and experience allowed researchers to obtain a plasma with an electron temperature of about 1 keV and an ion temperature of a few hundred electronvolts in the T-3 tokamak and its subsequent modifications. Stable thermonuclear neutron emission was observed for the first time [11] in experiments with deuterium plasma in the T-3A device. Investigations of plasma thermal insulation in the T-3 and TM-2 tokamaks showed that the plasma energy confinement time in these devices was several times longer than that predicted by the empirical Bohm formula [12]. Recall that the investigations of the energy confinement time in stellarators performed at Princeton (USA) agreed with the Bohm formula. If the plasma confinement in toroidal devices were really described by the Bohm formula, the prospects of creating a fusion reactor would be doubtful because the energy confinement time would be too short.

By the mid-1960s, a large number of tokamak investigations had been carried out at the Kurchatov Institute. The main results can be summarized as follows:

[1] This paper and the paper by Yu.N. Dnestrovskij are devoted to the 25th anniversary of the T-10 tokamak.

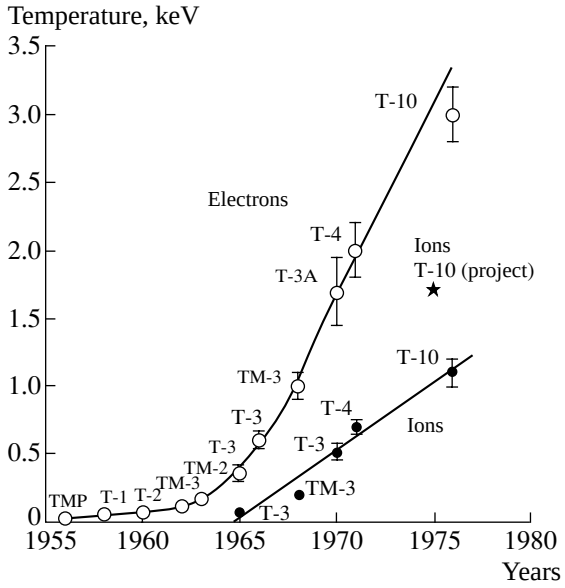

Fig. 1. Maximum electron and ion temperatures measured in the first tokamaks with ohmic heating.

(i) Conditions for the macroscopic stability of the current-carrying plasma column in the magnetic field were investigated theoretically and experimentally (Kruscal–Shafranov criterion).

(ii) The dominant role of the line radiation of impurity atoms and ions in the heat loss from the plasma was revealed.

(iii) Conditions for the toroidal plasma equilibrium along the major radius and in the vertical direction were demonstrated experimentally and validated theoretically.

(iv) Experiments showed that the plasma thermal insulation in tokamaks was several times better than that predicted by the Bohm formula, which, at that time, was confirmed by American experiments in stellarators (toroidal systems where the rotational transformation is produced by currents in external coils).

Experimental and theoretical investigations of plasma heating and cooling and progress in experimental techniques resulted in the improvement of plasma thermal insulation and an increase in the plasma temperature. The development of plasma diagnostics provided more information on the plasma parameters. Figure 1 presents the maximum electron and ion temperatures that could be obtained under ohmic heating in various tokamaks at that time.

In the late 1960s, the scientific community actively discussed the prospects and directions of investigations on controlled thermonuclear fusion [13, 14]. In 1967, a special commission under the chairmanship of E.P. Velikhov was organized by the joint resolution of the USSR Academy of Sciences and the State Committee for Atomic Energy. The commission's goal was to recommend further directions in fusion research and development. The commission became acquainted with the progress and activities in all fusion centers in the USSR and unambiguously recommended as a first priority the development of the tokamak program.

Experiments in tokamaks at the Kurchatov Institute were conducted in the department headed by Academician L.A. Artsimovitch. He was also a supervisor of the overall fusion program in the USSR. The parameters of a next-generation device were actively discussed in the tokamak department at the end of 1966. According to Artsimovitch, it would be "an ultimate device with ohmic heating." To achieve high temperatures, it was necessary to increase the ohmic heating power, i.e., to increase the plasma current, whose maximum value, according to the Kruscal–Shafranov criterion, was determined by the stabilizing toroidal magnetic field. On the other hand, a comparison of the results of experiments carried out in the T-3 tokamak with the results obtained in the twice-as-small TM-2 tokamak showed that the energy confinement times in plasmas with similar parameters approximately differed by a factor of 4. This pointed to the diffusion nature of losses; hence, an increase in the device dimensions would result in a higher plasma temperature.

Therefore, an analysis of experimental data and theoretical considerations showed that the limiting temperature should increase with the toroidal magnetic field and device dimensions, i.e., with the total energy stored in the toroidal magnetic field and, consequently, with the supplied power. Two main versions of the power supply were discussed: several impact-excitation generators (similar to those operating in T-3) in which energy is stored in flywheels or power supplied directly from the Moscow power grid through controlled thyristor converters. The latter version was actively supported by the director of the Kurchatov Institute Academician A.P. Alexandrov, who saw in it not only a new technical solution, but also the possibility of upgrading the energy capabilities of the institute as a whole. The coordination of this problem with the administration of the Moscow power grid showed that a power of up to 200 MW could be extracted over 10 seconds.

The final decision on the device operation parameters was made by L.A. Artsimovitch based on preliminary estimates performed at the Efremov Research Institute of Electrophysical Apparatuses (ERIEA) assuming the maximum available electric power consumption to be 200 MW.

In 1968, the physical project of the T-10 tokamak was formulated in detail. The project was based on the popular ideas at that time about the mechanisms for plasma heating and energy loss. The greatest uncertainty was related to the extrapolation of empirical scalings for the energy confinement time τ_E. Calculations with various τ_E dependences on the plasma parameters and tokamak dimensions were performed. It was shown that the maximum achievable temperature should increase with the energy stored in the power supply of

the toroidal field coils. A version with a high plasma current density and a moderate increase in linear dimensions (less than twice as large) in comparison with the T-3 device was adopted. The maximum values of the toroidal magnetic field and plasma current at the axis of the discharge chamber were accepted to be 5 T and 800 kA, respectively. The major radius of the torus was 1.5 m, and the minor radius of the toroidal discharge vessel was 0.39 m.

In November 1969, a meeting of the Fusion Section of the Scientific and Technology Council of the State Committee for Atomic Energy approved the preliminary design of the T-10 device developed at the ERIEA.

The design was based on the principles tested in previous devices: a magnetic transformer with an iron core allowed one to induce the plasma current with minimal stray fields, and an all-metal discharge vessel baked up to 500°C made it possible to attain an ultrahigh vacuum. The vessel consisted of silphons constituting a torus. The silphons ensured the high mechanical strength of a thin-walled vessel against both external and internal stresses, as well as a high ohmic resistance in the toroidal direction. In optimum modes of tokamak operation, the current flowing along the vessel amounted to a few percent or even less than one percent of the total plasma current. The plasma equilibrium against fast variations was provided by image currents in the copper shell surrounding the vessel, and slow variations were compensated by currents in a special controlling coil. A multiturn toroidal field coil was designed and manufactured with maximum accuracy in order to minimize stray magnetic fields. The design of the device provided its high reliability and allowed scientists to carry out experiments for more than 25 years without fundamental modernization of its main components. A large role in the development and implementation of the project was played by the collective of the ERIEA, headed by Academician V.A. Glukhikh. Special recognition is given to the now-deceased N.A. Monoszon for his contributions.

The implementation of the T-10 project required the reconstruction of certain buildings. The corresponding design was developed at the GIPRONII of the USSR Academy of Sciences.

Besides the construction of a vacuum vessel, coils, and power supply and the reconstruction of buildings, the creation of a large-scale tokamak includes the development of a research program. In parallel with the construction of T-10, experiments in the T-3A, T-4, TM-2, TM-3, and T-6 tokamaks were continued. Here, new phenomena were discovered; research programs were refined; new plasma diagnostics were developed; and, most importantly, the research team grew quantitatively and qualitatively.

In cooperation with specialized organizations, new diagnostics systems for measurements in T-10 were developed and created. The decree of the Soviet government in 1971 about the T-10 construction stimulated the intensification of fusion research in the USSR. An important role in the organization of these studies, the involvement of new institutes, and the development of international cooperation was played by N.S. Cheverev, the Deputy Head of the Accelerator and Thermonuclear Research Department of the State Committee for Atomic Energy.

As the deadline for putting the device into operation (the second quarter of 1975) approached, the rate of development increased. During the final stage, qualified specialists from many organizations worked hard and quickly on the creation of T-10. For example, the assembly of the first of the four vessel sections was started as late as March 1975; however, by June, the tokamak was already assembled, supplied with diagnostics, vacuum-tested, and pumped (Fig. 2). The mounting and adjustment of other systems in the autonomous mode was completed. At the end of June, the first attempts to obtain plasma began. At first, we did not succeed in achieving the simultaneous (without failure) operation of all systems. Then, all of the systems apparently operated, but a discharge was not ignited and, consequently, plasma was not produced. Finally, on Sunday, June 29 (the deadline was June 30), the first plasma current was observed in the 15th shot. The current was 15 or 30 kA. The exact current value was then unimportant; the main achievement was that the current existed. Putting T-10 into operation looked like an explosion of energy and enthusiasm. On July 1, 1975, a meeting devoted to this remarkable event was held.

In the autumn of 1975, regular T-10 experiments began. In the May issue of JETP Letters for 1976, the first paper on T-10 results was published [15]. In the summer of 1976, results of T-10 experiments were reported at the 6th International Conference on Plasma Physics and Controlled Fusion Research (Berhtesgaden, Germany) [16]. The tokamak was equipped with numerous diagnostics (Fig. 3), and the measurements pointed to high plasma parameters (Fig. 4). At the same conference, results obtained in the American PLT tokamak, which was put into operation somewhat later than T-10, were also reported [17].

Later, the ohmic heating of a pure plasma ($Z_{\text{eff}} \le 2$) was investigated in detail in T-10. In low-density regimes, the electron temperature attained 3 keV. An ion temperature of up to 1.1 keV was achieved in high-density regimes with a plasma density of up to 10^{14} cm^{-3}. The maximum energy confinement time was 80 ms, and the neutron yield from the *d*–*d* reaction was $(4–6) \times 10^9$ neutron/s. Stable discharges with a low safety factor at the edge $q = 1.7–2.5$ were obtained. An analysis of the plasma energy balance allowed one to determine the effective electron heat conductivity, which was very different in different plasma regions. The minimum electron heat conductivity was in the intermediate plasma region, whereas, at the axis, where $q < 1$, and at the edge, where $q > 2$, it increased. The behavior of

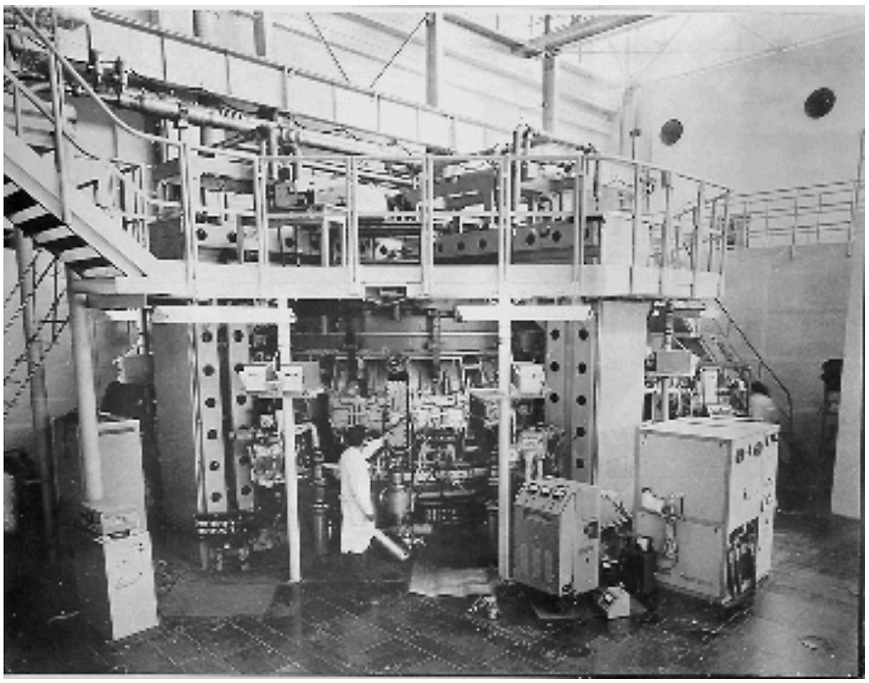

Fig. 2. General view of T-10 just after putting it into operation.

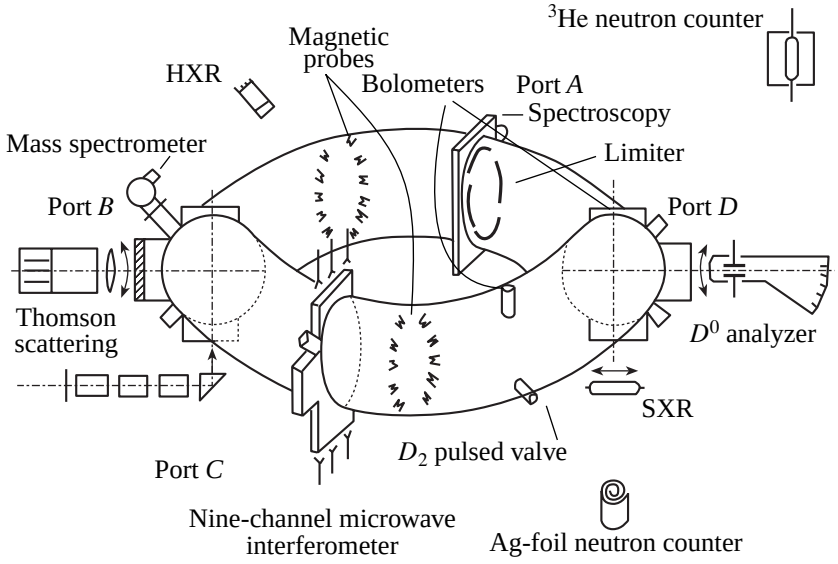

Fig. 3. Diagnostics facility of the T-10 tokamak (1976).

impurities and the confinement of the main particles were investigated. It was shown that, besides the intrinsic outward diffusion due to the density gradient, particle fluxes directed toward the plasma axis exist [18–21].

However, experiments in T-10 encountered a series of difficulties and failures. The greatest failure was related to the overheating of the toroidal field coils, which led to the destruction of the coil insulation and resulted in extensive repairs. The cause of this accident was, so to speak, excessive vigilance and reassurance. An energy sufficient for supplying a town with a population of about 100 000 citizens with electrical power

was concentrated in a volume of about 10 m^3. This represented a potential risk of failure; for this reason, all the necessary means of protection and blocking were envisaged in the design of the tokamak. However, the originality of experiments, the high cost of the device, and the great concentration of magnetic energy forced scientists to be overcautious at first. During the first years, the magnetic field was less than 3 T; therefore, it was decided not to elevate the coil voltage to the nominal level and to operate at a certain intermediate voltage. Thus, even under a failure of the control system, the current in the coils would be less than the limiting value. However, it happened that prolonged operation of the tokamak for one day led to a certain increase in the ohmic resistance of the coils. At such a lowered voltage, the coil current in this particular shot was less than the prescribed value. The control system did not receive the signal that the nominal value of the field was reached and, correspondingly, did not give the command to terminate the current after the prescribed time (1 s). The coil current flowed for a very long time (10–20 s) and was switched off manually by the operator. Overheating led to repairs and resulted in stopping the experiments for several months.

The plasma ohmic resistance decreases with plasma temperature, but the current density is limited. As time elapsed, researchers began to feel that the program of ohmic heating had run its course. Therefore, besides ohmic heating, it was decided to use additional methods of plasma heating and current drive in order to expand the experimental capabilities of the device. Owing to the structural features of the device, neutral beam injection was inappropriate; hence, it was necessary to choose between RF heating at the ion cyclotron resonance frequency and microwave heating at the electron cyclotron resonance (ECR) frequency.

Initially, both methods were tested; then, a choice was made in favor of ECR heating. There were many years of successful joint experiments in the TM-3 tokamak together with scientists from the Institute of Applied Physics (Nizhni Novgorod). Powerful microwave generators (gyrotrons) developed at that institute under the leadership of Academician A.V. Gaponov-Grekhov allowed one to increase the plasma heating power severalfold. The electron temperature reached 10 keV, which exceeded the expected limiting temperature for ohmic heating by more than a factor of 3. The profile of the deposited power and driven current over the plasma cross section could be varied and the plasma was able to be stabilized. These modern experiments are the subject of a paper by Dnestrovskij [22].

In the T-10 experiments, a large number of investigations were performed by teams from the Kurchatov Institute, the Ioffe Physicotechnical Institute, St. Petersburg State Technical University, the Institute of Applied Physics, and the Kharkov Institute of Physics and Technology (Ukraine), as well as by physicists from Great Britain, the Netherlands, Germany, Hungary, and other countries.

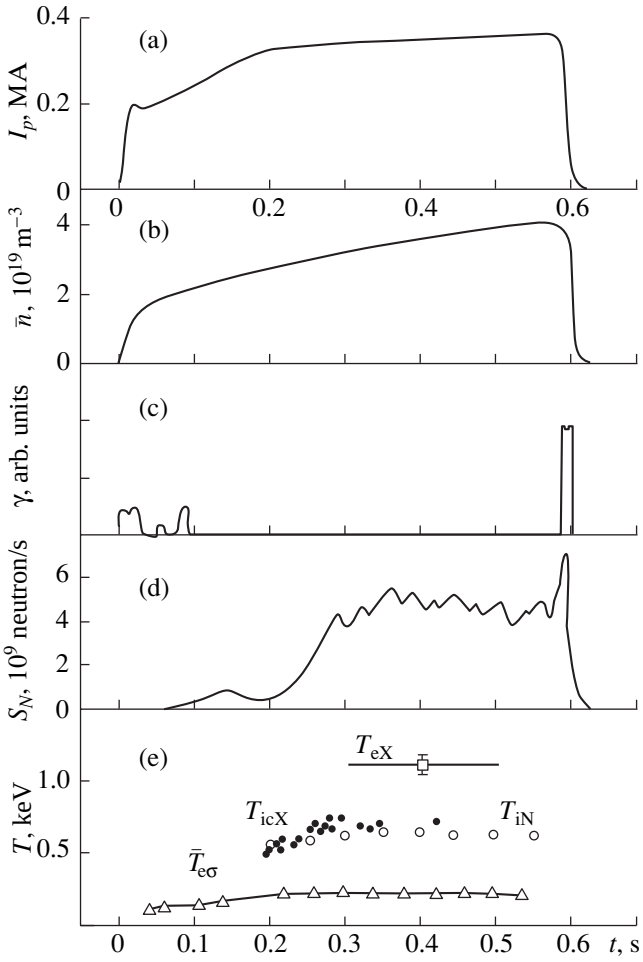

Fig. 4. Example of waveforms obtained in a stable T-10 shot: (a) plasma current; (b) line averaged density; (c) HXR intensity; (d) neutron yield; and (e) electron temperature T_{eX} deduced from the SXR spectrum, temperature $\bar{T}_{e\sigma}$ determined from the average electrical conductivity, ion temperature T_{icX} measured from the spectrum of charge-exchange neutrals, and ion temperature T_{iN} obtained from the neutron yield and plasma density.

ACKNOWLEDGMENTS

I am grateful to everyone who worked and are presently working on the T-10 tokamak. Twenty-five years is quite a long time for both scientists and the device, but it was the activity of the researchers that made it possible to formulate and solve important present-day problems of T-10. I would especially like to thank E.P. Gorbunov, V.S. Zaveryaev, and S.E. Lysenko for their assistance in preparing the manuscript. This work was supported by the Russian Foundation for Basic Research, project no. 00-15-96536.

REFERENCES

1. A. L. Bezbatchenko, I. N. Golovin, P. I. Kozlov, *et al.*, in *Plasma Physics and the Problem of Controlled Nuclear Fusion* (Akad. Nauk SSSR, Moscow, 1958), Vol. 4, p. 116.
2. I. E. Tamm, in *Plasma Physics and Problem of CTR* (Akad. Nauk SSSR, Moscow, 1958; Pergamon, Oxford, 1961), Vol. 1.
3. A. D. Sakharov in *Plasma Physics and Problem of CTR* (Akad. Nauk SSSR, Moscow, 1958; Pergamon, Oxford, 1961), Vol. 1.
4. I. E. Tamm in *Plasma Physics and Problem of CTR* (Akad. Nauk SSSR, Moscow, 1958; Pergamon, Oxford, 1961), Vol. 1.
5. V. S. Strelkov in *Plasma Physics and Problem of CTR* (Akad. Nauk SSSR, Moscow, 1958; Pergamon, Oxford, 1961), Vol. 4.
6. V. D. Kirillov, Zh. Tekh. Fiz. **30**, 320 (1960) [Sov. Phys. Tech. Phys. **5**, 295 (1960)].
7. G. G. Dolgov-Savel'ev, V. S. Mukhovatov, V. S. Strelkov, *et al.*, Zh. Éksp. Teor. Fiz. **38**, 394 (1960) [Sov. Phys. JETP **11**, 287 (1960)].
8. V. S. Vasilevskiĭ, V. S. Mukhovatov, V. S. Strelkov, and N. A. Yavlinskiĭ, Zh. Tekh. Fiz. **30**, 1137 (1960) [Sov. Phys. Tech. Phys. **5**, 1075 (1960)].
9. E. P. Gorbunov, G. G. Dolgov-Savel'ev, V. S. Mukhovatov, *et al.*, Zh. Tekh. Fiz. **30**, 1152 (1960) [Sov. Phys. Tech. Phys. **5**, 1089 (1960)].
10. V. S. Mukhovatov, in *Proceedings of the Conference on Plasma Physics and Controlled Nuclear Fusion Research, Culham, 1966* (IAEA, Vienna, 1966), Vol. 2, p. 177.
11. L. A. Artsimovich, A. M. Anashin, E. P. Gorbunov, *et al.*, Pis'ma Zh. Éksp. Teor. Fiz. **10**, 130 (1969) [JETP Lett. **10**, 82 (1969)].
12. L. A. Artsimovich, G. A. Bobrovskij, S. V. Mirnov, *et al.*, At. Énerg. **22**, 259 (1967).
13. L. A. Artsimovich, Usp. Fiz. Nauk **91**, 365 (1967) [Sov. Phys. Usp. **10**, 117 (1967)].
14. B. B. Kadomtsev, Usp. Fiz. Nauk **91**, 380 (1967) [Sov. Phys. Usp. **10**, 127 (1967)].
15. A. B. Berlizov, N. V. Vasin, V. P. Vinogradov, *et al.*, Pis'ma Zh. Éksp. Teor. Fiz. **23**, 502 (1976) [JETP Lett. **23**, 457 (1976)].
16. A. B. Berlizov, G. A. Bobrovskij, A. A. Bagdasarov, *et al.*, in *Proceedings of the Conference on Plasma Physics and Controlled Nuclear Fusion Research, Berchtesgaden, 1976* (IAEA, Vienna, 1977), Vol. 1, p. 3.
17. D. Grove, V. Arunasalam, K. Bol, *et al.*, in *Proceedings of the Conference on Plasma Physics and Controlled Nuclear Fusion Research, Berchtesgaden, 1976* (IAEA, Vienna, 1977), Vol. 1, p. 21.
18. V. S. Strelkov, Vestn. Akad. Nauk SSSR **8**, 39 (1977).
19. A. A. Bagdasarov, A. B. Berlizov, N. N. Vasin, *et al.*, in *Proceedings of the Conference on Plasma Physics and Controlled Nuclear Fusion Research, Innsbruck, 1978* (IAEA, Vienna, 1979), Vol. 1, p. 35.
20. A. B. Berlizov, V. I. Bugarja, V. V. Buzankin, *et al.*, in *Proceedings of the Conference on Plasma Physics and Controlled Nuclear Fusion Research, Brussels, 1980* (IAEA, Vienna, 1981), Vol. 1, p. 23.
21. A. B. Berlizov, V. V. Buzankin, V. P. Vinogradov, *et al.*, Fiz. Plazmy **6**, 249 (1980) [Sov. J. Plasma Phys. **6**, 138 (1980)].
22. Yu. N. Dnestrovskij, Fiz. Plazmy **27**, 873 (2001) [Plasma Phys. Rep. **27**, 825 (2001)].

Translated by G. V. Shepekina

Plasma Physics Reports, Vol. 27, No. 10, 2001, pp. 825–842. Translated from Fizika Plazmy, Vol. 27, No. 10, 2001, pp. 873–891.

TOKAMAKS

Physical Results of the T-10 Tokamak

Yu. N. Dnestrovskij, on behalf of the T-10 Team

Institute of Nuclear Fusion, Russian Research Centre Kurchatov Institute, pl. Kurchatova 1, Moscow, 123182 Russia

e-mail: dnyn@nfi.kiae.ru

Received April 26, 2001

Abstract—The history of the T-10 tokamak and scientific results obtained over the last 15–20 years are reviewed. The following issues are discussed in detail: electron cyclotron resonance heating (ECRH), the consistency of the electron temperature profiles, the density limit, the electron cyclotron current drive, suppression of sawtooth oscillations, experiments with reversed shear and the search for internal transport barriers, the H-mode and the edge transport barrier, pellet injection into the ECRH plasma, suppression of the higher MHD modes, and the investigation of turbulence. © *2001 MAIK "Nauka/Interperiodica".*

1. SHORT HISTORY OF T-10 FROM 1982 TO 2000

The decision to create the T-15 tokamak in the building of the Plasma Physics Division at the Kurchatov Institute of Atomic Energy was made in 1978. The first step in creating the new machine—the reconstruction of the building—began at the end of the 1970s. By 1982, five small tokamaks (TM-G, TM-4, T-8, T-9, and T-11) were disassembled. The first superconducting tokamak in the world, T-7, was also shut down. Scientific investigations were continued only in T-10 and the small T-13 tokamak.

However, in 1983–84, it became clear that creating T-15 would be delayed for about four to five years. Also, the plasma physics community suddenly realized that the T-15 project did not provide for the continuation of the T-10 operation, which would also be shut down very soon. After several months of active discussions, it was decided to change the T-15 project in order to preserve T-10 and to develop investigations with it.

As the first step, the gyrotron array was radically upgraded in collaboration with the Institute of Applied Physics (Nizhni Novgorod). Over two years, eleven gyrotrons with cryostats and systems for feeding power to the plasma were installed and the power supply was modified. The gyrotron array consisted of seven tubes with a wavelength of $\lambda = 3.69$ mm (81.4 GHz) and four tubes with $\lambda = 4$ mm (75 GHz). To heat the plasma at the first electron cyclotron harmonics, an O-wave was launched perpendicularly to the magnetic field. The power of each tube was 0.2–0.3 MW; thus, the total array power exceeded 2 MW at a pulse duration of about 100 ms. By 1987, the array development was completed and experiments began.

Approximately one year later, ideas about experiments with the electron cyclotron current drive (ECCD) emerged. For this purpose, the array was reconstructed in 1990. In some ports, mirrors were mounted in order to reflect microwave rays in the toroidal direction. A launching angle of 21° with respect to the major radius was fixed. Such a system allowed us to perform efficient ECCD experiments. Figure 1 shows a schematic of the T-10 gyrotron array as it was in 1990 [1].

The operation of the array consisting of eleven gyrotrons was hampered by large stray magnetic fields. For this reason, in the early 1990s, when higher frequency (140–160 GHz) and more powerful (up to 0.4 MW) gyrotrons with a longer pulse duration (up to 0.4 s) were developed, it was decided to reconstruct the array again. At the end of 1992, the reconstruction was completed. Instead of eleven old gyrotrons, four new ones with a total power of up to 1.5 MW were installed. The ray geometry remained unchanged, but now the second harmonics of the X-mode was used [2].

Over the next decade, the gyrotron array remained virtually unchanged. The disintegration of the USSR and reductions in science funding did not allow any upgrades to be performed in spite of significant progress in gyrotron technology. By using the tradi-

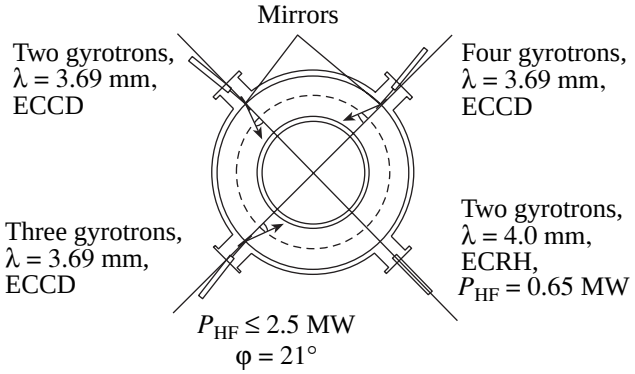

Fig. 1. Arrangement of the T-10 gyrotron array in 1990.

1063-780X/01/2710-0825$21.00 © 2001 MAIK "Nauka/Interperiodica"

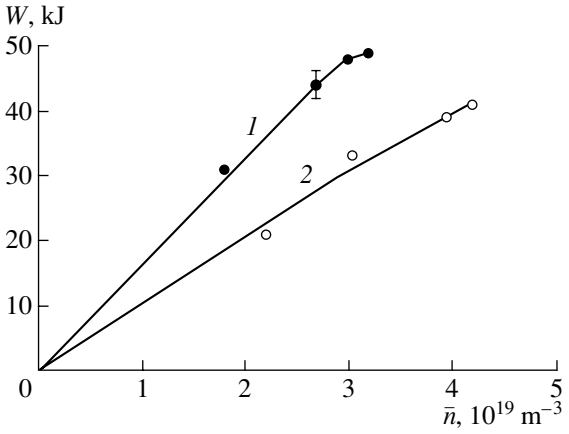

Fig. 2. Linear dependence of the stored plasma energy on the plasma density. Curves *1* and *2* correspond to the total power P_{tot} = (*1*) 2 and (*2*) 1.2 MW.

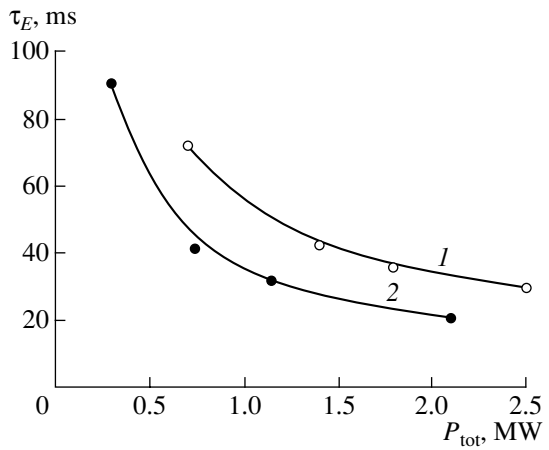

Fig. 3. Energy confinement time vs. the deposited power (*1*) at the current I_p = 420 kA and density $\bar{n} = 4.4 \times 10^{19}$ m^{-3} and (*2*) at I_p = 210 kA and $\bar{n} = 3 \times 10^{19}$ m^{-3}.

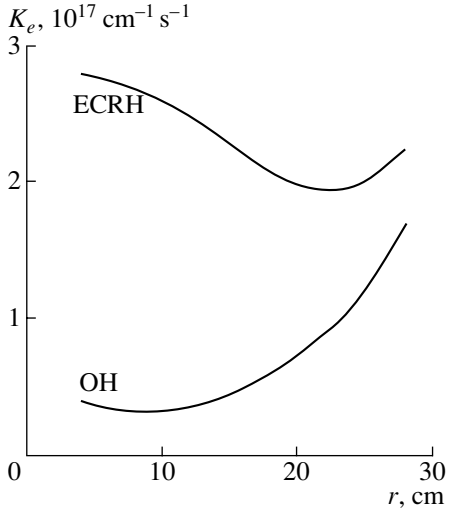

Fig. 4. Profiles of the thermal conductivity in the ohmic mode and under ECRH at the power P_{EC} = 1 MW, I_p = 170 kA, and $\bar{n} = 3 \times 10^{19}$ m^{-3}.

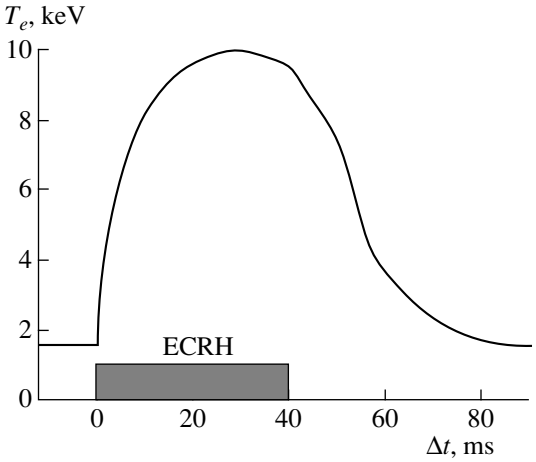

Fig. 5. Waveform of the central electron temperature in a shot with a record value of $T_e(0) \sim 10$ keV obtained in 1987.

tional cooperation with the Institute of Applied Physics, we just managed to keep the array capable of operating.

During the 1990s, in spite of financial problems, the T-10 diagnostics complex was developed considerably. Even in the Soviet era, the device possessed a multichannel interferometry (up to 16 channels) for measuring the plasma density profile. The number of channels for measurements of the electron temperature profile using the second harmonic of electron cyclotron emission was permanently upgraded. A multichannel soft X-ray (SXR) tomographic system was developed. The first measurements of the plasma potential were performed using a unique heavy ion beam probing (HIBP) diagnostics with an ion energy of up to 230 keV. Frequency-scanning reflectometry allowed us to measure the plasma density gradients. Rapidly developing correlation reflectometry made it possible to study the spatial and spectral characteristics of plasma turbulence in various regimes, including regimes with an internal transport barrier (ITB).

2. SCIENTIFIC RESEARCH

2.1. Electron Cyclotron Resonance Heating

For several years after installing the new gyrotron array in 1986–87, experiments were aimed at studying the main characteristics of plasma heating [3, 4]. As early as the beginning of the 1980s, it was shown that the total energy stored in the plasma $W = \int_V n(T_e + T_i)dV$ under

electron cyclotron resonance heating (ECRH) scales linearly with the electron density. New experiments confirmed this scaling. The linear growth of W is observed up to densities of $\bar{n} \sim 3 \times 10^{19}$ m^{-3}, at which the refraction of waves with a frequency of $f \sim 80$ GHz becomes appreciable (Fig. 2). Investigations of the energy confinement time τ_E as a function of the total input power P_{tot} showed that confinement deteriorates with power: $\tau_E \sim 1/P_{\text{tot}}^{1/2}$ (Fig. 3). This result is in good agreement with a more recent ITER scaling [5], based on the data obtained in different devices operating in the L-mode.

The measurements of the electron temperature profiles under ECRH allowed us to study heat transport in more detail. It was shown that, under ECRH, the local values of thermal conductivity $K_e = n\chi_e$ increase in comparison with the ohmic heating phase (Fig. 4). At an input power of ~1 MW, the value of K_e in the plasma core increases by a factor of 4–5.

In one of the experiments carried out in 1987, a record (for that time) electron temperature of T_e = 10 keV was achieved (Fig. 5). Therefore, the widespread opinion about the existence of a limiting electron temperature of $T_e^{\max} \sim 5$–7 keV in tokamaks turned out to be erroneous. Note that the record of T-10 was then surpassed in larger tokamaks; however, even now (i.e., 15 years later), the maximum values of the electron temperature do not exceed 15 keV.

2.2. Consistency of the Electron Temperature Profiles

A strange plasma behavior—the consistency of the electron temperature profile under external action—was first pointed out by Coppi [6]. He also formulated the "profile consistency principle," according to which, in the ohmic regime and in the L-mode, the electron temperature distributions tend to certain peculiar ("canonical") profiles. Later, Kadomtsev [7] and other authors [8, 9] derived analytical expressions for canonical profiles. Then, a relevant transport model was developed [10].

The T-10 gyrotrons with different frequencies made it possible to verify the canonical profile principle. Figure 6 shows the results of experiments with two groups of gyrotrons with approximately the same total power [1]. In the first series of experiments, three gyrotrons with the same frequency were used. In this case, the profile of the power deposition was very peaked on the axis, the maximum specific power deposition being up to 3 W/cm^3. In the second series, one gyrotron providing on-axis power deposition and four gyrotrons providing off-axis power deposition (at a distance of 16 cm from the axis) were used. In this case, the power deposition profile was almost flat. The specific power on the axis was lower than in the first series by a factor of 4 and did not exceed 0.7 W/cm^3 (Fig. 6a). Figure 6b

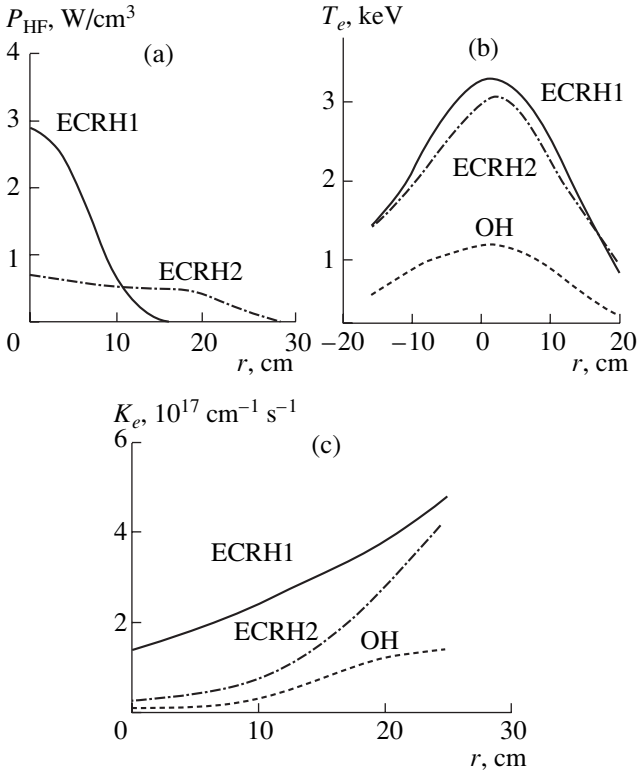

Fig. 6. Experiments with the peaked (ECRH1, P_{EC} = 0.63 MW) and flat (ECRH2, P_{EC} = 0.85 MW) profiles of the deposited power (a). The corresponding electron temperature profiles (b) are close to each other, but the thermal conductivities (c) differ severalfold. Dashed lines correspond to the ohmic mode.

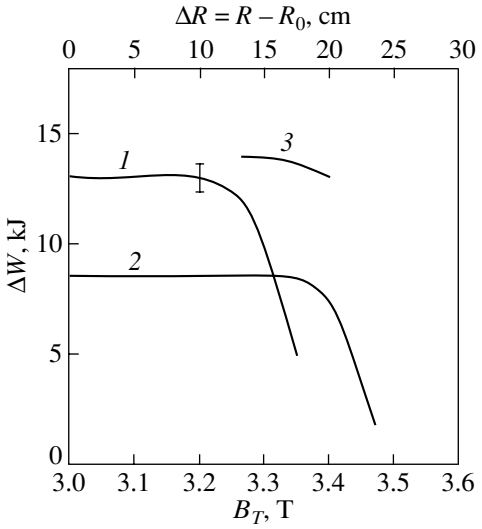

Fig. 7. Increment in the stored plasma energy vs. the toroidal field (the position of the ECRH region) for (*1*) I_p = 170 kA, $\bar{n} = 3 \times 10^{19}$ m^{-3}, and P_{EC} = 820 kW; (*2*) I_p = 270 kA, $\bar{n} = 3 \times 10^{19}$ m^{-3}, and P_{EC} = 640 kW; and (*3*) I_p = 270 kA, $\bar{n} = 4.5 \times 10^{19}$ m^{-3}, and P_{EC} = 920 kW. The top scale shows the distance between the center of the ECRH region and the plasma axis.

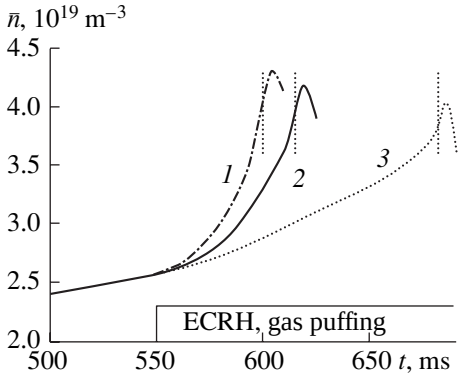

Fig. 8. Time evolution of the average plasma density at a fixed heating power P_{EC} = 330 kW and different gas puffing rates. Curves *1–3* are numbered in descending order of the gas puffing rate.

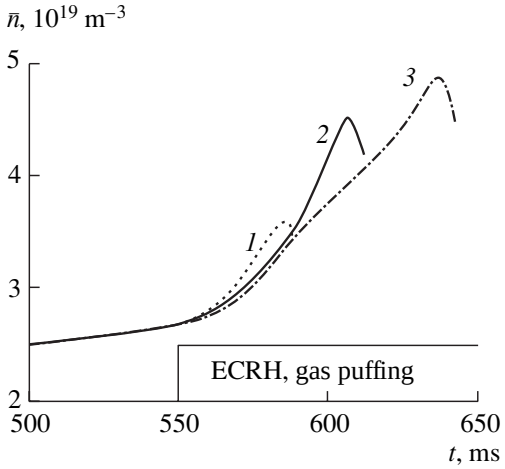

Fig. 9. Time evolution of the average plasma density at a fixed gas puffing rate and different ECRH: P_{EC} = (*1*) 0, (*2*) 1, and (*3*) 1.6 MW.

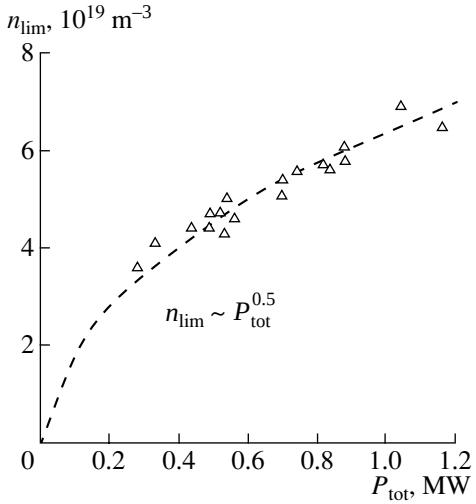

Fig. 10. Experimental dependence of the density limit on the total deposited power at a fixed current. The dashed line corresponds to the dependence $n_{lim} \sim P_{tot}^{0.5}$.

shows the results of the experiments, which seem to be quite exciting. The absolute values of the electron temperature and its gradients differ by less than 10%. However, the corresponding values of the thermal conductivity K_e in the plasma core differ by a factor of more than 5; i.e., heat fluxes in the plasma changed sharply to maintain the electron temperature profile.

In other experiments, the behavior of the global plasma parameters was studied as a function of the outward radial shift of the power deposition profile. Figure 7 presents the dependences of the increment in the stored plasma energy ΔW on the toroidal magnetic field B_T for different discharge currents and plasma densities. The corresponding shift ΔR of the position of the power deposition maximum from the plasma axis is shown at the top of Fig. 7. It can be seen that, up to $\Delta R \sim 15$–20 cm, the value of ΔW changes only slightly. In this case again, heat fluxes in the plasma are redistributed so as to keep the temperature profile unchanged. A more detailed analysis shows that, at high B_T, ΔW starts to decrease when the power deposition region approaches the position of the resonant magnetic surface $q(r_S) = 2$.

2.3. Density Limit

The existence of the density limit n_{lim} in tokamaks was discovered in the 1960s. As the average plasma density $\bar{n}$ approaches n_{lim}, MHD oscillations arise, which is followed by discharge disruption.

The value of n_{lim} depends on many factors. Particularly, it can be increased by cleaning the plasma chamber wall. For a sufficiently clean chamber, M. Greenwald proposed the scaling [11]

$$n_{lim} \approx n_{Gr}(10^{20}\ \text{m}^{-3}) = I\ [\text{MA}]/(\pi a^2\ [\text{m}^2]), \quad (1)$$

which relates the density limit to the average current density. T-10 experiments showed that n_{lim} increases with deposited power.

In experiments on the density limit [12–14], the dependence of n_{lim} on the T-10 discharge conditions under ohmic heating and ECRH was studied in detail. Figure 8 shows the time evolution of the plasma density at different gas puffing rates and the fixed heating power P_{EC} = 0.33 MW. We can see that the increase in the gas puffing rate leads to an increase in the density growth rate dn/dt. However, the limiting density, at which MHD oscillations arise and the density starts to fall, is almost independent of the gas puffing rate. The situation illustrated in Fig. 9 is opposite. Here, the gas puffing rate is fixed and the total deposited power P_{tot} is varied. It can be seen that the density limit increases with P_{tot}. The results of these experiments are summarized in Fig. 10, which shows the experimental values of n_{lim} for different shots with approximately the same

currents as functions of P_{tot}. We can see that n_{lim} scales with power approximately as

$$n_{lim} \sim P_{tot}^{1/2}. \quad (2)$$

Formula (2), first derived for T-10, does not contradict experiments in other tokamaks.

Special attention was paid to a comparison of the experimentally determined density limit n_{lim} with the Greenwald scaling n_{Gr} (1). It was shown (Fig. 11) that, as the current decreases, the n_{lim} value becomes considerably higher than n_{Gr}. Therefore, instead of (1), a new formula for n_{lim} was proposed:

$$n_{lim} \approx n_{Gr}^{mod}\,(10^{20}\ \mathrm{m}^{-3}) = I\ [\mathrm{MA}]/(\pi a_C^2\ [\mathrm{m}^2]), \quad (3)$$

where a_C is the current radius defined as the radius of the magnetic surface enclosing 95% of the plasma current [13].

An analysis of the plasma behavior at densities close to the density limit shows that the particle confinement at the edge strongly deteriorates. The particles that are created at the edge cannot penetrate into the core, but are rapidly expelled. As a result, the density profile is peaked and energy confinement is not degraded up to the densities $\bar{n} \sim 0.9 n_{lim}$.

2.4. Electron Cyclotron Current Drive

The mounting of mirrors deflecting EC waves in the toroidal direction at an angle of 21° to the major radius allowed us to begin ECCD experiments in 1990. The driven current I_{CD} was measured by comparing the loop voltages during co-current drive (co-CD) and counter-current drive (counter-CD). Here, co-CD means the current generation in the direction of the main (ohmic) plasma current and counter-CD means the current generation in the oppose direction [15].

First, we note that the electron distribution function is modified by obliquely propagating waves. Figure 12 shows SXR spectra (a) for microwave launching at an angle of 21° and (b) for microwave launching perpendicularly to the magnetic field (the first harmonic of the O-mode). We can see that, at the perpendicular launching, the distribution function is Maxwellian up to energies of ~$10T_e$. In this case, the driven current is absent. At the oblique launching, the waves drive the current and the electron distribution function deviates from Maxwellian at energies of 4–$5T_e$. Calculations show that an appreciable fraction of the driven current I_{CD} is carried by electrons with energies of 5–$6T_e$.

Recall that the onset of the driven current is characterized by two time scales, τ_{ee} and τ_S. Here, τ_{ee} is the time during which the electron distribution function is modified after gyrotrons are switched on. It is determined by the rate of electron-electron collisions at energies of ~$5T_e$ and is usually less than 0.1–0.2 ms. The rapid growth of the driven current I_{CD} over the time

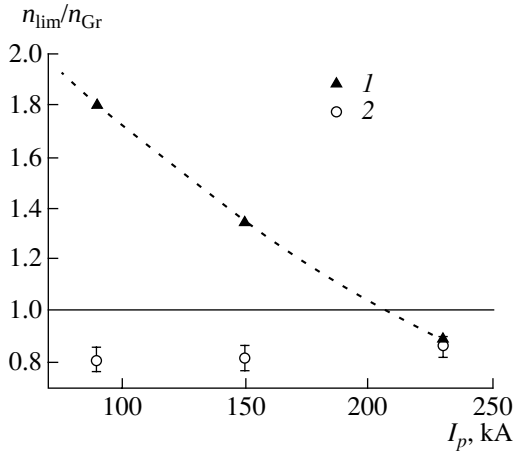

Fig. 11. (*1*) The ratio of the experimental density limit to the Greenwald density n_{lim}/n_{Gr} vs. the plasma current and (*2*) the modified Greenwald density scaling n_{lim}/n_{Gr}^{mod} proposed in [13].

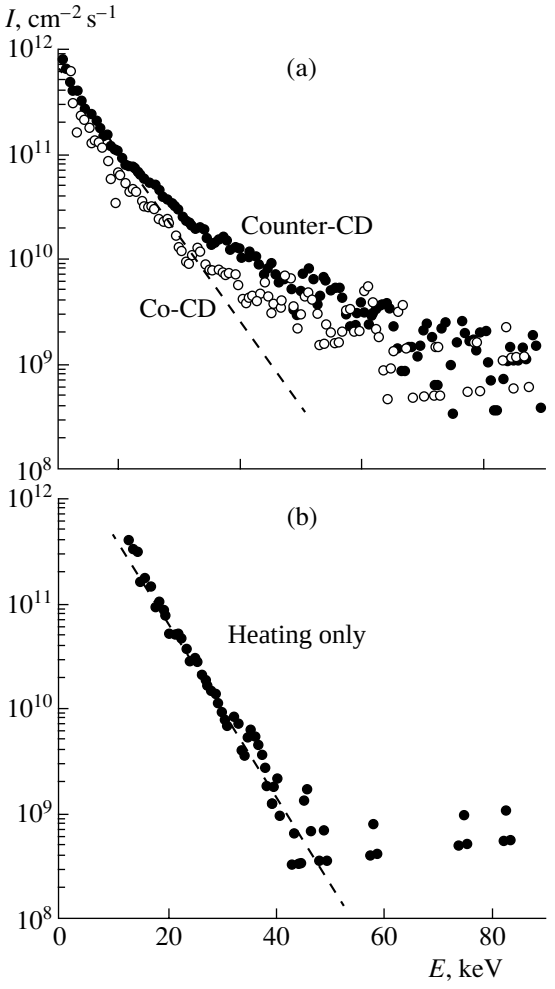

Fig. 12. SXR spectra obtained with (a) oblique (co-CD shot no. 52 407, counter-CD shot no. 52417, T_e = 5.38 keV, t = 620–720 ms, 1.9-cm chord) and (b) perpendicular (shot no. 52407, T_e = 5.25 keV, t = 420–520 ms, 1.9-cm chord) launching of EC waves into the plasma.

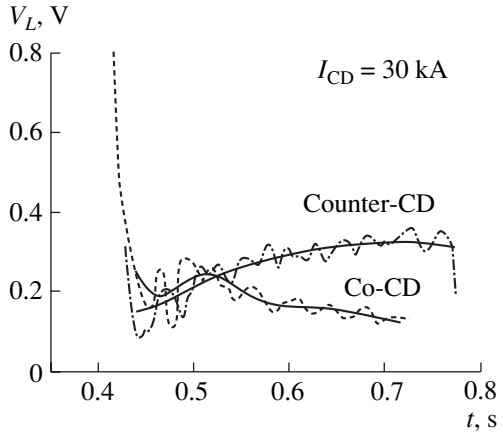

Fig. 13. Time evolution of the loop voltage during co- and counter-CD.

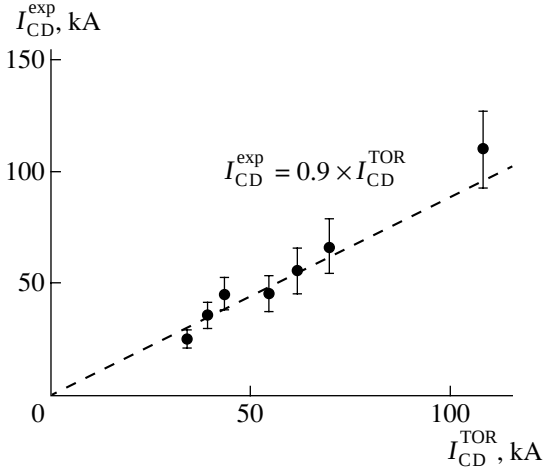

Fig. 14. Comparison of the measured current driven by the first EC harmonic with that calculated by the TORAY code.

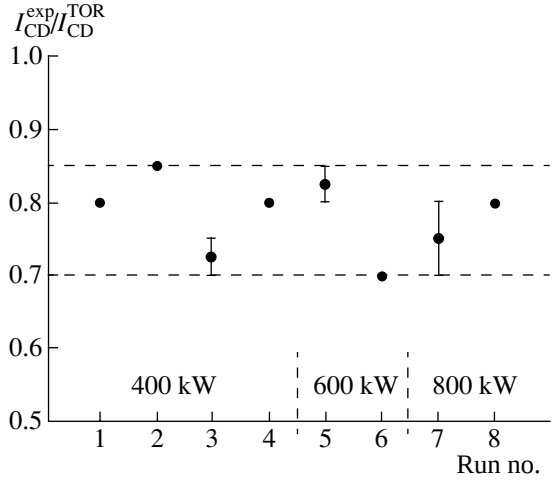

Fig. 15. The ratio of the measured current driven by the second EC harmonic to that calculated by the TORAY code for different experimental runs.

τ_{ee} leads to the appearance of the induced ohmic current, which has the same magnitude but flows in the opposite direction, thus balancing the current I_{CD}. The induced current relaxes with the characteristic time τ_S, which depends on the ratio I_{CD}/I_p, and, in T-10, is equal to 100–200 ms (three orders of magnitude greater than τ_{ee}). Only after this time is a steady state established and does the loop voltage at the edge correspond to the driven current.

In experiments, the total plasma current I_p is kept unchanged by feedback. Therefore, co-CD (counter-CD) finally leads to a decrease (increase) in the loop voltage to the value $\Delta U^{Co} < 0$ ($\Delta U^{Counter} > 0$). At the heating power $P_{EC} \sim 1$ MW and $T_e \sim 4$ keV, the change in the voltage is small, $|\Delta U^{Co}| \sim |\Delta U^{Counter}| \sim 0.1$–$0.15$ V. Hence, the requirements of the discharge reproducibility are rather strict. Moreover, since the T-10 mirrors are fixed, we have to compare discharges with oppositely directed currents I_p. When operating with eleven gyrotrons, additional problems arise due to the short pulse duration (~100 ms) of each tube. Therefore, the array has to be divided into groups and these groups need to be switched on sequentially, one after another. As an example, Fig. 13 shows the waveforms of the loop voltage in two shots with co- and counter-CD.

Theoretical calculations of the ECCD efficiency were usually performed with the ray-tracing code TORAY [16]. This code calculates the ray trajectories in the quasi-classical approximation, and the wave absorption is determined by the anti-Hermitian part of the weakly relativistic plasma permittivity tensor.

The results of experiments performed in 1990 at the first EC harmonic are summarized in Fig. 14, where the experimental and calculated values of the current I_{CD} are compared. We can see that the maximum current attained in experiments is ~110 kA and the ratio $h = I_{CD}^{exp}/I_{CD}^{TOR}$ is higher than 0.9. Here, I_{CD}^{TOR} is the current calculated by the TORAY code.

After gyrotrons with the frequency f = 140 GHz were installed, ECCD experiments were continued, but at the second EC harmonic. Preliminary estimates showed that, in this case, the ECCD efficiency should be half as much as that at the first harmonic and, accordingly, the driven current should decrease. After two years of hard work, researchers acquired skill in reliable measurements of small driven currents. Results of experiments with the second EC harmonic are summarized in Fig. 15, where the ratio $h = I_{CD}^{exp}/I_{CD}^{TOR}$ is shown for a series of shots with different microwave powers. We can see that $h \sim 0.8$. A subsequent detailed analysis of these experiments showed that, in actuality, $h \sim 1$, because only a fraction of the microwave power was launched into the plasma as the X-mode. For the electron temperature $T_e \sim 3$–4 keV, the experimental CD efficiencies at the first and second EC harmonics are

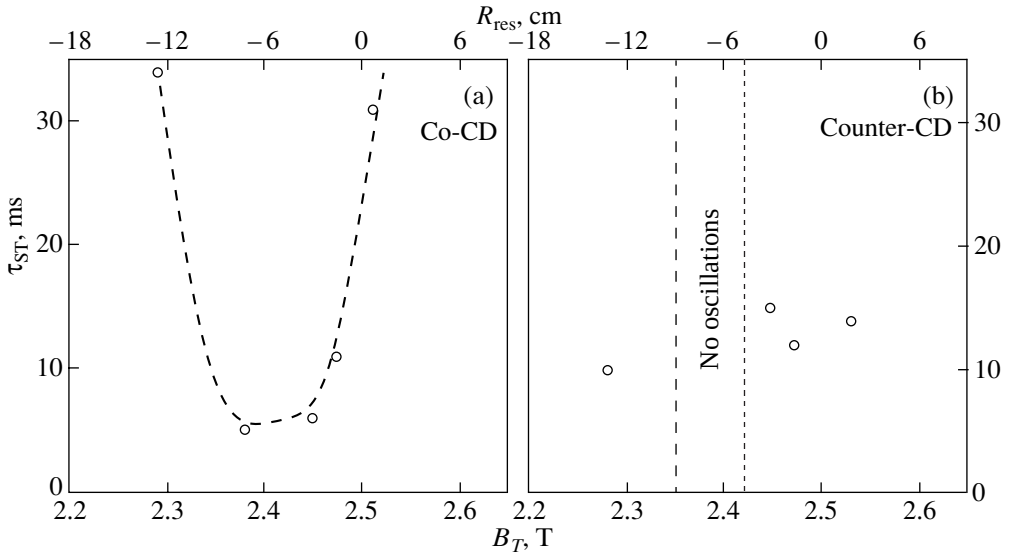

Fig. 16. Sawtooth oscillation period τ_{ST} vs. the toroidal magnetic field for (a) co- and (b) counter-CD. The top horizontal axis shows the position of the resonant surface R_{res}.

$\gamma = nI_{CD}R/P_{EC} = 3 \times 10^{18}$ and 1.3×10^{18} m^{-2} MA/MW, respectively.

2.5. Suppression of Sawtooth Oscillations

Investigations of ECCD opened wide opportunities to use this phenomenon to act on the plasma [17, 18]. For example, Fig. 16 demonstrates how ECCD modifies sawtooth oscillations. The figure shows the dependence of the sawtooth period on the toroidal magnetic field B_T under (a) co- and (b) counter-CD. In order to correctly understand Fig. 16, we should bear in mind that, at the oblique microwave launching, the center of the absorption zone R_{EC} is shifted by 5–6 cm outward with respect to the resonant surface R_{res}. In Fig. 16, the top horizontal scale shows the position of the resonant surface. Due to the shift, the value $R_{res} = -6$ cm approximately corresponds to the on-axis power deposition, $R_{EC} \approx 0$.

We can see from Fig. 16 that, under on-axis co-CD, the sawtooth period decreases. This corresponds to intuitive ideas about the behavior of sawtooth oscillations when the current profile is peaked. Both decreasing and increasing R_{EC} result in an increase in the sawtooth period. Finally, at $|R_{EC}| > 6$–7 cm, sawtooth oscillations are suppressed. The effect of total suppression of sawtooth oscillations was observed for the first time in T-10.

For counter-CD, the situation is quite different. Under on-axis ECRH, sawtooth oscillations are suppressed. When the resonance is shifted by more than 3 cm, sawtooth oscillations with a period close to that in the ohmic regime appear.

2.6. Experiments with Reversed Shear and the Search for the Internal Transport Barrier

Another example of applying ECCD is experiments with the formation of a flat or hollow current profile in the plasma core [19–21]. In this case, the profile of the safety factor $q(r)$ also becomes flat or nonmonotonic and the quantity $s = r/q\, dq/dr$ (the magnetic shear) at the point where q is minimum changes its sign. The larger the ratio I_{CD}/I_p, the larger q_{min} value that can be attained. The zone where $s < 0$ is usually called the reversed shear zone.

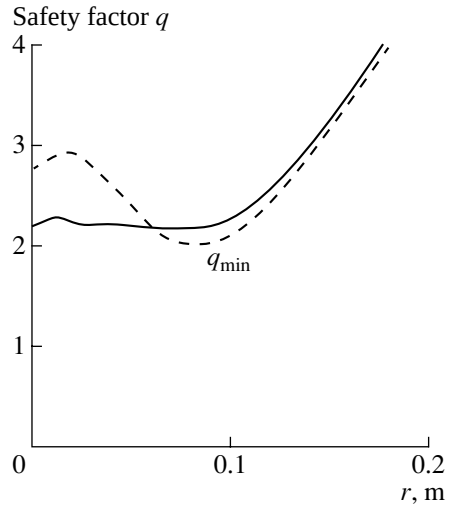

Fig. 17. Typical calculated $q(r)$ profiles for on-axis counter-CD (dashed line) and off-axis co-CD (solid line).

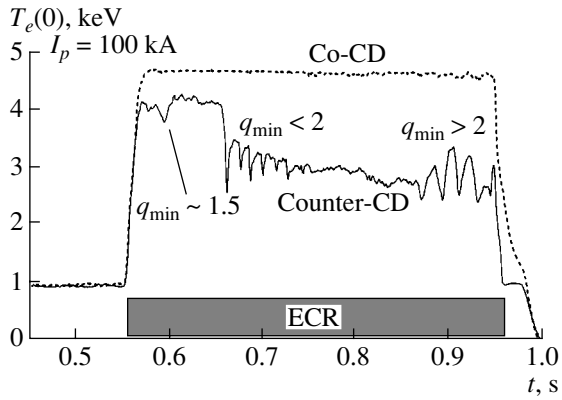

Fig. 18. Time evolution of the central electron temperature during co- and counter-CD for the current I_p = 100 kA, absorbed power P_{ab} = 0.85 MW, and plasma density $\bar{n} = 10^{19}$ m^{-3}.

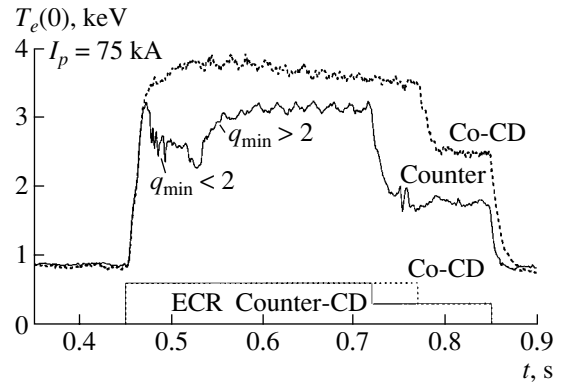

Fig. 19. Time evolution of the central electron temperature during co- and counter-CD for the current I_p = 75 kA, absorbed power P_{ab} = 0.84 MW, and plasma density $\bar{n} = 10^{19}$ m^{-3}.

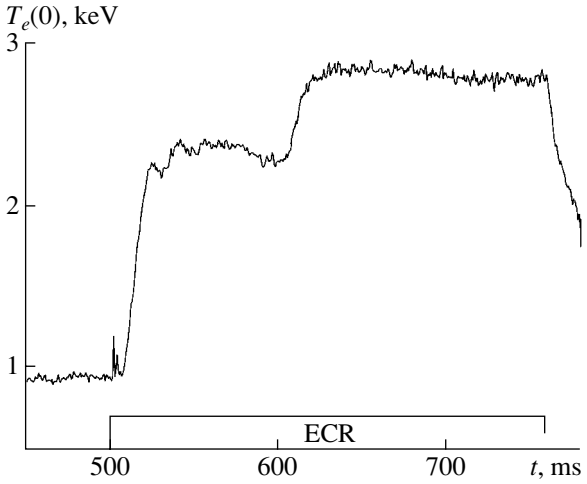

Fig. 20. Time evolution of the central electron temperature during off-axis co-CD (shot no. 20918). The increase in the temperature at $t \sim 620$ ms corresponds to the formation of an ITB.

Experiments performed in other tokamaks have shown that, at a small or reversed shear, an internal transport barrier (ITB) can form. A common opinion is that, for an ITB to appear, two conditions should be satisfied. First, the pressure gradient should exceed a certain critical value. Second, the value q_{min} (or q_{pl} at the plateau of the current profile) should be close to the rational value $q = m/n$ with sufficiently small m and n. The main problem is that, if the q profile is nonmonotonic and q takes the resonant value $q = m/n$ twice, then MHD oscillations (typically, the double tearing mode) arise. This MHD activity impedes the barrier formation and leads to the deterioration of energy confinement in the core.

A flat or non-monotonic current profile can form under on-axis counter-CD or off-axis co-CD [19]. In T-10 experiments, both of these cases were studied (Fig. 17). Since the absolute value of the current I_{CD} driven by the second EC harmonic is small, we operated at low discharge currents. Even for I_p = 150 kA and the high microwave power $P_{EC} \sim 1$ MW, the value of q_{min} was no higher than 1.5. Therefore, the main features related to the $q \sim 2$ value manifested themselves only at currents of $I_p \le 100$ kA.

Figure 18 shows the time evolution of the central electron temperature for on-axis power deposition, plasma current I_p = 100 kA, and two ECCD directions [20]. We can see that, in the reversed shear regime (counter-CD), 100 ms after the gyrotron is switched on, a series of internal disruptions occurs, which sharply deteriorates energy confinement. These disruptions look like saturated sawtooth oscillations. A detailed analysis of multichord SXR measurements shows that, at this time, two resonant $q = 2$ surfaces exist, between which the plasma is being mixed. As the current profile evolves, the oscillations transform into "humps." The occurrence of the humps can be explained by the periodical formation and destruction of ITBs. Sometimes, the humps are accompanied by intermediate internal disruptions; such humps are called "humpbacks." This phase is not clearly seen in Fig. 18. Apparently, at that instant, $q_{min} \le 2$. Then, internal disruptions disappear and the amplitude of humps increases (Fig. 18, $t > 0.85$ s). Possibly, in this case, we have $q_{min} \sim 2$.

If the total plasma current is less than 100 kA, then the driven current is sufficient for q_{min} to be higher than 2. Figure 19 shows the same as in Fig. 18 but for the current I_p = 75 kA. In this case, due to the current diffusion, after the initial deterioration of energy confinement, the temperature suddenly jumps to its previous value before the onset of the MHD activity. Apparently, in this regime, $q_{min} > 2$ at $t > 0.55$ s, which correlates with variations in the SXR signals.

In experiments with off-axis co-CD, an ITB occurred at the radius $r_{ITB} \sim$ 8–9 cm [21]. Figure 20 shows the time evolution of the central electron temperature in this case for I_p = 75 kA, B_T = 2.3 T, and P_{ab} =

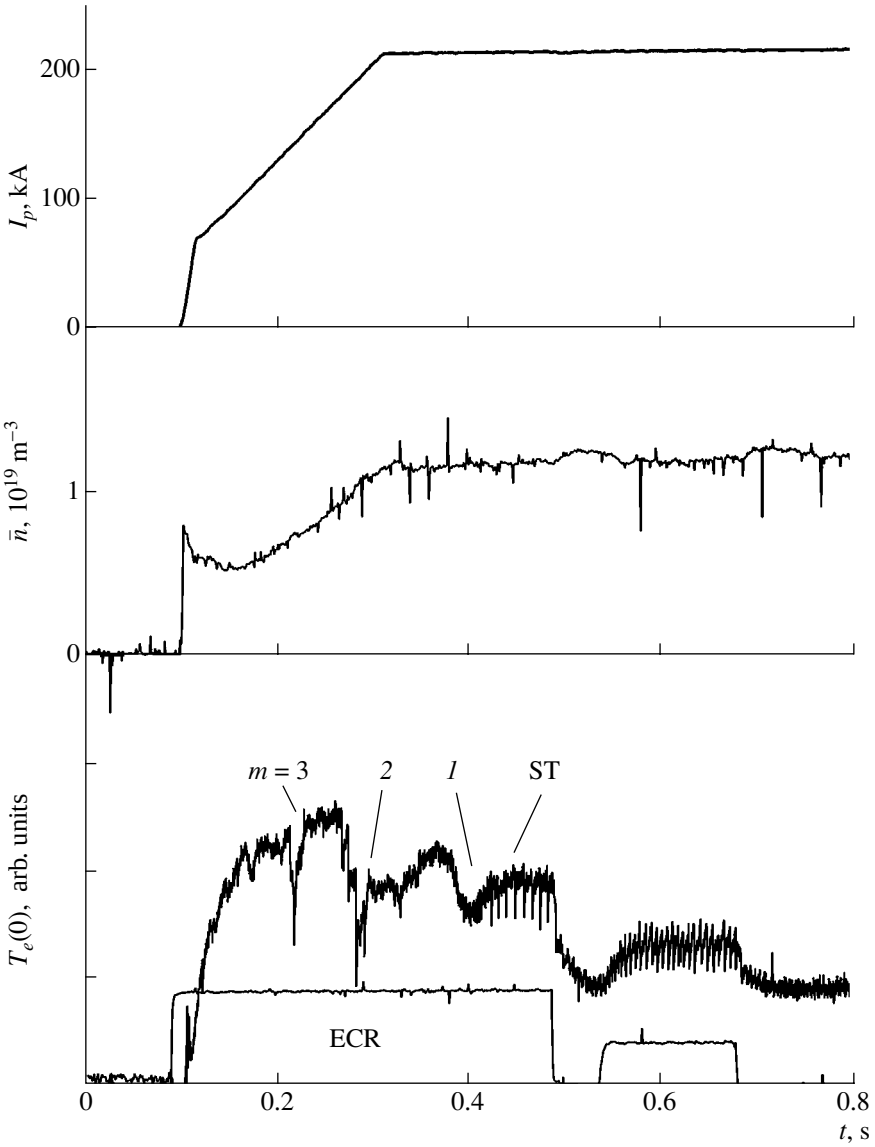

Fig. 21. Waveforms of the current I_p, plasma density $\bar{n}$, and the central electron temperature $T_e(0)$ in shot no. 20711; the ECRH power (P_{EC} = 0.37 MW, counter-CD) is switched on at the very beginning of the discharge; arrows mark the appearance of various MHD modes and sawtooth oscillations.

0.8 MW. One can see that, at $t \sim 620$ ms, the electron temperature suddenly increases by more than 0.5 keV. Calculations show (Fig. 17) that, in this case, the q profile is flat and has no minimums. This confirms the assumption that the existence of a reversed shear region is not necessary for the ITB formation.

The experimental results presented in Figs. 18–20 show that it is not an easy matter to achieve the ITB formation during the steady-state phase of the discharge with the available ECRH power. Therefore, attempts were made to obtain an ITB during the current ramp-up. Figure 21 illustrates one of the first attempts [20]. Here, gyrotrons were switched on at the very beginning of the current ramp-up, when the q value was large. At first, $T_e(0)$ increased to a high value. Possibly, in this stage, an electron ITB was formed. However, MHD activity with the mode numbers m = 3 and 2 arose very quickly, which probably destroyed the ITB. Then, the onset of sawtooth oscillations and the transition to the usual L-mode were observed.

The ITB formation was also observed under off-axis heating with $R_{EC} \sim 18$ cm (Fig. 22), when the driven current was small. In this case, the plasma potential profile $\Delta\varphi$ was measured by the HIBP diagnostics. The maximum energy of the probing ions attains 230 keV, which, at a field of B_T = 2.5 T, allows us to measure the plasma potential at $r/a > 0.35$ [22]. The spatial and temporal scanning of the sampling volume allows the evo-

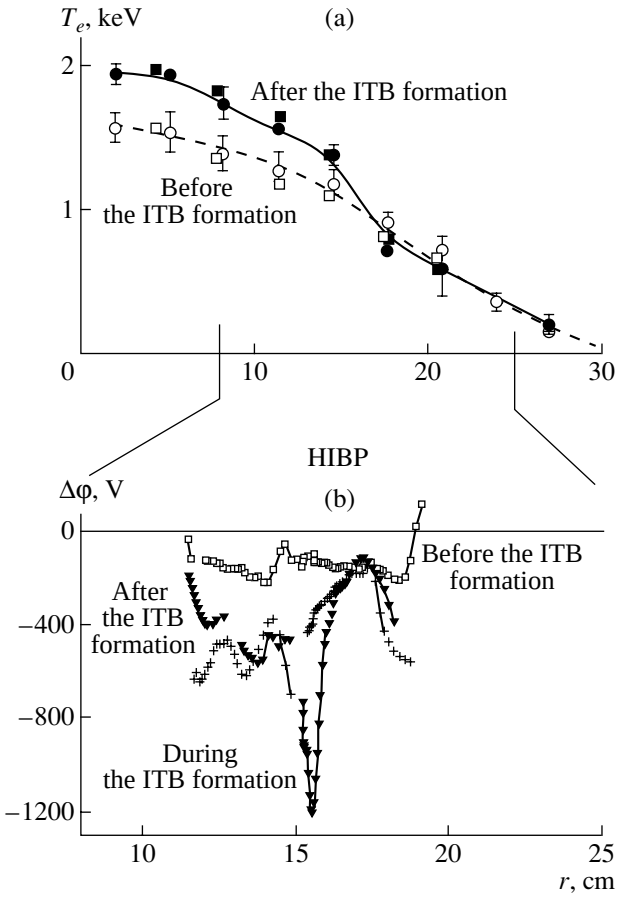

Fig. 22. Profiles of (a) the electron temperature and (b) plasma potential before and after the ITB formation under off-axis ECRH for I_p = 0.29 MA and P_{EC} = 600 kW (shot nos. 24264–24273). A deep potential well is seen during the ITB formation.

lution of the potential profile to be traced. The measurements show that the ITB formation is followed by rapid variations in the Δφ profile. Figure 22 presents the profiles of (a) $T_e(r)$ and (b) Δφ(r) during the barrier formation. We can see that, during the evolution, a narrow potential well with a depth of Δφ ~ 1 kV and width of 1.5–2 cm appears in the barrier zone. The electric field here reaches 1 kV/cm, and the calculated speed of the corresponding poloidal electric drift is $v_E \sim 3 \times 10^6$ cm/s. Then, at the steady-state phase, the potential well transforms into the potential jump Δφ ~ 0.5 kV in the layer with a width of about 3 cm.

2.7. H-mode and the Edge Transport Barrier

Regimes with improved confinement and an edge transport barrier (H-mode) have been observed in most tokamaks (both with separatrix and limiter configurations). Therefore, it is surprising that the H-mode was not observed in T-10 up to the end of the 1990s. Now, this can be explained by many reasons: a small excess of the ECRH power P_{EC} over the threshold power for the L–H transition P_{thr}, a narrow parameter range where the H-mode exists in limiter devices, increased attention to ECCD problems, and so on. Systematic investigations of the H-mode in T-10 have begun only recently.

Let us consider the typical features of the observed H-mode [23, 24]. Figure 23 shows the evolution of the main plasma parameters during the L–H transition in a shot with a low initial density of $\bar{n} \sim 1.5 \times 10^{19}$ m^{-3}, a current of I_p = 330 kA (q_a = 2.2), and an absorbed ECR power of P_{ab} = 750 kW. We can see that, approximately 100 ms after the gyrotron is switched on, the intensity of the D_α line falls and the plasma density grows. Simultaneously, the total energy stored in the plasma increases and the temperature does not decrease in spite of the density growth. The density profiles in the L and H phases of the discharge are shown in Fig. 24. It is seen that, in the H-mode, a narrow region with a width of 2–3 cm and steep density gradient is formed near the outermost plasma periphery. This is an attribute of the density edge transport barrier. At the same time, the profile and absolute values of the electron temperature change only slightly and the temperature transport barrier is not observed.

The formation of the edge transport barrier is accompanied by the appearance of the radial electric field inside the barrier. Figure 25 shows the plasma potential profiles in the edge region for several instants during the barrier formation measured by HIBP. We can see the potential jump Δφ ~ –400 V in a layer with a width of about 2 cm; the electric field in the layer reaches ~0.2 kV/cm. According to modern concepts, this electric field results in a poloidal drift, which suppresses turbulent transport inside the barrier.

The proximity of the discharge parameters to the power threshold is demonstrated in Fig. 26, where the dependence of the ratio $H_L = \beta_p^H/\beta_p^L \approx \tau_E^H/\tau_E^L$ on the total heating power P_{tot} is shown. Here, β_p^L and β_p^H are the values of $\beta_p \sim W/I_p^2$ at the end of the L and H phases of the discharge, respectively. We can see that the developed H-mode is achieved only at $P_{tot} \sim 1$ MW; in this case, $H_L \sim 1.6$. As the initial density and/or safety factor q_a increase, the energy gain from the transition to the H-mode decreases. For the density $\bar{n} \sim (3–4) \times 10^{19}$ m^{-3} and/or $q_a \sim 4$, the plasma energy increases only slightly after the transition to the H-mode.

To correctly understand the consequences of the transition to the H-mode, it is necessary to recall the main features of energy confinement in the L-mode in T-10 under ECRH:

(a) the energy confinement time τ_E is proportional to the plasma density [3, 4]; and

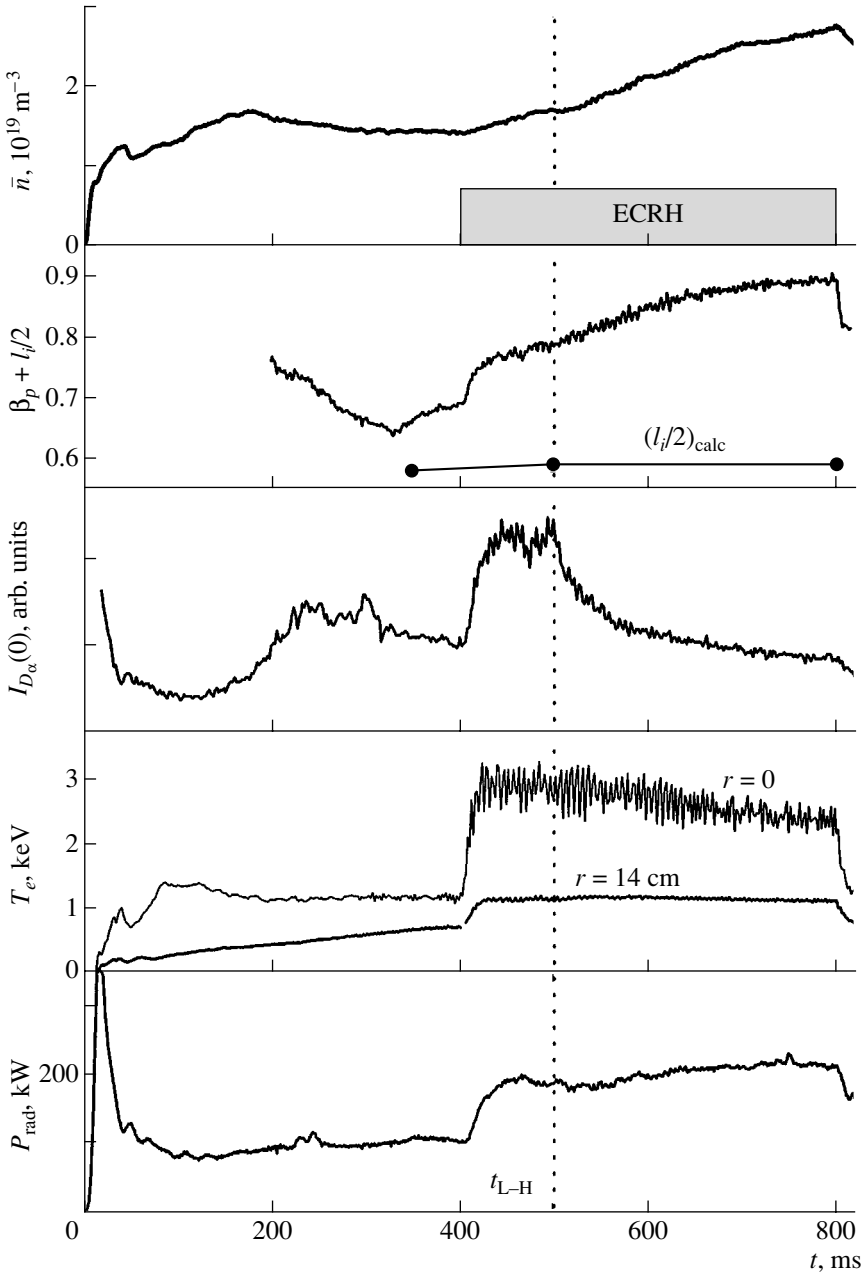

Fig. 23. Waveforms of the plasma density $\bar{n}$, the values of $\beta_p + l_i/2$ and $l_i/2$, the D_α line emission intensity, the electron temperature T_e, and the radiation power P_{rad} in shot no. 26154 with the L–H transition at $t_{L–H} = 500$ ms.

(b) at moderate densities of $\bar{n} \sim (3–4) \times 10^{19}$ m^{-3}, the energy confinement time is equal to

$$\tau_E \approx \tau_E(\text{ITER-98P}) \equiv \tau_E^{\text{IT-L}}, \quad (4)$$

where $\tau_E^{\text{IT-L}}$ is the energy confinement time determined by the ITER L-mode scaling [5]. The dependence on the plasma density in this scaling is very weak ($\sim n^{0.4}$); hence, for low densities in the L-mode, we have $\tau_E < \tau_E^{\text{IT-L}}$. In particular, for $\bar{n} \sim 1.5 \times 10^{19}$ m^{-3}, we obtain $\tau_E \approx 0.5\,\tau_E^{\text{IT-L}}$.

This explains why the energy stored in the plasma increases only slightly after the transition to the H-mode in T-10. The observed improvement of confinement manifests itself only in that τ_E approaches the value that follows from the ITER L-mode scaling. We did not observe any better confinement than that predicted by the ITER scaling.

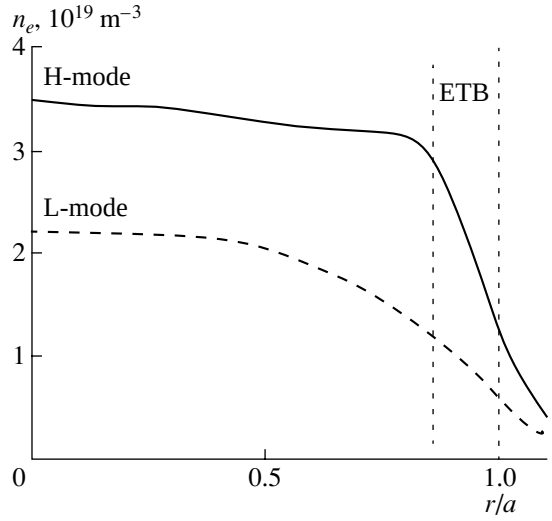

Fig. 24. Plasma density profiles in the L and H phases of the discharge. The region with a steep density gradient corresponds to the edge transport barrier (ETB).

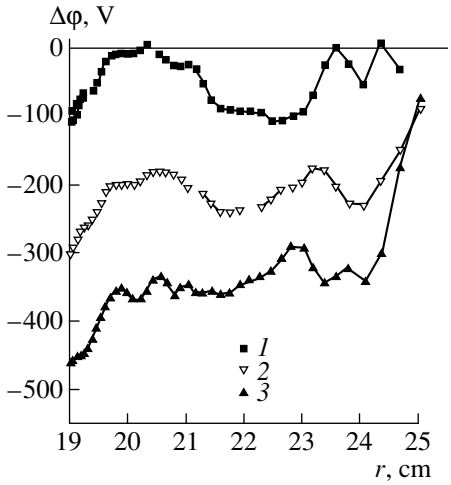

Fig. 25. Evolution of the plasma potential profiles in shot no. 23724 (the limiter radius is 25 cm, and the width of the edge transport barrier is ~1.5 cm) during the L–H transition: (*1*) t = 735 ms (L-mode), (*2*) t = 854 ms, and t = (*3*) 874 ms (H-mode).

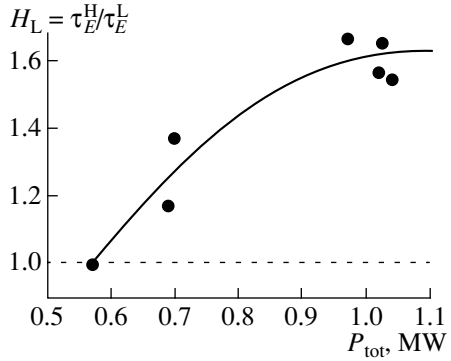

Fig. 26. The ratio of the measured energy confinement time in the H-mode τ_E^H to the confinement time in the L-mode τ_E^L vs. the total deposited power P_{tot}.

2.8. Pellet Injection into the Plasma during ECRH

The injection of a deuterium pellet in T-10 led to unexpected results [25]. Usually, the pellet noticeably affects the discharge during a short time interval on the order of two to three energy confinement times. Then, the plasma returns to its previous state. However, in T-10, pellet injection leads to a drastic improvement of energy confinement; this new state lasts up to the end of the gyrotron pulse (for five or six energy confinement times). In this case, the absolute values of τ_E recover the values typical of the ohmic phase.

Figure 27 shows the evolution of the energy stored in the plasma and the line-averaged plasma density in a shot with pellet injection at a current of I_p = 300 kA and an absorbed ECRH power of P_{ab} = 570 kW. For comparison, the behavior of the same parameters in a shot without pellet injection is also shown. We can see that the average density after pellet injection first ramps up by 12–15% and, then, returns to the previous level. At the same time, the stored energy increases by 60% just after injection and stays at this level for 250 ms. This new regime was called the pellet enhanced confinement (PEC) mode. In this mode, the confinement factor $H_H = \tau_E^{PEC}/\tau_E^{IT\text{-}H}$ reached a record value for T-10 on the order of 1.3. Here, τ_E^{PEC} is the energy confinement time in the PEC mode and $\tau_E^{IT\text{-}H}$ is the energy confinement time defined by the ITER H-mode scaling [5].

Figure 28 shows the $n(r)$ and $Z_{eff}(r)$ profiles in different phases of the discharge. In the PEC-mode, the density profile is more peaked and the $Z_{eff}(r)$ profile is hollow. The electron temperature profile changes only slightly. The ion temperature profile broadens, and the absolute value of the ion temperature increases. The evolution of the total radiation power P_{rad} and the intensity of the carbon CIII line are shown in Fig. 29. We can see that, after pellet injection, the radiation power increases and reaches 40–45% of the input power; simultaneously, the radiating region gradually shifts toward the plasma periphery. These features indicate that the PEC mode is similar to the so-called radiative improved (RI) mode, obtained in the TEXTOR tokamak with Ne or Ar seeding [26]. We note that, due to the long energy confinement time and the reemission of a significant fraction of the deposited power, the PEC mode is attractive for use in future tokamak reactors.

2.9. Suppression of the higher MHD modes

The local deposition of the ECRH power allows one to use it to suppress magnetic islands. For "rough" MHD perturbations (such as external modes), the current drive effect is negligible. It is only sufficient to use ECRH in the vicinity of the island [27, 28]. Figure 30 shows the dependence of the amplitude A_{MHD} of magnetic perturbations for the m/n = 2/1 mode (measured by magnetic probes at the plasma edge and proportional

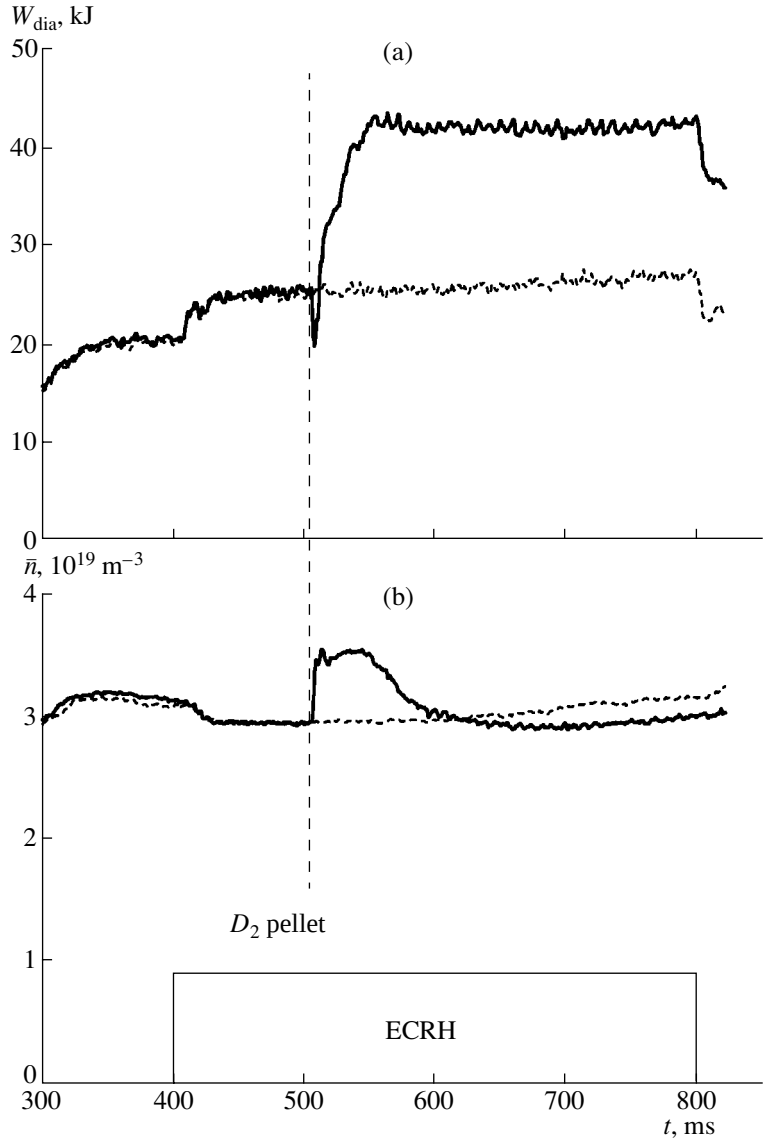

Fig. 27. Waveforms of (a) the stored plasma energy W_{dia} and (b) plasma density $\bar{n}$ for a shot with ECRH and deuterium pellet injection (I_p = 300 kA, P_{EC} = 570 kW). The dashed curves show the waveforms for a shot without pellet injection.

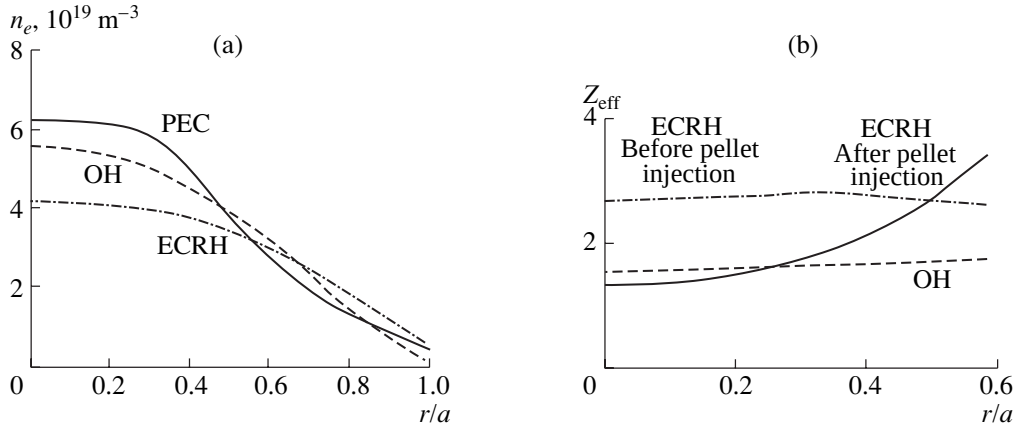

Fig. 28. Profiles of (a) the plasma density and (b) Z_{eff} in different phases of a shot with ECRH and pellet injection.

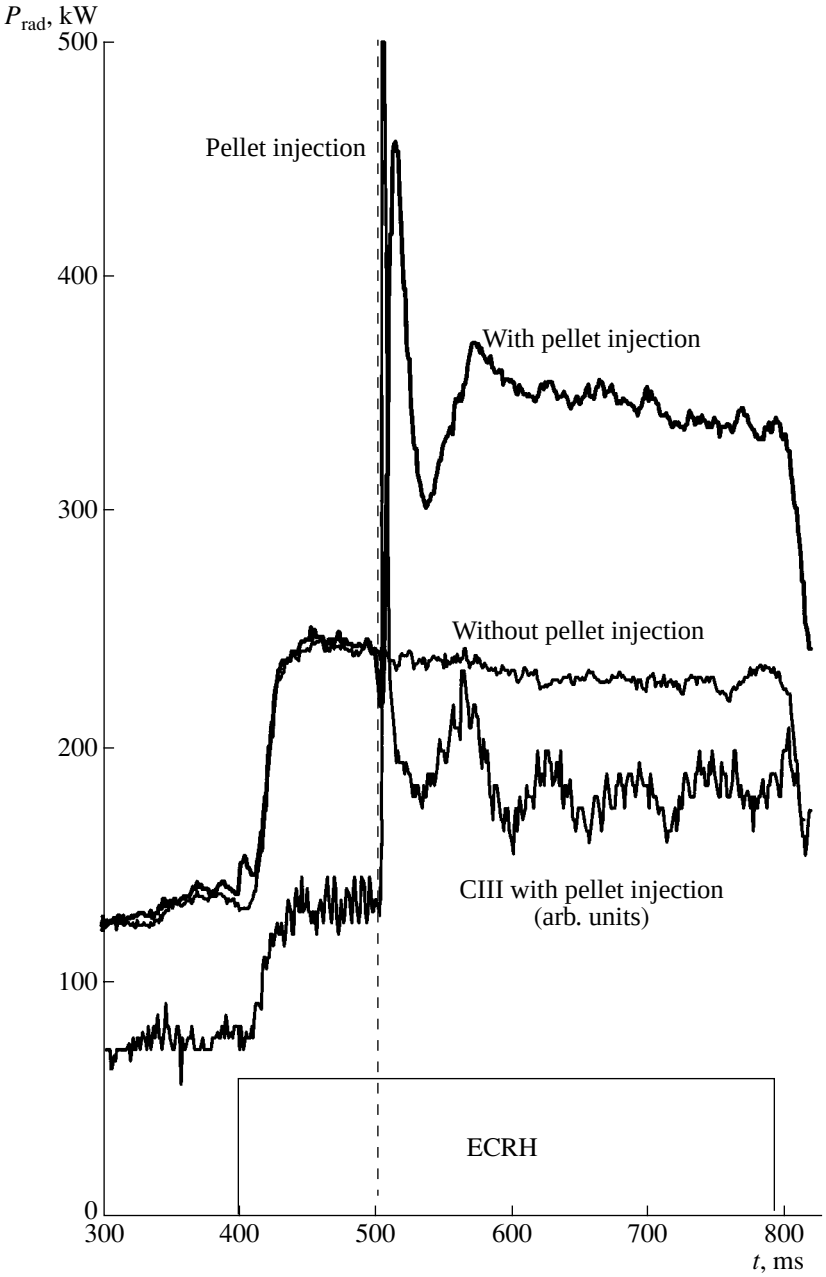

Fig. 29. Waveforms of the total radiation power P_{rad} and the CIII line emission intensity in a shot with pellet injection.

to the square of the island width) on the toroidal magnetic field B_T, which determines the location of the power deposition region. We can see that the effect is resonant in nature. As the power deposition region is shifted by 2 cm (the top scale in Fig. 30), the amplitude A_{MHD} changes by a factor of 2. After passing through the resonance, the amplitude of perturbations is recovered. However, the resonant character of the suppression of this mode was observed only at rather low plasma densities. As the density increases, the mode is suppressed at any location of the power deposition region.

The suppression of the neoclassical tearing modes (NTMs) with $m/n = 3/2$ and 2/1 in T-10 is a more complicated process. The reason for this is that these modes occur only at sufficiently large values of $\beta_N = \beta(\%)(aB_T/I_p)$ and β_p, where $\beta = 8\pi\langle n(T_e + T_i)\rangle/B_T^2$, $\beta_p = 8\pi\langle n(T_e + T_i)\rangle/B_{pa}^2$, a is in m, B_T is in T, and I_p is in MA. Due to the onset of NTMs, the plasma pressure does not increase and even decreases. Under the conditions in T-10, the deposited power is no higher than 1 MW and the excitation of NTMs is only possible at small currents of $I_p \sim 75$–100 kA, when $\beta_N \sim 1$ and $\beta_p > 1$.

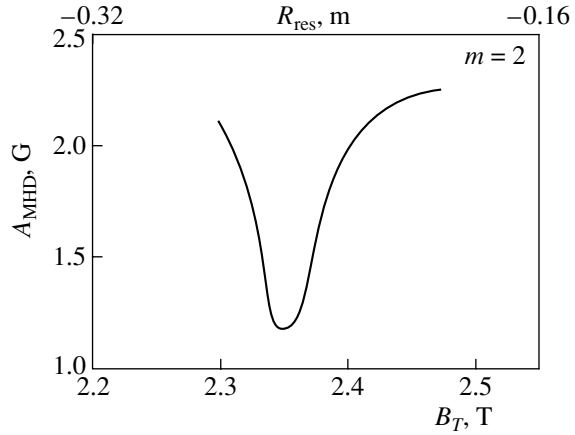

Fig. 30. Amplitude of magnetic field perturbations in the $m = 2$ mode at the plasma edge vs. the toroidal magnetic field (the position of the resonant magnetic surface) under ECRH. The minimum of the curve corresponds to the resonance position near the $q = 2$ surface.

This is a specific feature of T-10 as compared to tokamaks with a large excess of heating power.

Figure 31 [29] shows the evolution of the parameters of a low-current discharge. We can see the bursts of the $m/n = 3/2$ mode at $t \sim 640$ ms and the $m/n = 2/1$ mode at $t \sim 670$ ms. Simultaneously, β_p decreases by 10–15% (the so-called "soft β-limit"). In suppressing these modes, the current drive effect plays an important role. Experiments on the NTM suppression in T-10 are now in progress.

2.10. Investigations of Turbulence

To investigate small-scale density fluctuations in T-10, a correlation reflectometry diagnostics was developed. It consists of an array of antennas shifted with respect to each other in the toroidal and poloidal directions [30, 31]. The broad frequency band of the diagnostics allows us to vary the critical density n_{cr}, at which the incident wave is reflected, in the range $n_{cr} =$

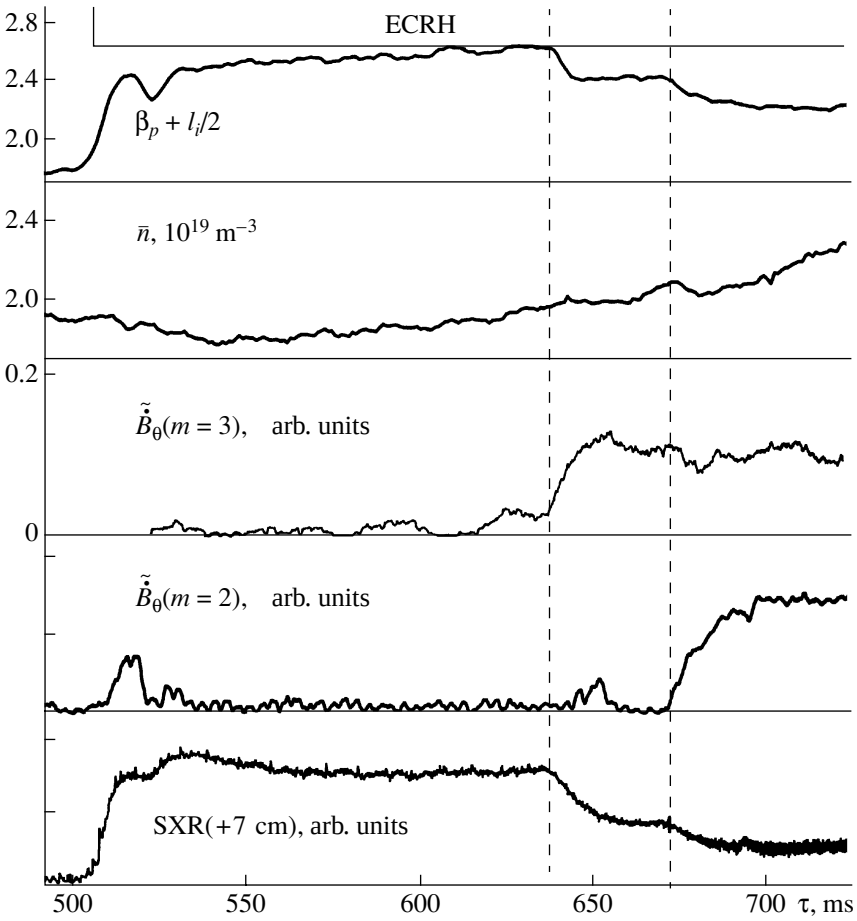

Fig. 31. Waveforms of $\beta_p + l_i/2$, plasma density $\bar{n}$, amplitude of magnetic field perturbations in the $m = 3$ and $m = 2$ modes, and SXR emission intensity in a low-current discharge. The appearance of magnetic field perturbations decreases the $\beta_p + l_i/2$ value (soft β-limit).

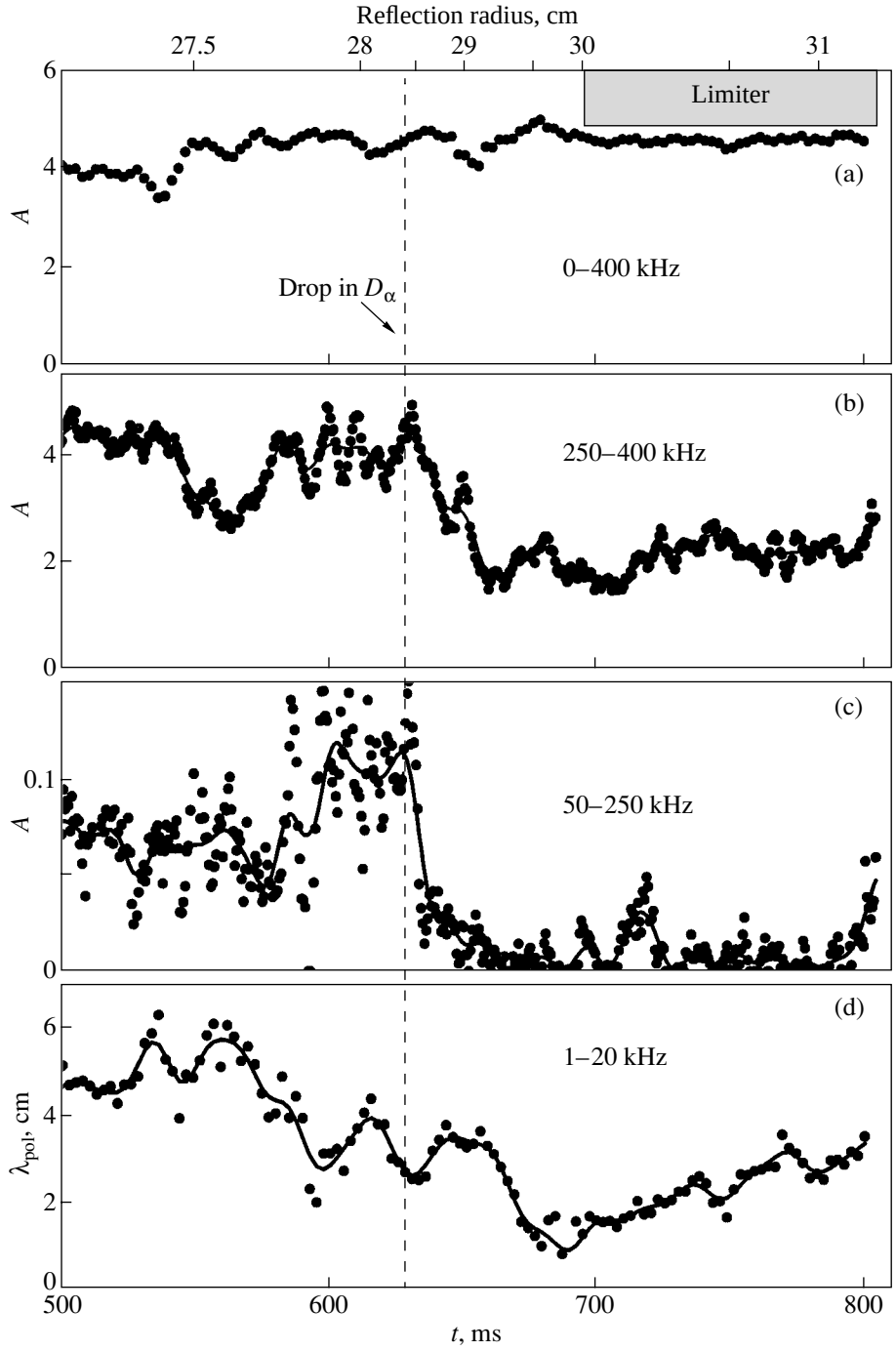

Fig. 32. Time evolution of (a) the amplitude of fluctuations in the frequency band 0–400 kHz, (b) the amplitude of fluctuations in the band 250–400 kHz, (c) the amplitude of quasi-coherent fluctuations in the band 50–250 kHz, and (d) the poloidal correlation length λ of low-frequency fluctuations in the band 1–20 kHz (shot no. 26058). The instant of the L-H transition is marked by the vertical dashed line. The increase in the plasma density results in the outward shift of the reflection point (the radius of the reflection point is shown on the top scale). After the L–H transition ($t \sim 690$ ms), the value of λ inside the barrier decreases by a factor of 5.

$(0.8–8) \times 10^{19}$ m^{-3}. The amplitude and phase of the reflected waves are recorded at a sampling rate of up to 1 MHz. The software developed allows us to process the large amount of data to reveal the temporal and spatial correlations.

For example, consider the evolution of fluctuations during the L–H transition. Figure 32 shows the time evolution of (a) the amplitude of fluctuations in the frequency band 0–400 kHz, (b) the amplitude of fluctuations in the band 250–400 kHz, (c) the amplitude of

quasi-coherent fluctuations in the band 50–250 kHz, and (d) the poloidal correlation length λ of low-frequency fluctuations in the band 1–20 kHz. The instant of the L–H transition is marked by the vertical dashed line. At that instant, the intensity of the D_α line falls abruptly. The increase in the plasma density results in an outward shift of the reflection point (the radius of the reflection point is shown on the top scale). Within the time interval t = 650–700 ms, the reflection point is situated inside the transport barrier. We can see that the amplitude of random fluctuations varies only slightly in a broad frequency band. At the same time, the amplitude of coherent fluctuations in the region adjacent to the transport barrier decreases to a great extent and the correlation length inside the barrier decreases by a factor of 5. Correspondingly, the size of turbulent cells decreases. Beyond the barrier, the correlation length also decreases, but not to such an extent.

As a whole, we can conclude that the temporal and spatial coherency of fluctuations (rather than their amplitude) determine the plasma transport. The large coherency length in the L-mode ($\lambda \sim 5$ cm) implies that the plasma is highly self-organized. The heat and particle fluxes in this case are large. The destruction of spatial coherency leads to the partial destruction of self-organization and to the appearance of transport barriers; in this case, transport is reduced.

3. CONCLUSION

Owing to its gyrotron array, the T-10 tokamak was considered the top of the line in fusion research up to the middle of the 1990s. However, during the last 5 years, such arrays have been installed in many tokamaks and the T-10's preeminence has diminished. To recover it (at least partially), we need to

(i) increase the power of the T-10 gyrotron array up to 2–3 MW,

(ii) upgrade the diagnostics radically, and

(iii) involve talented young scientists.

ACKNOWLEDGMENTS

I am grateful to the members of the T-10 team and especially its veterans V.V. Alikaev, K.A. Razumova, and Yu.V. Esipchuk for providing me with experimental data and numerous valuable remarks. I am also very grateful to S.E. Lysenko for assistance in preparing the manuscript. This work was supported by the Russian Foundation for Basic Research (project no. 00-15-96536) and Agreement no. 105F between the RRC Kurchatov Institute and the Ministry of Atomic Energy of the Russian Federation.

REFERENCES

1. V. V. Alikaev, A. A. Bagdasarov, A. A. Borschegovskij, *et al.*, Nucl. Fusion **32**, 1811 (1992).
2. V. V. Alikaev, A. A. Bagdasarov, A. A. Borshchegovskij, *et al.*, Fiz. Plazmy **19**, 291 (1993) [Plasma Phys. Rep. **19**, 149 (1993)].
3. V. V. Alikaev, A. A. Bagdasarov, N. L. Vasin, *et al.*, Fiz. Plazmy **14**, 1027 (1988) [Sov. J. Plasma Phys. **14**, 601 (1988)].
4. Yu. V. Esipchuk, A. Ya. Kislov, K. N. Tarasyan, *et al.*, J. Mosc. Phys. Soc., No. 1, 119 (1991).
5. ITER Physics Basis, Chapter 2, Nucl. Fusion **39** (11) (1999).
6. B. Coppi, Comm. Plasma Phys. Controlled Fusion **5**, 261 (1980).
7. B. B. Kadomtsev, Fiz. Plazmy **13**, 251 (1987) [Sov. J. Plasma Phys. **13**, 443 (1987)].
8. D. Biskamp, Comm. Plasma Phys. Controlled Fusion **10**, 165 (1986).
9. J. Y. Hsu and M. S. Chu, Phys. Fluids **30**, 1221 (1987).
10. Yu. N. Dnestrovskij and G. V. Pereverzev, Plasma Phys. Controlled Fusion **30**, 47 (1988).
11. M. Greenwald, J. Terry, S. M. Wolfe, *et al.*, Nucl. Fusion **28**, 2199 (1988).
12. V. V. Alikaev, A. A. Bagdasarov, A. A. Borschegovskij, *et al.*, in *Proceedings of the 17th EPS Conference on Plasma Physics and Controlled Fusion, Amsterdam, 1990*; ECA **14B** (3), 1080 (1990).
13. V. V. Alikaev, A. A. Borshchegovskij, V. V. Volkov, *et al.*, Fiz. Plazmy **26**, 1059 (2000) [Plasma Phys. Rep. **26**, 991 (2000)].
14. V. V. Alikaev, A. A. Bagdasarov, G. A. Bobrovskij, *et al.*, in *Proceedings of the 13th IAEA Conference on Plasma Physics and Coltrolled Nuclear Fusion, Washington, 1990* (IAEA, Vienna, 1990), Vol. 1, p. 163.
15. Yu. V. Esipchuk, Plasma Phys. Controlled Fusion **37**, A267 (1995).
16. P. H. Cohen, Phys. Fluids **31**, 421 (1988).
17. D. A. Kislov, V. V. Chistyakov, Yu. V. Esipchuk, *et al.*, in *Proceedings of the 22nd EPS Conference on Controlled Fusion and Plasma Physics, Bournemouth, 1995*; ECA **19C** (1), 369 (1995).
18. D. A. Kislov, V. V. Alikaev, Yu. V. Esipchuk, *et al.*, Nucl. Fusion **37**, 339 (1997).
19. K. A. Razumova, V. V. Alikaev, A. A. Borschegovskij, *et al.*, Plasma Phys. Controlled Fusion **42**, 973 (2000).
20. V. V. Alikaev, A. A. Borshchegovskij, M. M. Dremin, *et al.*, Fiz. Plazmy **26**, 195 (2000) [Plasma Phys. Rep. **26**, 177 (2000)].
21. V. V. Alikaev, A. A. Borschegovskij, V. V. Chistyakov, *et al.*, in *Proceedings of the 27th EPS Conference on Controlled Fusion and Plasma Physics, Budapest, 2000.*
22. A. V. Mel'nikov, L. G. Eliseev, L. I. Krupnik, and S. M. Khrebtov, in *Proceedings of the 26th EPS Conference on Controlled Fusion and Plasma Physics, Maastricht, 1999*; ECA **23J** (2), 829 (1999).
23. V. V. Alikaev, A. A. Borshchegovskij, V. A. Vershkov, *et al.*, Fiz. Plazmy **26**, 979 (2000) [Plasma Phys. Rep. **26**, 917 (2000)].
24. Yu. V. Esipchuk, V. V. Alikaev, A. A. Borschegovskij, *et al.*, in *Proceedings of the 18th IAEA Fusion Energy Conference, Sorrento, 2000*, paper IAEA-CN-77/EXP5/16.

25. Yu. D. Pavlov, Yu. N. Dnestrovskij, A. A. Borschegovskij, *et al.*, in *Proceedings of the 18th IAEA Fusion Energy Conference, Sorrento, 2000*, paper IAEA-CN-77/EXP5/17.

26. Yu. N. Dnestrovskij, S. V. Cherkasov, S. E. Lysenko, *et al.*, in *Proceedings of the 26th EPS Conference on Controlled Fusion and Plasma Physics, Maastricht, 1999*; ECA **23J** (2), 817 (1999).

27. N. V. Ivanov, A. M. Kakurin, V. V. Volkov, *et al.*, in *Proceedings of the 22nd EPS Conference on Controlled Fusion and Plasma Physics, Bournemouth, 1995*; ECA **19C** (3), 77 (1995).

28. The T-10 Team, presented by D. A. Kislov, in *Proceedings of the 18th IAEA Fusion Energy Conference, Sorrento, 2000*, paper IAEA-CN-77/EXP3/04.

29. V. A. Vershkov, V. V. Dreval, and S. V. Soldatov, Rev. Sci. Instrum. **70**, 1700 (1999).

30. V. A. Vershkov, S. V. Soldatov, D. A. Shelukhin, and V. V. Chistyakov, Nucl. Fusion **39**, 1775 (1999).

31. The T-10 Team, presented by D. A. Kislov, in *Proceedings of the 18th IAEA Fusion Energy Conference, Sorrento, 2000*, paper IAEA-CN-77/OV5/2.

Translated by G. V. Shepekina

Plasma Physics Reports, Vol. 27, No. 10, 2001, pp. 843–851. From Fizika Plazmy, Vol. 27, No. 10, 2001, pp. 892–902.

PLASMA DYNAMICS

Laboratory Simulation of the Collision of Supernova 1987A with Its Circumstellar Ring Nebula[1]

Y.-G. Kang[1, 2], H. Nishimura[1], H. Takabe[1], K. Nishihara[1], A. Sunahara[1], T. Norimatsu[1], K. Nagai[1], H. Kim[2], M. Nakatsuka[1], and H. J. Kong[3]

[1]*Institute of Laser Engineering, Osaka University, 2-6 Yamada-Oka, Suita, Osaka 565-0871 Japan*

[2]*Department of Materials Science and Engineering, Kwangju Institute of Science and Technology, 1 Oryong-dong, Puk-gu, Kwangju 500-712 Korea*

[3]*Department of Physics, Korea Advanced Institute of Science and Technology, Yusong-gu, Taejon 305-701 Korea*

Received April 20, 2001

Abstract—The collision of the remnant of supernova 1987A with its circumstellar ring is laboratory-simulated by using the Gekko XII laser fusion facility at the Institute of Laser Engineering, Osaka University. The pure hydrodynamic approximation was applied using the invariance of the Euler equations. The basic properties of the formation of a young supernova remnant and its collision with the ring are illustrated. Shock wave propagation and plasma flow with triple wavy, vortex ringlike structures were observed using gated X-ray shadowgraphy. The observed hydrodynamic behaviors compare favorably with one- and two-dimensional numerical simulations and further illustrate important qualitative trends. Our experiments suggest the shock reverberation between the ring and the contact discontinuity in the supernova remnant 1987A and resultant oscillation and enhancement of X-ray emission, as well as the emergence of downstream vortex structures. © *2001 MAIK "Nauka/Interperiodica".*

1. INTRODUCTION

Astrophysics has been immensely advanced with the development of observational technology and sophisticated numerical simulations. Our understanding of astrophysical phenomena has been greatly deepened, while a number of attempts have been made since the early part of the 20th century [1] to simulate celestial bodies in a terrestrial laboratory; this branch of physics is called *laboratory astrophysics.* Despite huge differences in time and space scales and other parameters between astronomical phenomena and laboratory environments, the idea of laboratory simulation is based on the fact that both systems are described generally by pure hydrodynamic or magnetohydrodynamic motions; thus, there exist similarities. For example, the plasma universe concept, which suggests that general laws of plasma physics hold from laboratory, magnetospheric, and heliospheric plasmas to interstellar and intergalactic plasmas, gives insight into cosmic plasma [2–4].

The linear dimensions of plasma in the universe vary by a factor of 10^{27} in three jumps of 10^9: laboratory plasmas (0.1 m), magnetospheric plasmas (10^8 m), interstellar clouds (10^{17} m), and the Hubble distance (10^{26} m). Inclusion of laser fusion experiments at 10^{-6} m (after implosion) brings the total up to 32 orders of magnitude. This vast variety of differences in scale under the same name *plasma* suggests that laboratory experiments contribute to the understanding of the universe and to the observation and theoretical approach.

The use of laser-produced plasma to model hydrodynamic phenomena in space was first suggested just after the invention of the laser [5]. With the development of sophisticated technology of laser fusion [6], which includes high-power lasers, microtarget fabrication, and plasma diagnostics, it is possible to recreate physical conditions in the laboratory that are a scaled version of those in astronomical objects [7–9]. This allows astrophysical theories, modeling, and codes to be tested in the laboratory, where experimental parameters and conditions are well characterized. Model experiments on the hydrodynamic instabilities of supernova explosions were conducted [10], and the collisionless deceleration of supernova remnants with magnetic fields was investigated using laser produced plasmas [11]. For recent astrophysics experiments using high-power lasers and historical laboratory astrophysics experiments, see [12, 13].

In the next section, we briefly explain the astrophysical motivation of the present investigation and two closely related previous experiments. We discuss the scaling of SN 1987A to the laboratory system and the experimental design in Section 3. In Section 4, we describe the experimental measurements. Next, 2D hydrodynamic simulation results will be described for comparison with the experimental results. Finally, we discuss the scope of our work and its relevance and implications to SN 1987A.

[1] This article was submitted by the authors in English.

1063-780X/01/2710-0843$21.00 © 2001 MAIK "Nauka/Interperiodica"

2. EJECTA–RING COLLISION OF SN 1987A

Observations of the supernova (SN) 1987A with its circumstellar structures [14] and the origin of its remarkable triple ring nebulae have been a source of intense discussions [15]. Recently, Hubble Space Telescope observations reported a rapidly brightening "hotspot," which is attributed to the collision of the ejecta of SN 1987A with the inner circumstellar ring structure [16]. More recently, new hotspots have been observed in the inner ring around SN 1987A [17]. X-ray emission and evolution of the ejecta–ring collision were investigated in terms of hydrodynamic simulations showing that the dynamics is greatly affected by the structure of the circumstellar gas with the ring nebula [18–21].

Laboratory simulations were performed to investigate generic hydrodynamic properties of a young supernova remnant (SNR) formation [22] and the interaction of the SN shock with an interstellar cloud [23]. Drake *et al.* [22] observed a forward shock and stagnated ejecta; this is achieved by the impact of an exploded foil upon a low-density foam. In the experiment of Klein *et al.* [23], a strong shock wave was driven through a copper sphere embedded in a CH plastic ambient medium. Both experiments were conducted using the Nova laser [24] and a strong shock wave generated by irradiating a target with X rays. The former experiment, however, did not consider the subsequent collision with the ring, and the latter experiment dealt only with a planar shock–sphere interaction, which did not involve the supernova remnant formation. In this paper, we report the first hydrodynamic model experiment to more realistically simulate the ejecta–ring collision of SN 1987A. Since a density structure of a young SNR may play an important role in the interaction of SN 1987A with its circumstellar ring, we configured the experimental setup so as to observe downstream topographic effects of the subsequent collision after the formation of a density structure that is analogous to a young SNR.

3. SCALING AND EXPERIMENTAL DESIGN WITH 1D SIMULATION

Despite the huge differences in parameters between SN 1987A and laser-produced plasma, it is assumed that laboratory simulations correctly describe the astrophysical situation as far as collisional processes are concerned. Two different fluids having similar geometry and the same Reynolds numbers are said to be *similar*. There are two main conditions that need to be satisfied for the similarity to be achieved. First, dissipative processes such as viscosity, thermal conductivity, and radiative cooling should be negligible. Second, the internal energy should be proportional to the pressure [8].

The hydrodynamic equations are invariant under the following transformation: $t \longrightarrow tM$, $p \longrightarrow p/M^2$, $v \longrightarrow v/M$, and $E \longrightarrow E/M^2$, which is called the Mach number scaling, where $M = v\sqrt{\rho/\gamma p}$ is the Mach number, ρ is the density, p is the pressure, γ is the adiabatic constant, t is time, v is the fluid velocity, and E is energy. Alternatively, a scaling with an Euler number $v\sqrt{\rho/p}$ was presented and applied to compare the recent laboratory experiments using a laser-produced plasma under the conditions corresponding to SN 1987A [8]. The invariance of the Euler equations showed that the Euler number is kept constant under the linear transformations of the fluid parameters, such as density, pressure, and time. We adopted the latter to directly compare our experimental parameters with those of the previous investigation.

For a purely hydrodynamic approximation, the Péclet number ($Pe \equiv hv/\chi$) and the Reynolds number ($Re \equiv hv/\nu$) of fluids in different systems must be much larger than unity, so that conduction and viscous effects are negligible. Here, h is the scale length, χ is the thermal diffusivity, and ν is the kinematic viscosity. As is seen in the table, very large values of the Péclet and Reynolds numbers were achieved in the experiment. The Euler numbers of $\mathrm{Lab}_{\mathrm{SNR}}$ and SNR 1987A are comparable. Although the density jump across the foam–

Parameters of the present experiment and of SN 1987A; $\mathrm{Lab}_{\mathrm{SNR}}$ and $\mathrm{Lab}_{\mathrm{Ring}}$ are calculated at 4 and 6 ns, respectively, based on our 1D simulations. For SN 1987A, we filled in the values calculated by Ryutov *et al.* [8] for comparison

Parameters	Laboratory		Supernova	
	$\mathrm{Lab}_{\mathrm{SNR}}$	$\mathrm{Lab}_{\mathrm{Ring}}$	SN 1987A	SN 1987A Ring
Scale length (cm)	5.0×10^{-2}	1.5×10^{-2}	3.0×10^{16}	1.0×10^{17}
Velocity (cm/s)	7.0×10^{6}	7.0×10^{6}	9.5×10^{8}	1.0×10^{9}
Density (g/cm^3)	0.7	20	1.0×10^{-22}	2.2×10^{-19}
Pressure (dyne/cm^2)	2.5×10^{12}	5.0×10^{12}	1.0×10^{-5}	3.5×10^{-5}
$v\sqrt{\rho/p}$	3.7	14	3.0	79
Péclet number (Pe)	2.0×10^{5}	1.2×10^{4}	10^{7}	7.0×10^{9}
Reynolds number (Re)	1.3×10^{8}	1.8×10^{9}	6.0×10^{8}	3.0×10^{11}

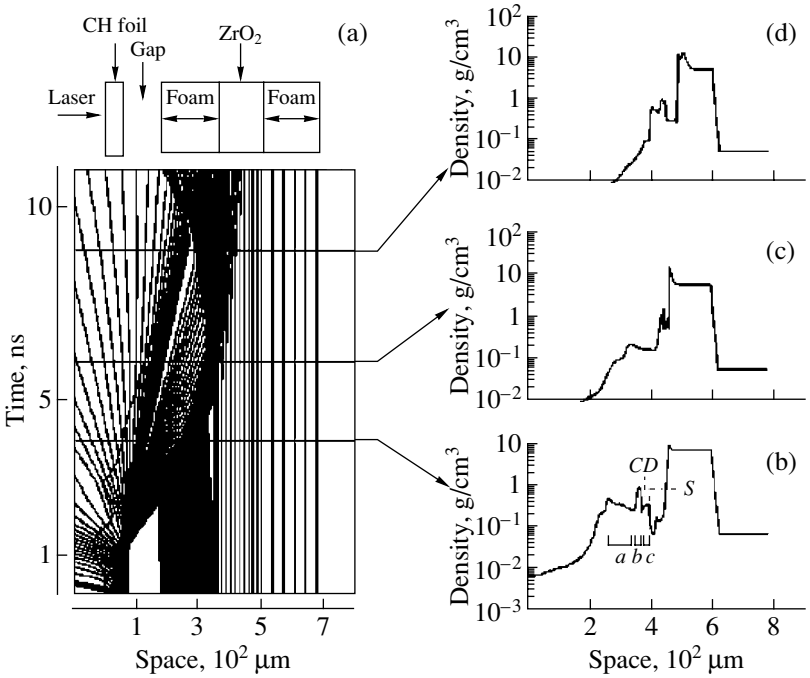

Fig. 1. Results of the hydrodynamic simulation with the code ILESTA-1D: (a) space-time diagram and (b–d) the density profiles at 4.0 ns, 6.0 ns, and 8.9 ns, respectively.

ZrO_2 interface is relatively small compared with that of SN 1987A (which is responsible for the difference of the Euler numbers of the Lab_{Ring} and the SN 1987A Ring), the hydrodynamic responses of both systems may be similar because the shocks are in the strong shock regime. Besides, Ryutov *et al.* [8] envisaged a time scale that represents a similar temporal dependence of each external drive as $h\sqrt{\rho/p}$, which is denoted as the strong drive time scale. The experimental time scale is that of the laser pulse duration (one nanosecond), and the supernova remnant time scale is about a sidereal year.

In the Drake experiment [22], in which ejected materials with steep gradients stagnated against the contact discontinuity, the density profile was qualitatively similar to that of the early stage of supernova remnant formation. This is in agreement with the density profile of the similarity solution of young SNRs [25]. We performed one-dimensional simulations to duplicate the density profile of the Drake experiment, but our simulations incorporated the ejecta–ring collision by including a high-density material. The main purpose of the 1D simulation is to define the parameter range of our experiment.

We have used the 1D Lagrangian radiation hydrodynamic code ILESTA-1D [26]. The code is based on the one-fluid two-temperature model with a realistic equation of state. It includes laser absorption by inverse bremsstrahlung with a ray tracing method. The flux-limited Spitzer–Harm model is used for electron heat conduction. The radiation transport is calculated with the multigroup flux-limited diffusion model. The photon energy of 50 eV to 3 keV is divided into 100 groups. The spectral opacity and emissivity are calculated by the evaluation of the non-LTE (local thermodynamic equilibrium) population of bound electrons based on the average ion model.

In the 1D simulation, a laser beam with a wavelength of 0.53 μm and an intensity of 2×10^{14} W/cm^2 irradiated a target (the configuration is depicted in the upper part of Fig. 1a). The pulse shape is quasi-Gaussian with a duration of 1 ns and rise time of 300 ps. In order to create in the incident material a density gradient similar to that of the SN ejecta, we have introduced a CH ejecta. After a laser-driven shock passes through a CH foil, the rear surface of the CH foil explodes and a rarefaction wave (CH ejecta) propagates toward the foam. This plasma motion is analogous to the hydrodynamic problem of a moving piston and can be approximately described as an isothermal similarity rarefaction wave with the velocity $v = c_T \log(\rho_1/\rho_0) = (x/t) - c_T$, where $c_T = \sqrt{\partial p/\partial \rho} = \sqrt{RT/\mu}$ is the isothermal sound velocity of the CH ejecta, R is the gas constant, T is the temperature, μ is the molecular weight of the gas, ρ_1 is the density of the shocked CH ejecta, and ρ_0 is the density of the foam [27].

This expansion wave strikes a low-density foam and launches a high-Mach-number (~20) shock wave inside the foam. The result of the simulation is shown by the space–time diagram in Fig. 1a. Upon impact of the expanding CH ejecta on the low-density foam, the

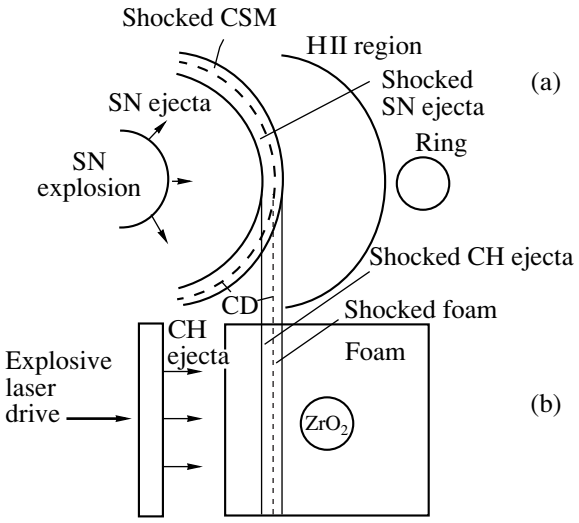

Fig. 2. Schematic structure of the shocked region: (a) the circumstellar region and (b) the ring of SN 1987A with an experimental design. The ejected material (SN ejecta and CH ejecta) and the low density medium (CSM and foam) are separated by a contact discontinuity (CD).

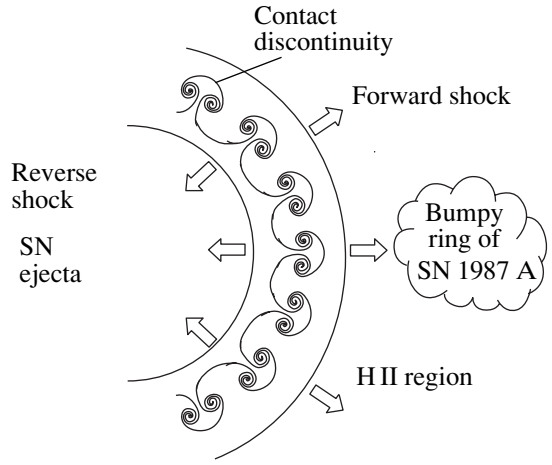

Fig. 3. Turbulent contact discontinuity of the circumstellar region and the bumpy ring of SN 1987A. This complicated environment is considered to be a more realistic situation.

ejecta material is stagnated. This results in a shock front in the foam, a contact discontinuity, and stagnated ejecta denoted in Fig. 1b as *S*, *CD*, and *b*, respectively. Figures 1c and 1d show that the strong shock wave propagates into ZrO_2. At 6 ns, the reflected shock compresses the CH ejecta and the transmitted shock compresses high-density ZrO_2. At 8.9 ns, the transmitted shock propagates inside ZrO_2. Based on these results, we selected target dimensions, laser irradiation conditions, and the diagnostic timing.

From the 1D simulation, we designed the experiment shown in Fig. 2. The circumstellar ring of SN 1987A is considered to be swept-up wind material of a red supergiant (RSG) and neutral prior to the explosion. The ring was considered to be photoionized by the blue supergiant (BSG) progenitor and a medium-density (10^2 cm^{-3}) H II region is formed due to evaporation from the ring. For simplicity, we ignored the H II region [28, 29]. In the upper part of Fig. 2, the shocked ejecta and circumstellar gas may be separated by a contact discontinuity, where the velocity and pressure are continuous, but the density and temperature may be discontinuous. The structure of this region is governed by the mass conservation equation and equations for momentum and energy together with the Rankine–Hugoniot relations at both the forward and reverse shocks. In the realistic situation of a young SNR like SN 1987A, it is widely perceived that the Rayleigh–Taylor (RT) and Richtmyer–Meshkov (RM) instabilities occur at the contact discontinuity as the forward shock moves [30, 31], which results in a turbulent contact discontinuity (see Fig. 3). However, it should also be noted that such a complicated feature is very sensitive to the structure of the progenitor.

The target is composed of a CH plastic foil and a high-density ZrO_2 sphere embedded in a low-density $C_{10}H_{14}O_4$ foam block. The foam block is a surrogate of the circumstellar medium of SN 1987A, and the ring nebula is modeled by the ZrO_2 sphere. The densities of the CH foil, sphere, and foam are 1.06, 6, and 0.06 g/cm^3, respectively. We used a sphere to model the circumstellar ring because the small nonuniformity of the laser drive will cause blurring of the image at the edge if we use a cylinder. The thicknesses of the CH foil are 30 or 50 μm, and the foam block is a cube with a dimension of 500 μm. A thin 0.01-μm Al layer is deposited onto the CH foil surface to prevent preheating of the target by shine-through from the laser light [32].

4. EXPERIMENTAL RESULTS

A schematic diagram of the experimental configuration is shown in Fig. 4. Three beams of the Gekko XII laser [33], whose characteristics are described earlier in the 1D simulation, irradiated the target. Random phase plates were used to provide uniform laser irradiation [34]. Another laser beam with the same condition irradiated an Al foil, and the resulting plasma provided an X-ray source as backlighter. X-ray transmission images through the foam block were taken at various times in order to observe the hydrodynamic evolution. The delay time of the backlight flash with respect to that of the main drive pulse was varied from 4 to 8.9 ns. The backlit images were recorded with an X-ray framing camera [35] with a 100-ps temporal resolution and 30μm spatial resolution.

Since numerical simulations predict the temperature of the shock compressed foam to be at most 20 eV, the 1.8-keV X-ray mass absorption coefficient μ averaged

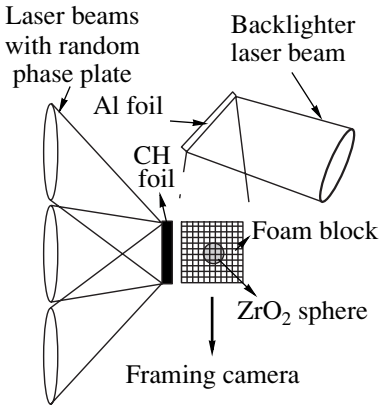

Fig. 4. Schematic view of the experimental configuration with a target, three drive beams, and gated X-ray shadowgraphy.

over the warmed CHO foam does not significantly change from that measured at room temperature. Thus, X-ray transmission is simply given by $\exp(-\mu_0 \int \rho dl)$, where ρ is the density of the foam, l is the length along the line of sight of the observation, and μ_0 is the mass absorption coefficient at room temperature. Hence, the X-ray transmission images provide us with information about the product of the density and depth.

Figure 5 shows the X-ray shadowgraphs at various times for the CH foils of 30 and 50 μm. Both the shocked and unshocked foam are relatively transparent to X-rays of the Al K-shell backlighter, while the CH plastic and ZrO_2 sphere are more opaque. The shock front (denoted as *S*) followed by a dense plasma flow (denoted as *E*) is clearly seen. The shock front had a diverging configuration that inherently comes from the intensity distribution of the drive pulse on the target. For the 50-μm CH foil, the shock front is not seen at 6 ns because it has already passed the sphere. However, for the 30-μm CH foil, the shock front is still observed at 6 ns. This is because the sphere is not placed exactly at the center, but on the left side of the center of the foam.

The measured velocities of the shock front inside the foam were $(1.1 \pm 0.15) \times 10^7$ cm/s for the 30-μm CH foil and $(7.5 \pm 1.5) \times 10^6$ cm/s for the 50-μm CH foil, respectively. Figure 6 shows the experimental data and simulation results showing the position of the shocks and ejecta. The measured velocities agree well with the 1D simulation results. After the first shock passage, the sphere starts losing its sphericity. Complicated density structures appear after the passage of the plasma flow around the sphere. The horizontal line graphs of images at 8.9 ns, which are shown in the fourth column of Fig. 5, demonstrate triple wavy structures. The similar shape of the triple dark striated structures (trough of the

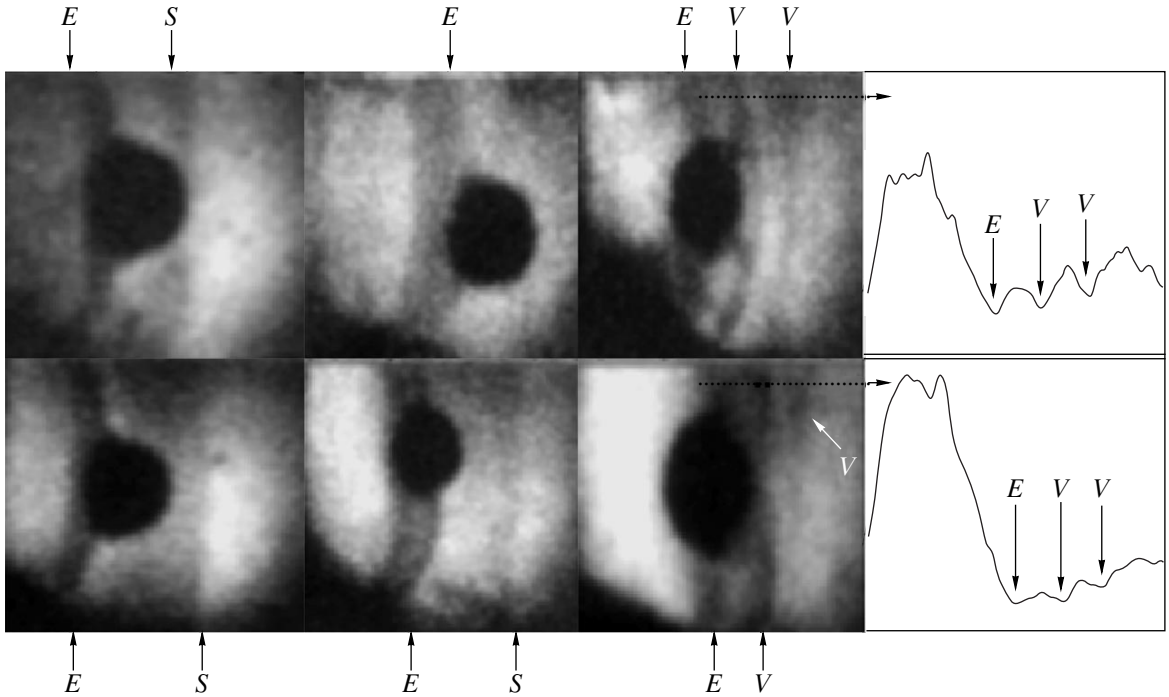

Fig. 5. X-ray shadowgraphs showing the shock wave propagation and the plasma flows behind the sphere. The shock front is denoted by *S* and the CH ejecta is denoted by *E*; *V* represents the downstream vortex ringlike structure. The first, second, and third columns are for t = 4.0, 6.0, and 8.9 ns, respectively. The upper and bottom rows are for the 50- and 30-μm CH foils, respectively. Triple wavy structures are shown in the third column, and the line graphs are shown in the fourth column.

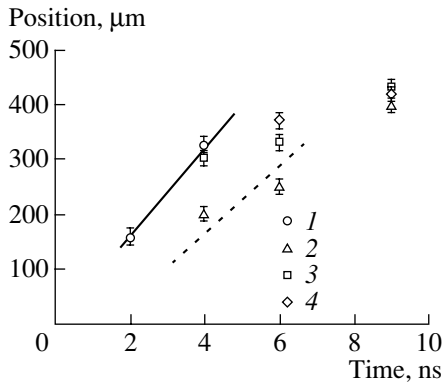

Fig. 6. Experimental data and 1D simulation results for two different CH foils. The positions of the forward shock and the peak of the stagnated ejecta are shown as functions of time after the arrival of the drive laser pulse: (*1*) forward shock (50 μm), (*2*) peak of the stagnated ejecta (50 μm), (*3*) forward shock (30 μm), and (*4*) peak of the stagnated ejecta (30 μm). The solid and dashed lines, which show the forward shock velocity and ejecta peak velocity from 1D simulations for a CH foil 50-μm thick, agree well with the experimental data.

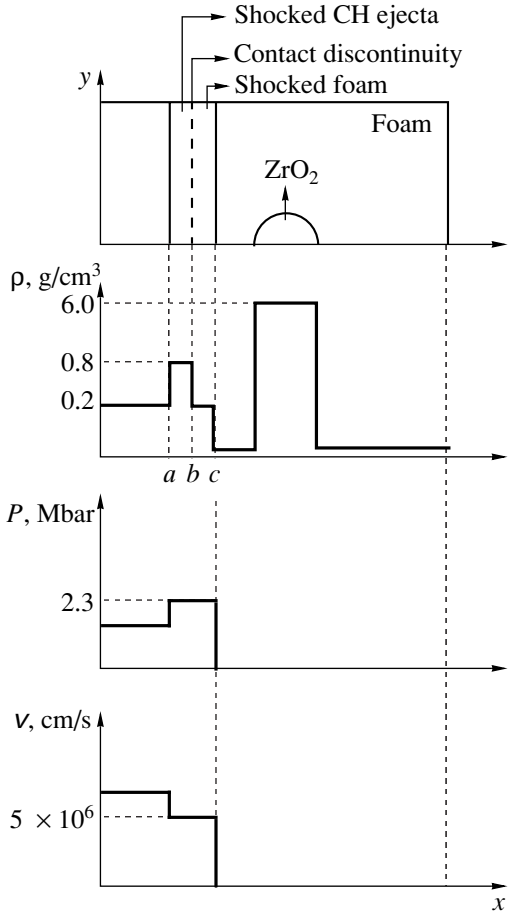

Fig. 7. The numerical region of 2D hydrodynamic simulations corresponds to the blast wave–sphere interaction (top) and the initial conditions for the density, pressure, and velocity. In the density condition, the region between *b* and *c* is the shocked foam and that between *a* and *b* is the stagnated ejecta. The contact discontinuity is at *b*.

wavy structures) behind the sphere was observed for both 30- and 50-μm foil thicknesses.

5. 2D AXISYMMETRIC HYDRODYNAMIC SIMULATION

In order to elucidate the experimental results, 2D hydrodynamic simulations were performed. The code uses a second-order Godunov scheme [36] with Van Leer's flux limiter [37]. We assumed an ideal, inviscid, and one-temperature gas. When calculating the energy transport processes, the different properties of each material are identified by the surface tracking method [38]. The calculated region corresponds to a rectangle including a semicircle under the assumption of axial symmetry in cylindrical coordinates r and z. The number of cells was 128×256. The initial values were set based on the ILESTA-1D simulations (see Fig. 7).

Figure 8 shows the temporal evolution of the density. As is seen in Figs. 8a and 8e, the initial condition corresponds to a shock wave accompanied by the plasma flow behind it. The shock wave, the plasma flow behind the shock around the sphere, and the propagation of an internal shock wave in the high density sphere are seen. The front of the high-density sphere is highly compressed by the strong shock wave. The shear between the sphere and the surrounding plastic and foam is also seen in Figs. 8c and 8g. The Kelvin–Helmholtz (KH) instability deforms the boundary of the high-density sphere and forms vortices downstream of the sphere (see Fig. 8c). Figure 9 shows the density and vorticity evolution. The longer distance between the shock front and the contact discontinuity is simulated in Fig. 10.

It can be inferred from the 2D simulations that the front side of the high-density sphere is highly compressed by the passage of the strong shock and that the turbulent mixing of the ZrO_2, CH, and $C_{10}H_{14}O_4$ foam plasmas gives rise to the wavy structures with higher opacity to the backlighter. However, in our 2D code, we have not yet included ionization and the realistic equation of state. In the experiment, the surface of the ZrO_2 sphere front can be evaporated and ionized, thus being mixed with CH and foam plasmas, but this is now only a conjecture based on the 1D radiation hydrodynamic code. To understand this phenomenon, further improvements of the 2D code are needed.

In Fig. 8b, the first reflected shock (R_1) collides with the incoming ejecta, and the re-reflected shock (R_2) propagates into the sphere again. R_1 penetrates into the ejecta (front surface of the ejecta) and punches through the ejecta (the rear surface of the ejecta); thus, a rarefaction wave is created upstream of the sphere (Fig. 8c). R_2 is reflected again by the sphere and propagates to the ejecta (let us call it R_3). R_3 also generates a secondary rarefaction wave upstream of the sphere. Thus, the upstream rarefaction waves, which are increasing in diameter, represent the shock reverberation (Fig. 8c).

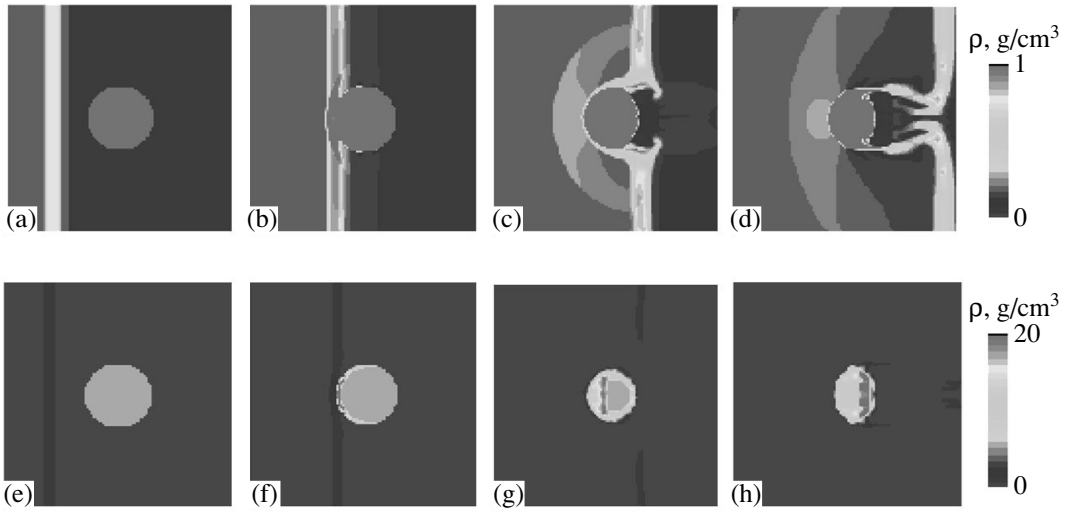

Fig. 8. The 2D simulation results obtained with the second-order Godunov scheme for t = (a, e) 4.0, (b, f) 6.0, (c, g) 8.9, and (d, h) 12.5 ns. The distance between the forward shock and the contact discontinuity is 20 μm. The internal shock wave propagation of the high-density sphere is shown in frames (e), (f), (g), and (h). The front of the high-density sphere is highly compressed by the transmitted shock.

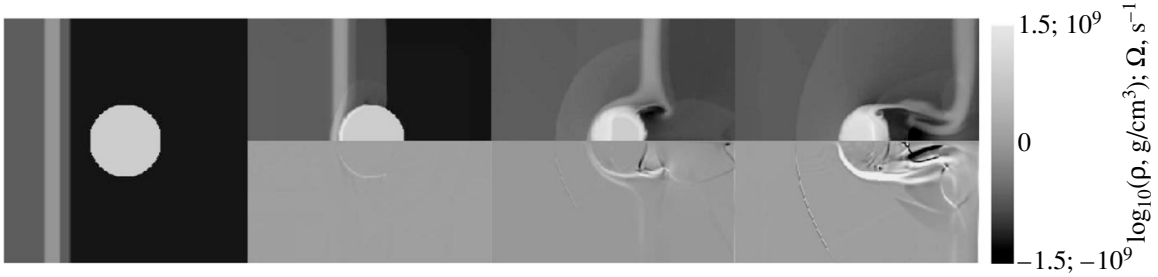

Fig. 9. Results of 2D simulations of the density and vorticity evolution. The first, second, third, and fourth columns are for t = 4.0, 6.0, 8.9, and 12.5 ns, respectively. Starting from the second column, the density and vorticity evolution are shown in the upper and lower rows, respectively.

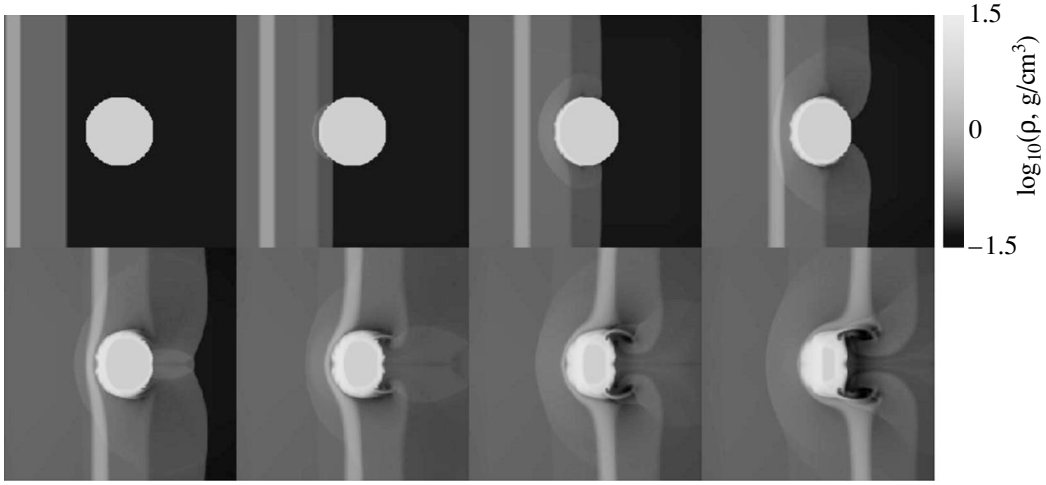

Fig. 10. Results of 2D simulation of the density evolution. The upper row (from left to right) is for 4.1, 5, 6, and 7 ns; the lower row is for 8, 9, 10, and 11 ns. The distance between the forward shock and the contact discontinuity is 100 μm. At t = 5 ns, the forward shock encounters the sphere and a reflected shock is developed and collides with the incoming CH plasma at t = 7 ns. The reverberating forward shocks are seen between 8 and 9 ns. At t = 10 ns, CH ejecta sweep the sphere, stripping the boundary layers at its top and bottom sides.

The longer distance (as compared to that in Fig. 8) between the shock front and the contact discontinuity is simulated in Fig. 10. Shock reverberation is also exhibited.

6. DISCUSSION AND CONCLUSION

It can be said that our experiment deals with a blast wave–sphere interaction, which involves the interactions of a sphere with a shock wave [39] accompanied by a contact discontinuity and plasma flow behind it. In Fig. 1b, region *a* represents the density gradient of the incoming CH plasma flow, region *b* is the stagnated CH ejecta, and *c* is the shocked foam. The density gradient region *a* contains a large continuous CH plasma flow. The incident double-humped density structure consisting of regions *a*, *b*, and *c* is considered to be a blast wave. This blast wave collides with ZrO_2. The momentum transfer to the sphere by the blast wave is repetitive due to the shock reverberation, which does not exist in the shock–sphere interaction [23, 40–42]. We assume that the CH ejecta at 6 ns (which is thicker as compared to those at 4 and 8.9 ns in Fig. 5) results from these oscillating shocks.

In numerical simulations of the shock–sphere interaction, the primary vortex ring appears as a result of the roll-up of the vorticity deposited on the interface during the incoming shock traversal of the interface [43]. Multiple vortex rings may result from the break-up of the initial dominant ring or from the roll-up of shear layers from triple points of the Mach reflection [44]. In the blast wave–sphere interaction, the shock reverberation may be another mechanism for multiple vortex ring formation. We conjecture that the wavy structures of the images of the third column in Fig. 5 correspond to the formation of multiple vortex rings caused by the repeated hydrodynamic impulses of the shock reverberation. The dark striations indicating such structures are seen in the direction perpendicular to its propagation. These multiple vortex ringlike structures behind the sphere were not observed in Klein's experiment [23] because there was no density gradient in the incident material in that work.

The RM, RT, and KH instabilities are considered to be important in the present experiment and also in the ejecta–ring collision of SN 1987A. In our experiment, the RM instability occurs when the shock front encounters the spherical perturbation. This instability also plays an important role when the shock wave is reverberated. The KH instability deforms the boundary of the high density sphere and forms vortices downstream of the sphere [45]. The tangential flow at the top and bottom of the sphere of the third column in Fig. 5 may be due to the shock diffraction and deformation of the sphere boundary, which is seen in Fig. 8c and the last two images (at 10 and 11 ns) in Fig. 10. At the contact discontinuity between the stagnated ejecta and the shocked foam, the heavy plastic ejecta is decelerated by the light foam; therefore, it becomes RT unstable. At the contact discontinuity between ZrO_2 and the shocked foam, it also becomes RT unstable due to the shock reverberation, which accelerates the ZrO_2 sphere.

Although the magnetic field effect may be crucial to the description of SNR evolution [46, 47], the hydrodynamic approach with judicious scaling is considered to be reasonable as described in Section 2. For MHD phenomena, scaling issues including magnetic fields have been investigated [48]. MacLow *et al.* [49] numerically investigated the interaction of an SN shock with an interstellar cloud in 2D geometry including the magnetic field effect. The magnetic field reduces the vorticity generation at the cloud interface and, thus, reduces the amount of fragmentation. They showed that significant cloud fragmentation still occurs, although the magnetic field prevents the small cloud from being totally destroyed. The MHD description is associated with the region of synchrotron radiation where the local amplification of the magnetic field occurs, while the hydrodynamic approximation is related to the region with high gas density, which yields high X-ray emission. For very young SNRs, the magnetic energy density is rarely higher than a few percent of the heat energy of the shocked gas [21, 28]. Therefore, the present experiment, a non-MHD approximation is validated to be relevant to the conditions in SN 1987A.

In conclusion, a model experiment has been performed for the ejecta–ring collision with a density profile similar to the astrophysical conditions in SN 1987A. A shock front followed by the stagnated ejecta and multiple vortex ringlike structures behind the sphere were observed. The shock reverberation and multiple vortex ringlike structures are unique features of the blast wave–sphere/cylinder interactions. Future numerical investigations may be concentrated on the rigorous verification of the conjectured vortex ringlike structures, which may clarify the interplay of reverberating shocks and multiple vorticity generation.

Implications of the experimental results to the collision of SN 1987A with the ring include the following:

(i) Possibility of shock reverberation between the ring and the contact discontinuity in the SNR. This possibility is indicated in the previous numerical investigations [18–21] and is exhibited in our experiment and 2D simulations. Oscillating X-ray emission may be observed, which may depend on the structure of the blast wave (including the distance between the forward shock and the contact discontinuity and the structure of the contact discontinuity) and the density distribution of the ring and the HII region.

(ii) Enhancement of X-ray emission due to the RM instability. This is because, when the shock reverberation occurs, muliply-shoched material becomes denser and hotter; this denser and hotter region will yield enhanced X-ray emission.

(iii) Emergence of downstream multiple vortex structures.

One can easily further speculate that faster oscillations in X-ray emission from SNR 1987A may be observed if the RT instability sufficiently enhances finger structures on the contact discontinuity (see Fig. 3), because such structures will give rise to an earlier encounter of the reflected shock with the contact discontinuity. Therefore, to predict the future X-ray observations, blast wave–sphere/cylinder interactions deserve further detailed experimental and numerical exploration. We anticipate that the primary application of our work would be to validate numerical simulations of the ejecta–ring collision of SN 1987A.

ACKNOWLEDGMENTS

We thank S. Bulanov, N. Bobrova, S. Blinnikov, and P. Lundqvist for valuable scientific discussions during the designing stage of this work. We acknowledge fruitful discussions with H. Azechi, R. Kodama, D. Ryutov, B. Remington, R.P. Drake, C.F. McKee, J. Zhang, D. Arnett, J. Kane, R. Klein, M. Tosa, and N.J. Zabusky. We are grateful to the target fabrication, laser operation, and diagnostic groups of the Institute of Laser Engineering. Y.-G. Kang gratefully acknowledges the Hiroshi Kondo scholarship of Osaka University and support by the Korean Ministry of Education through the Brain Korea (BK21) Project.

REFERENCES

1. A. Egeland and E. Leer, IEEE Trans. Plasma Sci. **PS-14**, 666 (1986).
2. H. Alfvén, Phys. Today **33** (9), 22 (1986).
3. G.-C. Falthammar, IEEE Trans. Plasma Sci. **PS-14**, 616 (1986).
4. A. L. Peratt, *Physics of the Plasma Universe* (Springer-Verlag, New York, 1992).
5. J. Dawson, Phys. Fluids **7**, 981 (1964).
6. J. D. Lindl, Phys. Plasmas **42**, 3933 (1995).
7. B. Remington, R. P. Drake, H. Takabe, and D. Arnett, Science **284**, 1488 (1999).
8. D. Ryutov, R. P. Drake, J. Kane, *et al.*, Astrophys. J. **518**, 821 (1999).
9. J. Kane, D. Arnett, B. Remington, *et al.*, Phys. Plasmas **284**, 1488 (1999).
10. J. Kane, D. Arnett, B. Remington, *et al.*, Astrophys. J. Lett. **478**, L75 (1997).
11. Yu. P. Zakharov, A. M. Orishich, A. G. Ponomarenko, and V. G. Poshukh, Fiz. Plazmy **12**, 1170 (1986) [Sov. J. Plasma Phys. **12**, 674 (1986)].
12. B. Remington, R. P. Drake, H. Takabe, and D. Arnett, Phys. Plasmas **7**, 1641 (2000).
13. R. P. Drake, J. Geophys. Res. **284**, 1488 (1999).
14. P. Plait, P. Lundqvist, R. Chevalier, *et al.*, Astrophys. J. **439**, 730 (1995).
15. C. J. Burrows, J. Krist, J. J. Hester, *et al.*, Astrophys. J. **452**, 680 (1995).
16. E. Michael, R. McCray, C. S. J. Pun, *et al.*, Astrophys. J. Lett. **509**, L117 (1998).
17. http://cfa-www.harvard.edu/iauc/07300/07360.html.
18. T. Suzuki, T. Shigeyama, and K. Nomoto, Astron. Astrophys. **274**, 883 (1993).
19. K. Masai and K. Nomoto, Astrophys. J. **424**, 924 (1994).
20. D. Luo, R. McCray, and J. Slavin, Astrophys. J. **430**, 264 (1994).
21. K. Borkowski, J. Blondin, and R. McCray, Astrophys. J. **477**, 281 (1997).
22. R. P. Drake, S. G. Glendinning, K. Estabrook, *et al.*, Phys. Rev. Lett. **81**, 2068 (1998); R. P. Drake, J. J. Caroll, K. Estabrook, *et al.*, Astrophys. J. Lett. **500**, L157 (1998).
23. R. Klein, K. Budil, T. Perry, and D. Bach, Astrophys. J., Suppl. Ser. **127**, 379 (2000).
24. J. T. Hunt and D. R. Speck, Opt. Eng. **28**, 461 (1989).
25. R. Chevalier, Astrophys. J. **258**, 790 (1982).
26. H. Takabe and T. Ishii, Jpn. J. Appl. Phys. **32**, 5575 (1993).
27. L. D. Landau and E. M. Lifshitz, in *Fluid Mechanics* (Nauka, Moscow, 1986; Pergamon, New York, 1959), Sect. 92.
28. R. Chevalier and V. Dwarkadas, Astrophys. J. Lett. **452**, L45 (1995).
29. P. Lundqvist, Astrophys. J. **511**, 389 (1999).
30. R. Chevalier, J. Blondin, and R. Emmering, Astrophys. J. **392**, 118 (1992).
31. J. Kane, R. P. Drake, and B. Remington, Astrophys. J. **511**, 335 (1999).
32. D. K. Bradley, in *Laser Interaction and Related Plasma Phenomena* (Plenum, New York, 1991), Vol. 9, p. 323.
33. C. Yamanaka, Y. Kato, Y. Izawa, *et al.*, IEEE J. Quantum Electron. **QE-17**, 1639 (1981).
34. Y. Kato, K. Mima, N. Miyanaga, *et al.*, Phys. Rev. Lett. **53**, 1057 (1984).
35. M. Katayama and Y. Izawa, Rev. Sci. Instrum. **62**, 124 (1991).
36. P. Colella and H. M. Glaz, J. Comput. Phys. **59**, 264 (1985).
37. B. van Leer, J. Comput. Phys. **32**, 101 (1979).
38. P. Loetstedt, J. Comput. Phys. **47**, 211 (1982).
39. C. F. McKee and J. Truelove, Phys. Rep. **256**, 157 (1995).
40. J. H. Hass and B. Sturtevant, J. Fluid Mech. **181**, 41 (1987).
41. J. Stone and M. L. Norman, Astrophys. J. Lett. **390**, L17 (1992).
42. R. Klein, C. F. McKee, and P. Collela, Astrophys. J. **420**, 213 (1994).
43. N. J. Zabusky and S. M. Zeng, J. Fluid Mech. **362**, 327 (1998).
44. N. J. Zabusky, Ann. Rev. Fluid Mech. **31**, 495 (1999).
45. P. Nulsen, Mon. Not. R. Astron. Soc. **198**, 1007 (1982).
46. J. E. Borovsky, M. B. Pongratz, R. A. Roussel-Dupre, and T. Tan, Astrophys. J. **280**, 802 (1984).
47. B. I. Jun and T. W. Jones, Astrophys. J. **511**, 774 (1999).
48. D. Ryutov, R. P. Drake, and B. Remington, Astrophys. J., Suppl. Ser. **127**, 465 (2000).
49. M. Mac Low, C. F. McKee, R. Klein, *et al.*, Astrophys. J. **433**, 757 (1994).

Plasma Physics Reports, Vol. 27, No. 10, 2001, pp. 852–859. Translated from Fizika Plazmy, Vol. 27, No. 10, 2001, pp. 903–911.

PLASMA OSCILLATIONS AND WAVES

Excitation of Growing Wake Waves by an Electron Bunch in a Plasma in an Intense Pump Wave

H. B. Nersisyan

Institute of Radiophysics and Electronics, National Academy of Sciences of Armenia, Ashtarak-2, 378410 Armenia

Received January 9, 2001; in final form, March 26, 2001

Abstract—A study is made of the excitation of wake waves by a one-dimensional electron bunch in an electron plasma in the presence of an intense monochromatic pump wave with circular polarization. In the main state (in the absence of a bunch), the interaction between a pump wave and a plasma is described by Maxwell's equations and the nonlinear relativistic hydrodynamic equations for a cold plasma. The excitation of linear waves by a one-dimensional bunch is investigated against a cold plasma background. It is shown that, in a certain range of parameter values of the bunch, pump wave, and plasma, the excitation is resonant in character and the amplitude of the excited wake waves increases with distance from the bunch. © *2001 MAIK "Nauka/Interperiodica".*

1. INTRODUCTION

Plasma-based methods of charged particle acceleration, which have been actively developed over the past decade, occupy an important place among novel acceleration schemes (see, e.g., [1, 2] and the literature cited therein). The excitation of wake waves by charged-particle bunches is one of the ways of generating strong (up to $E \sim 1$ GV/m) electromagnetic fields in plasmas. The induced wake fields can serve not only to accelerate charged particles but also to focus electron (positron) bunches [3] with the aim of generating high-density beams and ensuring high luminosity in the next generation of linear colliders.

Many papers have been devoted to the linear theory of one-dimensional wake waves [3–10]. The nonlinear theory of these waves was developed in [11–18].

This work is a continuation of paper [19], which was aimed at studying the effect of the field of a circularly polarized electromagnetic wave of arbitrary intensity $A \equiv eE_0/mc\omega_0$ (where E_0 and ω_0 are the amplitude and frequency of the electromagnetic field) on the excitation of electromagnetic wake waves by a one-dimensional relativistic electron bunch in a cold plasma, in which case the electron oscillatory velocity in the pump field can be close to the speed of light. It was shown that there are three ranges of parameter values of the pump wave, bunch, and plasma in which the linear equations for the induced longitudinal and transverse fields have three different solutions. The induced fields were studied only in the parameter range where the plasma is stable against the parametric instability, which was thoroughly analyzed in [20–23]. In this case, the induced fields were found to be a superposition of two harmonic oscillations with different amplitudes and frequencies [19].

The objective of the present paper is to investigate the role played by a strong electromagnetic wave with circular polarization in the excitation of one-dimensional linear wake fields in the parameter range in which the plasma is unstable against the parametric instability. As in [19], the pump wave–plasma interaction in the absence of a bunch is described by Maxwell's equations and nonlinear hydrodynamic equations in the cold plasma approximation. In this case, the plasma can be in a spatially homogeneous state [18, 20]. Then, perturbation theory is applied to derive and analyze the expressions for the induced fields under the assumption that a one-dimensional bunch propagating in the plasma distorts this state only slightly.

2. BASIC EQUATIONS AND THEIR SOLUTIONS

Assuming that the oscillatory velocity of the plasma electrons in an external field is much higher than the electron thermal velocity and the pump frequency ω_0 is far above the electron–ion collision frequency, we start with the following basic set of equations, which includes Maxwell's equations and the relativistic hydrodynamic equation of motion for a cold electron plasma:

$$\nabla \times \mathbf{B} = \frac{1}{c}\frac{\partial \mathbf{E}}{\partial t} - \frac{4\pi e}{c} n\mathbf{v} - \frac{4\pi e}{c}\mathbf{u} n_b(\xi), \tag{1}$$

$$\nabla \times \mathbf{E} = -\frac{1}{c}\frac{\partial \mathbf{B}}{\partial t}, \quad \nabla \cdot \mathbf{B} = 0, \tag{2}$$

$$\nabla \cdot \mathbf{E} = -4\pi e(n - n_0) - 4\pi e n_b(\xi), \tag{3}$$

$$\frac{\partial \mathbf{v}}{\partial t} + (\mathbf{v} \cdot \nabla)\mathbf{v} = -\frac{e}{m}\sqrt{1 - \frac{v^2}{c^2}}\left[\mathbf{E} + \frac{1}{c}\mathbf{v} \times \mathbf{B} - \frac{\mathbf{v}}{c^2}(\mathbf{v} \cdot \mathbf{E})\right], \tag{4}$$

1063-780X/01/2710-0852$21.00 © 2001 MAIK "Nauka/Interperiodica"

$$\frac{\partial n}{\partial t} + \nabla \cdot (n\mathbf{v}) = 0, \quad (5)$$

where $\xi = z - ut$, n_0 is the unperturbed electron plasma density, and $n_b(\xi)$ is the density of a given one-dimensional bunch propagating with the velocity $\mathbf{u}$ (such that $\mathbf{u} = u\mathbf{e}_z$, $|\mathbf{e}_z| = 1$) in a plasma. Since we are interested in relativistic bunches, we neglect oscillations of the bunch electrons in an external electromagnetic pump wave.

In the field of a circularly polarized electromagnetic wave propagating along the z-axis, the plasma can be in a spatially homogeneous state, in which the electromagnetic field and electron velocity are given by the relationships [18, 20]

$$\mathbf{E}_0 = E_0(\mathbf{e}_x \cos\psi + \mathbf{e}_y \sin\psi), \quad E_{0z} = 0, \quad (6)$$

$$\mathbf{B}_0 = \frac{k_0 c}{\omega_0} E_0(-\mathbf{e}_x \sin\psi + \mathbf{e}_y \cos\psi), \quad B_{0z} = 0, \quad (7)$$

$$\mathbf{v}_e = c\beta_e(-\mathbf{e}_x \sin\psi + \mathbf{e}_y \cos\psi), \quad v_{ez} = 0, \quad (8)$$

where $\psi = \omega_0 t - k_0 z$, $k_0 = (\omega_0/c)\sqrt{\varepsilon(\omega_0)}$, $\varepsilon(\omega) = 1 - \omega_L^2/\omega^2$, $\omega_L^2 = \omega_p^2\sqrt{1-\beta_e^2}$, $\beta_e = v_e/c$,

$$v_e = c\frac{A}{\sqrt{1+A^2}}, \quad (9)$$

$A = eE_0/mc\omega_0$, $\omega_p^2 = 4\pi n_0 e^2/m$ is the square of the plasma frequency, and c is the speed of light in vacuum.

We consider small perturbations that are driven in the plasma by an electron bunch with density n_b such that $n_b \ll n_0$. We represent all of the quantities in the form $f = f_0 + f'$, where f_0 stands for the unperturbed quantities in expressions (6)–(9), and switch from the x- and y-components of the fields and electron plasma velocities to the new variables

$$\begin{pmatrix} E^\pm \\ B^\pm \\ v^\pm \end{pmatrix} = \begin{pmatrix} E_x' \pm iE_y' \\ B_x' \pm iB_y' \\ v_x' \pm iv_y' \end{pmatrix} = \begin{pmatrix} \mathscr{E}^\pm(\xi) \\ \mathscr{B}^\pm(\xi) \\ \mathscr{V}^\pm(\xi) \end{pmatrix} \exp(\pm i\psi). \quad (10)$$

In other words, we pass over to a rotating frame of reference associated with the pump wave.

In [19], linearizing Eqs. (1)–(5) with allowance for transformation (10) yielded the following expressions for the components of the induced electromagnetic fields:

$$\begin{pmatrix} E_z'(\xi) \\ \mathscr{E}^+(\xi) \end{pmatrix} = \int_{-\infty}^{+\infty} d\xi' n_b(\xi') \begin{pmatrix} G_z(\xi' - \xi) \\ G_\perp(\xi' - \xi) \end{pmatrix}. \quad (11)$$

Here, $G_z^{(e)}$ and $G_\perp^{(e)}$ are the Green's functions for the quantities E_z' and $\mathscr{E}^+$,

$$G_z(s) = -2ie\int_{-\infty}^{+\infty} \frac{dk}{k} \frac{D_1(k,\omega)}{D(k,\omega)} \exp(iks), \quad (12)$$

$$G_\perp(s) = -\frac{2e\beta_e\omega_L^2}{c}\int_{-\infty}^{+\infty} dk(ku + \omega_0)\frac{R_{-1}(k,\omega)}{D(k,\omega)}\exp(iks), \quad (13)$$

where $\omega = ku$. According to Eqs. (2), the induced magnetic field is related to the transverse electric field as

$$\mathscr{B}^\pm(\xi) = \pm\frac{c}{u}\left\{ i\mathscr{E}^\pm(\xi) + \left(\frac{\omega_0}{u} - k_0\right)\int_{-\infty}^{\xi} d\xi' \exp\left[i\frac{\omega_0}{u}(\xi' - \xi)\right]\mathscr{E}^\pm(\xi')\right\}, \quad (14)$$

$$B_z' = 0,$$

where we introduce the notation

$$R_{\pm 1}(k,\omega) = (k \pm k_0)^2 - \frac{(\omega \pm \omega_0)^2}{c^2}\varepsilon(\omega \pm \omega_0), \quad (15)$$

$$D_1(k,\omega) = \omega^2 R_1(k,\omega)R_{-1}(k,\omega) + \frac{\beta_e^2\omega_L^2}{2}\left(k^2 - \frac{\omega^2}{c^2}\right)[R_1(k,\omega) + R_{-1}(k,\omega)], \quad (16)$$

$$D(k,\omega) = \omega^2\varepsilon(\omega)R_1(k,\omega)R_{-1}(k,\omega) + \frac{\beta_e^2\omega_L^2}{2}\left(k^2 - \frac{\omega^2}{c^2}\varepsilon(\omega)\right)[R_1(k,\omega) + R_{-1}(k,\omega)]. \quad (17)$$

The transverse components of the induced electric and magnetic fields can be found from expressions (10) by taking either a real or an imaginary part of the complex quantities $\mathscr{E}^+$ and $\mathscr{B}^+$. As a result, we obtain

$$E_x'(z,t) = E_r(\xi)\cos\psi - E_i(\xi)\sin\psi,$$
$$E_y'(z,t) = E_r(\xi)\sin\psi + E_i(\xi)\cos\psi, \quad (18)$$

where

$$E_r(\xi) = \mathrm{Re}(\mathscr{E}^+(\xi)), \quad E_i(\xi) = \mathrm{Im}(\mathscr{E}^+(\xi)). \quad (19)$$

Hence, expressions (18) for the transverse components of the induced fields describe modulational perturbations in the plasma. Note that, in the absence of a pump wave ($\beta_e = 0$), the transverse components of the per-

turbed quantities vanish and expressions (11) and (12) pass over to the familiar formulas for one-dimensional linear fields.

Now, we proceed to a calculation of the Green's functions defined in expressions (12) and (13). The poles of the integrals in these expressions are the roots of the dispersion relation $D(k, \omega) = 0$. In the general case (i.e., when the Cherenkov resonance condition $\omega = ku$ is not imposed), this dispersion relation was investigated in detail by Kalmikov and Kotsarenko [20]. In the absence of a pump wave ($\beta_e = 0$), Eq. (17) yields conventional dispersion relations for plasma waves, $\omega = \omega_p$, and for transverse (electromagnetic) waves, $\omega^2 = \omega_p^2 + k^2c^2$. The presence of a pump wave ($\beta_e \neq 0$) gives rise to coupled waves in a plasma. If the pump wave is sufficiently weak ($\beta_e \ll 1$), then the growth rate of the coupled waves increases linearly with β_e. Consequently, the coupled waves are parametrically unstable down to $\beta_e = 0$.

Under the Cherenkov resonance condition $\omega = ku$, Eq. (17) gives the dispersion relation

$$\left(k^2 - \frac{\omega_L^2}{u^2}\right)\left[k^2 - 4\gamma^4\left(k_0 - \beta\frac{\omega_0}{c}\right)^2\right] + \frac{\beta_e^2\omega_L^2}{u^2}\left(k^2 + \gamma^2\frac{\omega_L^2}{c^2}\right) = 0, \quad (20)$$

where $\beta = u/c$ and $\gamma^{-2} = 1 - \beta^2$.

We introduce the dimensionless wave vector χ, which is related to k by $k = (\omega_L/u)\chi$, in order to represent the solutions to Eq. (20) in the form

$$\chi_\pm^2 = \frac{1}{2a^4} + 2\beta^2\gamma^4F^2 \pm \sqrt{\left(\frac{1}{2a^4} + 2\beta^2\gamma^4F^2\right)^2 - \beta^2\gamma^2\left(\frac{a^4-1}{a^4} + 4\gamma^2F^2\right)}, \quad (21)$$

where

$$F = \sqrt{a^2\Delta^2 - 1} - \beta a\Delta, \quad (22)$$

$\Delta = \omega_0/\omega_p$, and $a^2 = \sqrt{1 + A^2}$. The character of the solutions to Eq. (20) (and, accordingly, the nature of the induced fields and electron plasma velocities) is largely governed by the sign of the expression under the square root in formula (21). We denote the regions where this expression is positive and negative by *I* and *III*, respectively. The boundary between these regions (at which this expression vanishes) is denoted by *II*. We equate the expression at hand to zero to obtain the following expression for Δ at boundary *II*:

$$\Delta_\pm^{(\mu)} = \frac{\gamma}{a}(\sqrt{1 + \gamma^2F_\mu^2} \pm \beta\gamma F_\mu), \quad (23)$$

where the index μ indicates a plus or minus sign and

$$F_\pm = \sqrt{\frac{2 - 1/a^4 \pm 2\gamma\sqrt{1 - 1/a^4}}{4\gamma^2(\gamma^2 - 1)}}. \quad (24)$$

With $\mu = +$ and $\mu = -$, expressions (23) are valid for $a > 1$ and $1 < a < a_0(\gamma)$, respectively, where

$$a_0(\gamma) = \left\{\frac{1 + \sqrt{1 - 1/\gamma^2}}{2\sqrt{1 - 1/\gamma^2}}\right\}^{1/4}. \quad (25)$$

Formulas (23)–(25) were obtained under the assumption $\gamma > \gamma_1 \approx 1.45$, where γ_1 is the real positive root of the equation $2\gamma^2(\gamma^2 - 2) = \gamma - 1$, satisfying the condition $\gamma > 1$. For a small-amplitude pump wave ($a - 1 \ll 1$), the function $\Delta_+^{(+)}$ coincides with $\Delta_+^{(-)}$ and the function $\Delta_-^{(+)}$ coincides with $\Delta_-^{(-)}$. The expressions for these functions, which will be denoted by $\Delta_\pm^{(0)}$, can be obtained from formulas (23) and (24):

$$\Delta_\pm^{(0)}(\gamma) = \gamma\sqrt{1 + \frac{1}{4(\gamma^2 - 1)}} \pm \frac{1}{2}. \quad (26)$$

Additionally, for $a = a_0(\gamma)$, the function $\Delta_+^{(-)}$ coincides with $\Delta_-^{(-)}$. For this function, which will be denoted by $\Delta_0(\gamma)$, formulas (23) and (24) give

$$\Delta_0(\gamma) = \frac{\gamma}{a_0(\gamma)} = \gamma\left\{\frac{2\sqrt{1 - 1/\gamma^2}}{1 + \sqrt{1 - 1/\gamma^2}}\right\}^{1/4}. \quad (27)$$

As a result, from the above expressions, we can see that boundary *II* is composed of the four curves $\Delta_\pm^{(+)}$ and $\Delta_\pm^{(-)}$, which envelop a closed region (the curves $\Delta_+^{(+)}$ and $\Delta_-^{(+)}$ close upon themselves at infinity). We denote the curves $\Delta_-^{(+)}$, $\Delta_-^{(-)}$, $\Delta_+^{(-)}$, and $\Delta_+^{(+)}$ by *a*', *b*', *c*', and *d*', respectively. In the case of relativistic bunches, two of the curves, *c*' and *b*', lie in the very narrow region $1 < a < a_0(\gamma) \approx 1 + 1/16\gamma^2$. The pump wave amplitude is maximum at $a = a_0(\gamma)$ and $\Delta = \Delta_0(\gamma)$:

$$E_{0\max}(\gamma) = \frac{E_p}{(2\sqrt{1 - 1/\gamma^2})^{1/4}(1 + \sqrt{1 - 1/\gamma^2})^{3/4}}, \quad (28)$$

where $E_p = mc\omega_p/e$. For relativistic bunches, we have $E_{0\max}(\gamma) \simeq (E_p/2)(1 + 5/16\gamma^2)$.

Figure 1 shows regions *I* and *III* and boundary *II* between them for $\gamma = 10$ and 100. The curves close upon themselves at infinity (i.e., for $E_0 \longrightarrow \infty$). Figure 1 also shows a part of the dependence of Δ on E_0 at boundary *II* (curves *a*', *b*', *c*', and *d*') for $\gamma = 100$ and for a small-amplitude pump wave such that $0 \le E_0 \le E_{0\max} \approx E_p/2$. For electromagnetic pump waves with intensities $I_L \le 10^{16}$ W/cm^2, parameter *a* is on the order of unity at a pump frequency of about $\omega_0 \approx 3 \times 10^{15}$ s^{-1}. Consequently, Fig. 1 and formulas (23)–(27) imply that, in order for the solutions to Eq. (20) in the parameter range $\omega_0 \approx 10^{15}$ s^{-1} and $n_0 < 10^{17}$ cm^{-3} ($\omega_p < 10^{13}$ s^{-1}) to lie at boundary *II*, the electron bunch should be ultrarelativistic ($\gamma \sim a\Delta > 100$). In what follows, we restrict ourselves to treating the problem in the parameter range corresponding to boundary *II* and to studying the induced fields for the relevant parameter values. The induced fields in region *I* were investigated in detail in [19]. As for the solutions in region *III*, expression (21) shows that the amplitude of the induced electric fields decreases exponentially when away from the bunch, so that these solutions are totally uninteresting for the generation of high accelerating or focusing electric fields in plasmas.

Now, we evaluate the Green's function for the parameters corresponding to boundary *II*. In the general case, expressions (21) describe coupled longitudinal and transverse waves with the wavenumbers $k_+ = (\omega_L/u)\chi_+$ and $k_- = (\omega_L/u)\chi_-$ (or the frequencies $\omega_+ = \omega_L\chi_+$ and $\omega_- = \omega_L\chi_-$). At boundary *II*, the expression under the square root in formula (21) vanishes and the equality $k_+ = k_-$ (or $\omega_+ = \omega_-$) holds. Consequently, at the boundary, the wave excitation is resonant in character. Taking into account the fact that the roots of Eq. (20) are multiple and lie in the upper half-plane of the complex variable *k*, we integrate expressions (12) and (13) over *k* to obtain

$$G_z(s) = 4\pi e\theta(s)[\cos(\sigma_\mu k_p s) + L_\mu(k_p s)\sin(\sigma_\mu k_p s)], \tag{29}$$

$$G_\perp(s) = \pi i e\sqrt{1-\frac{1}{a^4}}\frac{4Q_\pm^{(\mu)}}{\beta}[\theta(s)-\theta(-s)] - \frac{2\pi e\beta\gamma^2}{a^3\sigma_\mu^3}\sqrt{1-\frac{1}{a^4}}\theta(s)\{[\mathcal{A}_\pm^{(\mu)} + i\mathcal{B}_\pm^{(\mu)}(k_p s)]\sin(\sigma_\mu k_p s) - [\mathcal{A}_\pm^{(\mu)}\sigma_\mu(k_p s) - iC_\pm^{(\mu)}]\cos(\sigma_\mu k_p s)\}, \tag{30}$$

where

$$\sigma_\mu^2 = \frac{1}{a^2}\left(1+\mu\gamma\sqrt{1-\frac{1}{a^4}}\right), \quad L_\mu = \frac{\sigma_\mu^2 a^2 - 1}{2a^2\sigma_\mu}, \tag{31}$$

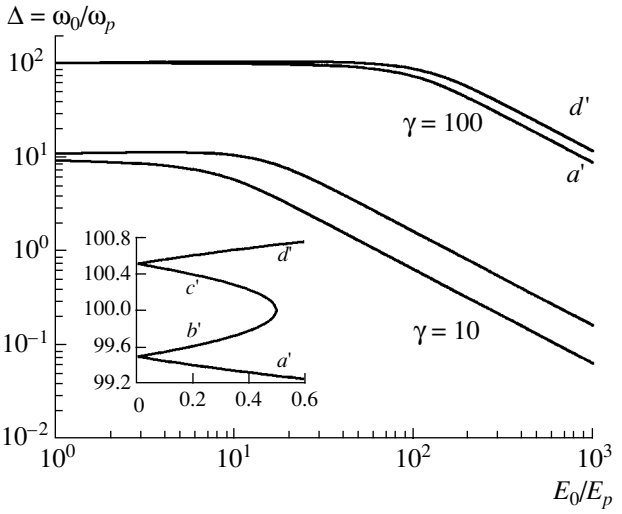

Fig. 1. The curves $\Delta = \Delta(E_0)$ (boundary *II*), on which the expression under the square root in formula (21) equals zero, for $\gamma = 10$ and 100. Regions *I* and *III* lie outside and inside the curves, respectively.

$$\mathcal{A}_\pm^{(\mu)} = \gamma(\sqrt{1+\gamma^2F_\mu^2} \mp \beta\gamma F_\mu),$$
$$\mathcal{B}_\pm^{(\mu)} = \pm\frac{2\beta\gamma^3}{a}F_\mu\sqrt{1+\gamma^2F_\mu^2} - \frac{1}{2a^5}, \tag{32}$$

$$C_\pm^{(\mu)} = 2\left(\frac{\mathcal{B}_\pm^{(\mu)}}{\sigma_\mu} + a\sigma_\mu\right),$$
$$Q_\pm^{(\mu)} = \frac{\beta^3\gamma^5F_\mu(\beta\gamma F_\mu \pm \sqrt{1+\gamma^2F_\mu^2})}{a^4\sigma_\mu^4}, \tag{33}$$

$k_p = \omega_p/u$, $\theta(s)$ is the Heaviside step function, and the function F_μ is defined by formula (24). In expressions (29)–(33) with $\mu = +$ and $\mu = -$, the parameter values of our problem lie on the curves $\Delta_\pm^{(+)}$ and $\Delta_\pm^{(-)}$, respectively. For $a = 1$ (i.e., in the absence of a pump wave), the function $G_\perp$ vanishes and the function G_z is given by the expression that coincides with the corresponding formulas presented in [24, 25].

3. WAKE FIELDS IN THE CASE OF A GAUSSIAN BUNCH

Here, we investigate the fields induced by a Gaussian electron bunch. We assume that the electron density in the bunch is described by the expression

$$n_b(\xi) = \frac{N_b}{\sqrt{\pi}}\exp\left(-\frac{\xi^2}{d^2}\right), \tag{34}$$

where N_b is the mean bunch density such that $N_b \ll n_0$.

We substitute formulas (29) and (30) and expression (34) into formula (11) to obtain the following expres-

sions for the fields induced by a moving bunch:

$$E_z'(\xi) = E_p\frac{N_b}{2n_0}\lambda\beta\Bigg\{[\mathcal{F}_\mu\cos(\sigma_\mu\zeta) + L_\mu\zeta\sin(\sigma_\mu\zeta)]\Phi_r\left(\frac{\zeta}{\lambda}, \frac{\sigma_\mu\lambda}{2}\right) + [L_\mu\zeta\cos(\sigma_\mu\zeta) - \mathcal{F}_\mu\sin(\sigma_\mu\zeta)]\Phi_i\left(\frac{\zeta}{\lambda}, \frac{\sigma_\mu\lambda}{2}\right)\Bigg\}, \quad (35)$$

$$\begin{aligned}\mathcal{E}^+(\xi) = E_p\frac{N_b}{n_0}\lambda\sqrt{1-\frac{1}{a^4}}\{-iQ_\pm^{(\mu)}[1-\Phi(\zeta/\lambda)] \\ + \frac{\beta^2\gamma^2}{4\sigma_\mu^3a^3}\Bigg\{\frac{\mathcal{A}_\pm^{(\mu)}\sigma_\mu\lambda}{\pi^{1/2}}e^{-\zeta^2/\lambda^2} \\ + [(\mathcal{A}_\pm^{(\mu)}Z_\mu - i\mathcal{B}_\pm^{(\mu)}\zeta)\sin(\sigma_\mu\zeta) \\ - (\sigma_\mu\mathcal{A}_\pm^{(\mu)}\zeta + i\mathcal{D}_\pm^{(\mu)})\cos(\sigma_\mu\zeta)]\Phi_r\left(\frac{\zeta}{\lambda}, \frac{\sigma_\mu\lambda}{2}\right) \\ + [(\sigma_\mu\mathcal{A}_\pm^{(\mu)}\zeta + i\mathcal{D}_\pm^{(\mu)})\sin(\sigma_\mu\zeta) \\ + (\mathcal{A}_\pm^{(\mu)}Z_\mu - i\mathcal{B}_\pm^{(\mu)}\zeta)\cos(\sigma_\mu\zeta)]\Phi_i\left(\frac{\zeta}{\lambda}, \frac{\sigma_\mu\lambda}{2}\right)\Bigg\},\end{aligned} \quad (36)$$

where $\zeta = k_p\xi$, $\lambda = k_pd$, $\Phi(x) = 1 - \mathrm{erf}(x)$, $\mathrm{erf}(x)$ is the probability integral, and

$$\mathcal{F}_\mu = 1 + \frac{\sigma_\mu^2a^2 - 1}{4a^2}\lambda^2, \quad Z_\mu = 1 + \frac{\sigma_\mu^2\lambda^2}{2}, \quad (37)$$

$$\mathcal{D}_\pm^{(\mu)} = 2a\sigma_\mu + \frac{1+Z_\mu}{\sigma_\mu}\mathcal{B}_\pm^{(\mu)}, \quad (38)$$

$$\begin{pmatrix}\Phi_r(x,y)\\ \Phi_i(x,y)\end{pmatrix} = \pm\frac{2}{\sqrt{\pi}}\int_x^\infty dt\exp(-t^2)\begin{pmatrix}\cos(2yt)\\ \sin(2yt)\end{pmatrix}. \quad (39)$$

Note that the functions $\Phi_r(x, y)$ and $\Phi_i(x, y)$ can be expressed in terms of the probability integral $\mathrm{erf}(x + iy)$ of the complex argument.

From expressions (35) and (39), we can see that, at large distances ahead of the bunch ($\xi > \sigma_\mu k_pd^2/2$), the longitudinal electric field is exponentially weak,

$$E_z'(\xi) \simeq E_p\frac{N_b}{2n_0}\lambda\beta\frac{1}{\sqrt{\pi}}\frac{e^{-\zeta^2/\lambda^2}}{\zeta/\lambda}, \quad (40)$$

and the transverse electric fields are unmodulated (i.e., are essentially independent of ξ),

$$\mathcal{E}^+(\xi) \simeq iE_p\frac{N_b}{n_0}\lambda\sqrt{1-\frac{1}{a^4}}\left(-Q_\pm^{(\mu)} + \frac{\beta^2\gamma^2\mathcal{D}_\pm^{(\mu)}}{4\sigma_\mu^3a^3}\frac{e^{-\zeta^2/\lambda^2}}{\pi^{1/2}(\zeta/\lambda)}\right). \quad (41)$$

Ahead of the bunch, the transverse electric fields are generated because the phase velocity $v_\varphi = \omega_0/k_0 > c$ of the pump wave is higher than the bunch velocity for arbitrary values of the plasma and wave parameters. Consequently, part of the perturbations driven by the pump wave and bunch in the plasma can propagate at a phase velocity higher than the bunch velocity and can thereby overtake the bunch. In addition, expressions (18), (19), and (41) yield the relationships $E_i(\xi) \gg E_r(\xi) \approx 0$, $E_x' \simeq -E_i(\xi)\sin\psi$, and $E_y' \simeq E_i(\xi)\cos\psi$.

As follows from expressions (18), (19), and (36), the transverse electric fields are modulated and circularly polarized. However, although the polarization vector of the transverse wave spans an entire circle, the circle's radius depends on the distance ξ from the bunch. In fact, from expressions (18) and (19), we have

$$E_x'^2 + E_y'^2 = E_r^2(\xi) + E_i^2(\xi) = E_{\max}^2(\xi). \quad (42)$$

In the general case, the electric field amplitude $E_{\max}$ is a function of ξ. Modulated transverse plasma waves are generated in the interaction between a pump wave and induced waves with frequency $\omega_L\sigma_\mu a$ and wavenumber $(\omega_L/u)\sigma_\mu a$. This interaction gives rise to oscillations with the combination frequencies $\omega_0 - \omega_L\sigma_\mu a$, $\omega_0 + \omega_L\sigma_\mu a$ and combination wavenumbers $k_0 - (\omega_L/u)\sigma_\mu a$, and $k_0 + (\omega_L/u)\sigma_\mu a$; the modulated wave results from the interference between these oscillations.

At large distances behind the bunch ($\xi < 0$, $|\xi| > \sigma_\mu k_pd^2/2$), expressions (35) and (36) take the form

$$E_z'(\xi) \simeq E_p\frac{N_b}{n_0}\lambda\beta \times \exp(-\sigma_\mu^2\lambda^2/4)[\mathcal{F}_\mu\cos(\sigma_\mu\zeta) + L_\mu\zeta\sin(\sigma_\mu\zeta)], \quad (43)$$

$$\begin{aligned}\mathcal{E}^+(\xi) \simeq E_p\frac{N_b}{n_0}\lambda\sqrt{1-\frac{1}{a^4}}\{iQ_\pm^{(\mu)} \\ + (\beta^2\gamma^2/2\sigma_\mu^3a^3)\exp(-\sigma_\mu^2\lambda^2/4) \\ \times[(\mathcal{A}_\pm^{(\mu)}Z_\mu - i\mathcal{B}_\pm^{(\mu)}\zeta)\sin(\sigma_\mu\zeta) \\ - (\sigma_\mu\mathcal{A}_\pm^{(\mu)}\zeta + i\mathcal{D}_\pm^{(\mu)})\cos(\sigma_\mu\zeta)]\}.\end{aligned} \quad (44)$$

In the above formulas, the terms that are proportional to ξ (or ζ) describe waves whose amplitude increases with distance from the bunch and whose wavelength is equal to $\lambda_p = \lambda_p^{(0)}/\sigma_\mu$, where $\lambda_p^{(0)} = 2\pi u/\omega_p$ is the wavelength

in the absence of a pump wave. Figure 2 shows the wavelength computed as a function of the pump wave amplitude for $\gamma = 10$ and 100. The parameters adopted for numerical calculations correspond to two boundary curves, a' and d'. One can see that the wavelength is maximum at $E_0 \approx 2^{-1/4}\gamma E_p$. In accordance with expression (31), the wavelength of the induced waves for the parameters corresponding to two other curves, b' and c', increases monotonically from $\lambda_p^{(0)}$ to $\lambda_p^{(0)}\sqrt{2}$ as the pump wave amplitude increases from zero to $E_{0\max}$ [see expression (28)]. Consequently, the pump wave can markedly change the wavelength of the excited waves; this effect is more pronounced for small values of γ (Fig. 2). Note that, in region *I*, the wavelength λ_p increases monotonically with the pump wave intensity [19].

Let us analyze the above formulas for the following, practically important parameter range: $n_0 \le 10^{17}$ cm^{-3} ($\omega_p \le 2 \times 10^{13}$ s^{-1}), $I_L \sim 10^{16}$ W/cm^2, $\omega_0 \approx 10^{15}$ s^{-1}, and $\gamma \gg 1$.

The coefficients in expressions (35) and (36) are comparatively easy to analyze in the two limiting cases $\Delta = \Delta_\pm^{(-)}$ (the parts of curves c' and b' in region *II*) and $\Delta = \Delta_\pm^{(+)}$ (the parts of curves d' and a' in region *II*). Thus, in the first case, formulas (31)–(33), (37), and (38) at $a \approx a_0(\gamma)$ give

$$\sigma_- \approx \frac{1}{2^{1/2}}, \quad L_- \approx -\frac{1}{2^{3/2}}, \quad \mathcal{F}_- \approx 1 - \frac{\lambda^2}{8}, \tag{45}$$

$$\mathcal{A}_\pm^{(-)} \approx \gamma, \quad \mathcal{B}_\pm^{(-)} \approx -\frac{1}{2}, \quad Q_\pm^{(-)} \approx 0,$$
$$\mathcal{D}_\pm^{(-)} \approx -\frac{\lambda^2\sqrt{2}}{8}, \quad Z_- \approx 1 + \frac{\lambda^2}{4}. \tag{46}$$

For $\Delta = \Delta_\pm^{(+)}$ and $\gamma\sqrt{1 - 1/a^4} \gg 1$, instead of formulas (45) and (46), we obtain

$$\sigma_+^2 \approx \frac{\gamma}{a^2}\sqrt{1 - \frac{1}{a^4}} \gg 1, \ L_+ \approx \frac{\sigma_+}{2}, \ \mathcal{F}_+ \approx 1 + \frac{\lambda^2\sigma_+^2}{4}, \tag{47}$$

$$\mathcal{A}_\pm^{(+)} \approx \gamma, \quad \mathcal{B}_\pm^{(+)} \approx \pm\gamma\sigma_+, \quad Q_\pm^{(+)} \approx \pm\frac{1}{2}\left(\frac{\gamma^2}{1 - 1/a^4}\right)^{3/4},$$
$$\mathcal{D}_\pm^{(+)} \approx \pm 2\gamma\left(1 + \frac{\lambda^2\sigma_+^2}{4}\right), \quad Z_- \approx 1 + \frac{\lambda^2\sigma_+^2}{2}. \tag{48}$$

A comparison of formulas (45) and (46) with formulas (47) and (48) shows that the coefficients that describe the induced fields are much larger at $\Delta = \Delta_\pm^{(+)}$ (the parameters of the problem correspond to curve a' or curve d'). In what follows, we restrict ourselves to considering curves a' and d'.

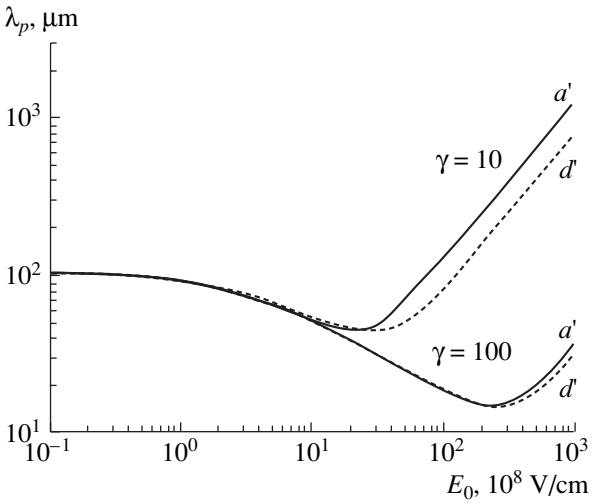

Fig. 2. Dependence of the wavelength λ_p of the induced waves on the pump field amplitude E_0 for $n_0 = 10^{17}$ cm^{-3} and $\gamma = 10$ and 100. The results obtained for curves a' and d' are shown by solid and dashed lines, respectively.

Ahead of the bunch, the transverse electric field at $a > 1 + 1/4\gamma^2$ is equal in order of magnitude to $|\mathcal{E}^+| \approx E_p(N_b/n_0)\lambda(1 - 1/a^4)^{-1/4}\gamma^{3/2}/2$. Behind the bunch, the amplitude of the longitudinal electric field increases with the bunch width (the quantity d) and reaches its maximum at $\lambda_{\max} = k_p d_{\max} \simeq \sqrt{2}/\sigma_+$. At sufficiently large distances from the bunch ($|\xi| > \sigma_\mu k_p d^2/2$) and for a longitudinal field close to its maximum value, formulas (47) give $L_+ \gg \mathcal{F}_+$. Consequently, the longitudinal electric field behind the bunch is largely determined by the second term in expression (43). At large distances behind the bunch, the amplitude of the transverse electric field is also maximum at $\lambda \approx \lambda_{\max}$; near this maximum, the transverse field is mainly determined by the second and third terms in the square brackets in expression (44). In addition, expressions (43), (44), (47), and (48) show that the induced field increases with the pump wave intensity. Consequently, for fixed but sufficiently large values of ζ, the induced field is maximum for sufficiently narrow bunches ($\lambda \ll 1$).

Now, we consider the dependence of the induced fields on the bunch energy (or equivalently on the relativistic factor γ). According to expressions (43) and (44), the amplitude of the longitudinal wave depends weakly on the bunch energy, while the amplitude of the transverse wave increases with γ approximately as $\gamma^{3/2}$ [see expression (44)] and is much larger than the longitudinal field amplitude. Consequently, for $\gamma \gg 1$, the induced wave is nearly transverse.

The characteristic features mentioned above are clearly seen from Figs. 3–5, which display the induced field amplitudes calculated from formulas (31)–(33) and (35)–(39) for the parameter values corresponding to curve d'. Note that, in Fig. 4, the dependence of the

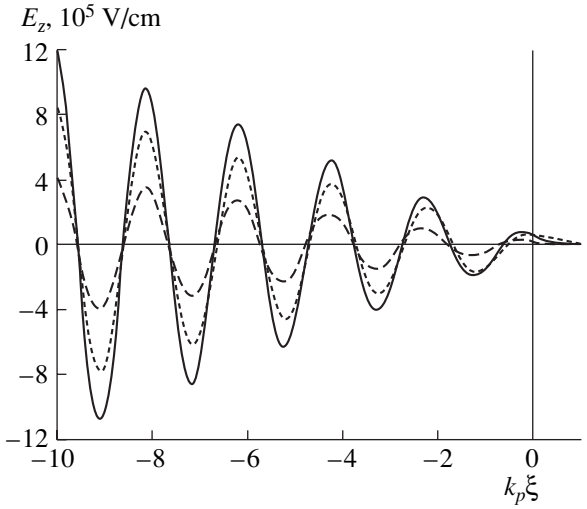

Fig. 3. Dependence of the amplitude of the induced longitudinal electric field on ξ at boundary *II* for n $n_0 = 10^{17}$ cm^{-3}, $n_b = 10^{14}$ cm^{-3}, $\omega_0 = 1.82 \times 10^{15}$ s^{-1}, $E_0 = 3.04 \times 10^9$ V/cm, $\gamma = 100$, and $k_p^{-1} = 16.8$ μm. The dotted, solid, and dashed curves were calculated for $k_p d = 0.7$, $k_p d = k_p d_{\max} = 0.432$, and $k_p d = 0.1$, respectively.

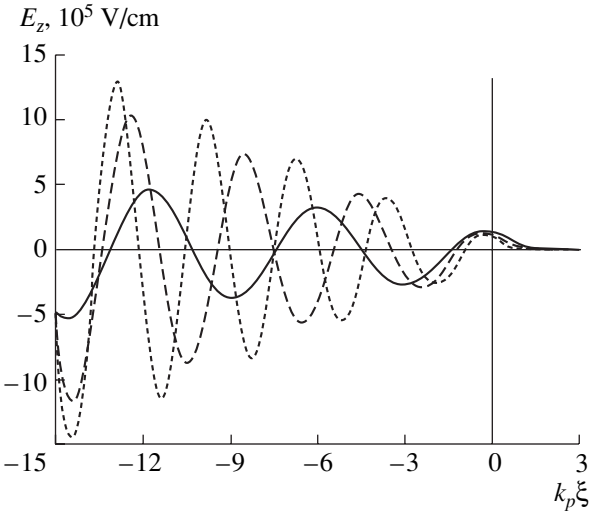

Fig. 4. Dependence of the amplitude of the induced longitudinal electric field on ξ at boundary *II* for $d = d_{\max}$. The solid curve corresponds to $E_0 = 10^8$ V/cm ($\Delta = 100.64$, $k_p d_{\max} \simeq 1.228$), the dashed curve corresponds to $E_0 = 5 \times 10^8$ V/cm ($\Delta = 100$, $k_p d_{\max} \simeq 0.87$), and the dotted curve corresponds to $E_0 = 10^9$ V/cm ($\Delta = 101.35$, $k_p d_{\max} \simeq 0.687$). The remaining parameter values are the same as in Fig. 3.

longitudinal field on the distance from the bunch was calculated for different intensities of the pump wave under the condition $E_0 < 2^{-1/4}\gamma E_p$. From this figure, we can see that the wavelength of the excited waves decreases with increasing E_0.

It should be noted that the amplitude of the transverse wake field increases with distance from the bunch only when the frequency and amplitude of the pump wave, the plasma density, and the bunch energy (the relativistic factor γ) all satisfy relationships (23), which determine boundary *II*. Although these parameters of the problem are independent of each other, the situation in which they exactly correspond to boundary *II* is very difficult to realize in practice. Assuming that E_0, ω_0, and n_0 are fixed, we briefly discuss the question about the width $\Delta\gamma$ of "region" *II*; i.e., we determine he maximum possible deviation of the relativistic factor from boundary *II* for which the amplitude of the wake waves still increases. We consider two bunch energies, γ and γ_0 ($|\gamma - \gamma_0| \ll \gamma_0$), assuming that the quantity γ lies in region *I* and that the quantity γ_0, together with E_0, ω_0, and n_0, satisfies relationships (23), or, in other words, the values of these four parameters exactly correspond to boundary *II*. In [19], it was shown that γ values lying in region *I* imply the excitation of two wake waves whose amplitudes and wavenumbers $\chi_\pm$ are independent of the ξ coordinate [see expression (21)]. Moreover, we have $\chi_+ \longrightarrow \chi_- \longrightarrow a\sigma_\pm$ as $\gamma \longrightarrow \gamma_0$, in which case the corresponding formulas derived in [19] yield expressions (29) and (30) for the Green's function. Consequently, the effect of the increase in the amplitude of the excited wake waves will also take place for region *I* under the conditions

$$k_p l < k_p L < \frac{a}{\Delta\chi}, \tag{49}$$

where *l* is the distance from the bunch, *L* is the longitudinal plasma dimension, and $\Delta\chi = (\chi_+ - \chi_-)/2 \ll \chi_\pm$.

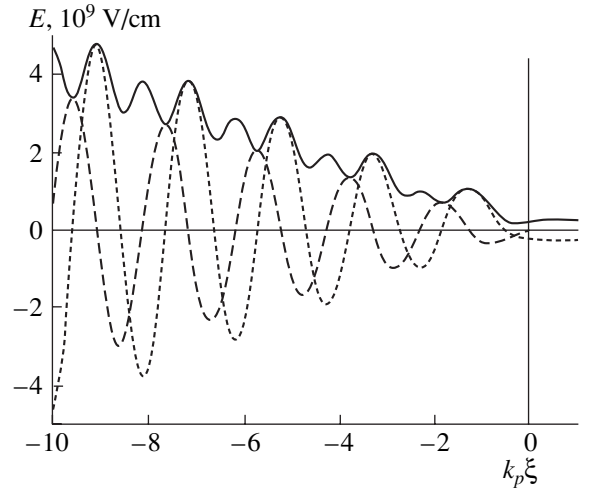

Fig. 5. Dependence of the amplitudes of the induced transverse electric field components E_r (dashed curve) and E_i (dotted curve) and the amplitude $E_{\max} = \sqrt{E_r^2 + E_i^2}$ (solid curve) on ξ at boundary *II* for $k_p d = k_p d_{\max} = 0.432$. The remaining parameter values are the same as in Fig. 3.

The second of the inequalities (49) implies that the wake wave amplitude will increase up to the plasma boundary. At $k_pL = a/\Delta\chi$, conditions (49) yield the following estimate for the maximum relative width of region *II*:

$$S = \frac{\gamma - \gamma_0}{\gamma_0} \simeq \frac{0.7a^2}{\gamma_0 (k_p L)^2} \frac{1}{\sqrt{\gamma_0 \beta_e}}. \quad (50)$$

Note that expression (50) is valid in the range $\gamma_0\beta_e > 1$. For the above parameter values and for $k_pL \sim 10$–10^3 ($L \sim 1$–10^2 cm), the relative width of region *II* is estimated as $S < 0.1\%$.

4. CONCLUSION

We have investigated the excitation of linear wake waves by a one-dimensional electron bunch propagating in a plasma in the presence of an intense electromagnetic pump wave with circular polarization. We have obtained and analyzed expressions describing the induced electromagnetic fields. It has been shown that there exist three ranges of the parameter values of the plasma, bunch, and pump wave in which the equations derived have qualitatively different solutions. In the most interesting case of resonant excitation (the parameter values correspond to curves *a*' and *d*' of boundary *II*), the amplitude of the transverse waves increases with increasing electron bunch energy and pump wave intensity. The amplitude of the longitudinal electric field depends weakly on the relativistic factor γ of the bunch electrons and increases with the pump wave intensity. The excitation of wake waves is most efficient in the case of narrow bunches such that $d \approx d_{\max} \approx \lambda_p/\pi\sqrt{2}$. For a sufficiently intense pump wave, the wavelength λ_p increases significantly as the bunch energy decreases.

In conclusion, note that, although much attention has been devoted to one-dimensional wake fields (see, e.g., [1–18] and the literature cited therein), a more realistic three-dimensional case is of greater importance from the standpoint of practical applications. It can be expected that the characteristic features of the wake fields that have been revealed in this paper will also persist in the three-dimensional case, in which, however, new features may arise, stemming from the dependence on the radial coordinate.

ACKNOWLEDGMENTS

I am grateful to my reviewer for a detailed critical analysis of the results obtained and for useful remarks.

REFERENCES

1. E. Esarey, P. Sprangle, J. Krall, and A. Ting, IEEE Trans. Plasma Sci. **24**, 252 (1996).
2. Ya. B. Faĭnberg, Fiz. Plazmy **23**, 275 (1997) [Plasma Phys. Rep. **23**, 251 (1997)].
3. P. Chen, Part. Accel. **20**, 171 (1987).
4. A. Ts. Amatuni, S. S. Elbakian, A. G. Khachatryan, and E. V. Sekhpossian, Part. Accel. **51**, 1 (1995).
5. P. Chen, J. M. Dawson, R. W. Huff, and T. Katsouleas, Phys. Rev. Lett. **54**, 693 (1985).
6. R. D. Ruth, A. W. Chao, P. L. Morton, and P. B. Wilson, Part. Accel. **17**, 171 (1985).
7. R. Keinigs and M. E. Jones, Phys. Fluids **30**, 252 (1987).
8. A. Ts. Amatuni, É. V. Sekhposyan, A. G. Khachatryan, and S. S. Elbakyan, Fiz. Plazmy **21**, 1000 (1995) [Plasma Phys. Rep. **21**, 945 (1995)].
9. A. G. Khachatryan, A. Ts. Amatuni, É. V. Sekhposyan, and S. S. Elbakyan, Fiz. Plazmy **22**, 638 (1996) [Plasma Phys. Rep. **22**, 576 (1996)].
10. Ya. B. Fainberg, N. Ayzatskij, V. Balakirev, *et al.*, in *Proceedings of the 15th International Workshop on Charged Particle Linear Accelerators, Alushta, 1997*, p. 16.
11. H. B. Nersisyan and S. S. Elbakian, Part. Accel. **63**, 279 (2000).
12. A. Ts. Amatuni, E. V. Sekhposyan, and S. S. Elbakyan, Fiz. Plazmy **12**, 1145 (1986) [Sov. J. Plasma Phys. **12**, 662 (1986)].
13. J. B. Rosenzweig, Phys. Rev. Lett. **58**, 555 (1987).
14. J. B. Rosenzweig, IEEE Trans. Plasma Sci. **15**, 186 (1987).
15. J. B. Rosenzweig, Phys. Rev. A **38**, 3634 (1988).
16. A. G. Khachatryan, Phys. Plasmas **4**, 4136 (1997).
17. J. M. Dawson, Phys. Rev. **133**, 383 (1959).
18. A. I. Akhiezer and R. V. Polovin, Zh. Éksp. Teor. Fiz. **30**, 915 (1956) [Sov. Phys. JETP **3**, 696 (1956)].
19. H. B. Nersisyan and S. S. Elbakian, Fiz. Plazmy **26**, 885 (2000) [Plasma Phys. Rep. **26**, 831 (2000)].
20. M. V. Kalmykov and N. Ya. Kotsarenko, Izv. Vyssh. Uchebn. Zaved., Radiofiz. **19**, 1481 (1976).
21. L. Stenflo, Plasma Phys. **19**, 1187 (1977).
22. C. Max and F. Perkins, Phys. Rev. Lett. **29**, 1731 (1972).
23. C. S. Liu and V. K. Tripathi, *Interaction of Electromagnetic Waves with Electron Beams and Plasmas* (World Scientific, Singapore, 1962).
24. M. E. Jones and R. Keinigs, IEEE Trans. Plasma Sci. **15**, 203 (1987).
25. H. S. Kim, S. Yi, A. Amin, and K. E. Lonngren, Phys. Rev. E **50**, 3962 (1994).

Translated by O. E. Khadin

Plasma Physics Reports, Vol. 27, No. 10, 2001, pp. 860–867. From Fizika Plazmy, Vol. 27, No. 10, 2001, pp. 912–920.

PLASMA OSCILLATIONS AND WAVES

Nonlinear Properties of Two-Dimensional Wake Waves Excited by Relativistic Electron Bunches in Plasma[1]

A. G. Khachatryan and S. S. Elbakian

Yerevan Physics Institute, Alikhanian Brothers str. 2, Yerevan 375036, Armenia

e-mail: khachatr@moon.yerphi.am

Received December 28, 2000; in final form, March 1, 2001

Abstract—The properties of a nonlinear plasma wake wave excited by an axially symmetric relativistic electron bunch are studied. It is shown that the nonlinear dependence of the wake wavelength on the transverse coordinate leads to distortion of the phase front of the wake wave and to steepening and oscillations of the transverse profile of the wakefield. The magnetic field of the wake wave is nonzero and oscillates at a frequency higher than the plasma electron frequency. Because of nonlinearity, the amplitude of the excited wake wave changes with distance from the bunch. The increase in nonlinearity leads to the development of turbulence and chaotization of the wakefield and results in the switching-on of the thermal effects and plasma heating. *© 2001 MAIK "Nauka/Interperiodica".*

1. INTRODUCTION

The problem of the excitation of strong electric fields (up to tens of GV/m) in plasma by means of charge separation continues to attract attention in connection with the opportunity of accelerating and focusing charged bunches in these fields. For the acceleration of charged particles up to ultrarelativistic energies, it is natural to use plasma waves propagating at nearly the speed of light. One could excite these waves by laser radiation or relativistic charged bunches. The amplitude of waves excited in a cold plasma is limited by the relativistic wave-breaking field $E_{\mathrm{rel}} = [2(\gamma - 1)]^{1/2}E_{\mathrm{WB}}/\beta$ [1], where $\gamma = (1 - \beta^2)^{-1/2}$ is the relativistic factor, $\beta = v_{ph}/c$ is the dimensionless phase velocity of the wave, $E_{\mathrm{WB}} = m_e\omega_{pe}v_{ph}/e$ (E_{WB} [V/cm] $\approx n_0^{1/2}$ [cm^{-3}]) is the conventional nonrelativistic wave-breaking field, $\omega_{pe} = (4\pi n_0 e^2/m_e)^{1/2}$ is the electron plasma frequency, n_0 is the equilibrium density of plasma electrons, and m_e and e are the mass and absolute value of the electron charge. At present, plasma-based accelerator concepts are actively being developed both theoretically and experimentally (see review [2] and references therein).

The scheme in which charged particles are accelerated in the wake field of a relativistic bunch or a series of bunches is called the plasma wakefield accelerator (PWFA). When the electron density in the bunch n_b is much less than the equilibrium density of plasma electrons n_0, the excited wakefield is described by linear equations that admit analytical solutions [3–5]. The amplitude of linear fields is proportional to $(n_b/n_0)E_{\mathrm{WB}}$, where $n_b/n_0 \ll 1$. The longitudinal accelerating field in the wake is maximum in the one-dimensional regime, when the radius of the bunch is much larger than the plasma wavelength ($k_p r_b \gg 1$, where r_b is the radius of the bunch and $k_p = \omega_{pe}/v_{ph}$ is the wavenumber of the plasma wave) and decreases with decreasing bunch radius. For narrow bunches ($k_p r_b \ll 1$), the amplitude of the accelerating field is reduced by a small factor $(k_p r_b)^2$. The transverse components of the field are negligibly small in the case of wide bunches ($k_p r_b \gg 1$) and are appreciable for bunches with $k_p r_b < 1$.

To obtain high gradients of the focusing field, one should use narrow bunches. To compensate for the charge of a bunch, the density of plasma electrons varies by an amount of $\delta n_e \sim n_b$. On the other hand, since the velocity of plasma electrons in the linear regime is much less than the speed of light ($v_e \ll c$), the current $j_e = -e\delta n_e v_e \sim en_b v_e$ induced in the plasma fails to compensate for the current of the relativistic bunch $j_b \approx -en_b c$. Thus, the electric current and, hence, the magnetic field of the bunch are not compensated and, because of the rough compensation of charges, self-focusing of the bunch may take place (like the attraction of parallel current-carrying conductors). In the linear case, the magnetic field in the wake is absent due to the smallness of v_e and the excited wave is potential.

It is worth noting that, besides the periodical component, the field excited inside the bunch also has an aperiodic component [5, 6] due to the Coulomb field of the bunch. The aperiodic components of the accelerating and focusing forces, as well as the components of the plasma electron momentum, decrease with γ; for $\gamma \gg 1$, they are negligible (except for the head of the bunch, where the Coulomb and periodic fields are comparable to each other [5, 6]). However, the aforesaid is not true for the radial electric field and the magnetic

[1] This article was submitted by the authors in English.

1063-780X/01/2710-0860$21.00 © 2001 MAIK "Nauka/Interperiodica"

field, and one should keep this in mind when choosing the boundary conditions for numerical simulations.

If the density of the bunch is comparable to or is higher than the equilibrium plasma density, then, in general, one should take into account nonlinear effects. The one-dimensional nonlinear wake waves excited by wide relativistic bunches ($k_p r_b \gg 1$) have been studied in sufficient detail [7–10] (including the cases of a train of bunches [9] and inhomogeneous and positively charged bunches [10]). These studies show that the electron bunches with $n_b \sim n_0/2$ [7, 8] and positively charged bunches with $n_b \sim \gamma$ [10] can excite relativistically strong longitudinal waves with field amplitudes up to the relativistic wave-breaking field E_{rel}. In reality, the transverse size of the bunch is usually comparable to or less than its longitudinal size. The allowance for the finite transverse size of the bunch and, accordingly, the transverse motion of the plasma electrons highly complicates the treatment of the problem in the nonlinear regime. In the general case, an analytical study of this regime seems impossible and the use of numerical methods is usually required. The properties of nonlinear two-dimensional (cylindrically symmetric) wake fields in the PWFA scheme were investigated in a number of works [11–13]. Mid-nonlinear two-dimensional wake fields (with an amplitude of the longitudinal electric field up to $0.6E_{\text{WB}}$) excited by a Gaussian electron bunch with characteristic longitudinal and transverse dimensions equal to $1.3/k_p$ and densities of $0.2n_0$, $0.4n_0$, and $0.6n_0$ were numerically calculated in [12]. The authors showed that nonlinearity results in the radial steepening of the excited fields.

Our aim here is to examine in the general case the influence of nonlinearity on two-dimensional wake-fields excited by relativistic bunches and to discuss the cause of the radial steepening of the field [12]. The bunches are assumed to be rigid; i.e., γ is assumed to be large enough. As was shown earlier, the typical time scales of the transverse and longitudinal dynamics of the bunch electrons are $\gamma^{1/2}/\omega_p$ and γ/ω_p, respectively [14]. Thus, if the time intervals are less than $\gamma^{1/2}/\omega_p$ (or the bunch traverses a distance less than $\gamma^{1/2}/k_p$ in the plasma), then one can assume the bunch to be rigid. For example, in a comparatively recent proposal on the PWFA experiment [15], it was suggested to use an electron bunch with an energy of 30 GeV, i.e., $\gamma \approx 6 \times 10^4$, which is fairly large.

This paper is organized as follows. In Section 2, we present the basic equations. In Section 3, the excitation of nonlinear two-dimensional waves by a wide bunch is considered. The results of numerically calculating the basic equations and their discussion are given in Section 4. In the Conclusion, the main results are summarized. The details of the numerical code used are described in the Appendix.

2. BASIC EQUATIONS

We will consider nonlinear steady-state fields excited in a homogeneous plasma by a rigid electron bunch. We suppose that $T_e/m_e c^2 \ll 1$ and $m_i \gg m_e$, where T_e is the plasma electron temperature and m_i is the plasma ion mass. Under these conditions (which are typical of laboratory experiments), the plasma can be considered cold and the ions can be assumed to be immobile [16]. Let the bunch travel along the z direction with the velocity v_0, which is close to the speed of light, and the charge distribution in the bunch not depend on the azimuthal angle θ. Then, in the laboratory frame, the density of the bunch electrons is $n_b = n_b(r, Z - v_0 t)$ and the current density is $\mathbf{j}_b = -\mathbf{e}_z e n_b v_0$. The excited steady-state fields are also independent of the azimuthal angle. Below, for convenience, we will use dimensionless variables. The space variables are normalized to $\lambda_p/2\pi = 1/k_p$ (i.e., to the linear plasma wavelength λ_p, which corresponds the variation of the dimensionless coordinate by 2π); the momenta and velocities are normalized to $m_e c$ and the speed of light, respectively; the density is normalized to the equilibrium density of plasma electrons n_0; and the electric and magnetic fields are normalized to the nonrelativistic wave-breaking field E_{WB}.

The basic nonlinear equations of motion and Maxwell's equations describing the plasma–relativistic bunch system are given in a series of works (see, e.g., [14]). For nonzero components of the plasma electron momentum and electromagnetic field, we have the following set of equations:

$$\beta \frac{\partial P_z}{\partial z} - \frac{\partial \gamma_e}{\partial z} - \beta^2 E_z = 0, \tag{1}$$

$$\beta \frac{\partial P_r}{\partial z} - \frac{\partial \gamma_e}{\partial r} - \beta^2 E_r = 0, \tag{2}$$

$$-\frac{\partial H_\theta}{\partial z} + \beta \frac{\partial E_r}{\partial z} + \beta_r N_e = 0, \tag{3}$$

$$\nabla_\perp H_\theta + \beta \frac{\partial E_z}{\partial z} + \beta_z N_e + \beta\alpha = 0, \tag{4}$$

$$\beta \frac{\partial H_\theta}{\partial z} - \frac{\partial E_r}{\partial z} + \frac{\partial E_z}{\partial r} = 0, \tag{5}$$

$$N_e = 1 - \alpha - \nabla_\perp E_r - \frac{\partial E_z}{\partial z}. \tag{6}$$

As usual, Eqs. (1) and (2) were derived taking into account that the curl of the generalized momentum is zero, $\beta^2 \mathbf{H} - \nabla \times \mathbf{P} = 0$, or, in our case,

$$\beta^2 H_\theta + \frac{\partial P_z}{\partial r} - \frac{\partial P_r}{\partial z} = 0. \tag{7}$$

In Eqs. (1)–(6), $\gamma_e = (1 + P_z^2 + P_r^2)^{1/2}$, $\beta_{z,r} = P_{z,r}/\gamma_e$, and $N_e = n_e/n_0$ are the relativistic factor, dimensionless velocity components, and dimensionless plasma electron density, respectively; $\beta = v_0/c$, $z = k_p(z - v_0 t)$, $\alpha = n_b(z, r)/n_0$, $\nabla_\perp = \partial/\partial r + 1/r$. Note that, according to Eq. (5), the field of forces acting on the bunch electrons $\mathbf{F}(-eE_z, -e(E_r - \beta H_\theta), 0)$ is a potential field because $\nabla \times \mathbf{F} = 0$. This assertion, which is the subject of the Panofsky–Wenzel theorem, is valid for arbitrary β both in linear and nonlinear cases. In the ultrarelativistic case ($\gamma \gg 1$, $\beta \approx 1$), for the transverse momentum $P_r = \beta_r \gamma_e$ from Eqs. (3) and (5), we have

$$P_r \approx -(\gamma_e/N_e)\partial E_z/\partial r. \tag{8}$$

Since $\gamma_e/N_e > 0$, the sign of the transverse momentum is opposite to that of the derivative $\partial E_z/\partial r$. We will use this inference in Section 4 when discussing the behavior of nonlinear fields in the wake.

3. CASE OF A WIDE BUNCH ($k_p r_b \gg 1$)

Let us consider a wide bunch. In this case, the transverse components of the excited field are small and the longitudinal components near the axis are approximately equal to those predicted by one-dimensional nonlinear theory. Here, we can apply the perturbation method, taking the one-dimensional nonlinear mode as a ground state. Therefore, for wide bunches we will seek the solution to Eqs. (1)–(6) in the vicinity of the bunch axis in the form

$$\begin{aligned} P_z &= P_0(z) + P_{z1}(z, r), \\ E_z &= E_0(z) + E_{z1}(z, r), \end{aligned} \tag{9.1}$$

$$\alpha = n_b/n_0 = \alpha_0(z) - \alpha_1(z, r), \tag{9.2}$$

$$P_{z1} \ll P_0, \quad E_{z1} \ll E_0, \quad \alpha_1 \ll \alpha_0, \tag{9.3}$$

where P_0 and E_0 are the longitudinal momentum and the electric field at the axis ($r = 0$). Furthermore, we will suppose that $P_{z1}, E_{z1}, P_r, E_r, H_\theta, \alpha_1 \ll 1$. Then, for P_0 and E_0, from Eqs. (1)–(6) we have

$$\frac{d}{dz}[\beta P_0 - (1 + P_0^2)^{1/2}] - \beta^2 E_0 = 0, \tag{10.1}$$

$$(\beta - \beta_0)\frac{dE_0}{dz} + (1 - \alpha_0)\beta_0 = 0, \tag{10.2}$$

where $\beta_0(z) = P_0/(1 + P_0^2)^{1/2}$ is the dimensionless longitudinal velocity of the plasma electrons. Equations (10.1) and (10.2) describe the one-dimensional nonlinear regime that has been studied fairly well (see, e.g., [7–10]).

In the first approximation in small values, from Eqs. (1)–(6) we obtain

$$(\beta - \beta_0)\frac{\partial P_{z1}}{\partial z} - \frac{d\beta_0}{dz}P_{z1} - \beta^2 E_{z1} = 0, \tag{11.1}$$

$$\beta\frac{\partial P_r}{\partial z} - \beta_0\frac{\partial P_{z1}}{\partial r} - \beta^2 E_r = 0, \tag{11.2}$$

$$-\frac{\partial H_\theta}{\partial z} + \beta\frac{\partial E_r}{\partial z} + \frac{N_0}{\gamma_0}P_r = 0, \tag{11.3}$$

$$\begin{aligned} &\nabla_\perp(H_\theta - \beta_0 E_r) + (\beta - \beta_0)\frac{\partial E_{z1}}{\partial z} \\ &\quad + \frac{N_0}{\gamma_0^3}P_{z1} - (\beta - \beta_0)\alpha_1 = 0, \end{aligned} \tag{11.4}$$

$$\beta\frac{\partial H_\theta}{\partial z} - \frac{\partial E_r}{\partial z} + \frac{\partial E_{z1}}{\partial r} = 0. \tag{11.5}$$

In Eqs. (11.1)–(11.5), $N_0 = 1 - \alpha_0 - dE_0/dz = \beta/(\beta - \beta_0)$ and $\gamma_0 = P_0/\beta_0 = (1 + P_0^2)^{1/2}$ are the dimensionless density and relativistic factor of the plasma electrons in the one-dimensional case. Since the longitudinal components of the field have extrema on the axis of the system, while the transverse components are zero, it is evident that, in the vicinity of the axis, we can write

$$P_{z1} \approx \rho_z(z)r^2, \quad E_{z1} \approx l_z(z)r^2, \quad \alpha_1 \approx \delta(z)r^2, \tag{12.1}$$

$$P_r \approx \rho_r(z)r, \quad E_r \approx l_r(z)r, \quad H_\theta \approx h_\theta(z)r. \tag{12.2}$$

The quantities $\rho_{z,r}$, $l_{z,r}$, δ, and h_θ are actually the coefficients of the Taylor expansions over the radius. Substituting expressions (12.1) and (12.2) into (11.1)–(11.5) and performing some algebraic manipulations, we obtain the equation for ρ_z:

$$\begin{aligned} &\frac{d^2\rho_z}{dz^2} - \left(\frac{2N_0}{\beta}\frac{d\beta_0}{dz}\right)\frac{d\rho_z}{dz} + \frac{AN_0}{\beta}\rho_z = \beta N_0 \delta, \\ &A = \frac{\beta N_0^2}{\gamma_0^3} - \frac{d^2\beta_0}{dz^2} \\ &= \frac{\beta N_0(1 - \alpha_0)}{\gamma_0^3} - \left(\frac{N_0}{\beta} - 3\beta_0\gamma_0^2\right)\left(\frac{d\beta_0}{dz}\right)^2. \end{aligned} \tag{13}$$

With known ρ_z, we can calculate the remaining quantities using the following equations:

$$\frac{1}{\gamma^2}\frac{d^2\rho_r}{dz^2} - \frac{\beta^2 N_0}{\gamma_0}\rho_r = 2\frac{d}{dz}[(1 - \beta\beta_0)\rho_z], \tag{14.1}$$

$$l_z = \frac{1}{\beta}\frac{d}{dz}\left(\frac{\rho_z}{N_0}\right), \quad l_r = \frac{1}{\beta}\frac{d\rho_r}{dz} - \frac{2\beta_0}{\beta^2}\rho_z, \tag{14.2}$$

$$h_\theta = \frac{1}{\beta^2}\left(\frac{d\rho_r}{dz} - 2\rho_z\right). \quad (14.3)$$

For the gradient of the focusing field, from Eqs. (11.1), (11.5) and (12) we have

$$\frac{f_r}{r} \equiv \frac{\beta H_\theta - E_r}{r} = -\frac{2\rho_z}{\beta N_0}. \quad (15)$$

Expression (13) is the equation of a nonlinear oscillator with friction and a driving force proportional to δ. In the linear case ($\beta_0 \ll 1$, $d\beta_0/dz \sim E_0 \ll 1$), we have harmonic oscillations with the plasma frequency, as is predicted by the linear theory. As the amplitude increases, the oscillations become more complicated and, in the general case, it seems hardly possible to find an analytical solution to Eq. (13). However, we can see that, in the nonlinear regime, both the period and the amplitude of oscillations change. This is also confirmed by numerically solving Eq. (13). In Fig. 1, we show the results of the numerical solution of Eqs. (10.1), (10.2), (13), and (15) for the longitudinal electric field E_0, density N_0, and focusing gradient f_r/r [see expression (15)], which are excited by a wide bunch with the length $\sigma_z = \Lambda_b/2 \approx 4.7$ and density $\alpha_0 = n_b(r = 0)/n_0 = 0.2$, where Λ_b is the nonlinear plasma wavelength inside the bunch (see [10]). The main qualitative differences of the 1D nonlinear regime from the linear one are the wave steepening and the increase in the wavelength (see [7–10] for details). For example, in our case, the nonlinear wavelength in the wake is $\Lambda_p \approx 6.65$, while in the linear regime, $\Lambda_p \equiv \lambda_p = 2\pi \approx 6.28$. It is seen from Fig. 1 that, although the amplitude of the excited transverse components is small, their wavelength is close to that of the one-dimensional nonlinear wave. Furthermore, the amplitude of the focusing gradient periodically changes with z. The numerical analysis shows that the modulation depth of the focusing gradient increases and the modulation period decreases as the amplitude of nonlinear longitudinal oscillations increases. This also takes place for other field components. In Fig. 1, the positions of the maximums (minimums) of the focusing gradient do not coincide exactly with those of the plasma electron density and the longitudinal electric field. The reason for the latter effect (as well as for the amplitude modulation) is that the maximums of the focusing force f_r at different r do not coincide, which, in turn, is related to the nonlinear change in the wavelength in the radial direction (see Section 4). It can be seen in Fig. 2 that the amplitude modulation and the change in the wavelength due to nonlinearity also occur inside a long bunch. The second term and the factor by the third term on the left-hand side of Eq. (13) are "responsible" for the change in the amplitude and wavelength, respectively.

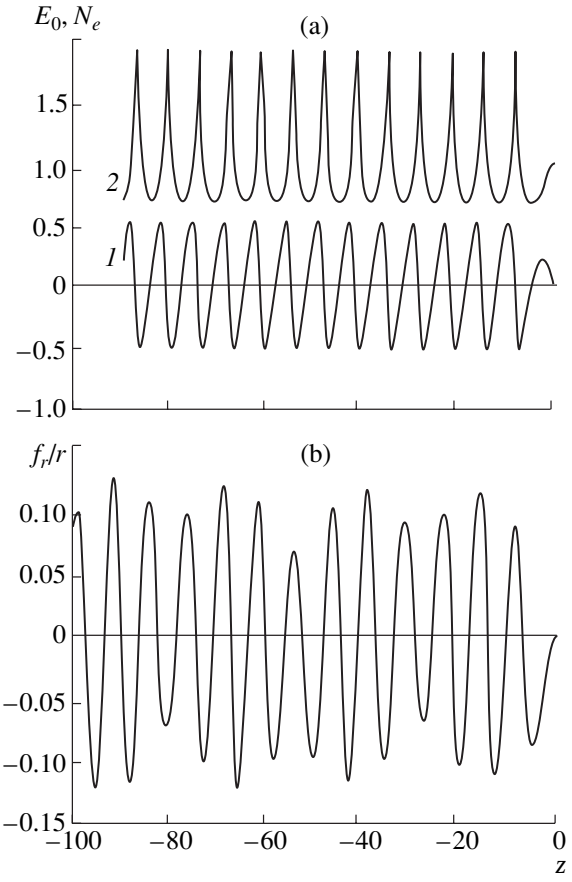

Fig. 1. Nonlinear wake wave excited by a wide bunch for the bunch length $\sigma_z = 4.7$, $\alpha_0 = n_{b0}/n_0 = 0.2$, $\delta = 0.2\alpha_0$, and $\gamma = 10$: (a) the longitudinal profiles of (*1*) the dimensionless longitudinal electric field $E_0(z)$ and (*2*) normalized plasma electron density at the bunch axis and (b) the longitudinal profile of the gradient of the dimensionless focusing field.

4. NUMERICAL RESULTS

In this section, we will discuss the results of the numerical solution of Eqs. (1)–(6), leaving the details of the numerical code to the Appendix. The density of the bunch was taken to have a Gaussian profile both in the longitudinal and transverse directions:

$$\alpha(z, r) = n_b(z, r)/n_0 = \alpha_0 \exp[-(z - z_0)^2/\sigma_z^2]\exp(-r^2/\sigma_r^2), \quad (16)$$

where $\alpha_0 = \alpha(z_0, 0)$ is the maximum value of the bunch density. The parameters of the problem were taken to be $\gamma = 10$ ($\beta \approx 0.995$), $\sigma_z = 2$, and $z_0 = 3\sigma_z$; α_0 was varied in the range 0.05–1; σ_r ranged from 0.1 to 10; and the counting was started from the point $z = 0$. For small amplitudes of the excited wake wave (at $\alpha_0 \ll 1$), the numerical solution agrees well (see Fig. 3) with the predictions of the linear theory [3–6]. It is seen in Fig. 3b that, in the linear case, the magnetic field excited in the plasma is localized in the region occupied by the bunch, while in the wake, we have $H_\theta \approx 0$; i.e., the wake is a

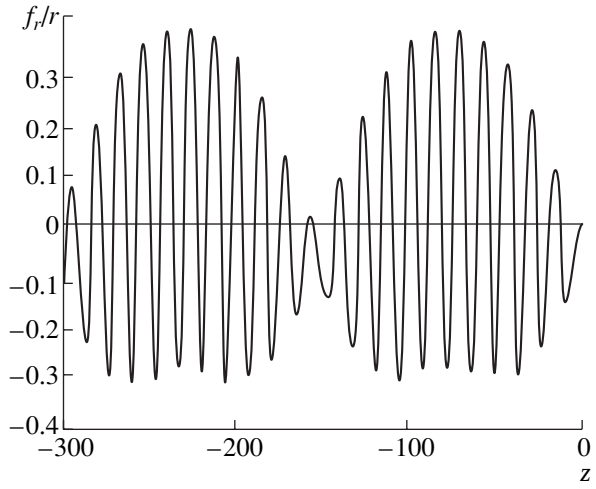

Fig. 2. Gradient of the dimensionless focusing field f_r/r inside a wide bunch for $\alpha_0 = 0.3$, $\delta = 0.05\alpha_0$, and $\gamma = 10$.

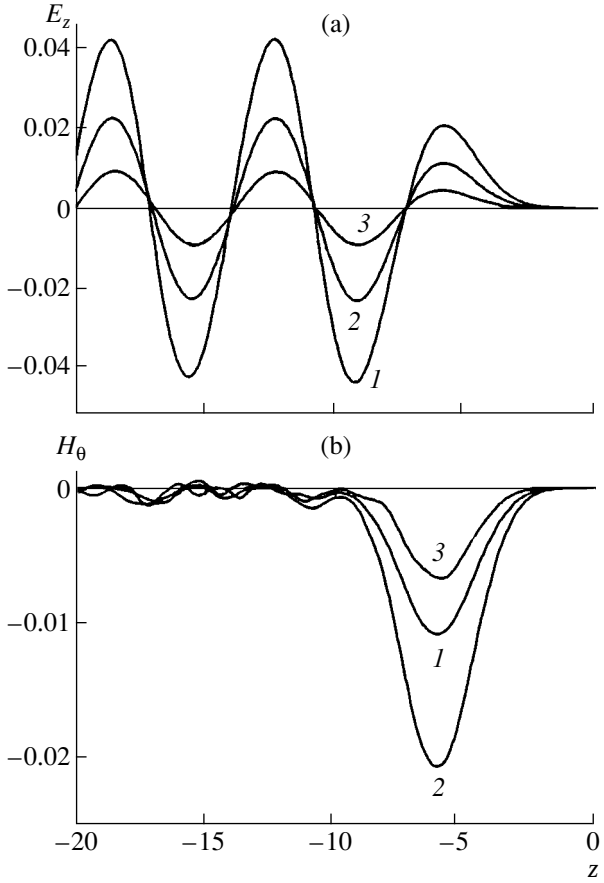

Fig. 3. Linear wakefield excited by an electron bunch with a Gaussian profile for $\alpha_0 = 0.1$, $\sigma_z = 2$, $\sigma_r = 0.5$, and $\gamma = 10$: (a) the dimensionless longitudinal electric field $E_z(z)$ at $r =$ (*1*) 0 (at the axis), (*2*) 1, and (*3*) 2; (b) the dimensionless azimuthal magnetic field at $r =$ (*1*) 0.2, (*2*) 0.75, and (*3*) 2.

potential wave. We also note that the wave is sinusoidal; the wavelength does not change with r (see Fig. 3); and, hence, the equiphase surfaces are planes $z = \text{const}$.

Figure 4 shows the amplitude of the longitudinal (accelerating) electric field in the wake at the axis ($r = 0$) as a function of the transverse bunch size σ_r for different densities α_0 of the bunch. In the linear regime (see the curve corresponding to the value $\alpha_0 = 0.1$), the amplitude increases only slightly for transverse bunch sizes higher than the linear plasma wavelength (we recall that the linear plasma wavelength corresponds to the change in the spatial coordinates by 2π) and approaches the value of the amplitude in the one-dimensional approximation. As the bunch density increases, the amplitude "saturates" at somewhat greater transverse bunch sizes, which is obviously due to nonlinearity.

In the nonlinear regime, the behavior of two-dimensional waves excited by the bunch changes qualitatively. In Fig. 5, we can see a nonlinear plasma wave that is excited by a bunch with $\sigma_z = 2$, $\sigma_r = 5$, and $\alpha_0 = 0.4$. The main difference from the linear case is the change in the shape and length of the wave with radius r, as well as the change in the amplitude in the longitudinal direction. For each fixed value of r, the profiles and wavelengths of the longitudinal components E_z and P_z are nearly the same as those in the one-dimensional wave of the same amplitude. For example, at the periphery of the bunch (at $r \gtrsim \sigma_r$), where the amplitude of the wave is small, the wave is almost sinusoidal and its wavelength is equal to the linear plasma wavelength. Moreover, the numerical analysis confirms the conclusion made in the previous section: although the amplitudes of the transverse components of the nonlinear wake wave close to the axis are small, their period in the longitudinal direction is nearly equal to the nonlinear wavelength corresponding to the longitudinal components for the same r (see Fig. 5c).

For a wide bunch ($\sigma_r \gg 1$), the motion of the plasma electrons behind the bunch at $r \lesssim \sigma_r$ is mainly longitudinal and the field near the axis conforms well to the one-dimensional case. When $\sigma_r < 1$, the amplitudes of transverse components of the field become comparable to or larger than those of the longitudinal components. For $\sigma_r < 1$ and $\alpha_0 \sim 1$, the excited electromagnetic field is linear or weakly nonlinear. For example, for $\sigma_r = 0.2$ and $\alpha_0 = 0.7$, the amplitudes of the wakefield components are about 0.1–0.15. However, the field becomes anharmonic; this is related mainly to the transverse components E_r, P_r, and f_r. In addition, the change in the plasma electron density becomes strongly nonlinear, $\delta N_e \sim \alpha_0$. Almost all of the plasma electrons leave the region $r \lesssim \sigma_r$, and radial oscillations (at fixed z) of the transverse electron velocity arise. The latter precedes the transverse multistream motion of the plasma electrons and the transverse wave breaking [17]. However, the wave breaking cannot be correctly described in the

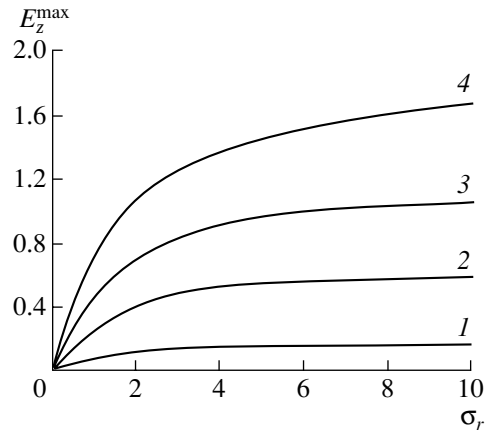

Fig. 4. Amplitude of the longitudinal electric field at the bunch axis vs. the transverse size of the bunch for $\sigma_z = 2$ and $\gamma = 10$ at $\alpha_0 = (1)$ 0.1, (2) 0.3, (3) 0.5, and (4) 0.7.

cold hydrodynamic approach (see below). As $|z|$ increases, the radial density perturbations become large ($\delta N_e \gg 1$), the radial density gradient increases, and the wakefield becomes more and more irregular. A study of the "blowout" regime ($\alpha_0 > 1$, $\sigma_r \lesssim 1$) reveals the development of the strongly turbulent motion of plasma electrons immediately behind the bunch, as was also noted in [11].

As is seen in Fig. 6, the magnetic field in the nonlinear wake wave is nonzero and oscillates at a frequency higher than the plasma frequency, which agrees with the predictions of the weakly nonlinear theory [18]. The magnitude of the higher frequency oscillations of the magnetic field along the z-axis increases in proportion to the nonlinearity. Such behavior of the magnetic field is a purely nonlinear effect. Indeed, in the linear case, we have $H_\theta \approx 0$ in the wake wave; i.e., the contribution of the momentum components oscillating at the plasma frequency in Eq. (7) is compensated. The nonlinearity of the wave implies the rise of higher harmonics in P_z and P_r. According to Eq. (7), the magnetic field arises due to these harmonics; this explains the appearance of higher frequency oscillations in Fig. 6. On the other hand, according to Eq. (7), the presence of a nonzero magnetic field in the wake means that the motion of the plasma electrons in the nonlinear wave is turbulent ($\nabla \times \mathbf{P} \neq 0$). The degree of turbulence (the measure of which is H_θ) increases in proportion to the nonlinearity. The qualitative behavior of the magnetic field in the radial direction is the same as that of the other transverse components of the field [18].

It is easily seen that, due to the dependence of the wavelength on r, the radial profile of the field becomes more chaotic as distance from the bunch increases. In fact, the plasma oscillations at different r start behind the bunch with nearly the same phases but different wavelengths. As $|z|$ increases, the phase shift in the transverse direction (for a fixed z) becomes more and more pronounced. This leads to the curving of the phase front and to the appearance of "oscillations" in the transverse direction. In addition, the dependence of the wavelength on r leads to a decrease in the acceler-

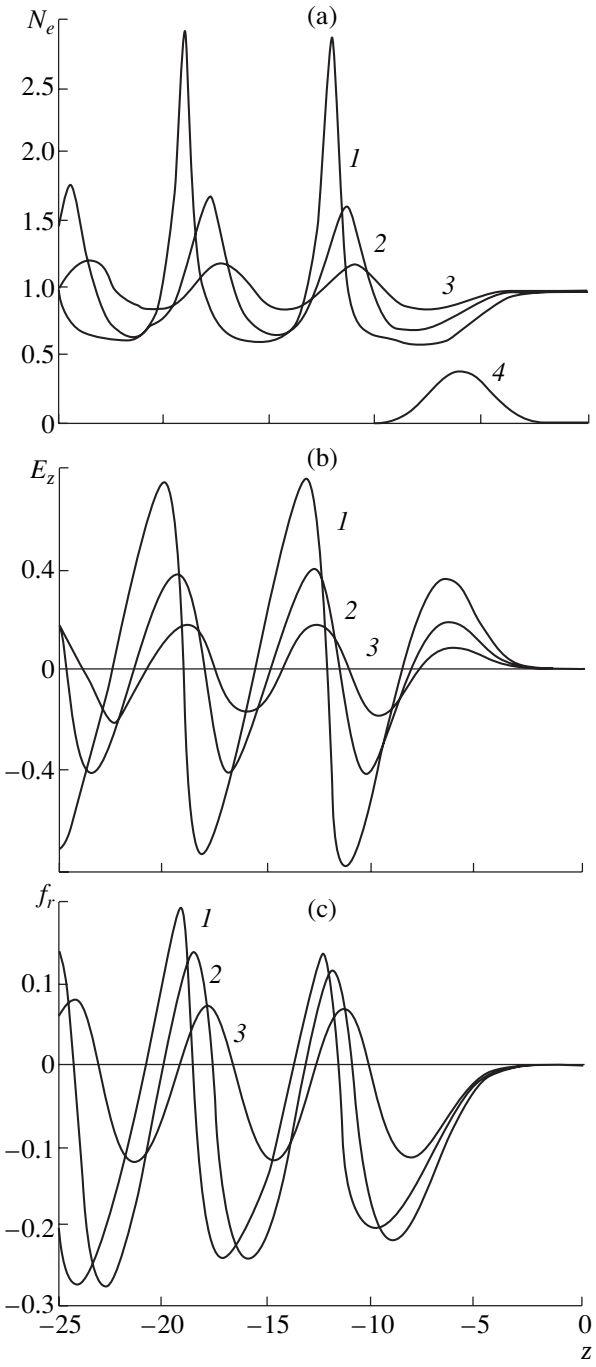

Fig. 5. Two-dimensional nonlinear wake wave for the bunch parameters $\alpha_0 = 0.4$, $\sigma_z = 2$, $\sigma_r = 5$, and $\gamma = 10$: the longitudinal profiles of (a) the density of plasma electrons N_e at $r = (1)$ 0 (at the axis), (2) 4, and (3) 6 and (4) the density of the bunch at the axis $\alpha(z, r = 0)$; (b) the longitudinal electric field at $r = (1)$ 0, (2) 4, and (3) 6; and (c) the focusing field $f_r = \beta H_\theta - E_r$ at $r = (1)$ 2, (2) 4, and (3) 6.

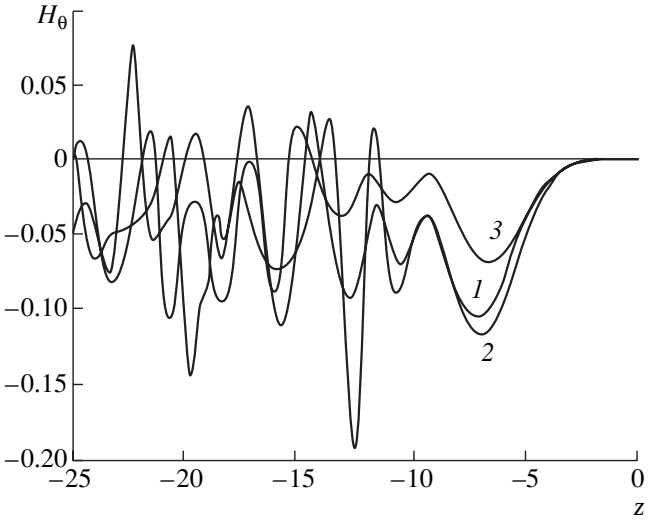

Fig. 6. The normalized magnetic field in the nonlinear wake wave for the parameters of Fig. 5 at r = (*1*) 2, (*2*) 4, and (*3*) 6.

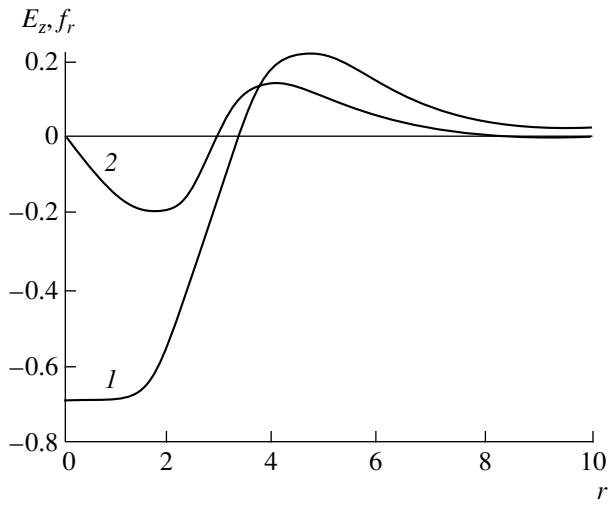

Fig. 7. Radial profiles of the electric field for the parameters of Fig. 5 for $z = -25$: (*1*) the longitudinal electric field $E_z(z = -25, r)$ and (*2*) the focusing field $f_r(z = -25, r)$.

ating field amplitude in the wake because the contributions to the field from the parts of the bunch with different r have different phases. On the other hand, the amplitudes of the transverse components (E_r, P_r, and f_r) increase with $|z|$ (see Fig. 5). These effects also take place in the wake wave excited by a short laser pulse in a plasma channel in which the equilibrium plasma density increases (and the plasma wavelength decreases) with r (see, e.g., review [2] and the results of experiments on laser wakefield excitation [19]). From the standpoint of the acceleration and focusing of charged bunches in the wake wave, the curvature of the nonlinear wave front is undesirable because the quality (the emittance and monochromaticity) of the driven bunch worsens. The possibility of the formation of a curved phase front due to nonlinearity was discussed qualitatively in [20]. One can define the spatial longitudinal parameter characterizing the transverse phase chaotization in the following manner. Let Λ_0 be the nonlinear wavelength at the axis. At the periphery of the bunch ($r \gtrsim \sigma_r$), where the field is weak (linear), the wavelength is close to the linear plasma wavelength λ_p. We can see that, if for some z_1 the oscillation phases at the axis and at the periphery were the same, then, for $|z| \approx |z_1| + \lambda_p\Lambda_0/2(\Lambda_0 - \lambda_p)$, the phases will be opposite. We introduce the value

$$\xi = \frac{\lambda_p}{2(1 - \lambda_p/\Lambda_0)} \tag{17}$$

as a characteristic longitudinal scale on which the nonlinear wave front becomes curved. As an example, we show in Fig. 7 the behavior of the longitudinal electric and focusing fields for $|z| \approx |z_1| + \xi$. Qualitatively, the radial dependence of the field differs from that in the linear case by the change in the field sign and the steepening of the field profile along r due to the curved wave phase front. The behavior of other variables is analogous. For example, for P_r, this directly follows from expression (8) and Fig. 7. The behavior of fields shown in Fig. 7 was also numerically revealed in [12]. The increase in the focusing force amplitude shown in Fig. 5c is due to the radial steepening of the accelerating field (see Fig. 7). According to the Panofsky–Wenzel theorem, we have $\partial E_z/\partial r = \partial f_r/\partial z$. Therefore, the increase in the radial derivative $\partial E_z/\partial r$ leads to an increase in $\partial f_r/\partial z$ and, hence, an increase in the focusing force. We also note the extension of the range of the focusing force ($f_r < 0$) in the nonlinear wake wave (see Fig. 5c).

Because of the decrease in the typical transverse scales in the wakefield (this also concerns the electron density N_e), it is necessary to take into account the thermal term, which is proportional to $\nabla(N_e T_e/\gamma_e)$ [21]. Taking into consideration the finite plasma temperature is also important for the description of the wave breaking even at low temperatures [16]. Moreover, in this case, it is necessary to use the kinetic approach [16]. Therefore, the cold hydrodynamic approach used in this paper fails to correctly describe the wake near the wave breaking. Thus, the reduction of the characteristic spatial scales in the wakefield eventually results in the "switching-on" of the thermal effects and plasma heating. Such nonlinear behavior of the plasma conforms to the general scenario of the conversion of large-scale motions into heat via the reduction of the typical spatial scales.

We also note that, due to the decrease in the typical radial scales of the wakefield, they become comparable to or less than the radial step of the numerical grid at some distance $|z_*|$ from the bunch. Hence, for $|z| > |z_*|$, the numerical results become incorrect.

5. CONCLUSION

The investigation of nonlinear effects in two-dimensional wake waves has shown that, in the nonlinear regime, the dependence of the wavelength on the transverse coordinate leads to the curving of the wave phase front and to steepening and "oscillations" of the field in the radial direction. In addition, the wave in the longitudinal direction becomes anharmonic and steepens similarly to the case of a one-dimensional nonlinear wake wave. We also note that, in the nonlinear wave, the longitudinal range of the focusing force is extended. It is shown that, in contrast to the linear case, the magnetic field in the nonlinear wake wave is different from zero due to the development of turbulence.

Finally, we note that the discussed nonlinear properties of the wake waves also hold (at least qualitatively) when the wake wave is excited by a high-intensity short laser pulse [22]. It was also shown in [22] that the curvature of the wave front of a two-dimensional nonlinear wake wave can be compensated by the radial variations of the equilibrium plasma density.

ACKNOWLEDGMENTS

This work was supported by the International Science and Technology Center, project no. A-405.

APPENDIX

Numerical Solution of the Basic Equations

In the fluid code that was developed for the numerical solution of Eqs. (1)–(6), we use the following discrete forms:

$$\frac{\partial y}{\partial z} \longrightarrow \frac{y_{i+1,j} - y_{i,j}}{h_z},$$

$$\frac{\partial y}{\partial r} \longrightarrow \frac{y_{i,j+1} - y_{i,j-1}}{2h_r},$$

$$\nabla_\perp y \longrightarrow \frac{y_{i,j+1} - y_{i,j-1}}{2h_r} + \frac{y_{i,j}}{(j-1)h_r},$$

where $y_{i,j} = y(z_i, r_j)$ is the value of the function in the nodes of the grid and h_z and h_r are the steps of the grid in the longitudinal and transverse directions, respectively. The system of nonlinear algebraic equations in the discrete form was solved at each ith layer by the Newton–Seidel iteration method. The calculations started at the distance $3\sigma_z$ from the center of the bunch in the forward direction; at this distance, the plasma was assumed to be unperturbed. In the transverse direction, calculations were performed up to a certain value $r_{\max}(\sigma_r)$ that was sufficient for the calculation results to remain almost unchanged. At $r = r_{\max}$, the plasma was assumed to be unperturbed.

The numerical stability of the scheme used was provided by choosing a sufficiently small step in the longitudinal direction: h_r was in the range $(0.5–1) \times 10^{-1}$, and h_z was in the range $(0.2–0.5) \times 10^{-4}$.

REFERENCES

1. A. I. Akhiezer and R. V. Polovin, Zh. Éksp. Teor. Fiz. **30**, 915 (1956) [Sov. Phys. JETP **3**, 696 (1956)].
2. E. Esarey, P. Sprangle, J. Krall, and A. Ting, IEEE Trans. Plasma Sci. **24**, 252 (1996).
3. P. Chen, J. M. Dawson, R. W. Huff, and T. Kalsouleas, Phys. Rev. Lett. **54**, 693 (1985).
4. R. D. Ruth, A. W. Chao, P. L. Morton, and P. B. Wilson, Part. Accel. **17**, 171 (1985).
5. R. Keinigs and M. E. Jones, Phys. Fluids **30**, 252 (1987).
6. A. G. Khachatryan, A. Ts. Amatuni, S. S. Elbakyan, and E. V. Sekhpossyan, Fiz. Plazmy **22**, 638 (1996) [Plasma Phys. Rep. **22**, 576 (1996)].
7. A. Ts. Amatuni, E. V. Sekhpossyan, and S. S. Elbakyan, Fiz. Plazmy **12**, 1145 (1986) [Sov. J. Plasma Phys. **12**, 662 (1986)].
8. J. R. Rosenzweig, Phys. Rev. Lett. **58**, 555 (1987).
9. A. Ts. Amatuni, S. S. Elbakian, A. G. Khachatryan, and E. V. Sekhpossian, Contemp. Phys. **28**, 8 (1993).
10. A. G. Khachatryan, Phys. Plasmas **4**, 4136 (1997).
11. J. R. Rosenzweig, B. Breizman, T. Kalsouleas, and J. J. Su, Phys. Rev. A **44**, R6189 (1991).
12. B. Breizman, T. Tajima, D. L. Fisher, and P. Z. Chebotarev, in *Research Trends in Physics: Coherent Radiation and Particle Acceleration*, Ed. by A. Prokhorov (American Institute of Physics, New York, 1992), p. 263.
13. N. Barov and J. B. Rosenzweig, Phys. Rev. E **49**, 4407 (1994).
14. K. V. Lotov, Phys. Plasmas **5**, 785 (1998).
15. R. Assman, P. Chen, F. J. Decker, *et al.*, Nucl. Instrum. Methods Phys. Res. A **410**, 396 (1998).
16. A. G. Khachatryan, Phys. Rev. E **58**, 7799 (1998).
17. S. V. Bulanov, F. Pegoraro, and J. Sakai, Nucl. Instrum. Methods Phys. Res. A **410**, 477 (1998).
18. A. G. Khachatryan, Phys. Plasmas **7**, 5252 (2000).
19. J. R. Marques, F. Dorchies, F. Amiranoff, *et al.*, Phys. Plasmas **5**, 1162 (1998).
20. S. V. Bulanov and A. S. Sakharov, Pis'ma Zh. Éksp. Teor. Fiz. **54**, 208 (1991) [JETP Lett. **54**, 203 (1991)].
21. L. D. Landau and E. M. Lifshitz, *Fluid Mechanics* (Nauka, Moscow, 1986; Pergamon, New York, 1987).
22. A. G. Khachatryan, Phys. Rev. E **60**, 6210 (1999).

Plasma Physics Reports, Vol. 27, No. 10, 2001, pp. 868–874. Translated from Fizika Plazmy, Vol. 27, No. 10, 2001, pp. 921–927.

PLASMA OSCILLATIONS AND WAVES

Quasilinear Theory of the Inversionless Generation of Electron Cyclotron Radiation

M. A. Erukhimova and M. D. Tokman

Institute of Applied Physics, Russian Academy of Sciences, ul. Ul'yanova 46, Nizhni Novgorod, 603600 Russia

Received March 22; in final form, April 20, 2001

Abstract—A study is made of the parametric generation of cyclotron radiation by a modulated electron ensemble that is stable against the generation of a monochromatic field—the classical effect characteristic of an inversionless maser. A quasilinear theory of inversionless cyclotron instability is developed. It is shown that, during quasilinear diffusion, the system of a modulated electron beam and an electromagnetic field relaxes to a certain steady state. © *2001 MAIK "Nauka/Interperiodica".*

1. INTRODUCTION

In the course of studies in quantum optics and laser physics over the past decade, much attention has been devoted to the effect of inversionless amplification, i.e., the amplification of electromagnetic radiation in the absence of population inversions on the working atomic transition [1]. This seemingly paradoxical phenomenon has attracted much interest because it holds great promise for generating and amplifying coherent radiation in new frequency bands.

Recent attempts to use novel ideas of quantum optics in classical microwave electronics and plasma physics have stimulated increased interest in searching for classical analogues of quantum systems in which the inversionless amplification effect takes place. In particular, the possibility of amplifying coherent radiation by an inversionless ensemble of classical electrons was investigated theoretically in [2–6]. Gaponov-Grekhov and Tokman [4] were the first to propose a cyclotron resonance–based inversionless maser, which is a direct classical analogue of an inversionless laser operating on the basis of the well-known quantum Λ-scheme [1]. They showed that, in the parametric interaction between two high-frequency waves in a modulated electron ensemble under the conditions of electron cyclotron resonance at two harmonics of the cyclotron frequency, the two waves can be amplified simultaneously in spite of the fact that the electron ensemble is inversionless; i.e., it is stable against the generation of each of the waves.

Note that, in classical electronics, the study of the analogues of inversionless quantum systems in the microwave frequency range is important for the following reason. As the radiation frequency increases, the spread in the resonant frequencies of the electrons, which is caused by the spread in their momenta and is governed by the Doppler effect and/or the relativistic shift of their gyrofrequency, eventually exceeds the reciprocal of the characteristic electron transit time through the interaction region (or through a distance equal to the reciprocal of the spatial growth rate). In this case, the energy exchange between the waves and electrons inevitably evolves into the kinetic regime, which is critical to the gradient of the electron distribution function along a certain direction in momentum space—the classical analogue of the population difference in quantum systems (see [7]). With certain restrictions on the properties of electron beams produced by particular electron sources, the method of modulating the electron distribution function with resulting inversionless generation may be more promising in comparison with the excitation of the standard kinetic instability; at least, this method might be worthy of further investigation. The fundamental problems of the inversionless generation of cyclotron radiation in classical systems were considered in [4, 5, 8].

The theory of the parametric generation of cyclotron radiation was constructed in [4, 5] under certain simplifying assumptions. However, this effect requires a more detailed investigation. In particular, it is necessary to refine Gaponov-Grekhov and Tokman's quasilinear theory of cyclotron instability [4]. One of the results obtained in [4] implies that the saturation of the cyclotron instability cannot be described in quasilinear theory without allowance for the "ballistic relaxation" and nonlinear processes. However, this result is not quite correct because some nonlinear effects should be taken into account in advance, i.e., in deriving the relationships of quasilinear theory. In the present paper, we carry out a more rigorous analysis of the quasilinear relaxation in a system with inversionless generation of cyclotron radiation.

Our paper is organized as follows. In Section 2, for the benefit of readers, we briefly describe the results obtained in the linear theory of the inversionless parametric generation of cyclotron radiation. In Section 3, we construct a quasilinear theory of parametric cyclo-

1063-780X/01/2710-0868$21.00

tron instability in the model under consideration. The results obtained are summarized in the Conclusion.

2. LINEAR THEORY OF THE PARAMETRIC CYCLOTRON INSTABILITY

Following [4], we consider the parametric cyclotron interaction of two linearly polarized plane electromagnetic waves with a modulated ensemble of relativistic electrons. We assume that the waves propagate across a constant magnetic field $\mathbf{B} = \mathbf{z}_0 B$ and are described by the vector potential

$$\mathbf{A} = \mathbf{y}_0 \sum_{j=1}^{2} \mathrm{Re}\, A_j \exp(ik_j x - i\omega_j t), \quad (1)$$

where $\mathbf{z}_0$ and $\mathbf{y}_0$ are the corresponding unit vectors of the coordinate system (x, y, z). We also assume that the waves interact resonantly with electrons with the energy $mc^2\gamma_0$ at two high harmonics N_1 and N_2 of the electron cyclotron frequency

$$\omega_j = N_j \omega_B / \gamma_0, \quad (2)$$

where $\omega_B = eB/mc$, m is the rest mass of an electron, c is the speed of light, and γ_0 is the relativistic gamma-factor. An electron ensemble with an energy spread near the resonance energy is described by the distribution function $f(w, \theta, X, t)$, in which $w = \gamma - \gamma_0$, θ is the phase of the electron cyclotron gyration and X is the transverse coordinate of the center of the Larmor circle. In accordance with the scheme proposed in [4], we consider an electron ensemble that has been modulated beforehand.[1] In other words, we assume that, at the initial time, the electron distribution function is modulated in X and θ:

$$f_{\mathrm{in}}(t = 0) = f_0(\omega) + f_L(w)\cos(\varphi_0 + L\theta + \kappa X), \quad (3)$$

where $L = N_1 - N_2$ and $\kappa = k_1 - k_2$. We also assume that the field frequencies are close to one another:

$$L \ll N_j. \quad (4)$$

The analysis of [4] was based on the solution of the kinetic equation

$$\left(\frac{\partial}{\partial t} + \omega_H \frac{\partial}{\partial \theta}\right) f - F \frac{\partial}{\partial w} f = 0 \quad (5)$$

and the reduced equations for the excitation of high-frequency waves,

$$\dot{\alpha}_j = (2\pi e/mc) I_j. \quad (6)$$

Here,

$$\omega_H = \frac{\omega_B}{\gamma_0}\left(1 - \frac{w}{\gamma_0}\right), \quad (7)$$

$$F = F_1 + F_2,$$
$$F_j = G_j \mathrm{Re}\,\alpha_j \exp(iN_j\theta + ik_j X - i\omega_j t), \quad (8)$$

where $j = 1, 2$; $G_j = (\rho_\perp^0/\gamma_0) J'_{N_j}(k_j r_H)$, $r_H = c\rho_\perp^0/\omega_B$, $\rho_\perp^0$ is the resonant value of the transverse electron momentum in units of mc; J'_{N_j} is the derivative of the Bessel function with respect to its argument; $\alpha_j = e\omega_j A_j/(mc^2)$; and the resonant harmonics I_j of the high-frequency current are expressed in terms of the electron distribution function (see [4]). Using the linear approximation in the field and neglecting the ballistic relaxation of the low-frequency modulation of the distribution function,[2] Gaponov-Grekhov and Tokman [4] obtained the following set of reduced equations describing the evolution of the amplitudes of the parametrically coupled waves:

$$\frac{d\alpha_1}{dt} + (\gamma_l + i\delta_l)\alpha_1 = -a(\gamma_n + i\delta_n)\alpha_2,$$
$$\frac{d\alpha_2}{dt} + ab(\gamma_l + i\delta_l)\alpha_2 = -(\gamma_n^* + i\delta_n^*)\alpha_1. \quad (9)$$

Here,

$$\gamma_l = -\frac{2\pi^2 e^2 G_1^2 \gamma_0}{m\omega_1} \left.\frac{df_0}{dw}\right|_{w=0},$$
$$\gamma_n = -\frac{\pi^2 e^2 G_1 G_2 \gamma_0}{m\omega_1} \left.\frac{df_L}{dw}\right|_{w=0} e^{i\varphi_0},$$
$$\delta_l = -\frac{2\pi e^2 G_1^2 \gamma_0}{m\omega_1} \int \frac{P df_0/dw}{w} dw,$$
$$\delta_n = -\frac{\pi e^2 G_1 G_2 \gamma_0}{m\omega_1} \int \frac{P df_L/dw}{w} dw e^{i\varphi_0}, \quad (10)$$
$$a = \frac{N_1}{N_2},$$
$$b = \frac{G_2^2}{G_1^2},$$

[1] The models with a preliminary modulation of an electron ensemble were discussed in [4, 5]. Presumably, the problems with continuous pumping require a separate analysis and go beyond the perturbation method used in this paper and in [4].

[2] This indicates that the analysis is restricted to time scales such that $Lt\langle\Delta w\rangle\omega_B/\gamma_0^2 \ll 1$, where $\langle\Delta w\rangle$ is the characteristic energy spread of the modulated component of the initial distribution function. On such time scales, the ballistic detuning of the temporal synchronism between the beatings of the high-frequency field and the low-frequency modulation is unimportant (see [8] for details).

where the symbol P denotes the principal value of the integral and γ_l is the standard linear damping rate of the wave in the absence of parametric coupling. If the electron ensemble is inversionless (i.e., $\partial f_0/\partial w\ (w = 0) < 0$, so that the electron ensemble is stable against the generation of each of the two waves), then the waves can be amplified at the expense of parametric coupling. In this case, one of the two exponentially increasing solutions to Eqs. (9) is unstable. In the simplest case, in which the coupling coefficients are close to one another ($G_1 \approx G_2$) or the frequency shifts δ_l and δ_n are both zero, the amplification condition has the form

$$\frac{1}{2}\left|\frac{\partial f_L}{\partial w}\right|_{w=0} > -\left(\frac{\partial f_0}{\partial w}\right)_{w=0}. \tag{11}$$

3. QUASILINEAR THEORY OF THE INVERSIONLESS PARAMETRIC GENERATION OF CYCLOTRON RADIATION

Here, we apply the methods of quasilinear theory to the plasma in order to investigate the energy processes in the system under discussion. As was noted in the Introduction, a similar problem was analyzed in [4]. However, below we will show that, in this analysis, no account was taken of the effect associated with the "partial" action of the components of the bichromatic field on the evolution of the modulated component of the electron distribution function. In quasilinear theory, taking into account this action makes it possible to correctly determine the conditions under which the cyclotron instability saturates. Let us analyze this point in more detail.

As is usually done in deriving quasilinear theory (see, e.g., [9]), we consider electromagnetic waves whose discontinuous frequency spectra $N_1\omega_B/\gamma_0$ and $N_2\omega_B/\gamma_0$ (with $p = 1, 2, 3, \ldots, \infty$) are very close to the frequencies $N_1\omega_p$ and $N_2\omega_p$,

$$N_j\left|\omega_p - \frac{\omega_B}{\gamma}\right| \ll \frac{\omega_B}{\gamma}, \tag{12}$$

and have random phases. In this case, the effective "force" in the kinetic equation (5) is represented as

$$\begin{aligned} F = \mathrm{Re}\sum_p & G_1\alpha_{1p}\exp(iN_1\theta + ik_{1p}X - i\omega_{1p}t) \\ & + G_2\alpha_{2p}\exp(iN_2\theta + ik_{2p}X - i\omega_{2p}t), \end{aligned} \tag{13}$$

where $\alpha_{jp}(t = 0) = \left|\alpha_{jp}^0\right|e^{i\phi_{ip}}$, with ϕ_{ip} as the random phases.

An important aspect of the problem as formulated is that it is necessary not only to trace the evolution of the averaged distribution function but also to derive a separate equation for the evolution of its low-frequency component and to take into account the correlations between the complex amplitudes α_{1p} and α_{2p} that originate in the interaction with the modulated electron ensemble.

We consider the time scales on which the ballistic relaxation of the modulated component of the distribution function does not manifest itself (see [4, 8]); in other words, we are interested in quasilinear processes that occur on shorter time scales.[3] In this case, the desired electron distribution function averaged over the ensemble of random phases can be represented as[4]

$$\begin{aligned} \langle f\rangle_\phi = & f_0(w, t) \\ & + f_L(w, t)\cos(\varphi(w, t) + L\theta + \kappa X - \Omega t). \end{aligned} \tag{14}$$

Under the above assumption that the ballistic relaxation can be neglected, conditions (4) and (12) allow us to use the same relationship between the frequencies and wave vectors for all sets of resonant modes:

$$\omega_{1p} - \omega_{2p} = L\omega_p \approx \Omega, \quad k_{1p} - k_{2p} \approx \kappa. \tag{15}$$

In this case, each pair of waves with amplitudes α_{1p} and α_{2p} that are in resonance with the identical electrons is described by Eqs. (9) of the linear theory. Condition (4) makes it possible to simplify these equations by setting

$$a \approx 1. \tag{16}$$

Under the assumption that the quasilinear processes are slower than the linear amplification or absorption, the general solution to the resulting equations is a superposition of the linearly independent, exponential solutions:

$$\begin{aligned} \alpha_{1p}(t) &= a_{1p}^+(t) + a_{1p}^-(t), \\ \alpha_{2p}(t) &= a_{2p}^+(t) + a_{2p}^-(t). \end{aligned} \tag{17}$$

Here, taking into account the time dependence of the coefficients $\gamma_{l,n}$ and $\delta_{l,n}$, which is associated with the time dependence of $f_0(w, t)$, $f_L(w, t)$, and $\varphi(w, t)$, we have

$$\begin{aligned} a_{1p}^\pm &= c_p^\pm A_p^\pm \exp\left(\int_0^t \mu_p^\pm d\tau\right), \\ a_{2p}^\pm &= c_p^\pm \exp\left(\int_0^t \mu_p^\pm d\tau\right), \end{aligned} \tag{18}$$

where[5]

[3] Since the characteristic time scale of the ballistic relaxation is governed only by the energy spread of the electrons and is independent of the electron density, the conditions under which the quasilinear diffusion processes dominate can always be achieved by varying the electron density and, accordingly, the linear growth rate of the cyclotron instability.

[4] Note that, in the general case, when the coupling coefficients G_1 and G_2 are not assumed to be equal to one another (as was done in [4]), it is necessary to take into account the change in the phase of the modulated component of the distribution function.

[5] In the expressions for $\mu_p^\pm$ and $A_p^\pm$, the sign of the square root determines a particular exponentially increasing solution and should be chosen so as to satisfy the condition that $\mu_p^\pm(t)$ and $A_p^\pm(t)$ be smooth functions. This choice becomes important if the expression under the square root changes sign during the evolution of the system.

$$\mu_p^{\pm} = -\frac{1+b}{2}(\gamma_{lp} + i\delta_{lp}) \pm \sqrt{\frac{(1-b)^2}{4}(\gamma_{lp} + i\delta_{lp})^2 + (\gamma_{np} + i\delta_{np})(\gamma_{np}^* + i\delta_{np}^*)},$$

$$A_p^{\pm} = \frac{\frac{b-1}{2}(\gamma_{lp} + i\delta_{lp}) \pm \sqrt{\frac{(1-b)^2}{4}(\gamma_{lp} + i\delta_{lp})^2 + (\gamma_{np} + i\delta_{np})(\gamma_{np}^* + i\delta_{np}^*)}}{-(\gamma_{np}^* + i\delta_{np}^*)}, \tag{19}$$

$$\gamma_{lp} = -\frac{2\pi^2 e^2 G_1^2}{m}\int \frac{\partial f_0}{\partial w}\delta(\omega_{1p} - N_1\omega_H)dw,$$

$$\gamma_{np} = -\frac{\pi^2 e^2 G_1 G_2}{m}\int \frac{\partial f_L}{\partial w}e^{i\varphi(w)}\delta(\omega_{1p} - N_1\omega_H)dw,$$

$$\delta_{lp} = -\frac{2\pi e^2 G_1^2}{m}\int \frac{\partial f_0}{\partial w}\frac{P}{\omega_{1p} - N_1\omega_H}dw, \tag{20}$$

$$\delta_{np} = -\frac{\pi e^2 G_1 G_2}{m}\int \frac{\partial f_L}{\partial w}e^{i\varphi(w)}\frac{P}{\omega_{1p} - N_1\omega_H}dw.$$

Let us derive equations for the slowly varying components $f_0(w, t)$ and $f_L(w, t)$ of the distribution function and the phase $\varphi(w, t)$. To do this, we as usual find the second-order corrections (which are proportional to $\sim\alpha^2$) in the kinetic equation (5) and then average this equation over the ensemble of random phases ϕ_{jp}. Taking into account relationships (15) and (16), we obtain the following equation for $\langle f\rangle_\phi$:

$$\left(\frac{\partial}{\partial t} + \omega_H\frac{\partial}{\partial\theta}\right)\langle f\rangle$$

$$= \frac{G_1^2}{2}\frac{\partial}{\partial w}\sum_p\left(\frac{\partial f_0}{\partial w}(\langle|\alpha_{1p}|^2\rangle_\phi + b\langle|\alpha_{2p}|^2\rangle_\phi)\right.$$

$$+ \frac{\partial f_L}{\partial w}\sqrt{b}\,\mathrm{Re}(\langle\alpha_{1p}\alpha_{2p}^*\rangle_\phi e^{-i\varphi})$$

$$\left. + 2\frac{\partial f_0}{\partial w}\sqrt{b}\,\mathrm{Re}(\langle\alpha_{1p}\alpha_{2p}^*\rangle_\phi e^{iL\theta + i\kappa X - i\Omega t})\right) \tag{21}$$

$$\times\pi\delta(\omega_{1p} - N_1\omega_H)$$

$$+ \frac{1}{2}\frac{\partial f_L}{\partial w}\mathrm{Re}\left(\left(\pi\delta(\omega_{1p} - N_1\omega_H) + i\frac{P}{\omega_{1p} - N_1\omega_H}\right)\right.$$

$$\times(b\langle|\alpha_{2p}|^2\rangle_\phi e^{i\varphi + iL\theta + i\kappa X - i\Omega t}$$

$$\left. + \langle|\alpha_{1p}|^2\rangle_\phi e^{-i\varphi - iL\theta - i\kappa X + i\Omega t})\right).$$

We use relationships (17) and (18) to express the averaged quantities $\langle\alpha_{ip}\alpha_{jp}^*\rangle_\phi$ in Eq. (21) in terms of the correlation functions $\langle|a_{2p}^{\pm}|^2\rangle_\phi$ and $\langle a_{2p}^{+}a_{2p}^{-*}\rangle_\phi$. Note that, for $t > 0$, the amplitudes of the modes at the frequencies ω_{1p} and ω_{2p} become correlated (the quantity $\langle\alpha_{1p}a_{2p}^*\rangle_\phi$ is nonzero) because the presence of the low-frequency modulation of the electron distribution function causes the modes to interact parametrically. In the above formulas, we can neglect the quantity $\langle a_{2p}^{+}a_{2p}^{-*}\rangle_\phi$.[6] We also convert from summation over the discontinuous spectrum to integration over the frequency by introducing the spectral intensity of the bichromatic modes:

$$\sum_p\langle|a_{2p}^{\pm}|^2\rangle_\phi(\ldots) \longrightarrow \int_\omega|a_\omega^{\pm}|^2(\ldots)d\omega. \tag{22}$$

As a result, we arrive at the following equations for the slow varying components of the distribution function and the phase:

$$\frac{\partial f_0}{\partial t} = \frac{\partial}{\partial w}\left((D_0^+(w) + D_0^-(w))\frac{\partial f_0}{\partial w}\right.$$

$$\left. + \frac{1}{2}(D_L^+(w) + D_L^-(w))\frac{\partial f_L}{\partial w}\right),$$

$$\frac{\partial f_L}{\partial t} = \frac{\partial}{\partial w}\left((D_L^+(w) + D_L^-(w))\frac{\partial f_0}{\partial w}\right. \tag{23}$$

$$\left. + \frac{1}{2}(D_0^+(w) + D_0^-(w))\frac{\partial f_L}{\partial w}\right),$$

[6] The quantity $\langle a_{2p}^{+}a_{2p}^{-*}\rangle_\phi$ can be neglected because, in accordance with relationships (18) and (19), it decreases at the linear rate $\mathrm{Re}(\mu_p^+ + \mu_p^{-*}) = -2\gamma_{pl}$, when $\partial f_0/\partial w < 0$ (i.e., when the electron ensemble is inversionless).

$$\frac{\partial \varphi}{\partial t} f_L = \frac{\partial}{\partial w}((H_0^+(w) + H_0^-(w))\frac{\partial f_0}{\partial w}$$

$$+ (H_L^+(w) + H_L^-(w))\frac{\partial f_L}{\partial w}\Big),$$

where

$$D_0^\pm(w) = \pi G_1^2 \int \left|a_\omega^\pm\right|^2 \frac{1}{2}(b + \left|A_\omega^\pm\right|^2)\delta(\omega - N_1\omega_H)d\omega,$$

$$D_L^\pm(w) = \pi G_1^2 \sqrt{b}\,\mathrm{Re}(e^{-i\varphi}\int \left|a_\omega^\pm\right|^2 A_\omega^\pm \delta(\omega - N_1\omega_H)d\omega),$$

$$H_0^\pm(w) = \pi G_1^2 \sqrt{b}\,\mathrm{Im}(e^{-i\varphi}\int \left|a_\omega^\pm\right|^2 A_\omega^\pm \delta(\omega - N_1\omega_H)d\omega), \quad (24)$$

$$H_L^\pm(w) = G_1^2 \frac{1}{4}\int \left|a_\omega^\pm\right|^2 (b - \left|A_\omega^\pm\right|^2)\frac{P}{\omega - N_1\omega_H}d\omega.$$

The equations for the spectral intensities $\left|a_\omega^\pm\right|^2$ follow from linear theory:

$$\frac{\partial}{\partial t}\left|a_\omega^\pm\right|^2 = 2\left|a_\omega^\pm\right|^2 \mathrm{Re}\,\mu_\omega^\pm, \quad (25)$$

where the quantities $\mu_\omega^\pm$ and $A_\omega^\pm$ are described by expressions (19).

Equations (23)–(25) constitute the basic set of equations in quasilinear theory. They describe the evolution of the modulated electron distribution function under the action of the bichromatic modes, which are driven by parametric instability and are in cyclotron resonance with the electrons.

Equations (23)–(25) possess the law of conservation of the number of particles,

$$\int f_0(w)dw = \mathrm{const} \quad (26)$$

and the energy conservation law,

$$mc^2 \int (\gamma_0 + w) f_0(w)dw + I_e = \mathrm{const}, \quad (27)$$

where $I_e = (m^2c^2/e^2)\int(\left|a_\omega^+\right|^2(1 + \left|A_\omega^+\right|^2)/(4\pi) + \left|a_\omega^-\right|^2(1 + \left|A_\omega^-\right|^2)/(4\pi))d\omega$ is the electromagnetic field energy.

In accordance with Eqs. (23)–(25), the evolution of the distribution function inevitably results in the saturation of the cyclotron instability and the establishment of a steady state described by the above expressions for the spectral intensity of the high-frequency field and for all components of the distribution function, namely, the "constant" component f_0 and the amplitude f_L and phase φ of the component modulated at the beat frequency of the high-frequency field.

We assume that the frequency band in which cyclotron radiation can be generated is fixed by external electrodynamic conditions and that only one particular mode is generated in this frequency band. (To satisfy these assumptions, it is sufficient to require that the averaged component of the distribution function be inversionless and the derivative of the amplitude of the modulated component with respect to energy be of constant sign within the corresponding range of resonance energies at the initial time.) Under these assumptions, we can equate the right-hand sides of the first two equations in set (23) to zero in order to show that, in the final steady state, the following two conditions should hold simultaneously:

$$\frac{1}{2}\left|\frac{\partial f_L^{\mathrm{st}}}{\partial w}\right| = -\frac{\partial f_0^{\mathrm{st}}}{\partial w}, \quad (28)$$

$$D_0^{\mathrm{st}}(w) = D_L^{\mathrm{st}}\,\mathrm{sgn}\Big(\frac{\partial f_L}{\partial w}\Big), \quad (29)$$

where the superscript st refers to the steady-state values of the functions. Taking into account expressions (24), (19), (20), and (28), we can reduce the second condition to the following integral condition on the energy-dependent phase $\varphi^{\mathrm{st}}(w)$ and function $f_0^{\mathrm{st}}(w)$:

$$\int_{\mathrm{in}} \frac{\partial f_0^{\mathrm{st}}}{\partial w}\Big(\frac{be^{-i\varphi^{\mathrm{st}}(w) + i\varphi^{\mathrm{st}}(\omega)} - e^{i\varphi^{\mathrm{st}}(w) - i\varphi^{\mathrm{st}}(\omega)}}{b-1} - 1\Big)\frac{P}{\omega - N\omega_H}dw$$

$$= \int_{\mathrm{out}} \Big(\frac{\partial f_0^0}{\partial w} + \frac{1}{2}\frac{\partial f_L^0}{\partial w}\mathrm{sgn}\Big(\frac{\partial f_L}{\partial w}\Big)_{\mathrm{in}} \quad (30)$$

$$\times \frac{be^{-i\varphi_0 + i\varphi^{\mathrm{st}}(\omega)} - e^{i\varphi_0 - i\varphi^{\mathrm{st}}(\omega)}}{b-1}\Big)\frac{P}{\omega - N\omega_H}dw.$$

Here, the domains of integration "in" and "out" denote the energy intervals inside and outside the generation region, respectively; f_0^0, f_L^0, and φ_0 are the components of the distribution function at the initial time; and $\varphi^{\mathrm{st}}(\omega) = \varphi^{\mathrm{st}}(w)|_{N\omega_H(w) = \omega}$. Conditions (28) and (29) are sufficient conditions for the right-hand sides of the equations describing the evolution of $\varphi(t)$ and $|a_\omega|^2(t)$ to vanish.

The quasilinear diffusion equations (23)–(25) can be substantially simplified under the assumption

$$G_2 \approx G_1 = G, \quad (31)$$

which implies that the initial phase of the modulated component of the distribution function remains unchanged with time, $\varphi(w) = \varphi_0$. In this case, the diffu-

sion coefficients and the rates at which the modes grow exponentially are described by the expressions

$$D_0^{\pm} = \pm D_L^{\pm} = \pi G^2 \int \left|a_\omega^{\pm}\right|^2 \delta(\omega - N\omega_H) d\omega,$$
$$\mathrm{Re}\,\mu_\omega^{\pm} = \frac{2\pi^2 e^2 G^2}{m} \int \left(\frac{\partial f_0}{\partial w} \pm \frac{1}{2}\frac{\partial f_L}{\partial w}\right) \delta(\omega - N\omega_H) dw. \quad (32)$$

At the decreasing (inversionless) part of the distribution function $f_0(w)$, the mode corresponding to the plus sign is amplified, while the mode corresponding to the minus sign is damped, provided that the distribution function satisfies the condition $(1/2)\partial f_L/\partial w > -\partial f_0/\partial w$. Under the condition $-(1/2)\partial f_L/\partial w > -\partial f_0/\partial w$, the mode corresponding to the minus sign is amplified and the mode corresponding to the plus sign is damped. The two modes can be amplified simultaneously only at the inverse part of the distribution function, $\partial f_0/\partial w > 0$. If we again assume that only one of the modes can be amplified over the entire energy interval in which the energy can be exchanged between the electrons and the field, then we arrive at the quasilinear diffusion equations

$$\frac{\partial f_0}{\partial t} = \frac{\partial}{\partial w}\left(D(w)\left(\frac{\partial f_0}{\partial w} + \frac{1}{2}\left|\frac{\partial f_L}{\partial w}\right|\right)\right),$$
$$\frac{\partial f_L}{\partial t} = \frac{\partial}{\partial w}\left(D(w)\left(\frac{\partial f_0}{\partial w} + \frac{1}{2}\left|\frac{\partial f_L}{\partial w}\right|\right)\right)\mathrm{sgn}\left(\frac{\partial f_L}{\partial w}\right), \quad (33)$$
$$D = \pi G^2 \int |a_\omega|^2 \delta(\omega - N\omega_H) d\omega,$$
$$\frac{d}{dt}|a_\omega|^2 = \frac{4\pi^2 e^2 G^2}{m} \int \left(\frac{\partial f_0}{\partial w} + \frac{1}{2}\left|\frac{\partial f_L}{\partial w}\right|\right) \delta(\omega - N\omega_H) dw,$$

where a_ω is the amplitude of the amplified mode. Note that Gaponov-Grekhov and Tokman [4] considered precisely this particular case; however, the equation that they derived for f_L does not contain the term that is proportional to $\frac{\partial f_L}{\partial w}$ and describes the evolution of the modulated component of the distribution function under the independent action of each component of the bichromatic field.

In this particular case, in which condition (31) holds, the relationship (28) between the components of the distribution function in a steady state becomes evident, especially if one takes into account the amplification condition (11). The steady state with relationship (28) corresponds to the threshold for the parametric instability under consideration.

Equations (33) imply that the function $f_0(w) - f_L(w)\,\mathrm{sgn}\left(\frac{\partial f_L}{\partial w}\right)$ is constant in time. Together with condition (28), this circumstance makes it possible to relate the steady-state distribution function to the initial distribution function:

$$\frac{\partial f_0^{\mathrm{st}}}{\partial w} = \frac{1}{3}\left(\frac{\partial f_0^0}{\partial w} - \left|\frac{\partial f_L^0}{\partial w}\right|\right),$$
$$\frac{\partial f_L^{\mathrm{st}}}{\partial w} = \frac{2}{3}\left(\frac{\partial f_L^0}{\partial w} - \frac{\partial f_0^0}{\partial w}\mathrm{sgn}\left(\frac{\partial f_L}{\partial w}\right)\right). \quad (34)$$

From Eqs. (34), we can see that, during the inversionless amplification of one of the bichromatic modes, the electron distribution function does not relax to the "standard" plateau shape; instead, its averaged component relaxes to a state with a negative derivative with respect to energy. Notably, the energy conservation law (27) implies that, during inversionless parametric generation, the high-frequency field acquires its energy from the electrons that are described by the constant component $f_0(w)$ of the distribution function, as is the case during the conventional maser instability. Moreover, a particularly important point here is that, in the energy interval in which the initial inversionless distribution function is unstable, a decrease in the energy of the electron ensemble during inversionless parametric generation is accompanied by the formation of a distribution function with a steeper slope along the energy axis in comparison to the slope of the initial distribution function. This effect corresponds to the depletion of the population of the upper state associated with the working atomic transition.

We assume that the width Δ of the generation region around $w = 0$ is small in comparison with the characteristic scale on which the functions $f_0(w)$ and $f_L(w)$ vary, so that they can be regarded as the linear functions of energy. Under this assumption, the energy conservation law (27), the conservation law (26) for the number of particles, and Eqs. (34) allow us to easily obtain an expression for the energy acquired by the field:

$$I_e = mc^2 \frac{2}{3}\left(\frac{\partial f_0^0}{\partial w} + \frac{1}{2}\left|\frac{\partial f_L^0}{\partial w}\right|\right)\frac{\Delta^3}{12} = K\frac{2}{3}\mathrm{Re}\,\mu, \quad (35)$$

where the coefficient is equal to $K = m^2c^2\omega\Delta^3/(24\pi^2e^2G^2\gamma_0)$ and $\mathrm{Re}\,\mu$ is the instability growth rate at the initial time.[7] Expression (35) is obviously analogous to the expression

$$I_e = mc^2 \frac{\partial f_0^0}{\partial w}\frac{\Delta^3}{12} = K\,\mathrm{Re}\,\mu, \quad (36)$$

which determines the energy acquired by the field during the conventional maser instability, when the distribution function that must be inverted relaxes to a plateau shape.

[7] Here and below, the derivatives of the functions f_0^0 and f_L^0 with respect to energy are taken at the point $w = 0$.

Hence, in the regime of quasilinear relaxation during inversionless generation, the energy exchange between the electrons and the wave field may be as efficient as that during the conventional maser instability.

4. CONCLUSION

The main results of our study can be summarized as follows.

We have constructed a quasilinear theory of inversionless parametric cyclotron instability. We have established that, if such saturating effects as ballistic relaxation and nonlinear frequency locking and shift are neglected, then, during the quasilinear diffusion, the system of a modulated electron ensemble and an electromagnetic field relaxes to a certain steady state. We have derived the equations describing this relaxation process under fairly general assumptions. The equations obtained have been investigated most completely for the particular case in which the coefficients G_1 and G_2 are close to one another. Note that this case is of special interest. As was shown in [4, 5], the inversionless generation that is governed by the mechanism analyzed above can be realized in a different scheme of generation (specifically, in the inversionless version of a maser based on the cyclotron autoresonance interaction) and also under the Cherenkov resonance conditions. In such systems, the coefficients G_1 and G_2 are automatically equal to each other.

Of course, in addition to the regime of quasilinear relaxation, it is also of interest to investigate nonlinear energy exchange processes with allowance for such effects as the trapping of particles by the strong field of a finite-amplitude bichromatic wave and nonlinear frequency shift.

ACKNOWLEDGMENTS

This work was supported in part by the Russian Foundation for Basic Research, project no. 99-02-16230.

REFERENCES

1. O. Kocharovskaya, Phys. Rep. **219**, 175 (1992).
2. B. Sherman, G. Kurizki, D. E. Nikonov, and M. O. Scully, Phys. Rev. Lett. **75**, 4602 (1995).
3. D. E. Nikonov, B. Sherman, G. Kurizki, and M. O. Scully, Opt. Commun. **123**, 363 (1996).
4. A. V. Gaponov-Grekhov and M. D. Tokman, Zh. Éksp. Teor. Fiz. **112**, 1176 (1997) [JETP **85**, 640 (1997)].
5. M. A. Erukhimova and M. D. Tokman, Zh. Éksp. Teor. Fiz. **118**, 291 (2000) [JETP **91**, 255 (2000)].
6. A. I. Artemiev, M. V. Fedorov, Y. V. Rostovsev, *et al.*, Phys. Rev. Lett. **85**, 4510 (2000).
7. V. V. Zheleznyakov, *Electromagnetic Waves in Space Plasmas* (Nauka, Moscow, 1977).
8. M. A. Erukhimova and M. D. Tokman, Izv. Vyssh. Uchebn. Zaved., Radiofiz. **44**, 190 (2001).
9. L. D. Landau and E. M. Lifshitz, *Electrodynamics of Continuous Media* (Nauka, Moscow, 1982; Pergamon, New York, 1984).

Translated by I. A. Kalabalyk

Plasma Physics Reports, Vol. 27, No. 10, 2001, pp. 875–885. Translated from Fizika Plazmy, Vol. 27, No. 10, 2001, pp. 928–939.

LOW-TEMPERATURE PLASMA

Plasma Parameters in the Channel of a Long Leader in Air

N. L. Aleksandrov*, É. M. Bazelyan, and A. M. Konchakov***

**Moscow Institute of Physics and Technology, Institutskiĭ pr. 9, Dolgoprudnyĭ, Moscow oblast, 141700 Russia*
***Krzhizhanovskiĭ Power Engineering Institute, Leninskiĭ pr. 19, Moscow, 117927 Russia*

Received April 19, 2001

Abstract—The time evolution of the electric field in the leader channel and other characteristics of the leader plasma in long air gaps are simulated. Calculations are performed in the one-dimensional time-dependent model with allowance for the time-varying energy deposition in the channel, the channel expansion, and the nonequilibrium ionization kinetics in the leader plasma. The calculations show that, at a gas temperature of 4500–6000 K, associative ionization becomes a dominant ionization mechanism in the leader channel; as a result, the electric field decreases to 100–200 V/cm in 10^{-4}–10^{-3} s under the conditions typical of the leader discharge. The calculated electric field agrees well with the data from the experimental modeling of long leaders by a spark discharge in short gaps. © *2001 MAIK "Nauka/Interperiodica".*

1. INTRODUCTION

The development of a leader in a spark discharge results in the formation of a plasma channel. The electron density in the channel does not decrease for a relatively long time (up to several hundredths of a second) in weak electric fields (down to the arc field). This process is enhanced by gas heating in the channel. In air, the gas temperature gradually grows to 5000–7000 K in laboratory gaps and even higher in lightning. The initiation and propagation of the leader is a decisive phase of the long spark: the bridging of the gap by the leader is inevitably followed by breakdown, i.e., by the formation of a highly conductive channel with a descending current–voltage (*I*–*V*) characteristic [1–3]. The longer the leader, the greater is the fraction of the applied voltage *U* that drops across the channel and the lesser is the fraction of the applied voltage that drops across the streamer zone, characterized by a higher electric field. For this reason, the breakdown voltage of very long gaps, to a great extent, is determined by the electric field in the leader channel.

Although the electric field in the leader channel is an important characteristic of spark breakdown, direct measurements of this quantity are lacking even for air, which is the best studied gas. Estimates based on indirect measurements differ by several tens of times, depending on the experimental conditions [4–8] (see also [3]). Another characteristic important for applications—the time evolution of the electric field in the streamer channel—has been little studied experimentally. There is reason to believe that, in a freshly formed part of the channel with a temperature of ~1000 K, the reduced electric field E/N (where N is the neutral density) is close to the critical value 10^{-15} V cm^2, at which the impact-ionization rate in air is equal to the rate of electron loss by attachment to O_2 molecules [3]. At atmospheric pressure, this gives $E \approx 10$ kV/cm. The convincing experimental data [9, 10] for very long (L = 150–200 m with allowance for the trajectory bending) spark discharges point to a substantially lower mean electric field in the leader channel. In these experiments, the leaders bridged the gap at a voltage U_0 no higher than 4 MV. At the instant of bridging, the applied voltage dropped partially across the leader channel and partially across the streamer zone in front of the leader head. Ignoring a higher electric field in the streamer zone, the upper estimate for the mean electric field in the channel is $E \approx U_0/L \approx$ 200–250 V/cm, which is several tens of times lower than that at the beginning of the leader process. It is difficult to expect that, in the immediate future, it will be possible to trace the time evolution of the electric field in the channel between these very different values.

Available theoretical models [1, 11–14] assume that the generation of electrons in the leader channel is governed by the electron-impact ionization of molecules, whereas the main effect of gas heating reduces to the detachment of electrons from negative ions and to the possibility of heating the electrons in a lower electric field due to a decrease in N at a constant pressure. Hence, the reduced electric field E/N does not vary during the leader development (at least up to 200 μs) and remains at a level of 8×10^{-16} V cm^2 [13, 14]. Assuming such behavior, the field E in the well-developed leader channel heated to nearly 6000 K [3, 6, 13] cannot be lower than 1 kV/cm, which is higher by a factor of 4 to 5 than that in the experiments providing reliable upper estimates [9, 10]. There are also leader-channel models in which the air conductivity is determined assuming that the plasma is in local thermodynamic equilibrium [15, 16]. These models allow one to estimate the plasma parameters in long-lived regions of the channel where the electric field is weak; however, they are certainly inapplicable for describing the transition from

1063-780X/01/2710-0875$21.00

the initial nonequilibrium channel state, which is characterized by a rather strong electric field, to the final equilibrium state.

A kinetic model adequately describing the generation and loss of electrons in a nonequilibrium leader plasma in air was developed in [17]. With this model, it was shown that gas heating substantially decreases the reduced electric field E/N because of both the formation of NO molecules, which have a low ionization energy, and the associative ionization collisions of O and N atoms. The latter electron generation reaction becomes dominant at $T > 4500$ K. However, in [17], the problem was solved in the zero-dimensional model. This model neglects the radial expansion of the channel and, hence, cannot provide even an approximate description of the time evolution of the electric field in the leader plasma, the plasma conductivity, and other characteristics that vary self-consistently as the cross section of the current channel increases.

The one-dimensional model of the leader channel developed in the present paper is free from the above drawbacks. This model is intended for analyzing the main mechanisms responsible for variations in the plasma resistance per unit length in electric fields that are inherent in the leader from its initiation up to the transition to the quasi-equilibrium state. The kinetic model for ionization is basically similar to the model proposed previously in [17]. In our paper, the evolution of the leader plasma parameters during the entire discharge in a long air gap is calculated self-consistently. The results of calculations of the electric field in the channel are compared with the available experimental data.

2. MODELING OF THE INITIAL PHASE OF THE DEVELOPMENT OF THE LEADER CHANNEL

In modeling the leader channel, it is necessary to self-consistently describe the time evolution of the electric field in the channel, the electron kinetics, the processes of the energy transfer between different degrees of freedom of molecules in the heated air, the change in the chemical composition of the medium due to chemical reactions, and the radial expansion of the channel with allowance for varying the energy deposition in the discharge. Taking into account all the above-listed effects is a complicated computational problem. The only realistic way of modeling the process over the long period of time needed for a long leader to develop is to introduce reasonable simplifications. The description of freshly formed parts of the leader is additionally complicated by the lack of reliable data on the initial conditions, which can be obtained only from the modeling of the streamer–leader transition. However, the mechanism governing this process is still the subject of controversy and a plausible quantitative description is lacking.

The limiting length of laboratory leaders attains several hundreds of meters, and the development time is no longer than 10 ms (for a lightning leader, this time is one order of magnitude longer). This time determines the modeling time interval. Many processes incorporated in the model occur on substantially different time scales. For example, the time during which the pressure is equalized over the radius of the leader channel is on the order of 10^{-7}–10^{-6} s, the relaxation time of the energy gained by the molecules due to the electron-impact excitation of their vibrational and electronic states is on the order of 10^{-5} s [13], and the radial cooling of the channel through molecular heat conduction under the conditions of interest begins only at times longer than 3×10^{-5} s. Therefore, to simplify the problem, it is reasonable to separately consider the processes associated with different time intervals. Such an approach is used below.

The modeling of the development of the leader channel in a long air gap is divided into two steps. First, we simulate the initial phase of the transformation of a freshly formed part of the channel. For this phase, the fast plasma kinetic processes are considered in detail, whereas the slower hydrodynamic processes are considered under rough assumptions. The objective of this simulation is to study the main mechanisms and the dynamics of the plasma channel heating, as well as the consequences to which this heating leads directly, rather than via decreasing the gas density. The description of the initial phase is based on the zero-dimensional model of the leader plasma (see [18–21] for details). We numerically solve the balance equation for the densities of electrons, ions, excited molecules, and neutral chemical compounds in air at a gas temperature of $T > 1000$ K and the balance equations for the vibrational temperature of N_2 molecules and the translational temperature of neutral particles. These equations are solved at a constant electric current I in the channel,

$$I = 2\pi \int_0^\infty jr\,dr = \text{const}, \qquad (1)$$

where $j = en_e w$ is the current density and e, n_e, and w are the charge, density, and drift velocity of electrons, respectively. The assumption that the electric current is constant is justified because the current I is governed by the ionization processes in the streamer zone, rather than the conductivity of the leader region under consideration; hence, it is, in fact, an external parameter for this region. It is assumed that the energy of molecular rotational states almost instantaneously (in a time on the order of the collision time) is converted into heat. It is also assumed that a definite fraction δ of the energy of electronically excited states of molecules is converted into heat in the same ultrashort time. There is indirect experimental evidence (see [21]) that $\delta \sim 30\%$ for air. The processes of the vibrational–translational relaxation of N_2 molecules involve collisions with N_2,

O_2, H_2O, and NO molecules and O atoms. The rate constants for these processes depend on the gas temperature and are taken from [22]. The initial concentration of H_2O was assumed to be 1%. For relatively short times, channel cooling due to heat conduction is neglected. All the plasma parameters in the channel are assumed to be radially homogeneous. Calculations are performed for two extreme cases: at a constant channel radius (neglecting the channel expansion) and taking into account the channel expansion in the isobaric approximation.

We choose the following initial conditions: the initial electron density is $n_e(t = 0) = 10^{13}$ cm^{-3}, the channel radius is $r_c(t = 0) = 0.03$ cm, and the initial gas temperature is $T(t = 0) = T_0 = 1000$ K in the channel and 300 K in the surrounding air. These values, on the whole, agree with the current concept of the leader channel state at the instant of leader formation [3]. Calculations were performed for an air pressure of $p = 1$ atm and a typical leader current of $I = 1$ A.

First of all, we note that the simulation results are only slightly sensitive to the poorly known value of the initial electron density in the channel. The choice of a too low $n_e(t = 0)$ at a fixed current results in a sharp increase in the channel field (Fig. 1), which rapidly (in several nanoseconds) increases the electron density by impact ionization. For a too high initial plasma density, the electron density decreases due to electron–ion recombination. In tens to hundreds of nanoseconds (which is negligible as compared to the characteristic time of the leader process), the self-tuning process comes to an end, the channel "forgets" the specified initial conditions, and the reduced field in the channel is established at a level of 8.5×10^{-15} V cm^2. The final simulation result is also slightly affected by the uncertainty in the energy fraction that is immediately transferred from the electronic degrees of freedom to heat. This can be seen from the results of a series of test calculations presented in Fig. 2. When this heating mechanism is excluded from calculations ($\delta = 0$), the temperature grows at a lower rate during the first 1–3 μs; however, the total heating time and the maximum temperature change only slightly. When we artificially increase the V–T relaxation time, the effect is more pronounced (Fig. 2, curve *3*); however, here again, the deflection of the result obtained lies within the methodic error of the model (~10%). Hence, it follows from model calculations that there is no reason to care about the uncertainty in the initial parameters in the energy balance equation.

The time evolution of the gas temperature T and the vibrational temperature of nitrogen molecules T_v calculated by the zero-dimensional model are shown in Fig. 3. Regardless of the calculation condition (r_c = const or p = const), the gas in the channel is rapidly heated; in several microseconds, its temperature becomes higher than 5000 K. Hence, the freshly formed, relatively cold region behind the head is short

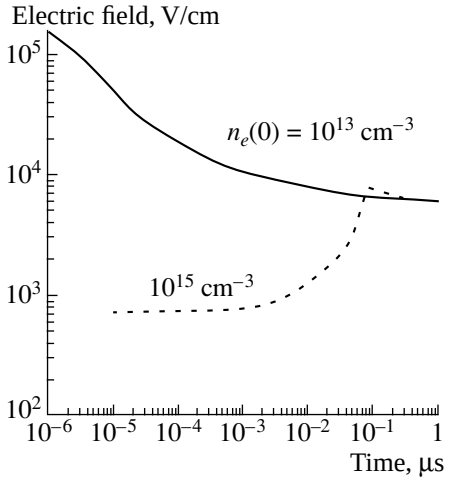

Fig. 1. Time evolution of the electric field in the self-tuning regime for different initial conditions.

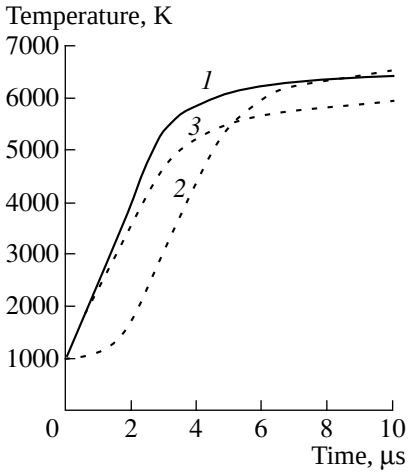

Fig. 2. Growth of the temperature in a 0.03-cm-radius leader channel at a current of 1 A: (*1*) $\delta = 0.3$, V–T relaxation is included; (*2*) $\delta = 0$, V–T relaxation is included; and (*3*) $\delta = 0$, V–T relaxation is excluded.

(about 10 cm for a typical leader velocity of $v_L \sim 10^6$ cm/s). As will be shown below, the temperature in the remaining part of a long leader channel varies only slightly, because its maximum value is limited from above by 6000–6500 K. The heating lasts for 20–40 μs. By this time, the vibrational–translational relaxation comes to an end (Fig. 3) and the remaining sources of thermal energy cannot provide a further increase in the temperature, because, at temperatures of $T \approx 6000$ K, the specific heat of air increases strongly due to the dissociation of N_2 molecules.

An important point is that, in times on the order of the time during which sound waves propagate along the channel radius, gas heating is moderate (≈300 K) as compared to the initial temperature. Hence, radial acoustic perturbations produced due to pulsed energy

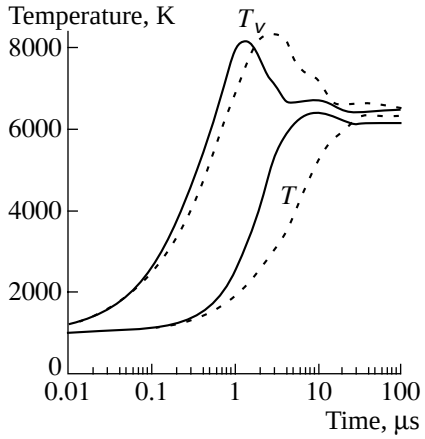

Fig. 3. Time evolution of the gas temperature and the vibrational temperature of N_2 molecules. The solid curves correspond to r_c = const, and the dashed curves correspond to p = const.

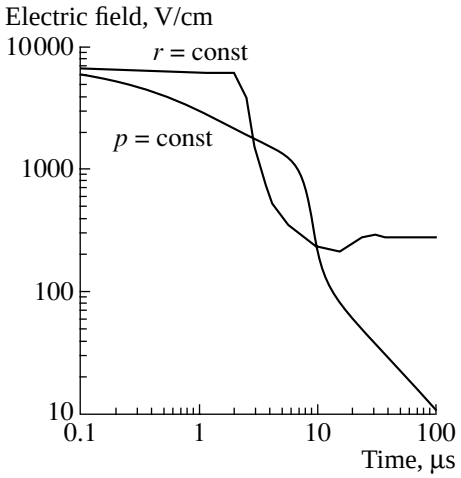

Fig. 4. Time evolution of the electric field under the conditions of Fig. 3.

deposition are small and we can use the isobaric approximation when describing the leader on long time scales. This is also confirmed by many experiments in which the velocity of the radial expansion of the leader channel in air was certainly subsonic [3, 6, 13]. We emphasize once again that the channel heating on short time scales is associated with both the fast relaxation of the energy of molecular electronic states due to collisions with unexcited molecules and the vibrational–translational relaxation of nitrogen molecules. Both these heat sources make nearly the same contributions. As was mentioned above, the artificial "switching-off" of any of these sources merely results in more protracted (either initial or final) phases of heating and does not change the general picture of the process (Fig. 2).

Figure 4 shows the time evolution of the electric field in the leader channel. It is seen that, in the zero-dimensional model, the time behavior of the electric field is quite different for r_c = const and p = const. In the nonexpanding channel, the field E decreases rather slowly as the temperature increases from 1000 to 4000 K. In the channel heated to 4000 K, the field still remains fairly high (about 6 kV/cm). Then, in the temperature range 4000–6400 K, the field drops by a factor of more than 20 (down to 250 V/cm) in approximately 10 μs. We emphasize that this effect is not related to a decrease in the gas density, because, for r_c = const, the density even somewhat increases due to the dissociation of molecules. The only reason why the field decreases so rapidly is that the reaction of associative ionization,

$$N + O \Rightarrow e + NO^+, \qquad (2)$$

comes into play. This reaction proceeds at an increasing rate in the heated air because both its rate constant and the densities of reacting atoms increase. The time during which the field decreases is $\sim 10^{-5}$ s, which is close to the gas heating time.

Simulations at p = const reflect most clearly the consequences of the increase in the E/N value in the heated air. In this case, the field in the channel decreases even before the associative-ionization reaction (2) comes into play. By the time at which the gas temperature in the channel reaches 4000 K, E does not exceed 1.3 kV/cm; as the temperature increases to 6400 K, the electric field drops to 15–20 V/cm. Characteristically, by 10 μs, E is again close to 250 V/cm. The further behavior of the electric field depends on the hydrodynamic processes in the channel, which clearly cannot be described in the zero-dimensional model.

Thus, the electric field in the channel drops very rapidly. At a current of $I \sim 1$ A, which is typical of laboratory leaders, the strong (on the order of 1 kV/cm) field exists only in a very short (~10-cm-long) region behind the leader head, where the gas is still cold. In the bulk of the channel, the field is substantially weaker. Although the zero-dimensional model fails to provide a quantitative description, it certainly gives reliable upper (for simulations with r_c = const) and lower (for simulations with p = const) estimates for the electric field; thus, under any circumstance, the long leader channel, to a greater extent, resembles a low-voltage arc channel, rather than a streamer channel with a relatively strong longitudinal field.

The time behavior of the rate constants of various electron production reactions in the initial phase of the leader development is very peculiar (Fig. 5). At $t <$ 0.5 μs, while the temperature is below 3000 K, electrons are produced via the electron-impact ionization of N_2 and O_2 molecules in the ground and excited states. For a short time, as the temperature approaches 3000 K, the dominant process is the ionization of NO molecules, whose density increases to 5×10^{16} cm^{-3}. One

microsecond later, at a temperature of ~4000 K, the associative-ionization reaction (2), which can proceed in the absence of the electric field, becomes dominant. Due to the rapid decrease in the electric field, all of the other electron-production processes become inefficient by the time $t = 3$ μs. A qualitatively similar behavior, but extended in time by a few microseconds, is also typical of simulations with p = const.

It is of interest to determine the time needed for neutrals to reach thermodynamic-equilibrium densities during the fast heating of the leader channel. In this connection, it is most important to know the concentrations of O and N atoms participating in reaction (2). At a low temperature and strong fields, the densities of these atoms are considerably higher than the equilibrium densities because of the electron-impact dissociation of molecules; however, even at a temperature of 3000 K, this difference almost disappears (Fig. 6). Among the active particles, the exception is NO molecules, for which the thermodynamic-equilibrium density at $p = 1$ atm has a maximum of ~10^{17} cm^{-3} in the temperature range 3000–3500 K. However, the actual maximum density in the same temperature range is nearly five times lower. This is of minor importance because the ionization of NO molecules plays a significant role during a very short time interval: it ceases to affect the processes in the channel just after the field in the channel begins to drop rapidly. All of this allows us to use the thermodynamic-equilibrium neutral densities when modeling the leader plasma at times on the order of or longer than tens of microseconds.

The zero-dimensional modeling confirms the validity of another simplification that is important for the hydrodynamic model. This concerns the calculation of the electron density at times $t > 10$ μs, when the electric field in the well-heated channel is already very low; for this reason, we can exclude all reactions except for the associative ionization reaction (2) and the electron–ion recombination. We believe that these reactions have time to adapt to the slowly varying temperature T and field, which allows us to use the time-independent homogeneous balance equation for the electron density n_e,

$$k_i^a N_O N_N - k_{ei} n_e^2 = 0, \quad (3)$$

where N_O and N_N are the densities of O and N atoms and k_{ia} and k_{er} are the rate constants for associative ionization and dissociative electron–ion recombination with the participation of NO^+ ions. The dependences $n_e(t)$ calculated by Eq. (3) are in good agreement with the simulation results just after the field in the channel begins to drop at $t > 10$μs (Fig. 6).

The possibility of using such a simplified kinetic scheme substantially facilitates the construction of the hydrodynamic model that should describe the plasma evolution in the heated leader channel at times from tens of microseconds to tens of milliseconds. Here, it is assumed that the chemical composition of the gas and the degree of vibrational excitation of molecules correspond to the thermodynamic equilibrium and the electron density varies slowly. (In the general case, the thermodynamic equilibrium for electrons is not achieved because of their heating in the electric field.) It is this model that is used below.

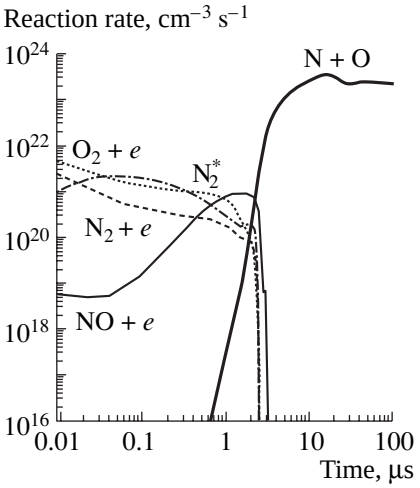

Fig. 5. Time evolution of the ionization rate in various reactions for r_c = const; the curve designated as N_2^* is calculated with allowance for electron-impact ionization and the associative ionization of electronically excited molecules.

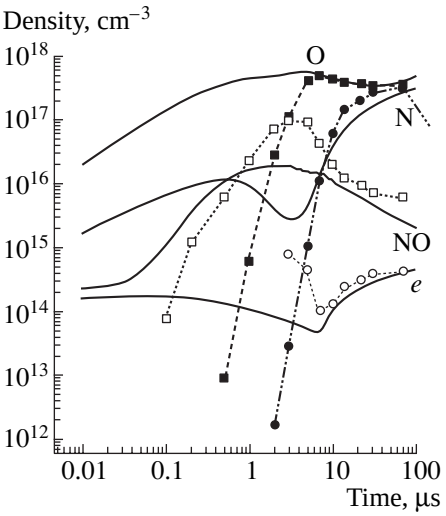

Fig. 6. Time evolution of the electron density and the neutral densities for p = const. The solid curves correspond to the simulation, and the symbols show the thermodynamically equilibrium neutral densities at a current value of the gas temperature and the n_e values determined from equation (3).

3. MODEL OF THE MAIN PHASE OF THE LEADER CHANNEL EVOLUTION

The model is intended for describing the time evolution of the plasma parameters in a certain cross section of the leader channel at a distance longer than 10–30 cm from the leader head. As follows from the foregoing, the gas in this region of the channel is already heated and the low electric field cannot maintain the electron-impact ionization reactions. The one-dimensional model allows for radial variations in the plasma parameters; substantially smaller longitudinal gradients are neglected. As initial conditions, we can use the results of calculations by the zero-dimensional model at the time corresponding to the end of fast heating (~10 μs at a current of ~1 A) or the parameters approximately corresponding to a freshly formed region in the leader channel ($T \sim 1000$ K and $E/N \sim 10^{-15}$ V cm^2). In the latter case, Eq. (3) is supplemented with impact ionization reactions. The processes involving negative ions are neglected, which is valid for $T > 1000$ K [13, 17]. Moreover, we ignore electron diffusion which is significantly slower than the volume processes under our conditions. The densities of neutral species are assumed to be equal to their thermodynamic-equilibrium values. Below, we consider the time evolution of the leader plasma at times from 30 μs to 10 ms after the leader initiation, which approximately corresponds to the channel regions lying at distances from 50 cm to hundreds of meters from the leader head.

In the E/N range under consideration, the energy gained by the electrons in the electric field is transferred to the electronic and vibrational degrees of freedom of the molecules (first of all, N_2 molecules). Since the modeled time is restricted to $t > 30$ μs, it is assumed that the internal energy of molecules has time to be converted into heat and, hence, the electron energy is almost totally spent on gas heating.

The time-dependent hydrodynamic model adopts the isobaric approximation. As was already pointed out, this is valid because many experiments point to the subsonic radial expansion of the leader channel in air at currents on the order of 1 A, which are typical of the initial phase of the process (see, e.g., [3, 13]). The set of equations includes the heat conduction equation

$$c_p \frac{\partial T}{\partial t} = jE + \frac{1}{r}\frac{\partial}{\partial r}\left(r\lambda\frac{\partial T}{\partial r}\right), \quad (4)$$

the time-independent homogeneous electron-density balance equation (3); and condition (1), assuming the constant electric field in the channel. Here, r is the radial coordinate, c_p is the specific heat at a constant pressure, and λ is the thermal conductivity.

According to our calculations, the plasma conductivity at $T > 6000$ K becomes so high and the electric field becomes so low (at a constant current) that the electron density is close to its equilibrium value. On the one hand, the kinetic description of the electrons under these conditions becomes more complicated because of the appearance of additional processes (e.g., the three-body electron–ion recombination); on the other hand, such a description is already unnecessary here. For this reason, in most calculations with $T > 6000$ K, the electric conductivity of the plasma was assumed to obey the local thermal equilibrium and its values were taken from the experimental data [23] instead of solving Eq. (3).

The values of $c_p(T)$ and the composition of the neutral components of the heated air were taken from the hydrodynamic calculations [24–26], and the values of $\lambda(T)$ were taken from the experimental data available in the literature [27]. The values of $k_i(E/N, T)$ and $w(E/N, T)$ were determined by numerically solving the Boltzmann equation for electrons in the two-term approximation for the expansion of the electron distribution function in spherical functions. The rate constants $k_{ei}(E/N, T)$ and $k_i^a(T)$ were taken by analogy with [17].

When it is required to approximately model the processes occurring during fast heating (starting from the instant the leader channel region under consideration is created) due to electron-impact electron production reactions, Eq. (3) can be rewritten in the form

$$k_i n_e N + k_i^a N_O N_N - k_{ei} n_e^2 = 0,$$

where the ionization rate constant k_i is averaged over the main neutral components of the gas (O_2, N_2, NO, O, and N in the ground and excited states). In this case, the boundary and initial conditions have the form

$$\frac{\partial T(t, r = 0)}{\partial r} = 0,$$

$$T(t, r = \infty) = T_\infty,$$

$$E/N\ (t = 0, r = 0) = 10^{-15}\ \text{V cm}^2.$$

The initial profiles $T(t = 0, r)$ and $n_e(t = 0, r)$ were taken either in the form of a homogeneous distribution over the channel of radius r_0 or in the form of a Gaussian distribution ($T(t = 0, r) = (T_0 - T_\infty)\exp[-(r/r_0)^2] + T_\infty$, $n_e(t = 0, r) = n_0\exp[-(r/r_0)^2]$). Most of the calculations were performed for $T_\infty = 300$ K, $T_0 = 1000$ K, and $r_0 = 0.005$–0.05 cm. The value of n_0 at $t = 0$ was determined from condition (1). The gas density N is determined from the condition that the pressure is constant; in all calculations, the pressure was assumed to be atmospheric.

4. SIMULATION RESULTS AND DISCUSSION

Until the present time, there has been no experimental data providing reliable information on the initial radius of a freshly formed part of a channel and, even more so, the radial profiles of the plasma parameters. To compensate for the lack of initial data, calculations were performed for various initial channel radii and

various radial profiles of the plasma parameters. A comparison of such calculations is presented in Fig. 7. Thus, we can conclude that the properties of the leader plasma at times longer than 50 μs depend slightly (within 10% or less) on the initial plasma parameters. The channel rapidly "forgets" its initial state. This is true for both the initial radial profiles of the plasma parameters and the value of the initial radius itself. This circumstance obviates the simulation uncertainty associated with the initial conditions.

The main result of the hydrodynamic model is the conclusion that the plasma in the leader channel is not steady. Short intense heating accompanied by an increase in the plasma density is followed by a long decay phase, during which the channel slowly expands and cools and the electron density decreases. It is this decay state that is reliably reproduced by the hydrodynamic model. The simulation results discussed below were obtained at a current of 1 A, which is typical of long laboratory sparks.

It can be seen in Fig. 8 that the temperature at the channel axis decreases monotonically from its maximum value of ~6500 K; however, for 10 ms (while the leader exists), it still exceeds 5000 K. This means that the main mechanism governing the kinetic processes in the channel remains the same and the plasma is maintained by the associative-ionization reaction (2). The calculated temperature agrees with the results of spectroscopic measurements [3, 6, 13], according to which the developed leader channel is heated to 5000–6000 K. The radial profiles of the temperature gradually broaden (Fig. 9), and the "thermal" radius of the channel increases with time. The growth of the thermal radius R_c estimated by the formula

$$T(r = R_c) = T(r = 0)/2,$$

is demonstrated in Fig. 10. The channel expands with a subsonic velocity and increases by one order of magnitude in several milliseconds. Thus, the mean expansion velocity within a 1-ms interval does not exceed 1.5 m/s. The calculated thermal radii and the channel expansion velocities correlate (within a factor of 2) with Schlieren photographs of real leaders in air gaps up to 10 m long (see [13]).

The electron density in the channel reduces over a rather long time, following the decrease in the gas temperature (Fig. 11). The reduction factor for n_e substantially exceeds the reduction factor for the temperature. This is due to the exponential dependence of the ionization rate on T, so that a small gas cooling leads to a rapid decrease in the plasma density. For example, by the time $t = 10$ ms, the electron density is about seven times lower than the maximum density equal to 4×10^{14} cm^{-3}, whereas the temperature decreases by no more than 30%. The same effect is responsible for the peaking of the radial density profile $n_e(r)$. The electron and, consequently, current radii of the channel are several times smaller than the thermal radius (cf. Figs. 9 and 12).

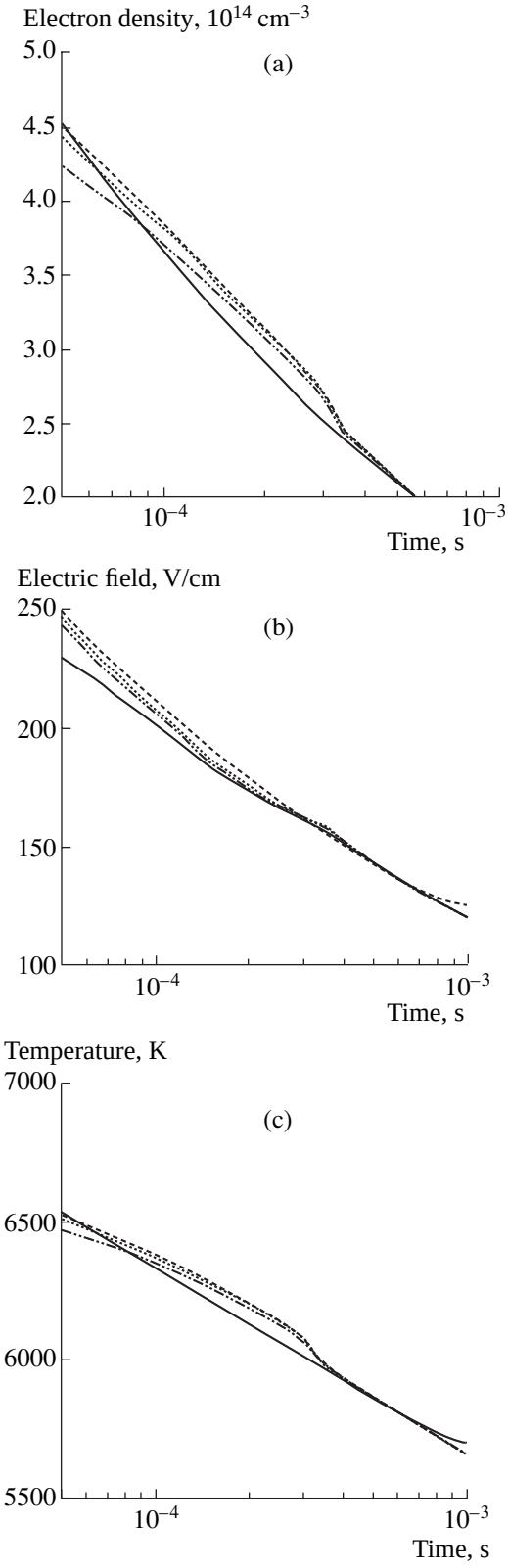

Fig. 7. Time evolution of (a) the electron density, (b) electric field, and (c) gas temperature for different initial conditions: a Gaussian distribution of the electron density with $r_0 = 0.03$ cm (solid line) and a uniform distribution with $r_0 = 0.005$ cm (dashed line), 0.03 cm (dotted line), and 0.05 cm (dashed-and-dotted line).

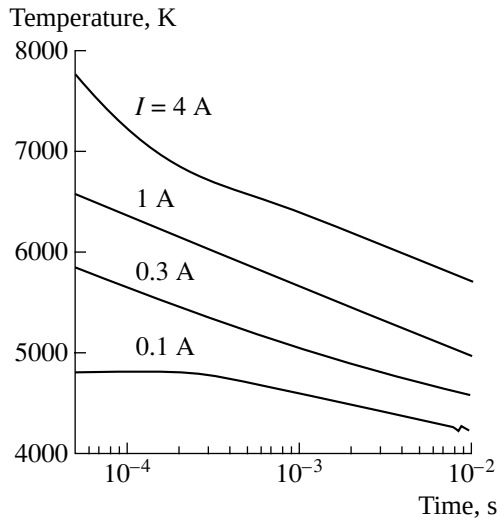

Fig. 8. Time behavior of the gas temperature at the axis of the leader channel.

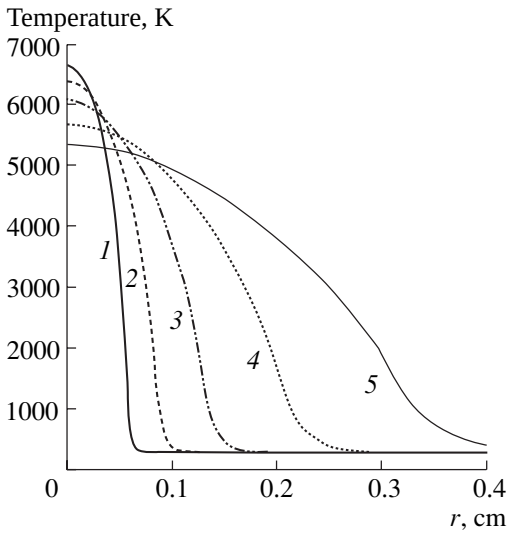

Fig. 9. Radial profile of the gas temperature in the leader channel at different instants: (*1*) 30, (*2*) 100, (*3*) 300, (*4*) 1000, and (*5*) 3000 μs.

However, the increase in the current channel turns out to be sufficient for the electric field $E(t)$ to monotonically decrease in the decaying leader plasma (Fig. 13). This process differs radically in nature from that occurring in a freshly formed part of the channel. For a lifetime of ~1–10 μs, the channel expansion due to heat conduction has no time to appear, the current cross section does not change, and the field decreases due to a rapid increase in the electron density and, hence, in the conductivity of the heating channel. According to zero-dimensional calculations for r_c = const in the time interval 1–10 μs, the density n_e increases by nearly one order of magnitude; as a result, a weak field of ~250–300 V/cm is sufficient to maintain the leader current. In contrast, on long time scales, the electron density at the channel axis decreases, whereas the hydrodynamic model demonstrates the expansion of the current channel and a noticeable increase in the total number of electrons N_e (per unit length) producing the current. For example, in the time interval from 100 to 1000 μs, N_e increases from 1.7×10^{12} to 3.4×10^{12} cm^{-1}, which results in a decrease in the field. In this case, the rate of this decrease is governed by a slow heat conduction process gradually enlarging the area of the channel cross section where the temperature is high and the current is concentrated, rather than by the rapid heating of a small gas volume. Evidently, the field decreases relatively slowly: at a current of 1 A, it falls from 250 to 70 V/cm in nearly 10 ms. It is important that this process does not terminate on long time intervals characteristic of extra-long (~100 m) leaders.

To solve the problem of optimizing the propagation conditions for a long leader and to determine the minimum breakdown voltages for gaps many meters long [3], it is necessary to have detailed data on the field reduction at various leader currents. The results from a series of calculations presented in Fig. 13 show that, as a first approximation, the dependences $E(t)$ can be represented on the logarithmic scale as parallel straight lines that are displaced as the leader current varies from 0.1 to 4 A. Hence, the increase in the current leads to the decrease in both the level to which the field falls in the initial phase of fast heating (from 800 V/cm at I = 0.1 A to 140 V/cm at I = 4 A) and the values of E during slow channel expansion due to heat conduction (from 300 to 30 V/cm at a time of 10 ms for the same current range). The increase in the leader current $I \approx C_L v_L U_h$ (where C_L and v_L are the capacitance per unit length and the leader velocity, respectively) requires an increase in the leader head potential U_h and, consequently, an additional

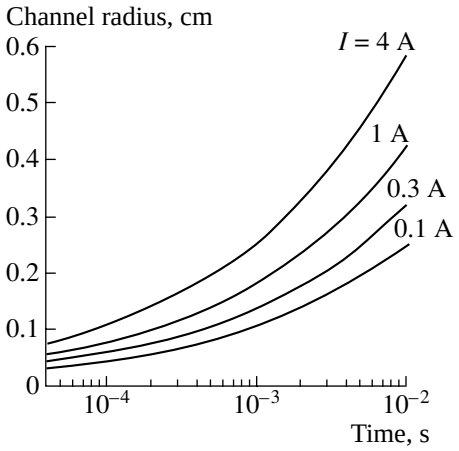

Fig. 10. Time evolution of the thermal radius of the leader channel.

increase in the applied voltage. Every specific length of the leader channel corresponds to a certain optimum level of the current at which the process requires a minimum voltage [3, 28]. The existence of a distinct minimum of the electric strength of long air gaps is a well-known experimental fact. The calculated dependences $E(t, I)$ open the possibility of numerically modeling the bridging of a long air gap under the action of voltage pulses of various shapes, which is important for high-voltage engineering.

It should be noted that varying the current over a wide range relatively weakly affects the maximum attainable gas temperature in the channel. As the current increases by a factor of 40, this temperature increases by only 60% (Fig. 8). There are two reasons for the temperature stabilization. First, as was mentioned above, the increase in the temperature above 5000 K is strongly hampered by the increase in the specific heat due to the energy consumption for nitrogen molecule dissociation, whose rate increases with temperature in the parameter range under consideration. Second, the Joule heat power per unit length is proportional to the current and the field in the channel, $P_D = IE$. In the initial phase of fast heating, when the channel expansion is still unimportant, we have $E \sim n_e^{-1}$. The electron density n_e, which, according to Eq. (3), is governed by the associative-ionization rate, and, consequently, E are very sensitive to the decrease in the temperature. When the temperature is insufficiently high, the field in the channel sharply increases, which, to a large extent, compensates for the increase in the deposited energy at low currents. The fact that spectroscopic measurements in different experiments give close temperature values may be easily explained. In laboratory experiments, the leader current varies within a relatively narrow range, which results in approximately the same temperature of 5000–6000 K.

The possibility of experimentally verifying the developed model is severely limited. Until the present time, direct measurements of the electric field in the leader channel are still lacking even for certain instances. Additionally, there are no experimental data on the time behavior of the field over extended time intervals. Indirect results that could be used for this purpose are very scarce. Data on the breakdown of extralong gaps at relatively low voltages indicate a very low mean field in the leader channel; however, these data can only be used for order-of-magnitude estimates. Hence, the measurements of the true channel length and the voltage distribution between the channel and the streamer zone at the instant of bridging are required. The former problem does not involve serious difficulties, because, to solve this problem, it is sufficient to have photographs of a spark discharge in two different planes. The latter problem can be resolved only by exactly measuring the length of the streamer zone at the instant the streamer makes contact with the surface of the grounded electrode, which is a rather complicated

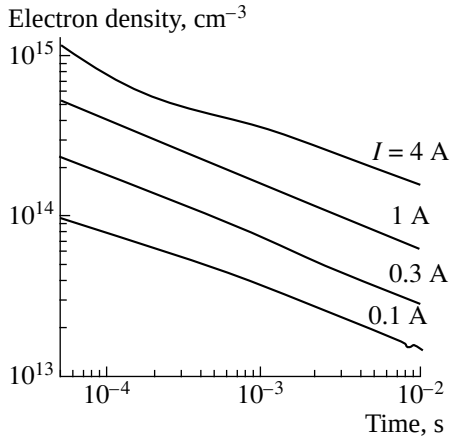

Fig. 11. Time evolution of the electron density at the axis of the leader channel.

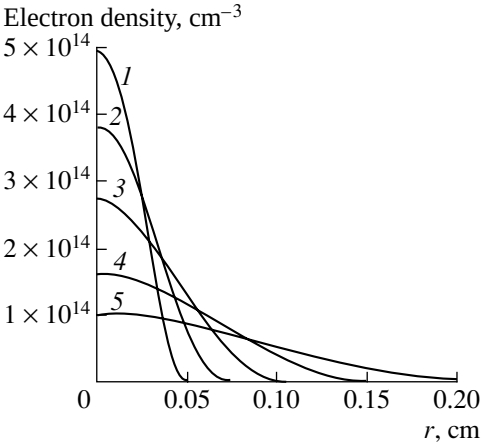

Fig. 12. Radial profile of the electron density in the leader channel at different instants: (*1*) 30, (*2*) 100, (*3*) 300, (*4*) 1000, and (*5*) 3000 μs.

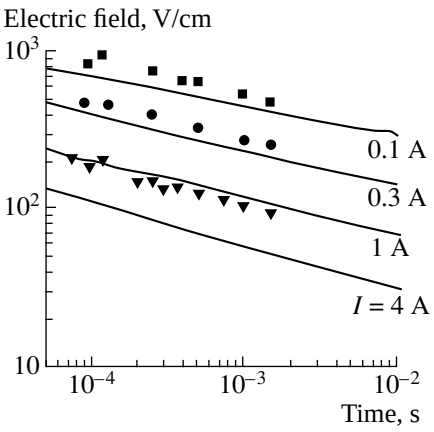

Fig. 13. Simulated time evolution of the electric field in the leader channel for different values of the electric current (solid lines). The symbols show the experimental results [11] for 0.13 (squares), 0.26 (circles), and 0.97 A (triangles).

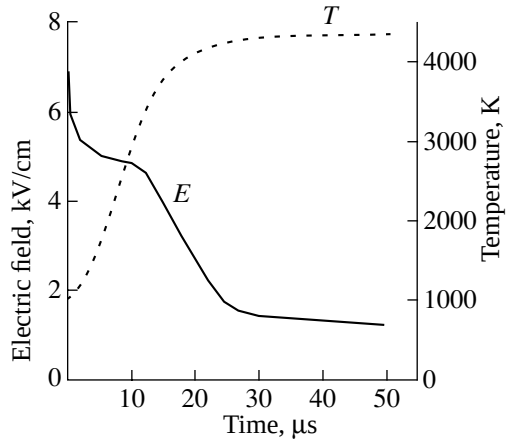

Fig. 14. Zero-dimensional simulations of the time evolution of the field and gas temperature in the channel at a current of 0.1 A and r_c = 0.03 cm.

problem from a technical standpoint. A rough estimate of the mean field made at the beginning of this paper can be refined in view of the result of theoretical analysis [3, 28], which shows that, under optimum conditions for leader development, the head potential and the gap voltage are related by the equality $U_h = 3/5U$. Hence, the voltage drop across the channel comprises only 40% of the total voltage across the gap, which decreases the estimate for the mean field in the channel of an extralong leader [9, 10] to 80–100 V/cm. The zero-dimensional model gives nearly the same estimate at times on the order of 10^{-3}–10^{-2} s.

Among other experimental data, the measurements reported in [11] deserve attention. Those measurements were performed not in the leader, but in a spark channel produced between two rod electrodes in a 7-cm gap. The experiment was arranged so as to diminish the inherent capacitance of the electrodes and other components of the circuit (a voltage divider, connecting wires, etc.) for the accumulated energy to be rapidly released in the spark channel after bridging the gap. Along with a high internal resistance of the generator, this resulted in the discharge current varying only slightly during the development of the spark, at the instant of bridging, and for a subsequent 1–2 ms. Such a spark was considered to be a physical model of part of a long leader at a fixed current. Figure 13 demonstrates good agreement between simulation results and the measured mean field in the spark channel.

We note another important detail concerning experiments [11]. In those experiments, particular attention was given to the estimates of the field in the channel of a newborn leader. For this purpose, the measuring-circuit was modified so as to make the response time of the gauges as short as possible. However, such a modification made the discharge current less stable. As a result, the actual time resolution was no less than 10–20 μs. With such a time resolution, attempts to detect fields exceeding 300 V/cm at a current of 1 A failed. Only when the current was decreased to 0.1 A did the measured field exceed 1 kV/cm. At that time, this result remained unexplained and was thought to be a methodic error caused by the additional heating of the spark channel due to the incompletely eliminated parasitic capacitance. From the present-day standpoint, the result obtained seems to be quite natural. The zero-dimensional simulations show that, at times of ~10 μs, a current of 1 A is sufficient to heat the channel up to temperatures giving rise to intense associative ionization and the field in the channel rapidly drops to 250–300 V/cm (Fig. 4). At a current of one order of magnitude lower, the temperature does not increase above 4000 K because of a lower energy deposition in the discharge; this temperature is close to the threshold of associative ionization (2) and is not accompanied by a sharp increase in the field (Fig. 14). Such measurements can be regarded as a qualitative confirmation of the simulation model.

5. CONCLUSION

In this study, the time evolution of the plasma parameters in a given cross section of the long-lived channel of a leader in air has been simulated. It is shown that the simulation results depend relatively weakly on the initial conditions, but they are very sensitive to the kinetic scheme of the plasma model. It is important for the model to be capable of correctly describing the dependence of the plasma density on both the electric field and the gas temperature.

According to the calculations, the plasma evolution in a given cross section of a long leader can be divided into two phases. In the first phase that lasts for ~10 μs, the gas in a freshly formed ~10-cm-long region behind the leader head is heated rapidly up to temperatures of ~6000 K; the electron density sharply increases due to the associative-ionization reaction with the participation of O and N atoms; and, consequently, the electric field in the channel drops by one order of magnitude or even lower. In the second phase, which lasts until the streamer-zone of the leader reaches the opposite electrode, the gas slowly cools at the axis of the channel and heats up at the periphery due to molecular heat conduction. In this phase, the channel expands and its conductivity per unit length increases in spite of the decrease in the plasma density near the channel axis. At a constant current, this leads to a slow decrease in the electric field to the values typical of the arc discharge.

The results of simulations of the time evolution of the electric field agree well with the results of experimental modeling of a real leader channel by a short spark.

ACKNOWLEDGMENTS

This study was supported in part by the Russian Foundation for Basic Research, project no. 00-02-17399.

REFERENCES

1. J. M. Meek and J. D. Craggs, *Electrical Breakdown in Gases* (Wiley, New York, 1987).
2. Yu. P. Raizer, *Gas Discharge Physics* (Nauka, Moscow, 1992; Springer-Verlag, Berlin, 1991).
3. E. M. Bazelyan and Yu. P. Raizer, *Spark Discharge* (Mosk. Fiz. Tekh. Inst., Moscow, 1997; CRC, Boca Raton, 1998).
4. I. S. Stekol'nikov, Izv. Akad. Nauk SSSR, Otd. Tekn. Nauk **5**, 133 (1957).
5. V. P. Larionov, Élektrichestvo, No. 8, 72 (1961).
6. Les Renardieres Group, Electra **53**, 3 (1977).
7. E. M. Bazelyan, V. I. Levitov, and A. Z. Ponizovsky, in *Proceedings of the 3rd International Symposium on High-Voltage Engineering, Milan, 1979*, p. 1.
8. R. T. Waters, IEE Proc. A **128**, 319 (1981).
9. E. I. Anisimov, O. V. Bogdanov, A. S. Gayvaronskii, *et al.*, Élektrichestvo, No. 11, 55 (1988).
10. A. S. Gayvoronskii and A. G. Ovsjannikov, in *Proceedings of the 9th International Conference on Atmospheric Electricity, St. Petersburg, 1992*, p. 792.
11. E. M. Bazelyan and I. M. Razhanskiĭ, *Spark Discharge in Air* (Nauka, Novosibirsk, 1988).
12. J. N. Ross, B. Jones, and R. T. Waters, Electra **53**, 85 (1977).
13. I. Gallimberti, J. Phys. (Paris) **40**, 193 (1979).
14. A. Bondiou and I. Gallimberti, J. Phys. D **27**, 1252 (1994).
15. Yu. N. Vershinin and I. M. Razhanskiĭ, Élektrichestvo, No. 6, 46 (1976).
16. I. M. Razhanskiĭ, Izv. Sib. Otd. Akad. Nauk SSSR, Ser. Tekh. Nauk, No. 3, 41 (1976).
17. N. L. Aleksandrov, E. M. Bazelyan, I. V. Kochetov, and N. A. Dyatko, J. Phys. D **30**, 1616 (1997).
18. N. L. Aleksandrov and E. M. Bazelyan, J. Phys. D **29**, 740 (1996).
19. N. L. Aleksandrov and E. M. Bazelyan, J. Phys. D **29**, 2873 (1996).
20. N. L. Aleksandrov, A. E. Bazelyan, E. M. Bazelyan, and I. V. Kochetov, Fiz. Plazmy **21**, 60 (1995) [Plasma Phys. Rep. **21**, 57 (1995)].
21. N. L. Aleksandrov, E. M. Bazelyan, N. A. Dyatko, and I. V. Kochetov, Fiz. Plazmy **24**, 587 (1998) [Plasma Phys. Rep. **24**, 541 (1998)].
22. R. L. Taylor, Can. J. Chem. **52**, 1436 (1974).
23. É. I. Asinovskiĭ, A. V. Kirillin, and V. L. Nizovskiĭ, *Stabilized Electric Arcs and Their Application in Thermophysical Experiment* (Nauka, Moscow, 1992).
24. A. S. Predvoditelev, E. V. Stupochenko, A. S. Pleshanov, E. V. Samuĭlov, and I. B. Rozhdestvenskiĭ, *Tables of Thermodynamic Functions of Air (at Temperatures from 200 to 6000 K and Pressures from 0.00001 to 10 atm)* (Vychisl. Tsentr Akad. Nauk SSSR, Moscow, 1962).
25. *Tables of Thermodynamic Functions of Air at Temperatures form 6000 to 12000 K and Pressures from 0.001 to 1000 atm*, Ed. by A. S. Predvoditelev (Akad. Nauk SSSR, Moscow, 1957).
26. N. L. Aleksandrov and E. M. Bazelyan, J. Phys. D **31**, 1343 (1998).
27. *Physics and Technology of Low-Temperature Plasma*, Ed. by S. V. Dresvin (Atomizdat, Moscow, 1972).
28. E. M. Bazelyan and Yu. P. Raizer, *Lightning Physics and Lightning Protection* (Nauka, Moscow, 2001; IOP, Bristol, 2000).

Translated by N. F. Larionova

Plasma Physics Reports, Vol. 27, No. 10, 2001, pp. 886–896. Translated from Fizika Plazmy, Vol. 27, No. 10, 2001, pp. 940–950.

LOW-TEMPERATURE PLASMA

Investigation of the Mechanism for Rapid Heating of Nitrogen and Air in Gas Discharges

N. A. Popov

Skobeltsyn Institute of Nuclear Physics, Moscow State University, Vorob'evy gory, Moscow, 119899 Russia

Received April 28, 2001; in final form, May 23, 2001

Abstract—A rapid heating of nitrogen–oxygen mixtures excited by gas discharges is investigated numerically with allowance for the following main processes: the reactions of predissociation of highly excited electronic states of oxygen molecules (which are populated via electron impact or via the quenching of the excited states of N_2 molecules), the reactions of quenching of the excited atoms $O(^1D)$ by nitrogen molecules, the VT relaxation reactions, etc. The calculated results adequately describe available experimental data on the dynamics of air heating in gas-discharge plasmas. It is shown that, over a broad range of values of the reduced electric field E/N, gas heating is maintained by a fixed fraction of the discharge power that is expended on the excitation of the electronic degrees of freedom of molecules (for discharges in air, $\eta_E \simeq 28\%$). The lower the oxygen content of the mixture, the smaller the quantity η_E. The question of a rapid heating of nitrogen with a small admixture of oxygen is discussed. © *2001 MAIK "Nauka/Interperiodica".*

1. INTRODUCTION

Interest in investigating the dynamics of heating of molecular gases stems from the need to optimize laser systems [1] and plasmochemical reactors [2] with respect to such parameters as the maximum energy deposition and the highest repetition rate of the applied-voltage pulses. The processes responsible for gas heating largely govern the stable stage of self-sustained volume discharges [3] and are recognized as a primary mechanism for the propagation of microwave discharges in fields below the breakdown field [4].

Gas heating is one of the main issues in the theory of breakdown because, as the gas temperature increases, additional ionization processes ensuring that the current–voltage characteristic is decreasing come into play [5]. It should also be noted that the formation of each subsequent element of the leader channel during the streamer–leader transition in air at atmospheric pressure is actually associated with the rapid gas heating (to temperatures of about 1500–2000 K [6]) within the leader head. For a leader channel propagating in air with a typical velocity of $(1–3) \times 10^6$ cm/s, the duration of such a heating process is no longer than 3×10^{-7} s [5]. Hence, the gas in the leader head should be heated at a rate of at least 3×10^9 K/s.

In this paper, the gas heating will be regarded as being fast if it occurs on time scales much shorter than the vibrational relaxation time. Papers [7–9] (as well as other papers devoted to rapid gas heating) present experimental data and numerical results on the heating of nitrogen and air in discharges in which the reduced electric field is relatively weak. In those papers, it was shown that, for $E/N > 40$ Td (1 Td = 10^{-17} V cm^2), the fraction of energy that is expended on the electron-impact excitation of translational and rotational degrees of freedom of molecules does not exceed 3–3.5%. However, in some experiments with stronger reduced electric fields, $E/N > 80–100$ Td (see, e.g., [10–16]), the rate of gas heating in the initial discharge stage was observed to be anomalously high (in comparison with the VT relaxation rate), in which case the fraction of the deposited energy that is expended on gas heating amounted to 10–15%.

Based on the experimental observations of gas expansion, Baranov *et al.* [10] determined how the temperature of molecular nitrogen evolves in the course of a self-sustained pulsed discharge (with the parameters $P = 100$ torr and $\tau_{pul} = 1$ μs, the deposited energy being about 0.5 J/(cm^3 atm)). They revealed that nitrogen was heated in two stages: a short stage with a duration of about 30 μs, during which nearly 10% of the deposited energy was released, was followed by a longer stage with a duration of about 500 μs, during which the energy release amounted to about 38%. Based on the results of theoretical investigations, Baiadze *et al.* [11] explained the longer stage of gas heating by the model of VV exchange in a system of anharmonic oscillators. At the same time, they failed to explain the experimental data on rapid heating in terms of the relaxation of the rotational energy of gas particles or the elastic collisions between the electrons and gas particles. However, they noted that the rapid gas heating may be a consequence of the energy release during the quenching of the electronically excited states of nitrogen molecules. Analogous results were obtained in [12, 13] for broader ranges of the released energy.

A major series of investigations [14, 15] was devoted to determining the temperature of molecular gases in pulsed microwave discharges. Most of the

1063-780X/01/2710-0886$21.00 © 2001 MAIK "Nauka/Interperiodica"

measurements were carried out in nitrogen and air in the pressure range P = 10–40 torr for an effective reduced electric field E_e/N ranging from 80 to 250 Td (here, $E_e = \frac{E\nu}{\sqrt{2(\nu^2 + \omega^2)}}$, where ν is the effective electron collision frequency and E and ω are the amplitude and frequency of the microwave field). The gas temperature in the discharge volume was determined from the relative intensity of the lines (0, 2) of the rotational spectrum of the second positive nitrogen system. In the postdischarge stage, the heating was investigated with the help of the second, lower power diagnostic pulse, which made it possible to record the emission intensity of the 2^+ system of N_2 molecules without changing the gas temperature. It should be noted that Berdyshev *et al.* [14] additionally determined the gas temperature by measuring the relative population of the rotational levels of the ground state of NH_2 radicals (from the absorption of laser light in the visible spectrum). Also, the experiments of [14, 15] were aimed at measuring the electron density and other parameters of the discharge plasma.

The results obtained in the cited experiments with microwave discharges confirmed earlier conclusions that there exists a mechanism for the rapid heating of a molecular gas at a strong reduced electric field E/N. Aleksandrov *et al.* [15] also showed that the heating rate increases with gas pressure and substantially increases with E/N.

Based on the analysis of the available experimental data, most researchers attribute rapid gas heating during the discharge to energy relaxation in the quenching processes of the electronically excited nitrogen molecules. The quenching processes may serve to explain the rapid heating at a strong reduced electric field E/N, when the fraction of the deposited energy that is expended on the excitation of the electronic states of molecules is large.

In [14, 15], it was supposed that the mechanism for rapid gas heating is associated with the self-quenching of the excited molecules $N_2(A^3\Sigma_u^+)$:

$$N_2(A^3\Sigma_u^+) + N_2(A^3\Sigma_u^+) \longrightarrow N_2(X^1\Sigma_g^+) + N_2(B^3\Pi_g, C^3\Pi_u) + \varepsilon_R.$$

However, the mechanism proposed in [14, 15] fails to explain the full set of experimental data. Thus, Bogatov *et al.* [16], who measured not only the gas temperature but also the concentration of $N_2(A^3\Sigma_u^+)$ molecules, emphasized that the experimental data on the dynamics of the gas temperature cannot be explained in terms of this mechanism. It is also well known that the concentrations of $N_2(A^3\Sigma_u^+)$ molecules in air and nitrogen differ by several times because, in air, the $N_2(A^3\Sigma_u^+)$ molecules are efficiently quenched by oxygen. Consequently, the gas heating rate should be lower in mixtures with higher oxygen contents. However, this conclusion contradicts the available experimental data [14–16].

The heat release processes associated with the quenching of vibrational-electronic levels of nitrogen molecules were studied by Bezmenov *et al.* [17] under the assumption that, during the quenching of high-lying electronic levels of nitrogen molecules, up to the levels $N_2(A^3\Sigma_u^+, v = 3.4)$ with an excitation energy of 6.6 eV, the deposited energy is entirely expended on gas heating. In other words, during the quenching of, e.g., the $N_2(a^1\Pi_g)$ state with an excitation energy of 8.6 eV, about 2 eV of the deposited energy should be expended on gas heating. However, the assumption made in [17] contradicts the experimental data obtained in [18, 19] (as well as some other papers), where it was shown that the electronic-vibrational transitions in molecular nitrogen are accompanied by a minimum energy transfer into the translational degrees of freedom of the reaction products.

Hence, at present, there exist several models for heat release [15, 17]. Although the processes underlying these models are poorly investigated, the models nevertheless make it possible to explain some of the experimental data on rapid gas heating in microwave discharges.

This paper is devoted to the development of a model of kinetic processes that occur in nitrogen–oxygen mixtures excited by a gas discharge. The gas heating is described with allowance for the processes of electron-impact dissociation of N_2 and O_2 molecules, quenching of electronically excited nitrogen molecules by oxygen molecules, and quenching of the metastable atoms $O(^1D)$ by N_2 molecules. The results of calculations are compared with the available experimental data.

2. DESCRIPTION OF THE MODEL

The proposed kinetic model is aimed at describing the dynamics of the main components of a nitrogen–oxygen mixture excited by a discharge with a relatively strong reduced electric field (when a significant fraction of the discharge energy is expended on the excitation of the electronic states of molecules). It is assumed that, under the conditions adopted in the model, the gas particles in the discharge are excited from the ground electronic state mainly by electron impact. The dependences of the rates of the corresponding processes on the reduced electric field E/N and the degree of vibrational excitation of molecules are taken from [20–22]. The main reactions involving neutral particles and related rate constants are presented in [20, 23–25].

Table

No.	Reaction	Rate constant	References
1	$N_2(A^3\Sigma_u^+) + O_2 \longrightarrow N_2(v) + 2O(^3P) + \varepsilon_1$	1.7×10^{-12} cm^3/s	[28, 29]
2	$N_2(A^3\Sigma_u^+) + O_2 \longrightarrow N_2(v) + O_2(b^1\Sigma_g^+, v)$	7.5×10^{-13} cm^3/s	[28, 29]
3	$N_2(A^3\Sigma_u^+) + N_2(A^3\Sigma_u^+) \longrightarrow N_2(v) + N_2(B^3\Pi_g)$	7.7×10^{-11} cm^3/s	[30]
4	$N_2(A^3\Sigma_u^+) + N_2(A^3\Sigma_u^+) \longrightarrow N_2(v) + N_2(C^3\Pi_u)$	1.6×10^{-10} cm^3/s	[31]
5	$N_2(A^3\Sigma_u^+) + N_2(v' > 4) \longrightarrow N_2(v) + N_2(B^3\Pi_g)$	$10^{-10}\exp(-1500/T)$ cm^3/s	[20]
6	$N_2(A^3\Sigma_u^+) + O(^3P) \longrightarrow N_2(v) + O(^1S)$	3.0×10^{-11} cm^3/s	[32]
7	$N_2(B^3\Pi_g) + O_2 \longrightarrow N_2(v) + 2O(^3P) + \varepsilon_7$	3.0×10^{-10} cm^3/s	[20]
8	$N_2(B^3\Pi_g, v = 0) + N_2 \longrightarrow N_2(A^3\Sigma_u^+) + N_2(v)$	1.0×10^{-11} cm^3/s	[30, 20]
9	$N_2(a'^1\Sigma_u^-) + O_2 \longrightarrow N_2(v) + O(^3P) + O(^1D) + \varepsilon_9$	2.8×10^{-11} cm^3/s	[33]
10	$N_2(a'^1\Sigma_u^-) + N_2 \longrightarrow N_2(v) + N_2(v)$	2.0×10^{-13} cm^3/s	[33]

The dynamics of gas heating during the discharge was modeled with allowance for the following processes.

1. Recombination of Molecular Ions with Electrons

$$e + O_2^+ \longrightarrow O(^3P) + O(^1D) + \varepsilon_R,$$
$$e + NO^+ \longrightarrow O(^3P) + N(^2D) + \varepsilon_R,$$
$$e + N_2^+ \longrightarrow N(^4S) + N(^2D) + \varepsilon_R.$$

The energy released in these reactions is distributed between the electronic and translational degrees of freedom of the produced atoms. Thus, in the electron–ion dissociative recombination reactions involving O_2^+ and N_2^+ ions, the quantity ε_R should be about 5 eV and 3.5 eV, respectively. However, for $E/N \le 300$ Td, these reactions do not play a governing role in gas heating because the energy expended on exciting the molecules is relatively low.

2. Dissociation of Nitrogen and Oxygen Molecules by Electron Impact

$$e + N_2 \longrightarrow e + N_2^*, \quad N_2^* \longrightarrow N(^4S) + N(^2D) + \varepsilon_R,$$
$$e + O_2 \longrightarrow e + O_2(B^3\Sigma_u^-, v),$$
$$O_2(B^3\Sigma_u^-, v) \longrightarrow O(^3P) + O(^1D) + \varepsilon_R,$$
$$e + O_2 \longrightarrow e + O_2(A^3\Sigma_u^+, C^3\Delta_u),$$
$$O_2(A^3\Sigma_u^+, C^3\Delta_u) \longrightarrow O(^3P) + O(^3P) + \varepsilon_R.$$

The N_2 and O_2 molecules are dissociated during a preliminary dissociation of the electronic states of these molecules [20], which are excited from the ground state by electron impact. The kinetic energy of the products of preliminary dissociation reactions may be significant (this is evidenced by the behavior of the vibrational and electronic terms of the N_2 and O_2 molecules [26, 27]).

3. Quenching of the Electronically Excited States of Nitrogen Molecules by Oxygen Molecules

These quenching processes are also accompanied by the population of the excited states $O_2(B^3\Sigma_u^-, v)$, $(A^3\Sigma_u^+, v)$, $O_2(c^1\Sigma_u^-, v)$, etc., of oxygen molecules. A preliminary dissociation of these states leads to the dissociation of O_2 molecules and the transfer of the excess energy into the translational degrees of freedom of the produced oxygen atoms. In turn, "hot" oxygen atoms are thermalized during several collisions; the energy released in these collisions is expended on the rotational excitation of molecules and gas heating. The rotational energy relaxes into the translational degrees of freedom during 10–30 collisions [20]. Hence, we can see that essentially all of the kinetic energy of the atoms produced in the quenching processes fairly rapidly goes into heating the gas mixture.

The main reactions of quenching of electronically excited states of N_2 molecules in nitrogen–oxygen mixtures are listed in the table.

It should be noted that the relative role of the dissociation and excitation of the bound states of oxygen molecules was investigated only for the reaction of

quenching of the vibrationally excited state $N_2(A^3\Sigma_u^+)$ [28] (see reactions 1 and 2 in the table). It is also well known that an increase in the population of the vibrational state $N_2(A^3\Sigma_u^+)$ may change not only the total rate constant of reactions 1 and 2 [29] but also the relative role of these reactions (in particular, the reactions of the dissociation of O_2 molecules begin to play a more important role in gas heating).

The reactions of the dissociation of O_2 molecules can also involve the electronically excited triplet states $N_2(B^3\Pi_g,\ B'^3\Sigma_u^-,\ W^3\Delta_u)$, which are efficiently produced from the ground state by electron impact. Incorporating the resonant nature of the energy exchange between the levels of these states [18–20] into the model makes it possible to describe the processes of oxygen dissociation by introducing the effective state $N_2(B)$, whose population rate is determined by the total concentration of molecules in these electronically excited states and whose quenching rate is determined from the corresponding data on the molecular state $N_2(B^3\Pi_g)$.

Analogous considerations are also valid for the excited singlet states $N_2(a^1\Pi_g,\ a'^1\Sigma_u^-,\ w^1\Delta_u)$ [34], which can be described in terms of the effective state $N_2(a)$. The quenching rate of the $N_2(a)$ state is set equal to that of the $N_2(a'^1\Sigma_u^-)$ state [33]. An analysis of the scheme of electronic terms of the singlet states of nitrogen molecules (Fig. 1) makes it possible to suggest that O_2 molecules that quench these excited states will be dissociated primarily by nitrogen molecules in the $B^3\Sigma_u^-$ state.

The amount ε_R of the energy that is transferred to the translational degrees of freedom of the products of reactions 1, 7, and 9 is determined from the scheme of the electronic terms of N_2 and O_2 molecules [26, 27]. A fragment of this scheme is shown in Fig. 1. Let us consider as an example reactions 1 and 9 of quenching of the states $N_2(A^3\Sigma_u^+)$ and $N_2(a'^1\Sigma_u^-)$ by oxygen molecules.

The state $N_2(a'^1\Sigma_u^-)$ is quenched in the reactions

$$N_2(a'^1\Sigma_u^-) + O_2(X^3\Sigma_g) \Leftrightarrow N_2(X^1\Sigma_g^+) + O_2(B^3\Sigma_u^-,\ v^*),$$

$$O_2(B^3\Sigma_u^-,\ v^*) \longrightarrow O(^3P) + O(^1D) + \varepsilon_9.$$

According to Fig. 1, the energy of the state $O_2(B^3\Sigma_u^-,\ v^*)$ is about $\varepsilon_a \simeq 8.48$ eV. The dissociation limit $O(^3P) + O(^1D)$ of the term $O_2(B^3\Sigma_u^-,\ v)$ is characterized by the energy $\varepsilon_d = 7.08$ eV; consequently, we have $\varepsilon_9 = \varepsilon_a - \varepsilon_d \simeq 1.4$ eV. Since, among the products of the reaction of quenching of the state $N_2(A^3\Sigma_u^+)$, no oxygen molecules in the excited state $O_2(B^3\Sigma_u^-,\ v)$ were recorded [35], it is presumably the $O_2(c^1\Sigma_u^-,\ v)$ state that is mainly populated in reaction 1 (Fig. 1). A preliminary dissociation of this state governs the gas heating in reaction 1, in which case we have $\varepsilon_A \simeq 6.22$ eV, $\varepsilon_d \simeq 5.12$ eV, and $\varepsilon_1 \simeq 1.1$ eV.

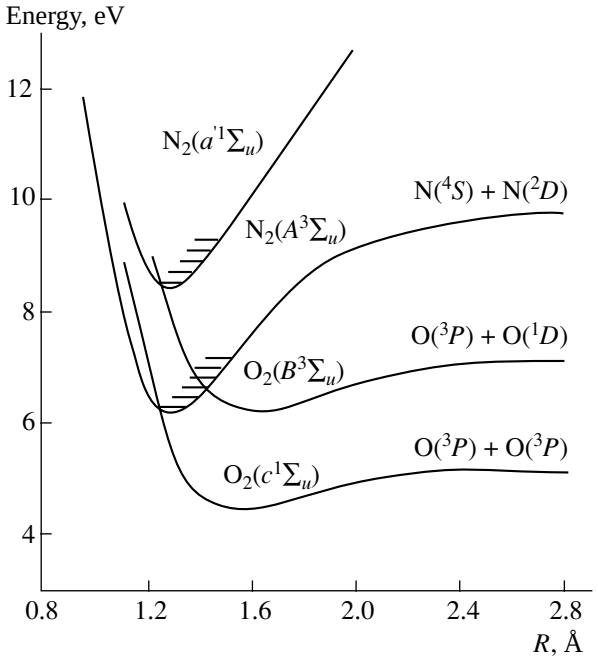

Fig. 1. Scheme of the electronic terms of N_2 and O_2 molecules [26, 27].

For a high degree of dissociation of O_2 molecules, it is necessary to take into account the quenching of the electronically excited nitrogen molecules by oxygen atoms. For nitrogen molecules in the state $N_2(A^3\Sigma_u^+)$, this quenching process was investigated in detail in [32, 36]. The data on the rate constants of quenching of the other metastable states of N_2 molecules by oxygen atoms are lacking. However, the role of other processes in the quenching of the electronic states under consideration seems to be less important, because these states are quenched by oxygen molecules far more rapidly than the state $N_2(A^3\Sigma_u^+)$ (see table).

4. Quenching of the Excited Atoms O(¹D)

The excited oxygen atoms $O(^1D)$ are produced in a significant number of reactions in which the O_2 molecules are dissociated. The excited atoms $O(^1D)$ are quenched primarily by O_2 and N_2 molecules:

$$O(^1D) + N_2 \longrightarrow O(^3P) + N_2(v) + \varepsilon_R,$$

$$O(^1D) + O_2 \longrightarrow O(^3P) + O_2(b^1\Sigma_g^+,\ v = 2).$$

The quenching of the excited atoms $O(^1D)$ by nitrogen molecules was studied in a number of papers, in which it was shown that the quenching reaction proceeds through the formation of an intermediate complex. The quenching rates calculated in [37] and some other papers agree well with experimental data. Later measurements [38] confirmed the theoretical predictions that $30 \pm 10\%$ of the energy released in this exoergic reaction is expended on the vibrational excitation of N_2 molecules. In accordance with the results of those papers, the model is supplemented with the assumption that about 70% of the excitation energy of the metastable atoms $O(^1D)$ is expended on gas heating.

5. Reactions of the VT Relaxation of the Vibrational Levels $N_2(v)$

The most important among these reactions is the reaction of VT relaxation by the excited oxygen atoms $O(^3P)$:

$$N_2(v) + O(^3P) \longrightarrow N_2(v-1) + O(^3P) + \varepsilon_R.$$

These reactions make a significant contribution to the total rate of gas heating when the degree of dissociation of O_2 molecules is sufficiently high. For calculations, the rate constants of the VT relaxation reactions were taken from [39].

3. RESULTS OF CALCULATIONS

The gas heating dynamics was simulated for conditions corresponding to the experiments of [40, 41], which were aimed at investigating the heating of nitrogen–oxygen mixtures by high-current pulsed discharges initiated in a tube with the radius $R = 0.5$ cm at pressures $P = 0.4$–1 torr. The discharge current density was $j = 0.5$–10 A/cm^2, the pulse duration being $\tau \leq 100$ μs. The gas temperature was determined from the relative emission intensities of the lines of the rotational structure of the $(0 \longrightarrow 2)$ transition in the second positive nitrogen system, the time resolution being about 1 μs. This method made it possible to determine the rotational temperature of the $N_2(C^3\Pi_u)$ state. It was found that the time scale τ_{rot} on which this temperature became equal to the gas temperature was about the mean free time [20]. The method of relative line intensities can be used to measure the gas temperature under the condition

$$\tau_C > \tau_{rot} \simeq \nu_g^{-1}, \quad (1)$$

where τ_C is the lifetime of the $N_2(C^3\Pi_u)$ state and ν_g is the frequency of the gas-kinetic collisions. Since the radiative lifetime of the $N_2(C^3\Pi_u)$ state is about $\tau_C \simeq 36$ ns [20], condition (1) is satisfied for $P \geq 2$ torr.

However, it should be noted that condition (1) is not a necessary one [42]. In fact, the method of relative line intensities can also be applied when the state from which the excited state at hand is produced is in equilibrium with respect to the translational and rotational degrees of freedom and, additionally, when the law according to which the rotational distribution function changes during the excitation is known. Since the ratio of the rotational constants of the $N_2(X^1\Sigma_g^+)$ and $N_2(C^3\Pi_u)$ molecular states is on the order of unity and the rotational temperature of the ground state of nitrogen molecules is essentially always equal to the gas temperature, the latter quantity in the pressure range $P < 2$ torr can be determined by applying the method of relative line intensities to the 2^+ system of nitrogen molecules [42].

In the model proposed here, the evolution of the discharge parameters and the content of the $N_2 : O_2$ mixture is described by solving a set of balance equations for neutral and charged particles together with the equation for the electric field. For a given discharge current I, the electric field at each instant is determined from the equation

$$E = \frac{I}{2\pi e \int_0^R N_e(r)\mu_e(r) r dr}, \quad (2)$$

where $N_e(r)$ and $\mu_e(r)$ are the radial profiles of the electron density and electron mobility.

The electron density is calculated from the equation

$$\frac{\partial N_e}{\partial t} = \frac{1}{r}\frac{\partial}{\partial r}\left(r D_a \frac{\partial N_e}{\partial r}\right) + N_e(\nu_{ion} - \nu_{att}) - Q_{rec} + Q_{det}. \quad (3)$$

Here, D_a is the ambipolar diffusion coefficient; ν_{ion} is the ionization rate; ν_{att} is the electron attachment rate; Q_{rec} is the electron–ion recombination rate; and the rate constant Q_{det} accounts for all the processes of electron detachment from negative ions by $O(^3P)$ atoms, metastable $O_2(a^1\Delta_g)$ molecules, etc. [23]. The model includes analogous balance equations for the charged particles of all species, specifically, the following ten species of positive and negative ions: O_2^+, O_4^+, $O_2^+ \cdot N_2$, N_2^+, N_4^+, NO^+, O^-, O_2^-, O_3^-, and O_4^-.

The dynamics of the gas temperature is described by the equation

$$C_v N \frac{\partial T}{\partial t} = \frac{1}{r}\frac{\partial}{\partial r}\left(r\lambda\frac{\partial T}{\partial r}\right) + \frac{\varepsilon_v - \varepsilon_v(T)}{\tau_{VT}} + W_R. \quad (4)$$

Here, C_v is the specific heat capacity of the gas at a constant volume, $\lambda(T)$ is the thermal conductivity, N is the concentration of molecules in the mixture, ε_v is the mean vibrational energy per N_2 molecule, τ_{VT} is the characteristic time of the VT relaxation of $N_2(v)$, and W_R is the gas heating rate in chemical reactions. Equa-

tion (4) describes isochoric gas heating corresponding, in particular, to the experimental conditions of [40, 41], under which the discharges were initiated over almost the entire volume of the system.

The boundary conditions for Eqs. (3) and (4) were chosen to conform to the assumptions that the central region of the discharge is axisymmetric, the charged particles at the wall of the discharge tube are absent, and the gas temperature at the wall is equal to the temperature T_w of the wall material:

$$\left.\frac{\partial N_e}{\partial r}\right|_{r=0} = 0, \quad \left.\frac{\partial T}{\partial r}\right|_{r=0} = 0,$$
$$N_e|_{r=R} = 0, \quad T|_{r=R} = T_w.$$

Under the above conditions and for $P \simeq 0.5$ torr, $R = 0.5$ cm, and $T \simeq 800$ K ($\lambda = 5.7 \times 10^{-4}$ W/(cm K) [43]), the characteristic time during which the gas is cooled due to the heat conduction is about $\tau_R \simeq 18$ μs, which is appreciably shorter than the pulse duration [40]. For this reason, the equation for gas temperature is supplemented with the heat conduction term.

Kalinin *et al.* [41] measured not only the gas temperature but also the relative concentration of oxygen atoms as functions of time. The concentration of the excited atoms $O(^3P)$ was reconstructed by applying the method of [44] to the experimental data on the relative intensity I_0/I_{N_2}—the ratio of the intensity of the line emission from the transition $O(3p^3P \longrightarrow 3s^3S)$ to the intensity of the 2^+ band system $N_2(C^3\Pi_u,\ v = 0 \longrightarrow B^3\Pi_g)$ of nitrogen. The radiating states $O(3p^3P)$ and $N_2(C^3\Pi_u,\ v = 0)$ are excited from the ground states mainly by electron impact [44]; the threshold energies for the excitation of these states from the ground state are equal to 10.99 and 11.03 eV, respectively. The Einstein coefficients for the transitions in question are nearly the same and are approximately equal to 2.5×10^7 s^{-1} [45]. Also, the dependences of the excitation cross sections on the electron energy are close to one another, as well as the maximum values of the cross sections [20, 45]. Consequently, in the first approximation, it can be assumed that $[O(^3P)] \propto [N_2] \cdot I_0/I_{N_2}$. The relative concentrations of oxygen atoms that were found as functions of time in the above manner in [41] are shown in Fig. 2 for $P = 0.4$ torr and $j = 1$ A/cm^2 and for different oxygen contents δ of the mixture. For comparison with the calculated results (which are illustrated in Fig. 2 by solid curves), the corresponding relative concentrations are multiplied by 6×10^{14} cm^{-3}. One can see that, regardless of the oxygen content of the mixture, the calculated results correlate reasonably well with the experimentally recorded dynamics of the concentration of oxygen atoms.

Figure 3 illustrates the results of modeling the dynamics of the main excited components at the axis of a discharge in air for the experimental conditions of [40, 41] and for $P = 0.5$ torr and $j = 2$ A/cm^2. A decrease in the concentration of nitrogen molecules in the excited state $N_2(A^3\Sigma_u^+)$ at $t \geq 30$ μs is associated with the production of atomic oxygen and an increase in the rate of quenching of this state in reaction 6. On time scales $t \geq 7$–10 μs, the concentrations $[O(^1D)]$, $[N_2(A^3\Sigma_u^+)]$, and $[N_2(a'^1\Sigma_u^-)]$ of the excited particles that take part in gas heating change insignificantly. Consequently, on these time scales, the gas heating rate

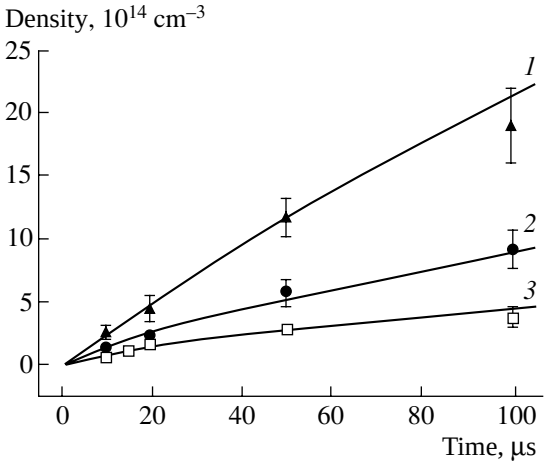

Fig. 2. Dynamics of the density of $O(^3P)$ atoms at the axis of a discharge in an $N_2 : O_2$ mixture for $P = 0.4$ torr; $j = 1$ A/cm^2; and different oxygen contents in the mixture, δ = (*1*) 20, (*2*) 8.5, and (*3*) 4%. The symbols refer to the experimental data of [41], and the solid curves show the numerical results.

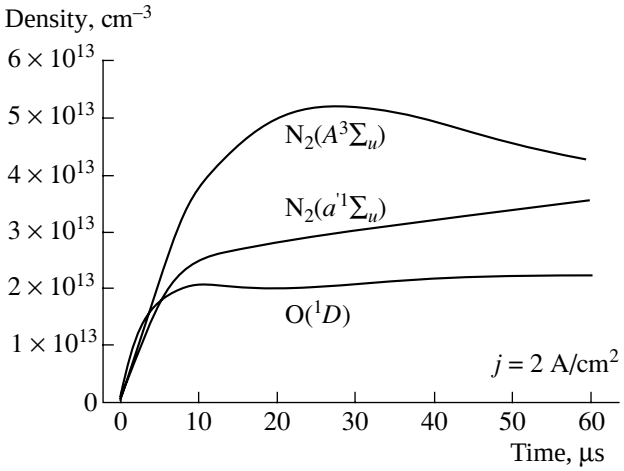

Fig. 3. Dynamics of the main excited components at the axis of a discharge in air for $P = 0.5$ torr and $j = 2$ A/cm^2.

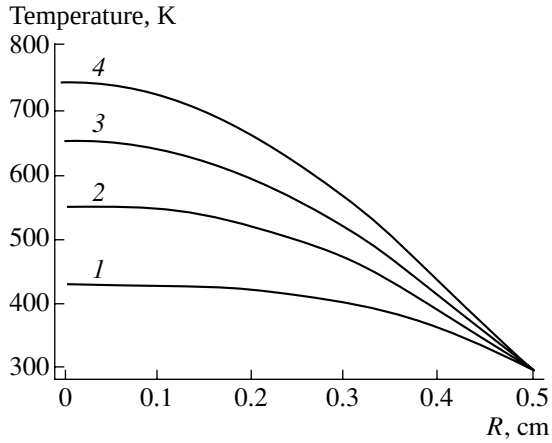

Fig. 4. Radial profiles of the air temperature calculated under the experimental conditions of [40, 41] for P = 0.5 torr and j = 2 A/cm^2 at t = (*1*) 10, (*2*) 20, (*3*) 30, and (*4*) 40 μs.

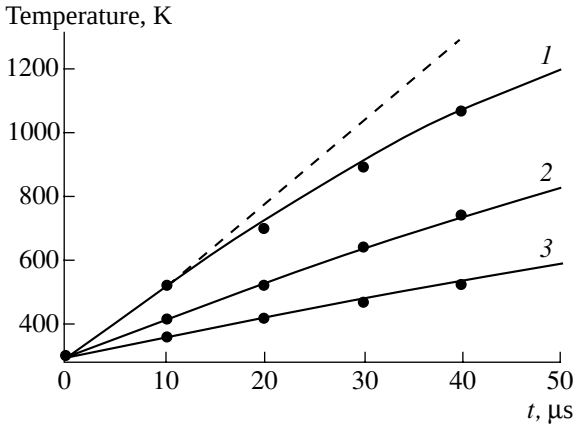

Fig. 5. Dynamics of the gas heating at the discharge axis for R = 0.5 cm; P = 0.5 torr; and different discharge current densities: (*1*) 4, (*2*) 2, and (*3*) 1 A/cm^2. The closed circles refer to the experimental data of [40], and the results calculated with and without allowance for heat conduction are shown by the solid curves and the dashed curve, respectively.

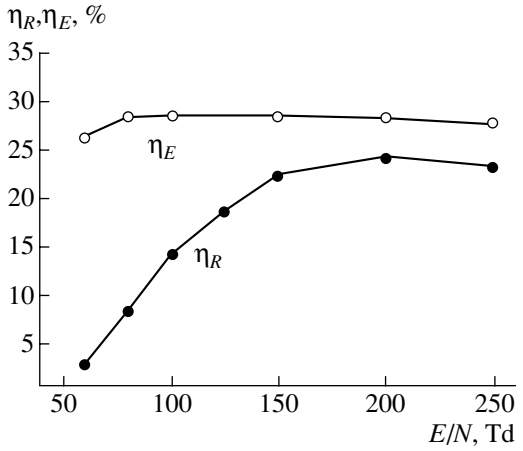

Fig. 6. Parameters η_R and η_E as functions of E/N in a discharge in an $N_2 : O_2 = 4 : 1$ mixture.

should be expected to be approximately constant, $\partial W_R/\partial t \simeq$ const.

Figure 4 displays radial profiles of the gas temperature calculated at different times for the experimental conditions of [40, 41] and for P = 0.5 torr and j = 2 A/cm^2. In the axial region of the discharge, the gas temperature in the radial direction changes only slightly. Presumably, the experimentally measured temperatures correspond to those in the central discharge region.

Figure 5 compares the experimental data of [40] and the results of numerical calculations of the dynamics of air heating near the discharge axis for P = 0.5 torr. Curves *1–3* were calculated for the discharge current densities j = 4, 2, and 1 A/cm^2, respectively. The dashed curve was calculated for j = 4 A/cm^2 without allowance for gas cooling via heat conduction. We can see that the results of calculations based on the proposed model adequately describe the experimental data. The effect of heat conduction becomes important for gas temperatures $T \geq$ 700–800 K.

Note that, under the conditions adopted in the model, an important role is played by the heterogeneous quenching of the excited particles at the wall of the discharge tube. The excited particles are quenched mostly in the diffusive regime. Thus, the rate of the heterogeneous quenching of $N_2(A^3\Sigma_u^+)$ molecules, which play a significant role in gas heating, is equal to

$$\nu_{\text{het}} = D_A\left(\frac{2.4}{R}\right)^2 \simeq 7 \times 10^3 \text{ s}^{-1}, \qquad (5)$$

where $D_A \simeq$ 310 cm^2/s is the diffusion coefficient for $N_2(A^3\Sigma_u^+)$ molecules in air at the pressure P = 0.5 torr [46]. Under the experimental conditions of [40, 41], the rate ν_{het} is comparable in magnitude to the volume quenching rates for $N_2(A^3\Sigma_u^+)$ molecules. The measured probabilities of quenching of the excited $N_2(A^3\Sigma_u^+)$ molecules at the walls of the discharge tubes made of different materials were found to be close to unity. According to [46], such high probabilities indicate that the fraction of energy that is released during the heterogeneous quenching of $N_2(A^3\Sigma_u^+)$ molecules and is expended on heating the gas and the wall will unlikely be high. For this reason, the heterogeneous quenching processes were not incorporated into the model for rapid gas heating.

For a simplified description of heat release in the discharge, it is worthwhile to analyze the behavior of the plasma parameters

$$\eta_R = \frac{W_R}{jEN}, \quad \eta_E = \frac{\eta_R}{\mu_E}.$$

Here, η_R and μ_E are the fractions of the discharge power that are expended on gas heating and the electronic excitation of molecules, respectively, and η_E is the fraction of the energy of the electronic degrees of freedom of molecules that is expended on gas heating. Figure 6 presents the parameters η_R and η_E calculated as functions of the reduced electric field in the discharge. We can see that the parameter η_E changes only slightly with E/N (as well as with the electron density and gas pressure). That is why this parameter can be used for a simplified description of gas heating in discharges.

The parameter $\eta_R(E/N)$, which describes the role of rapid gas heating in the overall energy balance of the discharge, decreases sharply with E/N (Fig. 6). In this case, the fraction of the discharge energy that is expended on the vibrational excitation of molecules increases [20] and, accordingly, the role of VT relaxation reactions becomes greater. However, in relatively weak electric fields such as E/N = 50–70 Td, the processes responsible for rapid gas heating may significantly influence the dynamics of the gas temperature. The reason for this influence is that the rate constants of the vibrational–translational exchange reactions depend strongly on the gas temperature [1]. Consequently, even an insignificant heating of the gas mixture in the initial stage of the discharge may have a great effect on the dynamics of the subsequent VT relaxation processes.

In [47], Klimov *et al.* presented the results of measurements of the gas temperature as a function of time in pulsed glow discharges with the current density j = 125 mA/cm^2 in air at the pressure P = 6 torr, the diameter of the discharge tube being $2R$ = 3 cm. In those experiments, the radial profiles and temporal behavior of the gas temperature were investigated by means of optical interferometry.

The model presented here was also tested by modeling gas heating in discharges with the parameters described in [47]. Under the experimental conditions of that paper, the reduced electric field lies within the range 50–70 Td and the bulk of the discharge energy is expended on the vibrational excitation of nitrogen molecules. Consequently, the gas is heated most efficiently in the reactions of VT relaxation on oxygen atoms. Figure 7 shows the radial profiles of the gas temperature calculated at different times. Under the experimental conditions of [47], heat conduction plays an insignificant role, so that the temperature profiles $T(r)$ follow the corresponding radial profiles of the deposited energy.

Figure 8 illustrates the experimental data of [47] and the related numerical results on the dynamics of the gas temperature near the discharge axis. We can see that the results obtained from the complete model, i.e., with allowance for rapid gas heating due to the relaxation of the electronically excited states of nitrogen molecules (curve *1*), agree well with the experimental data. For comparison, the time evolution of the temperature of the gas heated only via the processes of VT relaxation on oxygen atoms (the rapid gas heating is not taken into account) is also shown (curve *2*). In this case, the time delay in gas heating in the discharge volume amounts to 500–600 μs.

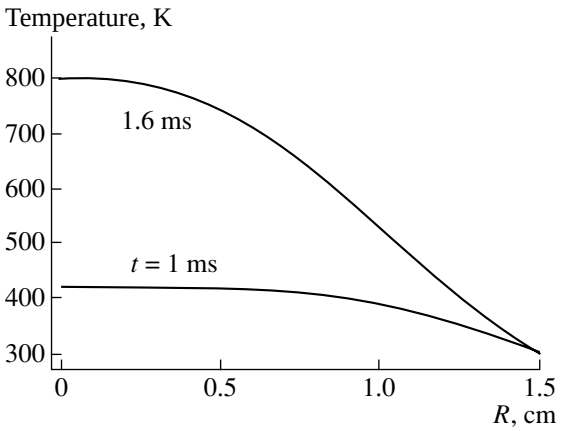

Fig. 7. Radial profiles of the gas temperature calculated under the experimental conditions of [47] for P = 6 torr and j = 125 mA/cm^2 at t = 1 and 1.6 ms.

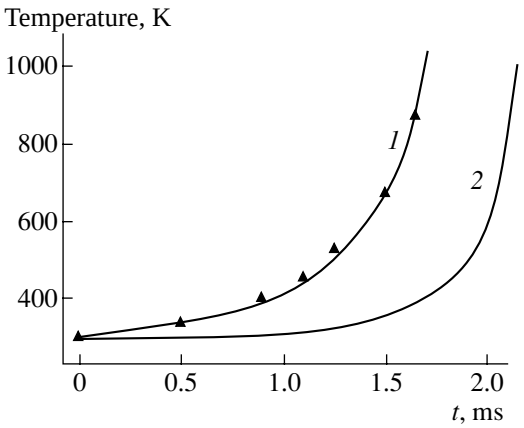

Fig. 8. Dynamics of the gas temperature at the axis of a glow discharge with the current density j = 125 mA/cm^2 in air at the pressure P = 6 torr. The closed triangles refer to the experimental data of [47], and the results calculated with and without allowance for rapid gas heating are shown by curves *1* and *2*, respectively.

In the proposed model of gas heating, an important role is played by reactions involving oxygen molecules. For this reason, the parameter η_E and the gas heating rate are expected to change with the oxygen content δ of the mixture. Figure 9 illustrates the experimental data of [41] and the results from calculations of the gas heating rate as a function of the oxygen content of an $N_2 : O_2$ mixture for P = 0.4 torr and j = 1 A/cm^2. The calculations based on the presented model (solid line) agree satisfactorily with experiments for mixtures with an oxygen content $\delta \geq 4\%$. However, for a low oxygen

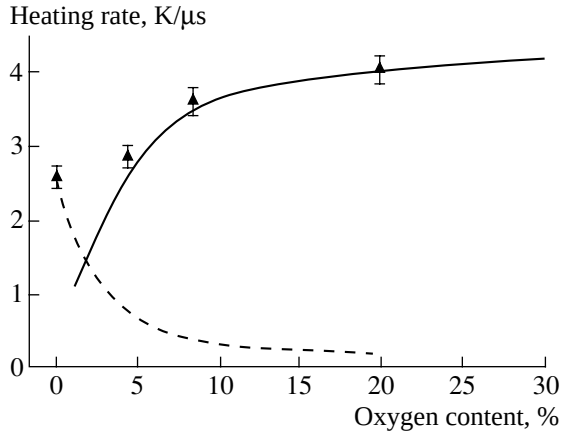

Fig. 9. Gas heating rate as a function of the oxygen content δ in the mixture for $P = 0.4$ torr and $j = 1$ A/cm^2. The symbols refer to the experimental data of [41], and the curves show the numerical results.

content δ, disagreement between the numerical results and the experimental data is far greater. This disagreement indicates that, in pure nitrogen with no O_2 admixtures, there may be an additional mechanism for gas heating. The dashed curve in Fig. 9 illustrates the calculations of the gas heating rate in reaction 3 with $\varepsilon_3 \simeq 4$ eV. Recall that this reaction is one of the processes underlying the model of rapid gas heating that was developed in [15, 40, 41] for nitrogen–oxygen mixtures. Reaction 3 makes it possible to explain the data of experiments with discharges in nitrogen with small O_2 admixtures. However, for mixtures with a higher oxygen content, the discrepancy with the experimental data becomes very significant, because, in reaction 3, the excited molecules $N_2(A^3\Sigma_u^+)$ are efficiently quenched by oxygen molecules.

However, special emphasis should be placed on the substantial disagreement between the results obtained in different experimental investigations of the rapid heating of nitrogen. The experiments of [14, 15] were aimed at studying nitrogen heating in microwave discharges at pressures $P = 10$–40 torr, the reduced electric field being $E/N \simeq 80$–150 Td. In those experiments, in which the total energy deposition amounted to 1.6 J/(cm^3 atm), the increment ΔT in the nitrogen temperature was measured to be higher than 450 K. On the other hand, in high-current pulsed discharges with energy depositions higher than 1 J/(cm^3 atm) in nitrogen at pressures $P = 115$ torr [48] and $P = 60$ torr [49] and at reduced electric fields in the range $E/N = 150$–200 Td, nitrogen was found to be heated insignificantly, $\Delta T \simeq 20$ K. In [48], Valyanskiĭ *et al.* determined the rotational distribution function from the spectrum of the Q-branch of the transition $v = 0 \longrightarrow 1$ in the 2^+ system of nitrogen molecules. They found that, 20 μs after the discharge came to an end, the distribution function was of the Boltzmann type, with the temperature $T = 320 \pm 20$ K. Analogous results were obtained by Devyatov *et al.* [49].

Akishev *et al.* [7] measured the fraction of energy that is expended on gas heating at reduced electric fields in the range $E/N = 40$–80 Td. They carried out experiments with self-sustained volume discharges in nitrogen of very high purity at pressures $P = 20$–80 torr. The experimental conditions were thoroughly controlled to keep the spatial distributions of the discharge parameters uniform. The gas temperature was reconstructed from the results of the interferometric measurements. Since, in the experiments of [7], the deposited energy was no higher than 0.25 J/(cm^3 atm), the gas-dynamic processes near the electrodes had an insignificant influence on the interferograms of a volume discharge plasma. It was found that, for $E/N \geq 75$ Td, the fraction of the deposited energy expended on gas heating did not exceed 1%. These results also contradict the experimental data of [14–16].

Hence, it seems that experimental data that can provide reliable and fairly complete information on rapid gas heating in microwave discharges in nitrogen are still lacking. That is why further investigations are required for an adequate description of rapid gas heating.

4. CONCLUSION

In this paper, a model has been developed that makes it possible to investigate the rapid heating of nitrogen–oxygen mixtures excited by microwave discharges. According to this model, the gas is heated mainly in the reactions of preliminary dissociation of highly excited electronic states of oxygen molecules that are produced either by electron impact or during the quenching of the excited states of N_2 molecules. The results of model calculations are found to adequately describe available experimental data on the dynamics of air heating in gas-discharge plasmas.

It is shown that, over a broad range of the reduced electric field E/N, the fraction of the discharge power that goes into heating the gas is fixed; specifically, it is the fraction that is expended on the excitation of the electronic degrees of freedom of molecules (for discharges in air, $\eta_E \simeq 28\%$). This circumstance can be used to simplify a description of heat sources in gas discharges. However, it should be noted that the condition $\eta_E = \text{const}$ may fail to hold for high degrees of dissociation of oxygen molecules (i.e., for high energy depositions), when the electronically excited nitrogen molecules are quenched primarily by $O(^3P)$ atoms. In this case, the reactions of VT relaxation on oxygen atoms may also play an important role in gas heating.

One of the calculated results, namely, the weak dependence of the parameter η_E on the gas pressure, seems to be especially important, because it characterizes the relative role of the mechanisms for rapid gas

heating and for gas heating in the VV and VT exchange processes. For prescribed values of N_e and E/N, the specific power of the heat released during the quenching of electronically excited nitrogen molecules is approximately constant, while the VT relaxation rate increases with gas pressure because of the increase in the concentration of $O(^3P)$ atoms. As a result, the contribution of the VT relaxation reactions to the total rate of gas heating should increase with gas pressure.

According to the model proposed, the lower the oxygen content in the mixture, the smaller the parameter η_E. For mixtures with an oxygen content $\delta \geq 4\%$, the results of the related model calculations agree with the experimental data. The question of the rapid heating of pure nitrogen or nitrogen with small oxygen admixtures remains open and requires further investigation. It is also of interest to study the heating of air at relatively strong reduced electric fields, E/N = 200–300 Td.

ACKNOWLEDGMENTS

I am grateful to K.S. Klopovskiĭ and T.V. Rakhimova for useful discussions. This study was supported in part by the Russian Foundation for Basic Research, project nos. 00-02-16508 and 00-15-96554.

REFERENCES

1. B. F. Gordiets, A. I. Osipov, and L. A. Shelepin, *Kinetic Processes in Gases and Molecular Lasers* (Nauka, Moscow, 1988).
2. V. D. Rusanov and A. A. Fridman, *Physics of Chemically Active Plasma* (Nauka, Moscow, 1984).
3. E. P. Velikhov, A. S. Kovalev, and A. T. Rakhimov, *Physical Phenomena in Gas-Discharge Plasma* (Nauka, Moscow, 1987).
4. S. V. Golubev, S. I. Gritsinin, V. G. Zorin, *et al.*, in *High-Frequency Discharge in Wave Fields* (Inst. Prikl. Fiz., Gorki, 1988), p. 136.
5. E. M. Bazelyan and Yu. P. Raizer, *Spark Discharge* (Mosk. Fiz. Tekh. Inst., Moscow, 1997 CRC, Boca Raton, 1998).
6. I. Gallimberty and A. Bondiou, J. Phys. D **27**, 1252 (1994).
7. Yu. S. Akishev, A. I. Zakharchenko, I. I. Gorodnicheva, *et al.*, Prikl. Mekh. Tekh. Fiz., No. 3, 10 (1981).
8. N. G. Basov, V. D. Zvorykin, I. B. Kovsh, *et al.*, Zh. Tekh. Fiz. **54**, 1294 (1984) [Sov. Phys. Tech. Phys. **29**, 746 (1984)].
9. A. A. Deryugin, D. S. Kotel'nikov, I. V. Kochetov, *et al.*, Fiz. Plazmy **12**, 1081 (1986) [Sov. J. Plasma Phys. **12**, 621 (1986)].
10. V. Yu. Baranov, F. I. Vysikaĭlo, A. P. Napartovich, *et al.*, Fiz. Plazmy **4**, 358 (1978) [Sov. J. Plasma Phys. **4**, 201 (1978)].
11. K. V. Baiadze, V. M. Vetsko, S. A. Zhdanok, *et al.*, Fiz. Plazmy **5**, 923 (1979) [Sov. J. Plasma Phys. **5**, 515 (1979)].
12. I. L. Kamardin, A. A. Kuchinskiĭ, V. A. Rodichkin, *et al.*, Teplofiz. Vys. Temp. **21**, 224 (1983).
13. I. L. Kamardin, A. A. Kuchinskiĭ, V. A. Rodichkin, *et al.*, Teplofiz. Vys. Temp. **23**, 653 (1985).
14. A. V. Berdyshev, A. L. Vikharev, M. S. Gitlin, *et al.*, Teplofiz. Vys. Temp. **26**, 661 (1988).
15. A. F. Aleksandrov, A. A. Kuzovnikov, and V. M. Shibkov, Inzh.-Fiz. Zh. **62**, 726 (1992).
16. N. A. Bogatov, M. S. Gitlin, S. V. Golubev, *et al.*, Fiz. Plazmy **13**, 629 (1987) [Sov. J. Plasma Phys. **13**, 364 (1987)].
17. I. V. Bezmenov, V. V. Rusanov, and V. P. Silakov, Preprint No. 30, IPM RAN (Moscow, 1992).
18. A. Rotem and S. Rosenwaks, Opt. Eng. **22**, 564 (1983).
19. R. Bachmann, X. Li, Ch. Ottinger, and A. F. Vilesov, J. Chem. Phys. **96**, 5151 (1992).
20. D. I. Slovetskiĭ, *Mechanisms for Chemical Reactions in Nonequilibrium Plasma* (Nauka, Moscow, 1980).
21. N. L. Aleksandrov, F. I. Vysikaĭlo, R. Sh. Islamov, *et al.*, Teplofiz. Vys. Temp. **19**, 22 (1981).
22. A. Kh. Mnatsakanyan and G. V. Naĭdis, in *Plasma Chemistry* (Énergoatomizdat, Moscow, 1987), Vol. 14, p. 227.
23. I. A. Kossyi, A. Y. Kostinsky, A. A. Matveev, and V. P. Silakov, Plasma Sources Sci. Technol. **1**, 207 (1992).
24. N. A. Popov, Fiz. Plazmy **20**, 334 (1994) [Plasma Phys. Rep. **20**, 303 (1994)].
25. Yu. S. Akishev, A. A. Deryugin, V. B. Karal'nik, *et al.*, Fiz. Plazmy **20**, 571 (1994) [Plasma Phys. Rep. **20**, 511 (1994)].
26. A. Lofthus and P. H. Krupenie, J. Phys. Chem. Ref. Data **6**, 288 (1977).
27. R. P. Saxon and B. Liu, J. Chem. Phys. **67**, 5432 (1977).
28. M. P. Iannuzzi, J. B. Jeffries, and F. Kaufman, Chem. Phys. Lett. **87**, 570 (1982).
29. A. R. DeSousa, M. Touzeau, and M. Petitdidier, Chem. Phys. Lett. **121**, 423 (1985).
30. L. G. Piper, J. Chem. Phys. **88**, 6911 (1988).
31. L. G. Piper, J. Chem. Phys. **88**, 231 (1988).
32. L. G. Piper, G. E. Caledonia, and J. P. Kennealy, J. Chem. Phys. **75**, 2847 (1981).
33. L. G. Piper, J. Chem. Phys. **87**, 1625 (1987).
34. W. J. Marinelli, B. D. Green, M. A. DeFaccio, *et al.*, J. Phys. Chem. **92**, 3429 (1988).
35. M. E. Fraser and L. G. Piper, J. Phys. Chem. **93**, 1107 (1989).
36. J. M. Thomas and F. Kaufman, J. Phys. Chem. **100**, 8901 (1996).
37. J. C. Tully, J. Chem. Phys. **62**, 1893 (1975).
38. T. G. Slanger and G. Black, J. Chem. Phys. **60**, 468 (1974).
39. A. Kh. Mnatsakanyan and G. V. Naĭdis, Teplofiz. Vys. Temp. **23**, 640 (1985).

40. A. P. Ershov, A. V. Kalinin, V. V. Lodinev, and V. M. Shibkov, in *Proceedings of the XX International Conference on Phenomena in Ionized Gases, Pisa, 1991*, Vol. 2, p. 379.

41. A. V. Kalinin, V. M. Shibkov, and L. V. Shibkova, Vestn. Mosk. Univ., Ser. 3: Fiz., Astron., No. 1, 38 (1996).

42. V. N. Ochkin, S. Yu. Savinov, and N. N. Sobolev, Tr. Fiz. Inst. Akad. Nauk SSSR **157**, 6 (1985).

43. *Handbook of Physical Quantities*, Ed. by I. S. Grigor'ev and E. Z. Meĭlikhov (Énergoizdat, Moscow, 1991).

44. A. S. Zarin, V. N. Kulikov, and V. E. Mitsuk, Pis'ma Zh. Tekh. Fiz. **12** (19), 1186 (1986) [Sov. Tech. Phys. Lett. **12**, 491 (1986)].

45. D. Pagnon, J. Amorim, J. Nahorny, *et al.*, J. Phys. D **28**, 1856 (1995).

46. O. V. Krylov and B. R. Shub, *Nonequilibrium Processes in Catalysis* (Khimiya, Moscow, 1990).

47. A. I. Klimov, G. I. Mishin, A. B. Fedotov, and V. A. Shakhatov, Pis'ma Zh. Tekh. Fiz. **15** (20), 31 (1989) [Sov. Tech. Phys. Lett. **15**, 800 (1989)].

48. S. I. Valyanskiĭ, K. A. Vereshchagin, V. Vernke, *et al.*, Kvantovaya Élektron. (Moscow) **11**, 1833 (1984).

49. A. A. Devyatov, S. A. Dolenko, A. T. Rakhimov, *et al.*, Zh. Éksp. Teor. Fiz. **90**, 429 (1986) [Sov. Phys. JETP **63**, 246 (1986)].

Translated by G. V. Shepekina

Plasma Physics Reports, Vol. 27, No. 10, 2001, pp. 897–900. Translated from Fizika Plazmy, Vol. 27, No. 10, 2001, pp. 951–954.

LOW-TEMPERATURE PLASMA

Optical Characteristics of the Plasma of a Glow Discharge in a He/H_2O Mixture

A. K. Shuaibov, L. L. Shimon, A. I. Dashchenko, and I. V. Shevera

Uzhhorod National University, Pidgirna str. 46, Uzhhorod, 88000 Ukraine

Received February 13, 2001

Abstract—The emission from the plasma of a steady-state electric discharge in a He/H_2O mixture in the wavelength range 130–670 nm is investigated. It is shown that, at a water vapor partial pressure of P = 2.0–2.5 kPa, the discharge mainly emits within the range 306–315 nm. The emission consists of an OH (A–X; 0–0) 307.4-nm narrow peak and a broad band with a maximum at λ_{max} = 309.1 nm. As the partial pressure of water vapor decreases to 50–150 Pa, VUV emission at wavelengths of λ = 186, 180, and 157 nm becomes dominant. In the visible region, H_α 656.3-nm and H_β 486.1-nm spectral lines and HeI lines in the range 447.1–667.8 nm, which are of interest for diagnosing the plasma, prevail. The intensities of the main bands and spectral lines are determined as functions of the helium partial pressure and discharge current. © *2001 MAIK "Nauka/Interperiodica".*

1. INTRODUCTION

Water vapor plasmas have been extensively studied in plasmochemistry for the purpose of hydrogen production [1]. Small admixtures of water vapor may substantially affect the output parameters of some gas lasers [2] and the performance of electric discharge systems for cleaning air of toxic agents [3, 4]. At large concentrations of water vapor ($\geq 10^{17}$ cm^{-3}) in air/H_2O mixtures, the plasma is overcooled and the production of long-lived ($t \geq 1$ s) plasma structures, like ball lightning, is possible [5]. Most attention in these studies has been concentrated on plasmas of air/H_2O and air/H_2O/CO_2 mixtures. Recently, it was shown that an ecologically safe, highly efficient ($\eta \geq 25\%$) lamp based on the OH (A–X; 0–0) 306.4-nm transition in the plasma of a glow (or an RF) discharge in He(Ar)/H_2O mixtures can be created. These experiments dealt with the optical and energy characteristics of the plasma in the 300- to 1000-nm wavelength range at low water vapor partial pressures ($P \leq 50$ Pa). In the short-wavelength spectral range or at higher water vapor partial pressures, the optical characteristics of the plasma of a glow discharge in the mixtures of noble gases with water vapor have been studied insufficiently. Under these conditions, the water clusters $(OH)_n \cdot (H_2O)_m$ and combined clusters like $Ar_n \cdot (H_2O)_m$ are of importance [6, 7]; however, their influence on the optical characteristics of an electric discharge plasma has not yet been studied.

In this paper, we present the results of studies of the emission from water vapor–helium plasmas.

2. EXPERIMENTAL SETUP

A dc glow discharge was ignited in a quartz tube with an inner diameter of 7 mm. The distance between the hollow cylindrical electrodes made of Ni foil was 50mm. A discharge tube with open ends was placed in a 10-liter buffer chamber connected (via a CaF_2 window) to a half-meter-long vacuum monochromator with a spectral resolution of 0.7 nm. The emission from the 6-mm-diameter central part of the cross section of the discharge tube was recorded. The emission from the other end of the tube in the visible and near UV spectral regions was recorded with the help of a monochromator (MDR-2)–photomultiplier (FEU-106) system. The emission was focused on the monochromator entrance slit with a quartz lens. The spectral resolution of the MDR-2 monochromator was 0.2 nm. The spectrometers were calibrated in the wavelength range 165–680 nm with the help of a band lamp and the continuous emission of molecular hydrogen. The data obtained for the 165- to 350-nm range were used to approximate the spectral sensitivity of the vacuum monochromator in the 130- to 165-nm range. The recording system is described in detail in [8, 9]. The glow discharge was powered from a high-voltage dc power supply ($U \leq$ 30 kV, $I \leq$ 100 mA). The discharge current varied within the range 2–50 mA, and the power deposited in the discharge was 40–60 W. Saturated water vapor at room temperature was produced by placing a reservoir with distilled water into the buffer chamber. The pressure of the saturated water vapor was determined using the data from [10]. At T = 17–21°C, it was within the range 2.0–2.5 kPa. Unsaturated water vapor was supplied from a separate vessel into a mixing tank, in

1063-780X/01/2710-0897$21.00

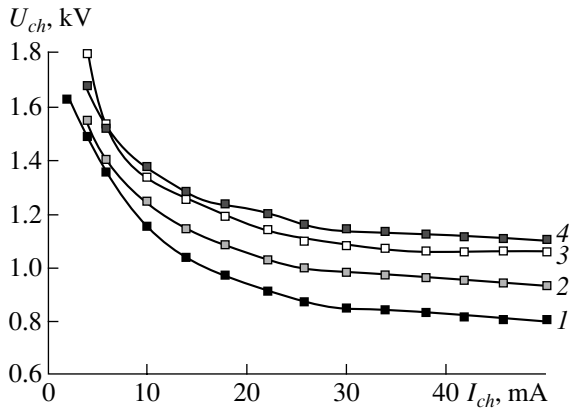

Fig. 1. Current–voltage characteristics of a glow discharge in (*1*) water vapor at a pressure of 2.5 kPa and in the (*2*) 2.0/2.5-kPa, (*3*) 4.0/2.5-kPa, and (*4*) 8.0/2.5-kPa He/H_2O mixtures.

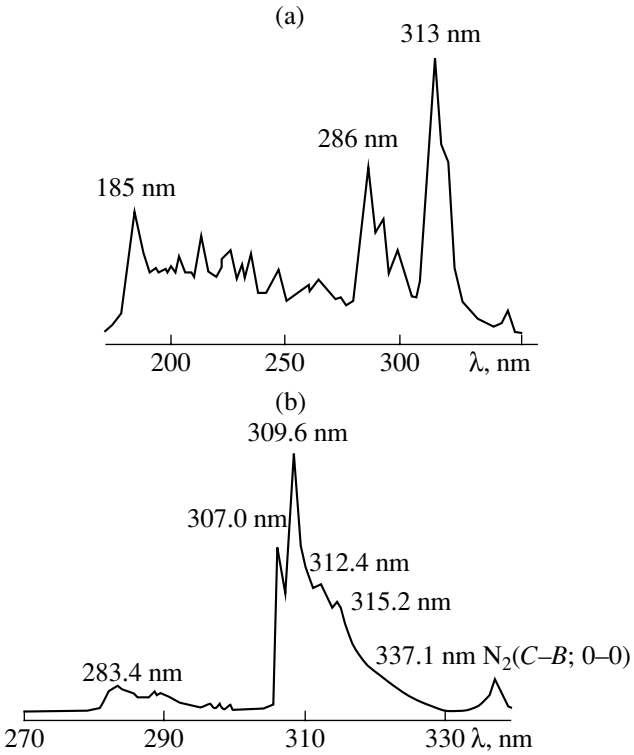

Fig. 2. VUV–UV emission spectra from the plasma of a glow discharge in a He/H_2O mixture.

which He/H_2O mixtures were also prepared. Then, the working mixture was puffed into the buffer chamber and the discharge tube.

3. ELECTRICAL AND OPTICAL CHARACTERISTICS

A glow discharge in saturated water vapor or He/H_2O mixtures was longitudinally homogeneous over the entire length of the discharge tube. The diameter of the discharge plasma was 3–4 mm; the distribution of the emission intensity over the tube radius was nonuniform, which was characteristic of a glow discharge in electronegative gases. The normal mode of the discharge operation, in which the discharge voltage depended only slightly on the discharge current, came into play at $I_{ch} \geq 25$–35 mA (Fig. 1). At low currents, the discharge operated in the subnormal mode [11]. In the normal mode of the discharge in He/H_2O = (1.0–8.0)/(2.0–2.5)-kPa mixtures, the value of U_{ch} increased from 930 to 1100 V with increasing helium pressure. In our experiments, U_{ch} was one order of magnitude higher and I_{ch} was one order of magnitude lower than those in [7, 12], respectively, although the average powers deposited in the glow discharge plasma were approximately the same.

The VUV–UV emission spectra from the plasma of saturated water vapor or water vapor–helium mixtures (Fig. 2a) were almost identical. The main constituents of the spectra were broad bands with edges at 313, 286, 262, and 185 nm. The 313-nm band had a fine structure, which was recorded using a higher-resolution spectrometer (Fig. 2b). The 286-nm and 262-nm bands had no fine structure. A typical spectrum of visible emission from the plasma of a He/H_2O mixture is shown in Fig. 3. The emission spectra were identified using the data from [13–15]. In the water vapor plasma, OH radicals are the main excited particles that emit in the VUV–UV range [12]. It is seen in Fig. 2b that the most intense band on the short-wavelength side contains a series of peaks at λ_{max} = 307.0, 309.6 (the main one), 312.4, and 315.2 nm. These peaks do not coincide with the edges of the OH (*A*–*X*; v_1–v_2) electronic–vibrational bands. The closest to the recorded peaks are the OH (*A*–*X*; 0–0) 306.4-nm (*R*-branch), OH (*A*–*X*; 0–0) 308.9-nm (*Q*-branch), OH (*A*–*X*; 1–1) 312.2-nm, and OH (*A*–*X*; 2–2) 318.5-nm bands. A broad band in the 300–310 nm range with peaks at 307.0, 308.3, and 309.1 nm (the main one) was also recorded in the emission from the plasma of an RF discharge in water vapor (P = 100 Pa); in [16], this band was assigned to the emission of the cluster molecules $(H_2O)_2$. The edges of the 286-nm and 262-nm bands correlate to the wavelengths of the OH (*A*–*X*; 1–0) 281.1- to 282.9-nm, OH (*B*–*A*) 278-nm, and OH (*A*–*X*; 2–0) 260.9- to 262.2-nm bands. The UV 185-nm band is close to the OH (*C*–*A*) 179.1-nm band. The control experiments with a glow discharge in He/H_2O = (1–8)/(0.05–0.15)-kPa mixtures show that, under the given discharge conditions, the edge of the VUV band shifts from 185 to 180 nm and a new intense band with λ_{max} = 157 nm, which corresponds to the OH (*B*–*X*) emission, arises. The total emission intensity in

the range 130–190 nm is one order of magnitude higher than the intensity of the 306- to 315-nm band. Based on the correlation between the locations of the edges of characteristic bands in the emission spectrum of the plasma of saturated water vapor and their behavior with decreasing water vapor pressure, these bands can be assigned to the emission of $(OH)_n^*$ and $(OH)_n^* \cdot (H_2O)_m$ ($n \geq 2$, $m \geq 1$) cluster molecules. In the simplest case, they are $(OH)_2^*$ hydroxyl dimers. If the plasma contains cluster water molecules, then the main reaction producing the excited hydroxyl molecules is [17]

$$e + (H_2O)_m \longrightarrow H^- \cdot (H_2O)_{m-1} + OH^*.$$

When two or more OH radicals (one of which is in an excited state) collide, cluster molecules like $(OH)_n^*$ can be produced and then transform into $(OH)_n^* \cdot (H_2O)_m$ clusters via hydration. As a result, the energies of the cluster upper energy levels become lower and the edges of the OH (*A–X*, *C–A*, *B–X*, etc.) characteristic bands shift to the long-wavelength side of the spectrum.

For He/H_2O mixtures, the linear emission of excited hydrogen atoms in the visible spectral region is accompanied by HeI 667.8-nm, 587.6-nm, 501-nm, and 447.1-nm lines. In the emission spectra of the water vapor plasma, a weak OH band with a maximum at λ = 628–630 nm is also observed. In the water vapor plasma, at I_{ch} = 50 mA, the ratio of the intensities of H_α, H_β, and H_γ spectral lines is 1000/40/10, which only qualitatively correlates to the ratio of the effective cross sections for the excitation of these lines via the electron-impact (ε = 50 eV) dissociative excitation of H_2O and H_2 molecules [18]. The ratio of the intensities of HeI 667.8-nm and 587.6-nm spectral lines was found to be 4.2, which was quite different from that obtained using the table data [15] (χ = 0.12). The upper levels of the HeI (^3D, ^1D) lines have an energy of 23.07 eV, whereas the energies of the lower levels of the yellow ($2p\ ^3P^0$) and red ($2p\ ^1P^0$o) HeI lines are 20.96 and 21.22 eV, respectively. The increase in the intensity of the HeI 667.8-nm line may be related to the high-speed reactions depopulating the HeI $2p\ ^1P^0$ state in collisions with water molecules and the products of water dissociation in the discharge.

The intensities of the main emission bands (λ = 313 and 286 nm) from the discharge in a He/H_2O mixture slightly decrease with the helium partial pressure (Fig. 4). The dependences of the intensities of these bands and the $H_{\alpha,\beta}$ and HeI spectral lines on the discharge current are close to linear (Fig. 5). At discharge currents of 3–50 mA, the band and line intensities increase with no tendency to saturation. This indicates that direct electron-impact excitation processes prevail in the plasma under study.

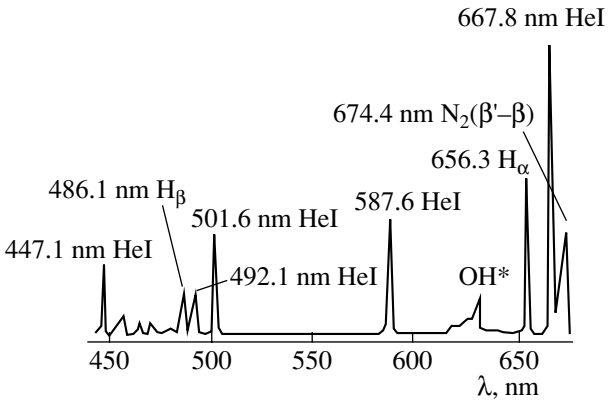

Fig. 3. Visible emission spectrum from the plasma of a glow discharge in a He/H_2O mixture.

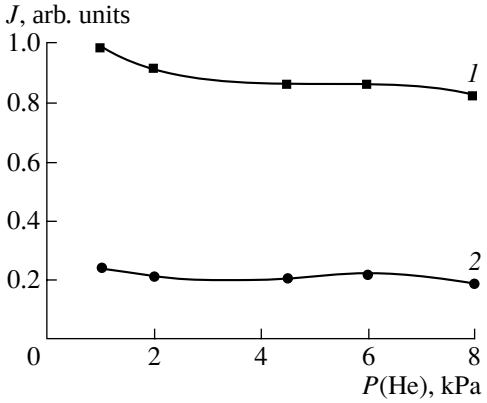

Fig. 4. Intensities of the characteristic emission bands from the plasma of a glow discharge in He/H_2O mixtures vs. the helium partial pressure for a water vapor partial pressure of 2.5 kPa and I_{ch} = 50 mA: λ = (*1*) 306–315 nm and (*2*) 286 nm.

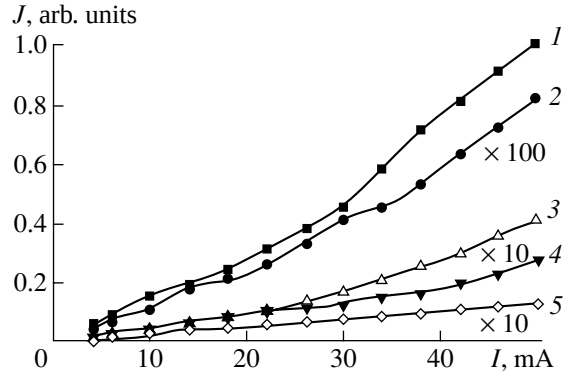

Fig. 5. Intensities of the main emission lines in the visible spectral region from the 1.0/2.5-kPa He/H_2O mixture vs. the discharge current: (*1*) HeI 667.8, (*2*) H_β 486.1, (*3*) HeI 587.6, (*4*) H_α 656.3, and (*5*) HeI 501 nm.

4. CONCLUSIONS

The results of investigations of the optical characteristics of a glow discharge in water vapor and He/H_2O mixtures can be summarized as follows:

(i) At a water vapor partial pressure of 2.5 kPa, the most intense emission bands are broad bands with edges at 309 and 286 nm, which are associated with the spontaneous decay of the excited OH-based cluster molecules.

(ii) At lower water vapor partial pressures of 50–150 Pa, the emission in the wavelength range140–190 nm, which is associated with the OH (*C*–*A*, *B*–*X*) bands, becomes the most intense. This emission is of interest for use in continuous-wave VUV lamps.

(iii) As the parameter *E*/*N* increases by an order of magnitude as compared to that used in the lamp based on the OH (*A*–*X*; 0–0) transition with $\lambda = 306.4$ nm [12] (the average discharge power being the same), the emission in the $\lambda \leq 190$ nm range from either high-lying OH (*C*, *B*) electronic states or OH-based clusters becomes dominant.

(iv) The intensities of the characteristic emission bands from the plasma of saturated water vapor depend slightly on the helium partial pressure, whereas the dependence of the intensities of these bands and the $H_{\alpha, \beta, \gamma}$ and HeI spectral lines on the discharge current indicates that direct electron-impact excitation of atoms and molecules is dominant.

(v) Spectral lines in the visible region are of interest for the optical diagnostics of a glow-discharge plasma (e.g., for the determination of n_e, T_e, and the metastable atom density).

REFERENCES

1. V. D. Rusanov, A. A. Fridman, and G. V. Sholin, Usp. Fiz. Nauk **134**, 185 (1981) [Sov. Phys. Usp. **24**, 447 (1981)].
2. A. A. Mavlyutov, A. I. Mis'kevich, and B. S. Salamakha, Opt. Spektrosk. **76**, 949 (1994) [Opt. Spectrosc. **76**, 847 (1994)].
3. V. L. Bychkov and V. A. Yurovskiĭ, Teplofiz. Vys. Temp. **31**, 8 (1993).
4. Yu. S. Akishev, A. A. Deryugin, V. B. Korol'nik, *et al.*, Fiz. Plazmy **20**, 571 (1994) [Plasma Phys. Rep. **20**, 511 (1994)].
5. E. T. Protasevich, Teplofiz. Vys. Temp. **27**, 1206 (1989).
6. A. N. Zavilopulo, A. I. Dolgin, and M. A. Khodorovsky, Phys. Scr. **50**, 696 (1994).
7. V. M. Milenin, N. A. Timofeev, A. Ya. Vul', *et al.*, Pis'ma Zh. Tekh. Fiz. **26** (18), 63 (2000) [Tech. Phys. Lett. **26**, 835 (2000)].
8. A. K. Shuaibov, Opt. Spektrosk. **88**, 875 (2000) [Opt. Spectrosc. **88**, 796 (2000)].
9. A. K. Shuaibov and A. I. Dashchenko, Kvantovaya Élektron. (Moscow) **30**, 279 (2000).
10. *Concise Physicotechnical Reference Book*, Ed. by K. P. Yakovlev (Fizmatgiz, Moscow, 1962), Vol. 3.
11. Yu. P. Raizer, *Gas Discharge Physics* (Nauka, Moscow, 1987; Springer-Verlag, Berlin, 1991).
12. A. Ya. Vul', S. V. Kidalov, V. M. Milenin, *et al.*, Pis'ma Zh. Tekh. Fiz. **25** (1), 10 (1999) [Tech. Phys. Lett. **25**, 4 (1999)]; Pis'ma Zh. Tekh. Fiz. **25** (8), 62 (1999) [Tech. Phys. Lett. **25**, 321 (1999)].
13. R. W. B. Pearse and A. G. Gaydon, *The Identification of Molecular Spectra* (Chapman and Hall, London, 1963).
14. L. Wallace, Astrophys. J., Suppl. Ser. **7**, 65 (1962).
15. A. R. Striganov and G. A. Odintsova, *Tables of Atomic and Ionic Spectral Lines* (Énergoatomizdat, Moscow, 1982).
16. M. Soskida, in *Abstracts of the 32nd European Group for Atomic Spectroscopy, EGAS, Vilnius, 2000*, p. 314.
17. A. A. Vostrikov, D. Yu. Dubov, and M. R. Predtechenskiĭ, Zh. Tekh. Fiz. **57**, 760 (1987) [Sov. Phys. Tech. Phys. **32**, 459 (1987)].

Translated by N. N. Ustinovskiĭ

Plasma Physics Reports, Vol. 27, No. 10, 2001, pp. 901–903. Translated from Fizika Plazmy, Vol. 27, No. 10, 2001, pp. 955–957.

BRIEF COMMUNICATIONS

Production of H_3^+ Ions in Low-Energy Collisions between Hydrogen Molecular Ions

V. A. Belyaev, M. M. Dubrovin, A. A. Terent'ev, A. E. Trenin, and G. V. Sholin

Nuclear Fusion Institute, Russian Research Centre Kurchatov Institute, pl. Kurchatova 1, Moscow, 123182 Russia

Received April 19, 2001

Abstract—The effective cross section for the $H_2^+ + H_2^+ \longrightarrow H_3^+ + p$ reaction in the energy range 5.7–11.5 eV is measured by the split beam method. The cross-section maximum at an energy of ~8 eV is related to the production of the H_4^{++} compound system. The reaction threshold $W_{thr} \approx 5$ eV provides evidence in favor of the classical model with the H_2^+ ion charge fixed on one of the two nuclei during the entire collision event. © *2001 MAIK "Nauka/Interperiodica".*

Among the processes that lead to the increase in the content of protons in low-temperature plasmas of the gas-discharge sources of proton beams, the reactions involving collisions between H_2^+ ions,

$$H_2^+ + H_2^+ \longrightarrow \begin{cases} H_2^+ + H + p \quad -2.65 \text{ eV} & (1) \\ H + p + H + p \quad -5.30 \text{ eV} & (2) \\ H_2 + p + p \quad -0.82 \text{ eV} & (3) \\ H_3^+ + p \quad +3.18 \text{ eV} & (4) \end{cases}$$

are of significant importance.

Previously, we measured the cross section for one of these reactions, namely, simultaneous dissociation of both colliding ions [reaction (2)] in the energy range 7.5–18.8 eV [1]. The results obtained show that this reaction is of minor importance for the production of protons at interaction energies of several eV, which is characteristic of plasmas of gas-discharge sources. The reason is that the overall probability of proton production in reactions (1)–(4) estimated for the lower limit of the energy range of interest is much higher [2]. Taking into account the fact that the effective cross section for reaction (1) is several times lower than for reaction (2) (see the calculations of [3]), it seems that proton production in collisions between H_2^+ ions at energies lower than 10 eV proceeds mainly via reactions (3) and (4); the former reaction, which has the lowest reaction threshold, results in the production of two protons, whereas the latter is an exothermic process.

The measured energy dependence of the H_3^+ ion production probability in collisions between two H_2^+ ions in an energy range of several electronvolts has a pronounced maximum at 7–8 eV (see figure).

The measurements were carried out by the split beam method [1]. To ensure pair collisions, a ribbon-shaped ion beam is split into two beams and then is focused so that the ion trajectories of the newly formed beams intersect in the focal region at a small angle φ. In the center-of-mass frame, the total kinetic energy of the colliding ions W (the interaction energy) is significantly less than in the laboratory frame. For equal ion masses, we have $W = 0.5\varphi^2 E$. Therefore, it is possible to carry out measurements in an energy range of several electronvolts for particle beams with energies of several keV, which greatly facilitates the experiment. The probability of an elementary process is determined by the production rate of the new (secondary) particles in the beams after they have crossed each other.

The experiments were carried out at the DIVO device (see [1] for details). The system for separating and recording the produced H_3^+ ions was modified taking into account the fact that their energy was 1.5 times higher than that of H_2^+ ions, because both the magnitude and direction of the ion velocity remained almost unchanged in the laboratory frame.

In our experiments, an RF discharge ion source produced H_2^+ ions in various vibrationally excited states. According to the calculations of [4], the ion lifetime outside the source is ~10^6 s. Since the probability of the H_3^+ ion production may depend substantially on the vibrationally excited states of H_2^+ ions at the instant of collision, we decreased the number of vibrationally excited ions in the source using a procedure described in [5]. A hydrogen–neon mixture (rather than pure hydrogen) with a volume ratio of 1 : 5 at a pressure of ~10^{-2} torr was supplied to the source. Under these conditions, among the reactions involving collisions of vibrationally excited $H_2^+(v)$ ions with Ne atoms, the

1063-780X/01/2710-0901$21.00

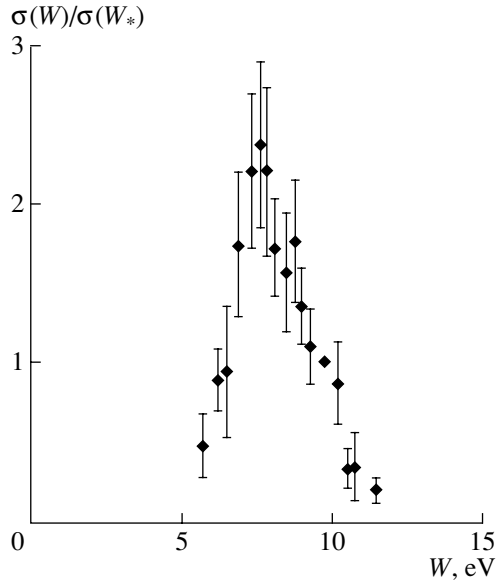

Energy dependence of the effective cross section (normalized to $\sigma(W_*)$, where $W_* = 9.75$ eV) for the $H_2^+ + H_2^+ \longrightarrow H_3^+ + p$ ion–molecular reaction. The value of $\sigma(W_*)$ is no less than 10^{-16} cm^2.

ion–molecular reaction $H_2^+(v \geq 2) + Ne \longrightarrow NeH^+ + H$ proceeds at a high rate because, for $v \geq 2$, it is exothermic. For $v \leq 1$, the reaction is endothermic and proceeds at a low rate [6]. As a result, most of the ions that leave the source and form a beam are in the ground ($v = 0$) and first ($v = 1$) excited states with dissociation energies of 2.645 and 2.374 eV, respectively. Since the estimated reaction threshold for this reaction is 2.1–2.2 eV [7], a certain amount of H_2^+ ($v = 2$) ions with a dissociation energy of 2.118 eV may also be present.

The measurements were carried out in the energy range $W = 5.7$–11.5 eV. The energy dependence of the $\sigma(W)/\sigma(W_*)$ ratio, where $W_* = 9.75$ eV, is shown in the figure. Preliminary calibration measurements showed that, at $W = W_*$, the effective cross section for ion–molecular reaction (4) can be estimated from below by a value equal to approximately 10^{-16} cm^2.

It is reasonable to interpret the results obtained based on the concept of [8], which was successfully used to analyze ion–molecular reactions. According to [8], the H_3^+ ions are produced via the formation of a compound system (in our case, H_4^{++} molecules). At the interaction energies of colliding particles $W < 20$ eV, the energy of molecular electrons changes adiabatically, because the velocity at which the molecules approach each other, $V(H_2^+) \approx (2$–$4) \times 10^6$ cm/s, is much less than the electron velocity $V(e) \sim e^2/\hbar \sim 2 \times 10^8$ cm/s. Since the ion de Broglie wavelength is much less than the molecular size, the collisions can be described within classical mechanics.

The compound system forms when the distance between the H_2^+ ions becomes so small that the electron clouds of the ions overlap. This distance depends not only on the mutual orientation of the H_2^+ molecular axes (linear, T-type, or collinear) but also on the theoretical model used to describe the molecular structure. Within the classical approach, both the hydrogen atom and proton in the H_2^+ molecular ion keep their individuality. In this case, the molecule can be regarded as a dumbbell with a charge concentrated on one of its ends. In contrast, the quantum mechanical approach implies that the electron cloud is distributed uniformly between the two nuclei and, consequently, each end of the dumbbell carries one-half of the proton positive charge. The center of the positive charge of the H_2^+ molecular ion resides exactly midway between the nuclei. As a result, the interaction energy required to create the compound system turns out to be quite different within the quantum mechanical and classical models of the H_2^+ ion. To overcome the Coulomb repulsion during the formation of the H_4^{++} system when the mutual orientation of the molecules is linear, the quantum mechanical model requires an interaction energy of $W_q^{(4)} \approx 7.8$ eV, whereas, in the classical model, we have $W_{cl}^{(4)} \approx 5.0$ eV and the cross section is $\sigma \sim (0.5$–$0.7) \times 10^{-16}$ cm^2. For the T-type mutual orientation of the axes, the classical model predicts $W_{cl}^{(4)} \approx 8.0$ eV and a substantially higher cross section $\sigma^T \sim 2 \times 10^{-16}$ cm^2. In the classical model, the threshold for reaction (3), in which two protons are produced, is $W_{cl}^{(3)} \approx 5.8$ eV for the linear orientation of the molecules and 8.6 eV for the T-type orientation.

In the quantum mechanical model, for the T-type mutual orientation of the molecules, the thresholds for reactions (4) and (3) are $W_q^{(4)} \sim 12.2$ eV and $W_q^{(3)} \sim 13$ eV, respectively. Unlike reactions (3) and (4), which proceed via the formation of the H_4^{++} molecular ion, the dissociation via reaction (1) or (2) can proceed as a direct reaction in which the momentum is transferred directly to the molecular protons. With allowance for the direct reaction (1) and especially reaction (2), the probability of producing the compound system is substantially reduced. According to [9], this probability may become zero when the interaction energy exceeds the threshold for reaction (4) by the so-called critical value

$$W^* = \frac{m_{H_2^+} + m_H}{m_p}(W^A - W^D),$$

where $W^A \sim 4$ eV is the H_2 molecule–proton affinity, W^D is the H_2^+ dissociation energy, and m denotes the masses of the corresponding particles. Consequently, the steep fall in the cross section of reaction (4) is related to the increasing role of the direct reactions (1)–(3).

Thus, the measured thresholds for reactions (2) [1] and (4) can be regarded as evidence in favor of the classical approach to describing the charge distribution during molecular collisions accompanied by ion–molecular reactions proceeding via the formation of compound systems. The main feature of the quantum mechanical model of the H_2^+ molecule is the averaging of the electron wave functions over positions with respect to the nuclei. In this case, a wave function corresponding to the one-center problem is actually used and the question of how often an electron jumps from one center to another remains open. In the classical approach, a proton is attracted to an H atom due to the polarization effect; as the proton moves inside the electron cloud, the attraction force decreases, whereas the Coulomb repulsion between the nuclei increases. Obviously, the equilibrium between nuclei in a molecule can only be dynamical: as the nuclei vibrate, the exchange of the electron cloud between them must correlate to the frequency of these vibrations. Since the duration of the collision event between H_2^+ ions, which results in the creation of the H_4^{++} compound system, is much shorter than the period of nuclei vibrations, the "instant picture" of the electron cloud (rather than the averaged quantum mechanical picture) is of importance. Thus, studying ion–molecular reactions in the near-threshold energy range may provide important data on electron cloud dynamics and its correlation with nuclear vibrations.

ACKNOWLEDGMENTS

We are grateful to N.N. Semashko, V.M. Kulygin, and Yu.M. Pustovoĭt for their continuing interest in this work and assistance.

REFERENCES

1. V. A. Belyaev, M. M. Dubrovin, N. N. Semenov, and A. I. Khlopkin, Fiz. Plazmy **20**, 316 (1994) [Plasma Phys. Rep. **20**, 287 (1994)].
2. V. A. Belyaev, M. M. Dubrovin, and A. I. Khlopkin, Pis'ma Zh. Tekh. Fiz. **8**, 1399 (1982) [Sov. Tech. Phys. Lett. **8**, 601 (1982)].
3. V. A. Belyaev, M. M. Dubrovin, L. I. Men'shikov, and A. I. Khlopkin, Preprint No. 762/12 (Inst. of Atomic Energy, Moscow, 1983); V. A. Belyaev, M. M. Dubrovin, L. J. Men'shikov, and A. N. Khlopkin, INDC (CCP)-24/GA (IAEA, Vienna, 1984).
4. D. R. Bates and G. Poots, Proc. Phys. Soc. London, Sect. A **66**, 784 (1953).
5. Sen Amarjit, J. W. McGowan, and J. B. A. Mitchell, J. Phys. B **20**, 1509 (1987).
6. W. A. Chupka and M. E. Russel, J. Chem. Phys. **49**, 5426 (1968).
7. Z. Herman and V. Pac'ak, Int. J. Mass Spectrom. Ion Phys. **24**, 355 (1977).
8. O. B. Firsov, Zh. Éksp. Teor. Fiz. **42**, 1307 (1962) [Sov. Phys. JETP **15**, 906 (1962)].
9. E. E. Nikitin, *Theory of Elementary Atomic and Molecular Processes in Gases* (Khimiya, Moscow, 1970; Clarendon, Oxford, 1974).

Translated by N. N. Ustinovskiĭ

Plasma Physics Reports, Vol. 27, No. 10, 2001, pp. 904–906. From Fizika Plazmy, Vol. 27, No. 10, 2001, pp. 958–960.

BRIEF COMMUNICATIONS

Potential of a Test Charge in a Dust–Electron Plasma[1]

P. K. Shukla[1, 2] and L. Stenflo[1]

[1]*Department of Plasma Physics, Umeå University, SE-90187 Umeå, Sweden*

[2]*Institut für Theoretische Physik IV, Fakultät für Physik und Astronomie, Ruhr-Universität Bochum, D-44780 Bochum, Germany*

Received January 18, 2001; in final form, April 19, 2001

Abstract—The potential of a slowly moving test charge in a positive-dust–electron plasma is calculated taking into account dust grain charge fluctuations, as well as collisions between neutral atoms and electrons and dust grains. The results should be useful for understanding the shielding in a dusty plasma sheath with levitated grains. © *2001 MAIK "Nauka/Interperiodica".*

It is well known [1–3] that the far-field potential of a moving test charge in a uniform electron–ion plasma decreases as the inverse cube of the distance r from the test charge. On the other hand, the far-field potential in a collisional electron–ion plasma [4, 5] may decay as r^{-2}.

Recently, several authors [6–9] investigated the potential around charged dust grains in a multicomponent dusty plasma when the dust grains are negatively charged. However, the dust grains can also be charged positively [10, 11] when they are heated by infrared/visible lasers or irradiated by UV radiation. This leads to a positive-dust–electron (PDE) plasma because most of the ions from the background are attached to the surface of the dust grains, which, in turn, acquire huge positive charges. Since, due to different charging models for positive dust grains, the dielectric properties [12] of such a two-component dusty plasma differ significantly from those of a plasma with negatively charged dust grains, it is of urgent interest to study the test charge potential in a collisional PDE plasma. This is the objective of this paper.

The electric potential of a test particle (with charge q_t) moving with a constant velocity $\mathbf{v}_0$ is [1]

$$\phi(\mathbf{R}, t) = \frac{q_t}{2\pi^2}\lim_{\epsilon \to 0}\int \frac{d\mathbf{k}\exp(i\mathbf{k}\cdot\mathbf{r} - \epsilon k)}{k^2 D(\mathbf{k}, -\mathbf{k}\cdot\mathbf{v}_0)}, \qquad (1)$$

where $\mathbf{r} = \mathbf{R} - \mathbf{v}_0 t$ and $D(\mathbf{k}, -\mathbf{k}\cdot\mathbf{v}_0)$ is the dielectric function of the PDE plasma. Following Montgomery *et al.* [1], the term $\lim_{\epsilon \to 0}\exp(-\epsilon k)$ has been included to ensure proper convergence of the integrals.

The calculation of the dielectric function for longitudinal disturbances in a PDE plasma containing a sufficient number of immobile neutrals requires knowledge of the number density perturbations of the electron and dust fluids. Employing the recently proposed model of Shukla [12], which accounts for the dust grain charge fluctuations, we readily obtain, for $|\mathbf{k}\cdot\mathbf{v}_0| \ll kv_{tj}$, the dielectric function

$$D(\mathbf{k}, -\mathbf{k}\cdot\mathbf{v}_0) = 1 + \chi_e + \chi_d + \chi_q. \qquad (2)$$

For $|\mathbf{k}\cdot\mathbf{v}_0| \ll \nu_{jn} \ll kv_{tj}$, where ν_{jn} is the effective collision frequency of the particle species j (j equals e for the electrons and d for the dust grains) with the neutrals and $v_{tj} = (T_j/m_j)^{1/2}$ is the thermal speed, the dielectric susceptibilities for our purposes are

$$\chi_e \approx \frac{k_e^2}{k^2}\left[1 - i\sqrt{\frac{\pi}{2}}\frac{\mathbf{k}\cdot\mathbf{v}_0}{kv_{te}}\left(1 + \frac{\nu_{en}}{kv_{te}}\right)\right], \qquad (3)$$

$$\chi_d \approx \frac{k_d^2}{k^2}\left[1 - i\sqrt{\frac{\pi}{2}}\frac{\mathbf{k}\cdot\mathbf{v}_0}{kv_{td}}\left(1 + \frac{\nu_{dn}}{kv_{td}}\right)\right], \qquad (4)$$

$$\chi_q = \frac{F}{k^2\lambda_e^2}\frac{\omega_{pe}}{(\nu + i\mathbf{k}\cdot\mathbf{v}_0)}, \qquad (5)$$

where T_j is the temperature; m_j is the mass; and $\nu_{en} \sim \sigma_{en}v_{te}n_n$ and $\nu_{dn} \sim \pi r_d^2 v_{tn}n_n m_n/m_d$ are the electron–neutral and dust–neutral (for hard sphere) collision frequencies, respectively (here, σ_{en} is the cross section for collisions of electrons with neutrals; n_n and m_n are the neutral density and mass, respectively; and v_{tn} is the thermal speed of the neutrals). The inverse Debye radii of the two species are defined as $k_e = \lambda_e^{-1} = (T_e/4\pi n_{e0}e^2)^{-1/2}$ and $k_d = \lambda_d^{-1} = (T_d/4\pi n_{d0}Z_{d0}^2 e^2)^{-1/2}$, where e is the magnitude of the electron charge and the equilibrium densities are related by $n_{e0} = Z_{d0}n_{d0}$. Here, Z_{d0} refers to the number of positive charges that reside on the surface of the dust grains, which are assumed to be spherical with radius r_d. We also have introduced the notation $F = 4\pi n_{d0}\lambda_e r_d^2(1 + \gamma_0)$, $\gamma_0 = Z_{d0}e^2/r_d T_e \equiv e\varphi_0/T_e$, and $\omega_{pe} = (4\pi n_{e0}e^2/m_e)^{1/2}$. Furthermore, ν is equal to the fre-

[1] This article was submitted by the authors in English.

quency ν_1 associated with dust charge fluctuations during the thermionic emission of the electrons and is equal to ν_2 during the emission of the electrons from the dust grain surface due to UV radiation [12]:

$$\nu_1 = \frac{\omega_{pe} r_d}{\sqrt{2\pi}\lambda_e}\left[1 + \frac{2}{n_{e0}}\left(\frac{m_e T_e}{2\pi\hbar^2}\right)^{3/2}\gamma_0 \exp(-\gamma_0 - W/T_e)\right],$$

$$\nu_2 = \frac{\omega_{pe} r_d}{\sqrt{2\pi}\lambda_e}\left[1 + \sqrt{2\pi}\frac{JY}{4\pi n_{e0} v_{te}}\sigma \exp(-\sigma\gamma_0)\right],$$

where $\hbar$ is the Planck constant, W is the work function, J is the UV photon flux, Y is the yield of photons, $\sigma = T_e/T_p$, and T_p is the average temperature of the photoelectrons. We note that χ_q is associated with the dust grain charge fluctuations [12] caused by the imbalance of the oscillating electron currents that are induced by the moving test charge in our PDE plasma. We have assumed that the electron mean free path in the gas is much larger than the dust radius. Furthermore, the efficiency of absorption of UV radiation is on the order of unity for $2\pi r_d/\lambda \gtrsim 1$, where λ is the radiation wavelength. Rosenberg *et al.* [11] have discussed in detail the underlying physics of positively charged dust grains.

Shukla [12] has shown that the dust charge fluctuations cause spatiotemporal damping of the dust acoustic waves in a PDE plasma. Below, we examine the influence of collisions and dust charge perturbations on the far-field potential of a moving test charge.

Let us consider the case where $\nu \gg |\mathbf{k}\cdot\mathbf{v}_0|$, so that dielectric function (2) takes the form

$$D(\mathbf{k}, -\mathbf{k}\cdot\mathbf{v}_0) \approx 1 + \frac{1}{k^2\lambda_0^2} - i\sqrt{\frac{\pi}{2}}\sum_{j=e,d}\frac{\mathbf{k}\cdot\mathbf{v}_0}{k^3 v_{tj}\lambda_j^2}\left(1 + \frac{\nu_{jn}}{k v_{tj}}\right) - i\frac{F}{k^2\lambda_e^2}\frac{\omega_{pe}\mathbf{k}\cdot\mathbf{v}_0}{\nu^2}, \quad (6)$$

where $\lambda_0^{-2} = \sum_{j=e,d}\lambda_j^{-2} + \lambda_e^{-2} F\omega_{pe}/\nu \equiv \lambda_e^{-2}\delta$ and $\delta = 1 + (Z_{d0}T_e/T_d) + F\omega_{pe}/\nu$. It turns out that the effective equilibrium electron number density $n_{e0}\delta$ in a PDE plasma is larger than n_{e0}. We note that, for typical laboratory dusty plasma parameters, namely, $n_{e0} \sim 10^8$ cm^{-3}, $n_{d0} \sim 10^6$ cm^{-3}, and $T_e \sim 1$ eV, we obtain $F\omega_{pe}/\nu \sim 7$ for $r_d \sim 1$ μm and $Z_{d0} \sim 100$.

Since our test charge is supposed to move very slowly ($|\mathbf{v}_0| \ll v_{tj}$), we have from expression (6)

$$\frac{1}{D} \approx \frac{k^2\lambda_0^2}{1 + k^2\lambda_0^2} + i\frac{k^4\lambda_0^4}{(1 + k^2\lambda_0^2)^2} \times\left[\sqrt{\frac{\pi}{2}}\sum_{j=e,d}\frac{\mathbf{k}\cdot\mathbf{v}_0}{k^3 v_{tj}\lambda_j^2}\left(1 + \frac{\nu_{jn}}{k v_{tj}}\right) + \frac{F}{k^2\lambda_e^2}\frac{\omega_{pe}\mathbf{k}\cdot\mathbf{v}_0}{\nu^2}\right]. \quad (7)$$

Substituting Eq. (7) into Eq. (1) and carrying out the integration in a straightforward manner, we readily obtain

$$\phi \approx \frac{q_t}{r}\exp\left(-\frac{r}{\lambda_0}\right) + q_t v_0\left(\frac{\alpha_2}{r^2} + \frac{\alpha_3}{r^3} + \frac{\alpha_4}{r^4}\right)\cos\gamma, \quad (8)$$

where $\alpha_2 \approx \sum \nu_{jn}\lambda_0^4/\lambda_j^2 v_{tj}^2$, $\alpha_3 \approx \sum \lambda_0^4/\lambda_j^2 v_{tj}$, and $\alpha_4 \approx \lambda_0^4 F\omega_{pe}^2/\lambda_e\nu^2 v_{te}$. Furthermore, γ is the angle between $\mathbf{r}$ and $\mathbf{v}_0$ and $r = |\mathbf{R} - \mathbf{v}_0 t|$ is the distance between the test charge and the observation point. The first term on the right-hand side of Eq. (8) is the usual Debye shielding term in which the electron Debye radius is reduced by a factor of $1/\sqrt{\delta}$ due to the consideration of the dust charge fluctuations in a PDE plasma. The α_3 term on the right-hand side of Eq. (8) is the far-field potential of a moving test charge caused by Landau damping, while the α_2 and α_4 terms represent the far-field potentials associated with collisions (between neutrals and electrons/dust grains) and dust charge perturbations, respectively. For large r ($r \gg \lambda_0$), we note that $\exp(-r/\lambda_0)$ can be so small that the first term in Eq. (8) is smaller than the three last (small) terms. Furthermore, we observe that the contribution of the α_2 term is smaller than that of the α_3 term (i.e., the far-field term which is well known in plasmas [1, 2]) for $r \ll (\sum \omega_{pj}^2/v_{tj}^3)/\sum \nu_{jn}\omega_{pj}^2/v_{tj}^4$.

In conclusion, we have investigated the potential around a slowly moving (in comparison with the electron and dust thermal speeds) test charge in an unmagnetized plasma whose constituents are electrons and positively charged dust grains. By employing an appropriate dielectric constant for such a dusty plasma, which also includes the contribution from dust grain charge fluctuations, we have derived an expression for the test charge potential. It is found that the Debye shielding as well as the far-field potentials of a moving test charge are considerably affected by the dust charge fluctuation dynamics. In fact, in our dusty plasma, the electron Debye screening radius is shorter than that in the electron–ion plasma; this, in turn, yields a weaker Debye–Hückel potential. Furthermore, the newly found far-field potentials are also significantly affected by collisions and dust charge perturbations. Finally, we stress that the results of our investigation should be useful for understanding the electric field profiles around a test charge in low-temperature laboratory [13] and space [14–16] plasmas in which dust grains are positively charged.

ACKNOWLEDGMENTS

This study was supported in part by the Swedish Natural Science Research Council, as well as by the European Union through the Human Potential Research and Training Network for carrying out the

project entitled “Complex Plasmas: The Science of Laboratory Colloidal Plasmas and Mesospheric Charged Dust Aerosols” through contract no. HPRN-CT-2000-00140.

REFERENCES

1. D. Montgomery, G. Joyce, and R. Sugihara, Plasma Phys. **10**, 681 (1968).
2. G. Cooper, Phys. Fluids **12**, 2707 (1969).
3. C. R. James and F. Vermeulen, Can. J. Phys. **48**, 349 (1970).
4. L. Stenflo, M. Y. Yu, and P. K. Shukla, Phys. Fluids **16**, 450 (1973).
5. L. Stenflo and M. Y. Yu, Phys. Scr. **8**, 301 (1973); M. Y. Yu. R. Tegeback and L. Stenflo, Z. Phys. **264**, 341 (1973).
6. J. E. Daugherty, R. K. Porteous, M. D. Kilgore, and D. B. Graves, J. Appl. Phys. **72**, 3934 (1992).
7. P. K. Shukla, Phys. Plasmas **1**, 1362 (1994).
8. O. Otani and A. Bhattacharjee, Phys. Rev. Lett. **78**, 1468 (1997); G. Lapenta, Phys. Plasmas **6**, 1442 (1999).
9. M. Lampe, G. Joyce, G. Ganguli, and V. Gavrishchaka, Phys. Plasmas **7**, 3851 (2000).
10. A. P. Nefedov, O. F. Petrov, and S. A. Khrapak, Fiz. Plazmy **24**, 1037 (1998) [Plasma Phys. Rep. **24**, 1037 (1998)].
11. M. Rosenberg and D. A. Mendis, IEEE Trans. Plasma Sci. **23**, 177 (1995); M. Rosenberg, D. A. Mendis, and D. P. Sheehan, IEEE Trans. Plasma Sci. **24**, 1422 (1996); **27**, 239 (1999).
12. P. K. Shukla, Phys. Rev. E **61**, 7249 (2000).
13. V. E. Fortov, A. P. Nefedov, O. S. Vaulina, *et al.*, Zh. Éksp. Teor. Fiz. **114**, 2004 (1998) [JETP **87**, 1087 (1998)]; A. A. Samaryan, O. S. Vaulina, A. P. Nefedov, *et al.*, Zh. Éksp. Teor. Fiz. **118**, 119 (2000) [JETP **91**, 106 (2000)].
14. O. Havnes *et al.*, J. Geophys. Res. **101**, 10839 (1996).
15. M. Horanyi, B. Walch, S. Robertson, and D. Alexander, J. Geophys. Res. **103**, 8575 (1998).
16. B. A. Klumov, S. I. Popel, and R. Bingham, Pis’ma Zh. Éksp. Teor. Fiz. **72**, 524 (2000) [JETP Lett. **72**, 364 (2000)].